From the Inner Shelf to the Deep Sea: Depositional Environments on the West Antarctic Peninsula Margin – A Sedimentological and Seismostratigraphic Study (ODP Leg 178)

Vom inneren Schelf zur Tiefsee: Ablagerungsräume am Westrand der Antarktischen Halbinsel – Eine sedimentologische und seismostratigraphische Studie (ODP Leg 178)

Tobias Mörz

Ber. Polarforsch. Meeresforsch. 427 (2002)
ISSN 1618 - 3193

TOBIAS MÖRZ

GEOMAR Forschungszentrum für marine Geowissenschaften
Wischhofstr. 1-3
D-24148 Kiel

Die vorliegende Arbeit ist die inhaltlich unveränderte Fassung einer Dissertation, die 2001 der Mathematisch-Naturwissenschaftlichen Fakultät der Christian-Albrechts-Universität zu Kiel vorgelegt wurde.

Eine farbige elektronische Fassung der Dissertation ist als PDF-Datei unter folgender Internet-Adresse verfügbar: http://e-diss.uni-kiel.de/diss_553/

Contents

Abstract

Aim of this study was to describe and characterize three typical West Antarctic Peninsula continental margin depositional environments. Seismic, downhole and laboratory tools and techniques were applied to record physical and chemical proxies for a mulifacetted and differenciated understanding of the particular environments.

A detailed seismostratigraphic characterisation of the unique Antarctic inner and outer shelf along the passive margin of the West Antarctic Peninsula has been complemented by logging informations that are tied to the seismic profiles via a new continuous depth vs. velocity profile. Logging information revealed that the shelf topsets consist of a series of stacked lodgement tills deposited as basal moraines. The palaeo-slopes (foresets) contain a diamictite / fines succession. Topsets and foresets are linked to the same depositional mechanism, advance and retreate of shelf ice sheets. Foresets have a better preservation potential since all deposits below the shelf break are protected from direct ice erosion. Imbricated fabric in ~200 mbsf (~2 Ma) with pebbles dipping to the S demonstrate deposition below a S-N oriented ice stream (consistent with the S-N oriented of a modern outlet-trough on the shelf west of Anvers Island) and witness the longevity of glacial outlet troughs on the shelf. Sealevel fall overcompensated by increased isostatic subsidence due to ice build-up that affected the continent and the adjacent shelfs is the most likely explanation for time synchronous start of topset preservation at ~2.8 Ma observed in Antarctic Peninsula and East Antarctic shelf records in conjunction with Nothern Hemnisphere Glaciation.

Based on morphological features of a new multibeam map and published low resolution seismic data, a new tectonic model in the context of the general margin evolution was established for Palmer Deep. Two major phases of deformation along one conjugate set of faults are addressed. Phase 1 is N-S compressional with a left lateral strike slip component and associated lateral E-W extensional escape. Phase 2, related to the back arc type Bransfield Strait extension, is N-S extensional with left lateral movement on the NW trending faults and right lateral movement on the NE trending faults. The ultra high resolution Holocene to latest Pleistocene record from Palmer Deep (> 25 cm/ka sedimentation rates) is divided into 5 climato-stratigraphic zones (Last Glacial Maximum-Neoglacial) on the base of core logs and sedimentological findings. New synthetic seismograms closely tie the core-based physical properties to high resolution single channel Deep Tow Boomer records (HDTB) and allow a basin wide mapping of the stratigraphic units. Digitization of the HDTB data with new processing soft- and hardware setup significantly improved vertical (< 0.4 m) resolution and horizontal coherency of the profiles and allowed the identification of a small-scale mud diapir

(> 4 m height, 30 m width) and pock marks. Mass flow introduced boyancy imbalance is identified to drive the diapirism at the foot of the steep basin walls.

Large mounts on the continental rise along the Antarctic Peninsula margin between 63°S and 69°S and within 200 km of the shelf break are interpreted as sediment drifts, separated by turbidity current channels. The internal seismostratigraphic drift architecture reveals an early pre-drift stage above the basement, a period of pronounced drift growth, and a late period of drift maintenance. Attempts to improve core to seismic ties with the use of synthetic acoustic profiles have been only partially successful. Instead in-situ velocity check shots with a downhole toole provided the most accurate depth vs. traveltime information. Fine-fraction (<63 µm) grain-size analyses of 530 samples allow a thorough assessment of the downhole grain-size distribution at Drift 7. The data is statistically processed and displayed using a variety of methods. Following an approach by Friedmann, skewness and standard deviation (sorting) have been chosen to differentiate the grain size data set into 3 distinct populations. Grain-size populations 1 and 2 are respectively identified as the result of glacial and interglacial mass wasting processes of the slope. Sediment samples of Population 3 are the result of hemipelagic settling modified by bottom current activity. The assessment of these spatial and temporal distribution of the poulations in the light of an existing facies model resulted in a simpler but directly process-related conceptual model of the sequences. Using a special standardized moving window counting routine the population 1 data has been transformed into a regional Antarctic Peninsula ice volume indicator curve that is in good agreement with the Lear et al., 2000 data over the past 10 Ma. This regional ice volume curve for the Antarctic Peninsula is the most significant finding of this thesis. All evaluated proxy data prove that the early Pliocene was a time of reduced global- and Antarctic ice volume (-70%) and sea ice extent. Never before and after during the last 10 Ma was palaeo productivity higher at the rise than during this time. During the late Miocene the ice sheet was highly dynamic with frequent advances and retreats. Starting at 3.2 Ma in concert with the Northern Hemisphere Glaciation the ice sheet became a permanent feature occupying the shelf during most of the glacial half cycles.

The new results from the Antarctic Peninsula illustrate the complex dependencies and inter-relationships between the continental ice, shelf, slope and rise and demonstrate the potential of drift settings in reconstructing Antarctic glacial history.

Zusammenfassung

Thema dieser Arbeit ist die Charakterisierung und Beschreibung von Ablagerungsräumen am Kontinentalrand der westlichen Antarktischen Halbinsel anhand dreier Fallbeispiele. Geophysikalische und chemische Proxiparameter aus Bohrloch- und Labormessungen wurden mit seismischen Profilen kombiniert, um interdisziplinär zu einem umfassenden Verständnis der verschiedenen Sedimentationsräume zu gelangen.

Eine detaillierte seismostratigraphische Charakterisierung des einzigartigen antarktischen inneren und äußeren Schelfs entlang des passiven Kontinentrandes der westlichen Antarktischen Halbinsel wurde vervollständigt durch Bohrlochdaten, die mit Hilfe eines neuen Geschwindigkeitsprofiles auf seismische Profile übertragen wurden. Die Bohrlochdaten zeigen, dass die Schelf *topsets* aus übereinandergelagerten Grundmoränenkörpern bestehen wohingegen die Paläohänge (*foresets*) aus Wechsellagen von groben Tilliten und feinerem Material aufgebaut sind. *Topsets* und *foresets* entstehen durch den Materialtransport von vorstoßendem oder sich zurückziehendem Schelfeis. *Foresets* sind gewöhnlich besser erhalten, da alle Ablagerungen unterhalb der Schelfkante vor direkter Eiserosion geschützt sind. Nach Süden einfallende Gerölle mit Dachziegellagerung in 200 m Tiefe (~2 Ma alt) beweisen die S-N Stoßrichtung des Eises (die auch mit der modernen Orientierung eines großen Schelfeistroges westlich von Anvers Island übereinstimmt) und die Langlebigkeit dieser Schelfeisströge. Ab 2.8 Ma kommt es zur Erhaltung von *topsets* der Schelfe der antarktischen Halbinsel und der Ost-Antarktis. Bei insgesamt fallendem eustatischem Meerespiegel im Zuge der Vereisung der nördlichen Halbkugel kann dies am besten durch eis-induzierte Subsidenz erklärt werden, die den Kontinent und die angrenzenden Schelfe zeitgleich erfasst und den eustatischen Meeresspiegelabfall kompensiert.

Für die Palmer Deep Depression wurde ein strukturelles Modell anhand einer neuen Multi-Beam-Karte und bestehender Seismik erstellt. Kernstück des Modells ist ein konjungiertes Störungssystem, das während zweier Deformationsphasen aktiv war. In Phase 1 erfolgte N-S Einengung mit Linksseitenversatz verbunden mit lateraler E-W Extension. Phase 2 ist mit der *back arc* ähnlichen Extensiongeschichte der Bransfield Straße verbunden und ist charakterisiert durch N-S Extension mit Linksseitenversatz entlang der NW und Rechtsseitenversatz entlang der NE verlaufenden Störungszonen. Die holozänen bis spätpleistozänen ultra-hochauflösenden Kerne von Palmer Deep (Sedimentationsraten > 25 cm/ka) lassen sich aufgrund von physikalischen und sedimentologischen Befunden in 5 klimatostratigraphische Zonen einteilen (Letztes Glaziales Maximum bis zum Neoglazial). Neue synthetische Seismogramme erlauben eine genau Korrelation der physikalischen Kerndaten mit der hochauflösenden tiefgeschleppten Boomer Seismik (HDTB) und somit ein beckenweites Kartieren der stratigraphischen Einheiten. Mit neuentwickelter Software und

unkonventioneller Hardware konnten die analogen HDTB-Profile digitalisiert werden. Dies führte zu einer deutlichen Verbesserung der vertikalen Auflösung (< 0.4 m) und der lateralen Kohärenz und die Entdeckung eines Miniatur-Schlammdiapirs (> 4 m Höhe, 30 m Durchmesser) und Pockmarken. Auftriebsungleichgewichte durch Hangrutschungen am Fuße der steilen Beckenwände erklären den Diapirismus.

Erhebungen am Kontinentalfuß entlang der Antarktischen Halbinsel zwischen 63°S und 69°S im Abstand von bis zu 200 km von der Schelfkante werden als sedimentäre Driftkörper interpretiert, die von Turbiditrinnen getrennt werden. Die interne Driftstruktur lässt drei Stadien erkennen: Vordriftstadium, Hauptdrift-Wachstum und ein spätes Stadium des Drifterhaltes. Versuche mit Hife von synthetischen Profilen die Korrelation der Kerne zu den seismischen Profilen zu verbessern waren nur zum Teil erfolgreich. Vertikale Bohrlochseismik ergab in diesem Fall die genauesten Laufzeit-/ Tiefen-Informationen. Mit Hilfe von 530 Feinfraktionsanalysen wurde eine detaillierte Tiefenverteilung des Korngrößenspektrums an Drift 7 erstellt. Die Ausgangsdaten wurden mit verschiedensten statistischen Methoden nachbearbeitet und dargestellt. Nach einer Methode von Friedmann konnten die Daten mit Hilfe ihrer Sortierungs- und Schiefewerte in drei klar abgegrenzte Populationen eingeteilt werden. Population 1 und 2 konnten entsprechend glazialen und interglazialen Hangrutschungsprozessen zugeordnet werden. Sedimente der Population 3 entstammen hingegen durch Bodenwasserströmung modifizierten hemipelagischen Ablagerungen. Der Vergleich der räumlichen und temporären Verteilung der Populationen mit einem existierenden Fazies-Model führte zu einem vereinfachten prozess-orientierten Sequenzmodel. Mit Hilfe einer speziellen, normierten Fenstertechnik wurde eine regionale Eisvolumenkurve für die Antarktische Halbinsel der letzten 10 Ma erstellt, die sehr gut mit globalen Daten von Lear et al., 2000 übereinstimmt. Die neue Eisvolumenkurve stellt das wichtigste Ergebnis dieser Arbeit dar. Das Untere Pliozän ist durch 70% reduziertes Eisvolumen, reduziertes Meereis und die bei weitem höchste Paläoproduktivität der letzten 10 Ma gekennzeichnet. Während des späten Miozäns zeigt das Eisschild ein sehr dynamisches Verhalten mit wiederholtem Vorstoß und Rückzug. Im Zuge der Vereisung der nördlichen Halbkugel, ab 3.2 Ma, wird das Eisschild stabiler und nimmt während der Glazialzeiten große Teile des Schelfs ein.

Die vorgestellten Ergebnisse veranschaulichen die komplexen Beziehungen und Abhängigkeiten zwischen kontinentalem Eis, Schelf, Hang und Hangfuß und demonstrieren das große Potential der Driftkörper bei der Rekonstruktion der glazialen Geschichte der Antarktis.

Danksagung

Herrn Prof. William Hay (GEOMAR, Kiel) gebührt mein herzlicher Dank für die Betreuung meiner Arbeit, fundiertem, weitblickenden, fachlichen Rat und die praktische Unterstützung beim Schreiben. Danken möchte ich Ihm auch für die unermüdliche, aufopferungsvolle Verbesserung des englischen Manuskriptes.

Herrn Prof. Jörn Thiede (AWI, Bremerhaven und GEOMAR, Kiel) und Dr. Warner Brückmann danke ich für die geduldige Unterstützung und die Projektleitung des DFG Projektes TH/200-37-1/2 in dessen Rahmen meine Arbeit entstand. Dr. Warner Brückmann danke ich besonders für seine Begleitung durch die Irrungen und Wirrungen des institutionalisierten Forscherlebens, die Ermöglichung von Forschungsaufenthalten im Ausland und seine Unterstützung bei der Bewerbung um die Teilnahme an ODP Leg 178. Meinen ganz herzlichen Dank auch an Frau Ortrud Runze, die mit Akribie und großer Geduld formelle Konsistenz in meine Arbeit gebracht hat.

Den JOIDES RESOLUTION Fahrtteilnehmern (Carlottta Escutia, Christine Lauer, Rob Laronga, Trevor Williams, Thomas Wolf-Welling, Paula Weiss, Carol Pudsey und Eugene Domack) und Co-Chiefs von Leg 178 möchte ich danken für die Aufnahme in ihrer Mitte, die unvergesslichen Erlebnisse während Leg 178 und die wissenschaftliche Zusammenarbeit, Bereitstellung von Abbildungen und Daten, und Miteinbeziehung bei der Bearbeitung von Proben und Profilen nach Abschluss von Leg 178. Insbesonders Angelo Camerlenghi und dem "Programma Nazionale di Ricerche in Antartide", Italy, danke ich für die Bereitstellung von reflexionsseismischen Profilen. Danke auch den Reviewern Christian Bücker, Giorgio Fontolan und Trevor Williams, die meine, in dieser Arbeit enthaltenen Veröffentlichungen, substanziell verbessert haben.

Dirk Kläschen (GEOMAR, Kiel) gilt mein Dank für eine Einführung in das Programm „Seismos" und seine unschätzbare Hilfe bei der Bearbeitung digitalisierter HUNTEC Daten. Danken möchte ich auch für die Gelegenheit, viel über das Prozessing gelernt zu haben und für seine Geduld beim Zuhören meiner Problemschilderungen.

Kate Moran, Larry Mayer, Dave Mosher, Robert Courtney, Austin Beus und vielen anderen Mitarbeitern und Ehemaligen des Bedford Institute of Oceanography, Dartmouth, Canada, danke ich für die Einführung in die Laborarbeit an Kernen und die grundlegende Vermittlung der Voraussetzungen für das seismische Modellieren.

Die wissenschaftlichen Hilfskräfte Daniel A. Hepp, Sina Müller und Dirk Harrie haben wesentlich zum effektiven Aufbereiten der Proben und der Umsetzung von unzähligen Grafiken beigetragen.

Für eine menschliche Atmosphäre und Integration in die Abteilung Paläo-Ozeanologie am GEOMAR hat vor allen Dingen die "Betriebssportgruppe Dart" gesorgt. Ihre Mitglieder - Manu (Danke für die Lösung von Computer- und Karten-Wehwehchen), Jan (Danke für Literatur) Sascha (Freude an der Geologie), Stefan, Claudia und Carolyn – haben manchen grauen Tag mit Freundlichkeit und Ironie erhellt.

Ein großes Dankeschön and meine Eltern und meine Großmutter, die mich von Anfang an für die Schönheit unserer natürlichen Umwelt und viele ihrer Mechanismen sensibilisiert haben. Meinen Schwiegereltern und Eltern möchte ich für die Unterstützung danken, mit der sie unsere junge Familie über so manche finanziellen Engpässe und mentale Tiefpunkte hinweggeholfen hat. Ganz besonders danke ich meiner Frau Martina, die mir durch ihre Hilfe und ihr Verständnis viel Kraft während der Endphase meiner Arbeit gab.

1 Introduction to Antarctic Peninsula Geology & ODP LEG 178

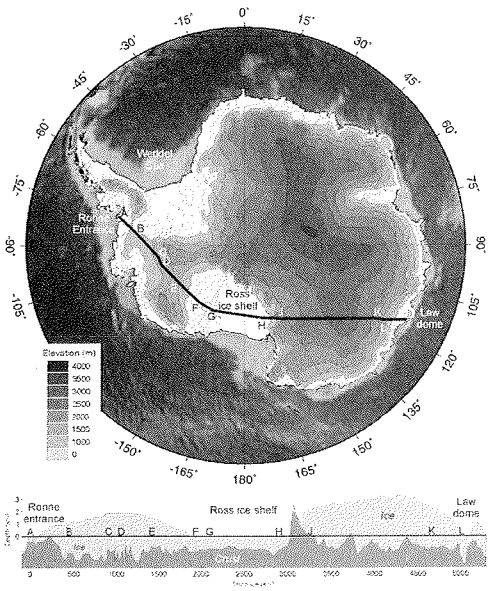

Fig. 1.1. Antarctica and the Antarctic ice sheets. Elevation of ice sheets show on East Antarctica the continental ice sheet and on West Antarctica the marine-based ice sheet, that is largely grounded below sea-level. The history and stability of these ice sheets differ: The West Antarctic ice sheet is less stable and developed later (late Miocene) than the East Antarctic ice sheet, which is believed to have developed to its present form by the middle Miocene (~14 Ma) (map modified from Kennett and Hodell, 1995).

With a surface area of 14.11 $*10^6$ km^2 and an ice cover up to 4.5 km thick (average ice thickness: ~2.5 km) over 98% of the land surface, Antarctica is the coldest, driest and highest continent. It is home of more than half of the world's continental ice (Geographie der Erde, 2000)[1]. Starting in late Eocene time Antarctica became the key player in determining the world's modern climatic fate (Lawver et al., 1992; Fitzgerald, 1999; Exon et al., 2000). The role of the West Antarctic ice sheet is especially important since most of it is grounded below sea-level (Fig. 1.1) and therefore susceptible to decay under changing environmental conditions (Barrett, 1996; Scherer, 1993).

This introductory chapter explains briefly the history and role of Antarctica, the special situation of the Antarctic Peninsula, modern oceanic conditions, the aim of ODP Leg 178 and my motivation to write this thesis.

[1] Verlagshaus Stuttgart im Bertelsmann Lexikon Verlag: Geographie der Erde. Neue Enzyklopädie. Stuttgart, Gütersloh, München, 2000.

1.1 Tectonic History

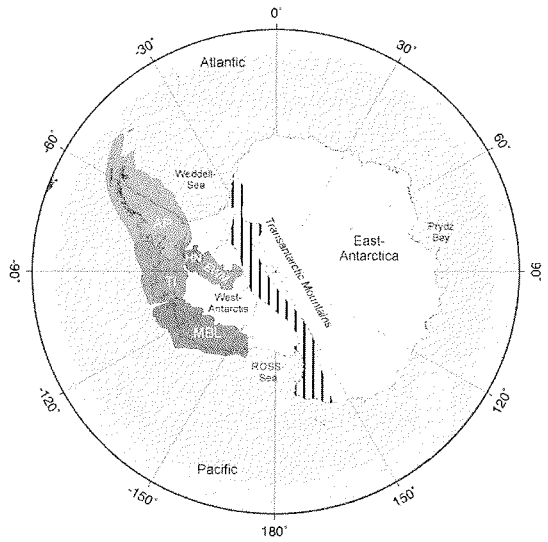

Fig. 1.1. "West Antarctica: problem child of Gondwanaland, tectonics" (Dalziel and Elliot, 1982). The West Antarctica micro-plate mosaic so far consists of 5 units: AP = Antarctic Peninsula; EMW = Ellsworth-Whitmore Mountains; HN = Haag Nunataks; MBL = Marie Byrd Land; TI = Thurston Island (Microplate boundaries after Lawver et al., 1991; Figure modified from Studinger, 1998).

1.1.1 Breakup of Gondwana – The Birth of the Southern Oceans

The continent of Antarctica is divided into two large geologic provinces: East and West Antarctica. The Transantarctic Mountains (Fig. 1.1), a suture zone, separate the Precambrian cratonic East from the younger West Antarctic and the Antarctic Peninsula (Dalziel et al., 1987).

According to Lawver et al. (1999) sufficient sea floor data are now available to allow a reliable reconstruction of Gondwana (around 200 Ma) based on marine magnetic anomalies, ocean crust ages (and derived sea floor spreading rates), sea floor bathymetry, and tectonic lineations. During this time at least three of the five structural units that today form the continental mosaic of West Antarctica (Antarctic Peninsula, Thurston Island, Block and Marie Byrd Land; Fig. 1.1) lay proximal to the tip of South America and were affected by the subduction of what is today the Pacific Plate. Extensive subduction related volcanism and plutonism (Tarney et al., 1982) and the abrupt termination of tectonic features at the Southern tip of South America indicate that before the breakup of Gondwana the Antarctic Peninsula microplate was part of the South American Andes.

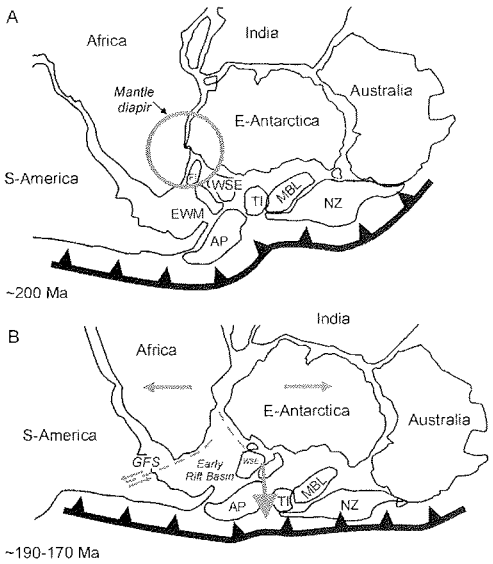

Fig. 1.1. The breakup of Gondwana and the location of the Bouvet-Mantle-Diapir (White and McKenzie, 1989) following the reconstruction of Storey et al. (1996), **(A)** around 200 Ma, **(B)** 190-170 Ma (Brewer et al., 1996; Lawver et al., 1991), start of rifting and formation of oceanic crust. AP = Antarctic Peninsula; EW = Explora Wedge; EMW = Ellsworth-Whitmore Mountains; GFS = Gastre-Faults-System; MBL = Marie Byrd Land; FI = Falkland/Malvinas-Islands; NZ = New Zealand; TI = Thurston Island; WSE = Weddell Sea Embayment (modified from Studinger, 1998).

The breakup of Gondwana started about 190 Ma ago (middle Jurassic) in what is today the Weddell Sea (Fig. 1.1). Large occurrences of continental flood basalts between Antarctica and Africa in the region of the Falkland-Plateau (Studinger, 1998) make rising mantle plumes in conjunction with differential forces of the subduction process the likely cause initiation of the breakup (Storey, 1997).

After an initial left lateral relative movement between South America and Africa documented in the Gastre Fault System (Storey et al., 1996; Fig. 1.1B) and continuing subduction beneath the Antarctic Peninsula block, the tension field changed and forced a North-South separation of Africa and East Antarctica. The Ellsworth Orogeny (200 Ma; Jankowsky and Drewry, 1981), the Palmer Land Deformation (150-140 Ma; Storey et al., 1996) and the Andean Orogeny (100 Ma) represent steps in the amalgamation process of the four Antarctic Peninsula microplates to East Antarctica. In the reconstruction of Grunow et al. (1991) the microplates were connected to East Antarctica around 125 Ma. By 100 Ma East and West Antarctica had reached their present-day position with respect to each other (Fitzgerald, 1999). The precise timing of this continental amalgamation process, and the role of the Ellsworth Whitmore and other blocks are still under debate (Studinger, 1998).

1.1.2 Cenozoic Plate Tectonic Scenario

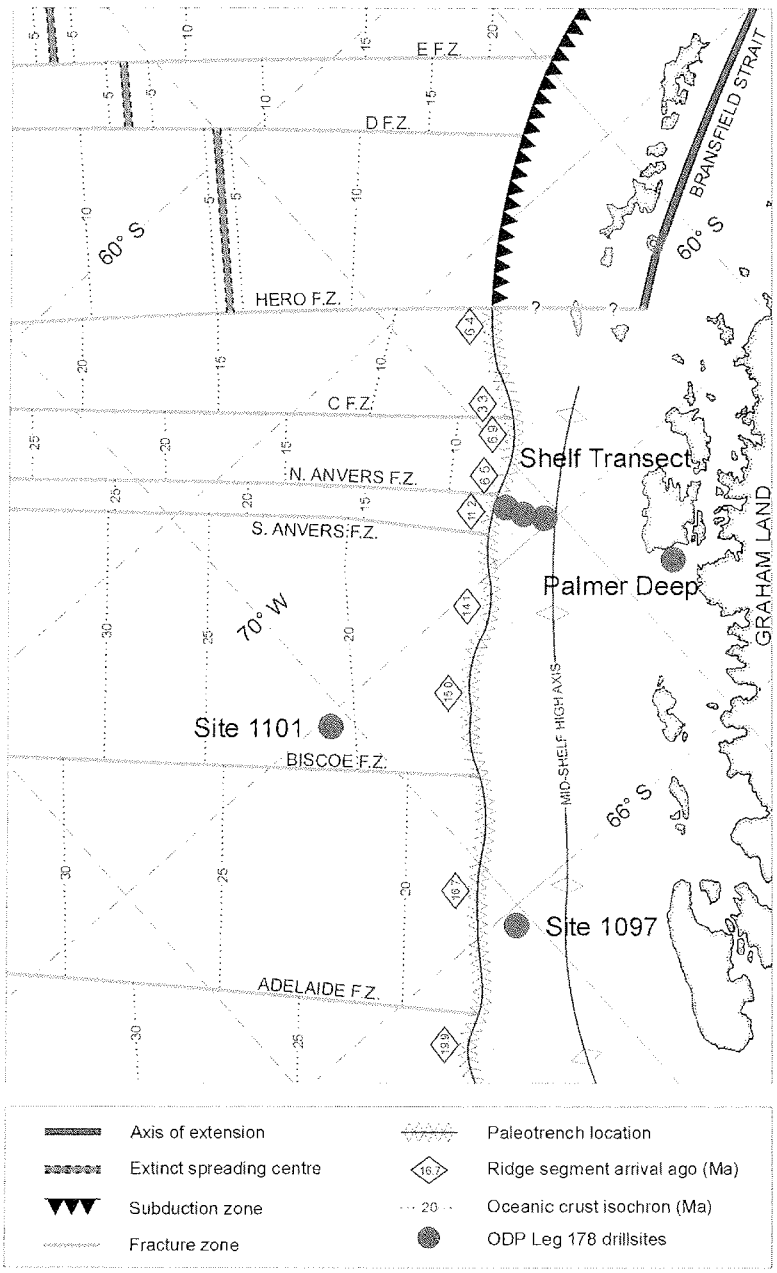

Fig. 1.1. Ridge crest-trench interaction along the West Antarctic Peninsula margin. Note the successively younger ages of the passive margin to the north. The drill sites of ODP Leg 178 in this area are indicated. Sites 1095 and 1096 are to the south of the map area (modified after Larter and Barker, 1991; Larter et al., 1997).

Subduction along the western margin of the Antarctic Peninsula was continuous from late Triassic until Cenozoic. Consumption of the Phoenix Plate and the arrival of ridge segments at the trench (Barker, 1982; Larter and Barker, 1991; Larter et al., 1997) forced northward migration of the subduction and the subsequent formation of a passive margin (Fig. 1.1). As each ridge-crest segment arrived at the trench, it locked up and subduction and spreading stopped. The last ridge-crest segment entered the subduction zone obliquely, southwest of the Hero Fracture Zone between 6.4 and 3.3 Ma (Larter et al, 1997). Subsequently the edge of Antarctic Peninsula has evolved a passive margin. The age of each passive margin segment can be determined by the age of the crust in front of the paleo trench (Fig. 1.1; Larter and Brker, 1991). Northeast of the Hero Fracture Zone spreading at the remaining part of the Antarctic-Phoenix ridge stopped in Pliocene time, leaving a relict triangle of the Phoenix plate and the the Antarctic-Phoenix ridge. The overall regime is still compressional and the consumption of the Phoenix Plate below the Antarctic Peninsula continues (Maldonado et al., 1994; Kim et al., 1995).

1.1.3 Recent Plate Tectonic Situation

Relative plate motions are especially complex between South America, Antarctica and Africa. The major active zones are visible in recent shallow earthquake records and sea floor morphology (Fig. 1.1). The accepted model after Forsyth (1975), Barker (1982), and others may be described as follows:

The three major plates (South America, Africa, Antarctica) meet in a ridge-transform-transform triple junction in the South Atlantic at about 55°S, 1°W. With respect to South America, Africa is moving to the NE and Antarctica to the E. The small Sandwich Plate is bounded by the South Sandwich Trench (subduction zone) in the W and a back arc spreading center (Scotia Ridge) in the East, the South Sandwich Islands are an island arc. Today, the Sandwich Plate and the Scotia Plate move East and override part of the South American Plate (Fig. 1.1B).

The North Scotia Ridge lies along transform fault bounding both the Scotia and Sandwich Plates to the North. In contrast the South Scotia Ridge is a diffuse transform with widely separated ridge segments bounding the Scotia and Sandwich Plate to the South (Barker, 1994) (Fig. 1.1B).

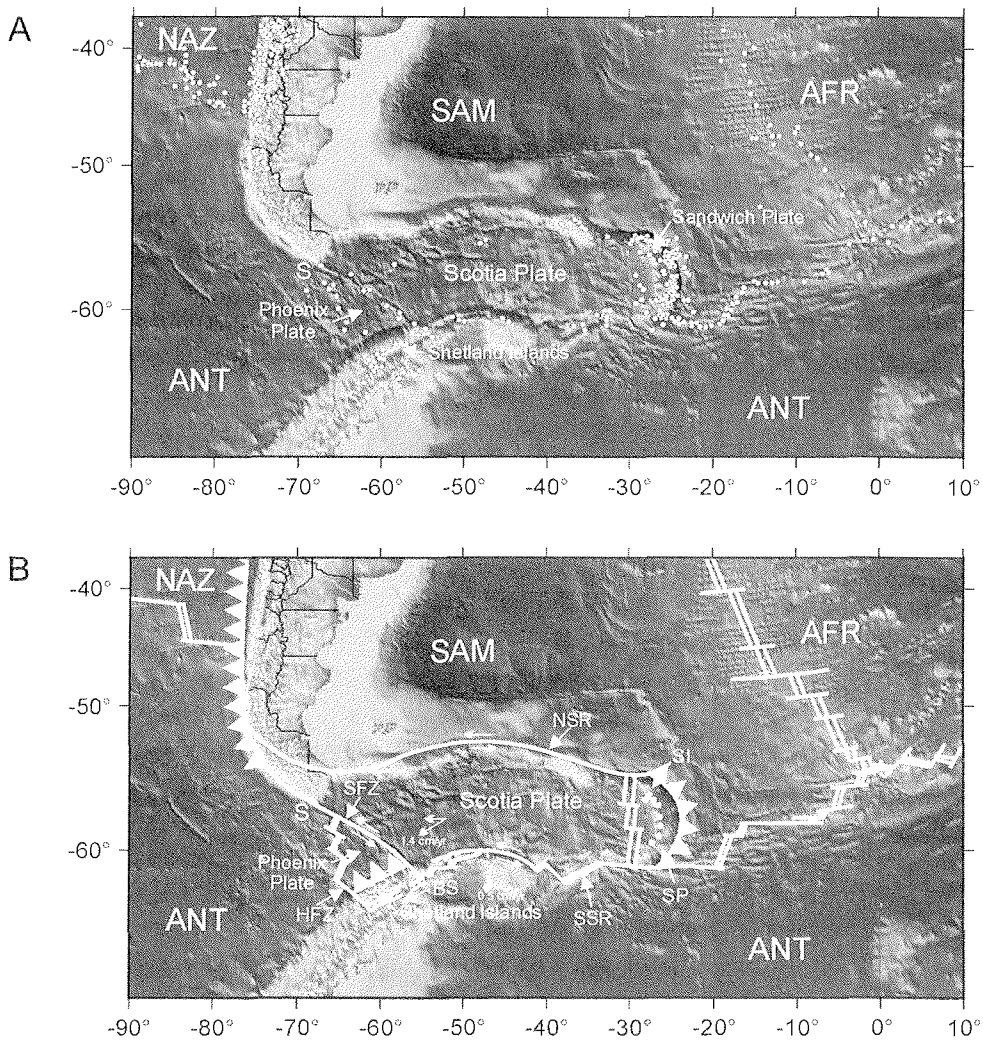

Fig. 1.1. **(A)** Shallow earthquake epicentres and **(B)** recent plate boundaries and relative plate motions in the Scotia Sea region (after Klepeis and Lawver, 1996). AFR = African Plate; ANT = Antarctic Plate; BS = Bransfield Strait; HFZ = Hero Fracture Zone; NAZ = Nazca Plate; NSR = North Scotia Ridge; SAM = South American Plate; SFZ = Shackleton Fracture Zone; SI = Sandwich Islands; SP = Sandwich Plate; SSR = South Scotia Ridge; SST = South Sandwich Trench. Older literature refers to the Phoenix Plate as Drake or Aluk Plate (modified from Barker, 1982; Barker and Dalziel, 1983).

The South Scotia Ridge extension is repeated further to the West in the opening of Bransfield Strait (Fig. 1.1 and Fig. 1.1B). The extension started around 4 Ma (Ercilla et al., 1998), about the time the last ridge segment of the Phoenix Spreading Center entered the trench to the SW (Larter, 1997). Bransfield Strait is regarded as an "abnormal" back arc basin (Gonzalez-Casado et al., 2000). It was associated with subduction rollback mechanisms by

Smellie et al., (1984), Maldonaldo et al., (1994) and Lawver et al., (1995; 1996) but is now thought to be the result of sinistral simple shear coupling between the Scotia and the Antarctic Plate. In any case the Bransfield Strait extension is causing compression in the South Shetland Islands (an extinct volcanic arc) due to a lack of subduction retreat (Gonzalez-Casado et. al., 2000). The extension is accomodated and compensated by the ongoing convergence at the South Shetland Trench to the N (Ercilla, 1998). The extension is expressed in normal faults trending dominantly NE-SW and less dominantly NW-SE. The existence of true oceanic crust is in debate, however, Bransfield Street extension may be seen as the very early stage of the opening of a new oceanic basin (Gonzalez-Casado et al., 2000).

1.2 The Southern Ocean

1.2.1 The Big Picture: Time, Plates, Convection, Ice and Isotopes

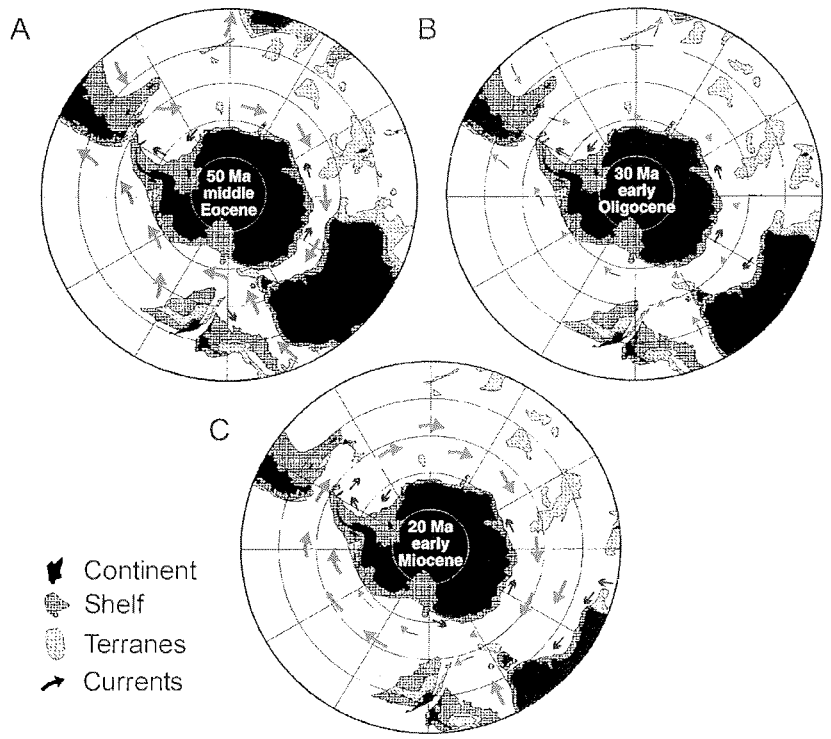

Fig. 1.1. Plate configuration of Antarctica and surrounding continents and the transition from the meridional to the modern circum-Antarctic circulation in middle Eocene (50Ma), early Oligocene (30 Ma) and early Miocene (20 Ma) times (after Lawver et al., 1992; Barrett, 1996; Figure modified from ODP Leg 178 Shipboard Scientific Party, 2001).

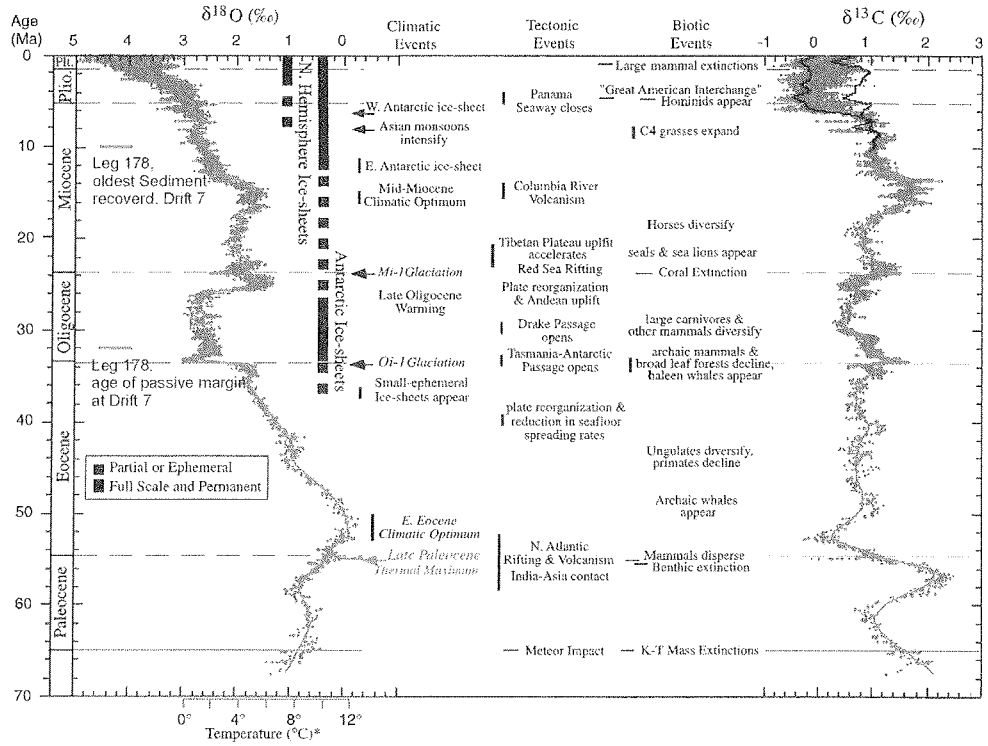

Fig. 1.2. Summary of global deep-sea oxygen and carbon isotope records based on data compiled from more than ~50 DSDP and ODP Leg 178 sites with pelagic sedimentary sections, dominanted by fine-grained, carbonate-rich (>50%) oozes or chalks. Most of the data are derived from analyses of *Cibicidoides* and *Nuttallides*. To correct for genus-specific isotope vital effects, the $\delta^{18}O$ values were adjusted by +0.64 and +0.4 $^{o}/_{oo}$, respectively. The absolute ages are based on the time scale of Berggren et al. (1995). The raw data were smoothed with a 5 point running average and a locally weighted mean. The carbon isotope record shows separate curve fits for the Atlantic (blue) and Pacific above the middle Miocene, illustrating the increase in basin-to-basin fractionation that exceeds ~1.0 $^{o}/_{oo}$ in some intervals. Prior to 15 Ma, interbasin gradients are insignificant or nonexistent. The $\delta^{18}O$ temperature scale was computed for an ice-free ocean [~1.2 $^{o}/_{oo}$ Standard Mean Ocean Water (SMOW)], and thus only applies to the time preceding the onset of large-scale glaciation on Antarctica (~35 Ma). From the early Oligocene to present, much of the variability (~70%) in the $\delta^{18}O$ record reflects changes in Antarctic and Northern Hemisphere ice volume. The vertical bars provide a rough qualitative representation of ice volume in each hemisphere relative to the Last Glacial Maximum (LGM), with the dashed bar representing periods of minimal ice coverage (≤50%), and the full bar representing close to maximum ice coverage (>50% of present). Some key tectonic and biotic events are listed as well. Reprinted with minor additions by permission of Zachos et al. (2001). Refer to the original paper for details.

The South Atlantic was open in late Cretaceous to late Eocene times (70-40 Ma; Nürnberg et al., 1991) and circulation was meridional. The link between South America and Antarctica still existed (Lawver et al., 1992) (Fig. 1.1A). The Antarctic Peninsula micro plates and other continental fragments blocked circulation from the Pacific to the South Atlantic. Tasmania and the South Tasman Rise also formed an effective barrier to high latitude zonal circulation

between Antarctica and Australia. However, some deep water circulation may have occurred between the Campbell Plateau and Marie Byrd Land, West Antarctica (Lawyer et al., 1992; Fitzgerald, 1999).

Spores and pollen from ODP Leg 178 cores (Leg 178 Shipboard Scientific Party, 1999) indicate that part of Antarctica was relatively warm during the late Cretaceous – late Eocene with temperate rain forest vegetation and little ice present. During this Eocene "Greenhouse" world the Australo-Antarctic Gulf to the east and the the widening Pacific Ocean to the west brought warm tropical waters to Australia and Antarctica (ODP Leg 178 Shipboard Scientific Party, 1999).

Spreading between Australia and Antarctica in the late Eocene (37-33.5 Ma) forced the Tasmanian Rise to separate from Antarctica (Lawver et al., 1992; 1997; Fitzgerald, 1999) (Fig. 1.1B). Subsequent subsidence of the broad Tasmanian shelves initiated cooler west to east surface circulation around Antarctica (Exon et al., 2000).

Movement of Antarctica to the east (relative to South Amercia), in conjunction with the opening of the Western Scotia Sea and formation of sea floor in the Drake Passage around 29 Ma (Barker and Burell, 1977; LaBrecque and Cande, 1985), cleared the Antarctic Peninsula from the tip of South America. However, according to ideas of Fitzgerald (1999) and Lawver et al., (1992) true circum-Antarctic deepwater circulation through the Drake Passage did not occur until 20-23 Ma (Fig. 1.1C). In contrast, Exon et al. (2000) attributed early Oligocene cooling and some ice-sheet formation to the cut-off of warm tropical currents from some parts of Antarctica by the developing Antarctic Circumpolar Current.

An earlier initiation of the thermal isolation of Antarctica is supported by oxygene isotope studies (Miller et al., 1987; Zachos et al., 1993; 2001) that show a sharp decline in $\delta^{18}O$ values at the Eocene-Oligocene boundary (33.5 Ma, Fig. 1.2). This decline is attributed to the build-up of continental ice containing isotopically lighter ^{13}O water, and hence enriching ^{18}O in the oceans. The data of Zachos et al. (2001) are from a global compilation of oxygen isotope values of 50 DSDP and ODP Leg 178 sites.

The opening of the Tasmanian Gateway between Australia and Antarctica and the opening of the Drake Passage between South America and the Antarctic Peninsula were followed by the establishment of the Antarctic Circumpolar Current, with enormous consequences for global climate and circulation. The opening of the circumpolar gateways led to the isolation of Antarctica from warm gyral surface circulation of the Southern Hemisphere oceans and provided the conditions that led to ocean conveyor circulation between the Atlantic and Pacific Oceans. Additionaly external planetary forcing in conjunction with the

gradually decreasing atmospheric CO_2 (DeConto and Pollard, 2001) that may have crossed a critical treashhold level in the early Oligocene (Pollard and DeConto, 2001; Berner, 1994) initiated the polar cryosphere in Antarctica during the Paleogene and early Neogene and later in the bipolar world during the start of late Neogene Northern Glaciation (ODP Leg 189 Shipboard Scientific Party 2000).

The changes in $\delta^{18}O$ (Fig. 1.2) following the onset of permanent continental ice sheets are the combined effect of changing ice volumes and temperature (Zachos et al., 2001). The lack of ice sheets prior to the Eocene-Oligocene boundary cannot be supported by direct physical-chemical proxies. However, evidence from high latitude deep sea samples in the form of ice-rafted detritus (IRD) and the abundances of clay minerals indicating changing physical continental weathering conditions support this assumption (Ehrmann and Mackensen, 1992). Accepting reasonable temperature limits on the basis of modern bottom and tropical surface waters and data from Mg/Ca thermometers 70-90 % of the sudden rise of $\delta^{18}O$ at 34 Ma may be attributed to the ice volume component. The remaining 10-30% of the rise in $\delta^{18}O$ can be attributed to the open gateways integrating cooler waters into global thermohaline circulation, inducing a decrease of greenhouse gases (CO_2).

Trusting the isotope record an ice volume indicator, the Antarctic ice sheet expanded rapidly and formed a stable feature throughout most of the Oligocene. A cover of temperate ice with 50% of todays extent is assumed by Hambrey et al., 1991. A warming trend at the end of the Oligocene (26-27 Ma) until 15 Ma resulted in increased bottom-water temperatures (Miller et al., 1991; Wright et al., 1992) probably reduced the extent of the ice sheet (Zachos, 2001). This relatively warm period reached its climax in the Mid-Miocene Climate Optimum (17-15 Ma; Fig. 1.2). It was interrupted only by a temporary cooling event at the Oligocene-Miocene transition (Mi-1 Glaciation, Fig. 1.2; Zachos, 2001; Barrett, 1999). Sealevel data (Haq et al, 1988) and oxygen isotopes record a reestablishment of permanent ice cover, accompanied by gradual cooling from 15 to 8 Ma. Following this cooling trend $\delta^{18}O$ values decrease again, marking a warming trend that started in the latest Miocene and persisted throughout the lower Pliocene to be abruptly terminated around 3.2 Ma (Zachos et al., 2001) when the large-scale glaciation of the Northern Hemisphere began. Since 3.2 Ma the isotope data reflect the combined effect of changes in bipolar ice volume and temperature. The Caribbean-Pacific Gateway closed around 4.5 Ma, and southern sourced deep–water expanded northward between 3.3 and 2.6 Ma (Tiedemann and Franz, 1997). From there on the Northern and Southern Hemispheres appear to be closely coupled with regard of ice volume build-up and decay.

1.2.2 A Dispute: EPD versus WSI

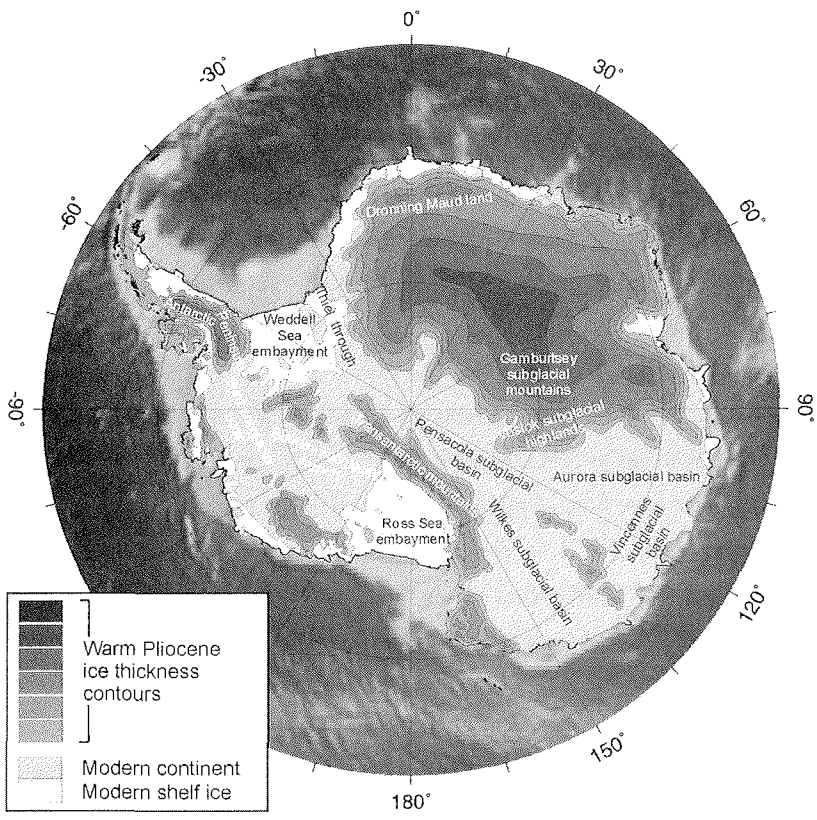

Fig. 1.1. Antarctica and its ice sheet during the warm Pliocene, according to the model of Denton et al. (1991) following the EPD hypothesis of Webb et al. (1984). Ice volume was reduced to a third of its modern value and the continent is bordened by shallow marine basins. Contours are relative thicknesses (modified from Denton et al., 1991).

The effect of late Miocene/Early Pliocene warming on the extent and behavior of the East and West Antarctic Ice sheets is disputed. The conflict between the stability hypothesis (WSI = Warm Stable Ice-Sheet) and the Early Pliocene Deglaciation (EPD) scenario (Webb et al., 1984; Webb and Harwood, 1991) is now almost 17 years old. The dispute started when Webb et al. (1984) described a diverse biota of diatoms, sponge spicules, radiolarians, palynomorphs (Barrett, 1999) and wood[2] in glacial diamicts of the Sirius Group in the Transantarctic Mountains. *Nothofagus* fossils occur in elevations of 1800 m and marine microfossil

[2] *Nothofagus*, a small tree, similar to scrub found in todays high alpine regions of Tasmania and Patagonia (Francis, 1999; Webb and Harwood, 1993).

assemblages at 2750 m. Marine diatoms of the assemblage dated as Pliocene in age have been interpreted by Webb et al. (1984) as being deposited in an ice-free flooded East Antarctic interior, subsequently to be glacially eroded and transported to their present location by a younger Antarcic ice sheet in cooler, late Pleistocene times. Two aspects of the proposed depositional processes for the fossil-bearing deposits of the Sirius Group are not questioned. The deposits at high elevation (including the type locality with the rich microfossil assemblage) were in fact deposited from the East Antarctic ice, once overtopping the mountain chain of the Transantarctic Mountains (Barrett, 1999). Low level occurrences along fjords may represent former valley fills deposited during an interglacial, being eroded and wrapped up along the re-advancing glacial tongue (as lateral and terminal moraines) during the following glacial halfcycle (Barker, 1995).

On the base of their fossil assemblages Webb and Harwood (1993) proposed mean annual temperatures of up to 5 °C. Models based on this scenario concluded that East and West Antarctica must have been deglaciated to a third of the present ice volume (Webb et al, 1984; Denton et al., 1991; Fig. 1.1). The EPD hypothesis gained further support by discovery of a vertebrate fauna, by $\delta^{18}O$ values of bivalves from the Vestfold hills (East Antarctica) (Quilty, 1993; Quilty, 1996), by sea-level high stands of the lower and middle Pliocene (Haq et al., 1988; Dowsett and Cronin, 1990) and by Pliocene planktic microfossil assemblages indicating warmer Antarctic surface waters (Abelmann et al., 1990; Ishman and Rieck, 1992).

In the recent years however, the EPD hypothesis has been attacked by advocates of the WSI hypothesis (Kennett and Hodell, 1993; Barker, 1995), including some former supporters (Barrett, 1999). A detailed discussion can be found in Barker (1995). The key arguments against a partial Pliocene deglaciation are:

- The diatom-based ages assigned to the microfossil assemblage of the Sirius Group are in doubt. Kellogg and Kellogg (1996) have filtered snow from the inland ice sheet at the South Pole and two other locations and found 40 species of marine and terrestrial diatoms. Barrett et al. (1997) reported that biogenic particles and diatom material sampled from Sirius Group tills and surrounding outcrop faces (not belonging to the Sirius Group) and snow fields containing similar diatom assemblages. Hence several atmospheric transport mechanisms have been proposed, including the Eltanin asteroid impact around 2.2 Ma (Gersonde, 1997).

- The *Nothofagus* remains may be older than Pliocene, Barker (1995) assigns a hypothetical middle Miocene age to them. This would resolve the problem since the oxygen isotopic record shows that the middle Miocene was a prolonged warm period.
- Kennett and Hodell (1995) and Barker (1995) discuss the effect of the observed reduced $\delta^{18}O$ values of benthic foraminifera in Early Pliocene times. They conclude that the proposed 60% reduction in Antarctic ice volume is only achievable if the 0.6°/00 decrease in $\delta^{18}O$ is totally the result of ice volume changes. This seems unrealistic since a major deglaciation would also be accompanied by a substantial increase in surface water temperature. They summarize that the observed changes in isotopic data (presented by Shackleton et al., 1995; Tiedemann et al., 1994) in the Early Pliocene of the Subantarctic are insufficient to accommodate both substantial Southern Ocean warming and major deglaciation.

Barker (1995), as one of the key stability proponents, developed a climate-coupled sedimentation model for both scenarios (Fig. 1.2). Starting conditions for a EPD are an inward sloping overdeepened Antarctic shelf profile and substantial Early Pliocene ice sheet retreat, with only small glacial-interglacial variations in the warm period. Ice advances probably did not reach the shelf edge and fluvial transported sediment had to fill the shelf depression before substantial amounts of sediment could reach the slope or rise (Pudsey et al., 1994). Trapping of sediment on the shelf would have caused low sedimentation rates on the continental slope and rise during the lower Pliocene. The late Pliocene cooling would have produced grounded ice-sheets again aided by the low sea-level stands during the Northern Hemisphere glaciation. This would increase sediment transport and deposition at the rise localities. Additionally, a re-advance of the ice would cause a major unconformity in the shelf record.

The Warm Stable Ice Sheet hypothesis (Barker, 1995) accepts that surface waters surrounding Antarctica in the Early Pliocene were moderately warmer than today but draws very different conclusions. The main effect of the SST warming would be increased snow accumulation („Snow Gun" hypothesis; Prentice and Matthews, 1991) and an increase in the temperature of the snow. This would lead to more ice and an increase in basal frictional melting at the base of the glaciers. The faster ice flow would lead to higher sedimentation rates on the rise when the ice was colder. The late Pliocene/Pleistocene cooling would have led to reduced snow accumulation and colder ice, reducing ice stream flow and reducing the rate of sedimentation on the rise (Fig. 1.2). Barker (1995) suggested lower sedimentation rates

for the onset of the cooling in the late Pliocene and all of the Pleistocene when compared to the Early Pliocene of his WSI case.

From the late Pliocene on his model sedimentation rates get identical with sedimentation rates suggested for the EPD case (Fig. 1.2). As in the EPD case, Barker assumes a removal of topsets on the shelf due to a thickening of grounded ice on the shelf.

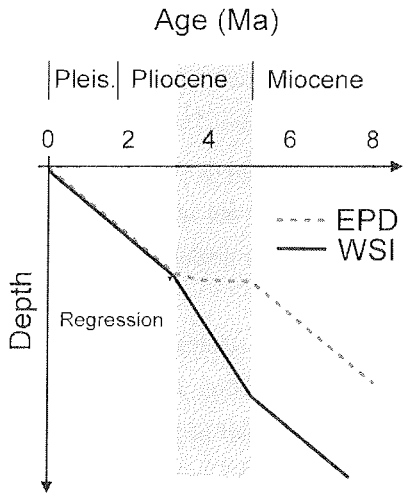

Fig. 1.2. Hypothetical sedimentation rates on the continental rise for a warmer early Pliocene. Depositional scenario of Barker (1995) for a proposed Warm Stable Ice Sheet hypothesis (WSI) and Early Pliocene Deglaciation (EPD). Both scenarios reunite at the beginning of the late Pliocene/Pleistocene Northern Hemisphere Glaciation, leading to a regression (modified from Barker, 1995).

The case in favor of the stability hypothesis (Kennett and Hodell, 1995; Barker, 1995; Barrett, 1999), is summarized by Barker et al. (1998):

> „ANTARCTIC PENINSULA: ODP LEG 178 ... SITES 1095, 1096 AND 1101 ON THE CONTINENTAL RISE ... It is clear that the continental rise is sensitive to variations in the glacial state of the continent, and that these reflect the orbital variation in insolation through much of the period examined. A downward change at Site 1095 that sees no cyclicity before about 9 Ma marks a change in the level or nature of glaciation on the shelf, if not its initiation. An additional point is that the cyclicity, taken here to indicate the cyclic provision of unsorted sediments to the continental shelf edge (and therefore a clear indication of the presence of a glacial regime onshore) was continuous through the Pliocene: there is no sign of Early Pliocene deglaciation, even at this most northerly outpost of the continent. This is consistent with several other studies (e.g. Huybrechts, 1993; Denton et al., 1991; Barker, 1995), but inconsistent with the original hypothesis of substantial deglaciation (Webb and Harwood, 1991)".

New data and links established within this thesis will use the *EPD* versus *WSI* dispute as background for new insights and a new model linking the ice, ocean, shelf and the deep sea of the Western Antarctic Peninsula continental margin.

1.2.3 Modern Regional Oceanography

The oceans surrounding the Antarctic continent play a critical role in the formation of two of the world's most important water masses: Antarctic Bottom Water (AABW) and Antarctic Intermediate Water (AAIW). These two water masses occupy 40% of the global ocean's volume and play a central role in the large scale circulation and transport of heat. The Southern Ocean connects the world's major oceans.

1.2.3.1 The Antarctic Circumpolar Current and its Frontal System

The Southern Ocean circulation is driven mostly in a clockwise (easterly) direction by the prevailing westerly winds between 35°S and 60°S (Fig. 1.1). Between 60°S and the Antarctic continent there is a narrow zone of slower westward flowing water, driven by easterly winds (Lozano and Hays, 1976; Tchernia, 1980) (Fig. 1.1). The boundary between these major wind and current systems, the Antarctic Divergence (AD) is a region of major upwelling forced by wind - induced Ekman flow (Gordon, 1988).

The dominant easterly current is called the West Wind Drift or Antarctic Circumpolar Current (ACC). It is intensified as it passes through the constriction of the Drake Passage to become one of the strongest currents in the world.

Bottom topography influences the latitudinal position of the ACC (Lozano and Hays, 1976), in response to conservation of vorticity. Depressions in the sea bottom morphology allow the current to move closer to the Antarctic shore. At restrictions such as the rises south of Tasmania, the ACC is forced to move north in order to conserve angular momentum (Gordon, 1988). South of the circumpolar ocean floor trough several cyclonic circulation gyres develop as the east flowing ACC interacts with coastline irregularities (peninsulas and embayments). Prominent examples are the Weddell Sea and Ross Sea Gyres (Fig. 1.1).

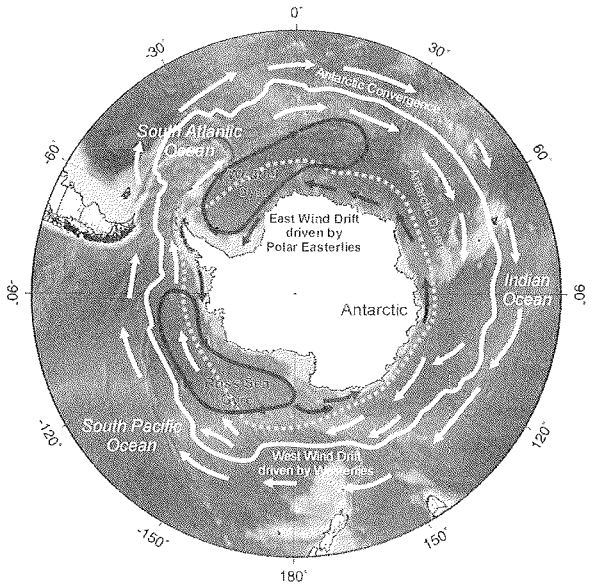

Fig. 1.1. The Antarctic Circumpolar Current system. Antarctic Convergence = Polar Front (PF), Antarctic Divergence. Modified from Internet[3].

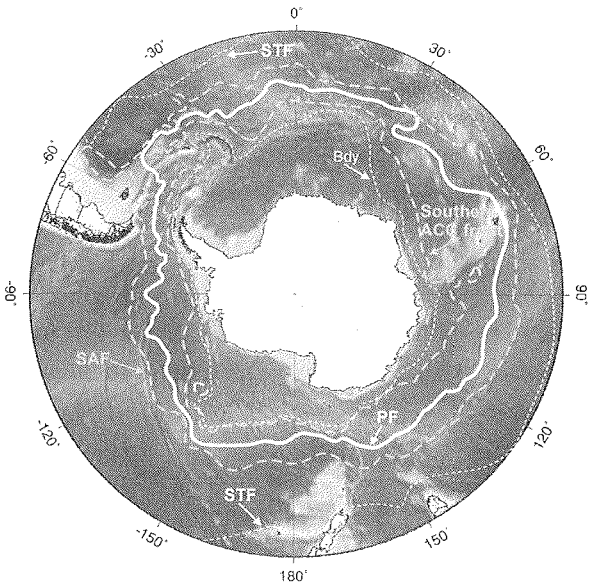

Fig. 1.2. Distribution of Antarctic Oceanographic Fronts. Note that the Subtropical Front (STF) does not pass through the Drake Passage. SAF: Subantarctic Front; PF: Polar Front; SACC: Southern Antarctic Circumpolar Front; Bdy, southern limit of Upper Central Deep Water. Fronts adapted from Orsi et al. (1995).

[3] http//:glacier.rice.edu/oceans/4_antsurfwater.htlm

The circum-Antarctic polar fronts include the Sub-Tropical Front, the Subantarctic Front, the Polar Front, and the Southern Antarctic Circumpolar Front (SACC, Fig. 1.2; Orsi et al., 1995). All frontal systems are dynamic features and vary in their spatial location over time (Rintoul et al., 1997; Howard and Prell, 1992; Weaver et al., 1998).

The Antarctic or Polar Front (PF) separates Antarctic from the Subantarctic waters. It was initially defined to be the position of the northernmost extent of the winter Antarctic Surface Water (ASW; Park et al., 1993). Today, the PF is commonly defined by a 2°C temperature minimum at a depth of 100 to 300 m (Belkin and Gordon, 1996). At the PF, the ASW sinks beneath the Subantarctic Surface Water, contributing to the formation of Antarctic Intermediate Water (AIW; Tschernia, 1980). At the sharply delineated PF the convergence of warm and cold water leads to the sudden death of many planktic organisms, hence increasing the flux of nutrient to the sea floor. The mixing zone has a high primary surface production of specially adapted planktic species that profit from the higher nutrients content of the colder southern waters (Überall, 2000). The northern limit of the ACC, the Sub-Tropical Front (SF), represents the southernmost extent of the warmer (13.5°C), high salinity (34.6 to 35.1 ‰), nutrient poor Sub-Tropical Surface Water (STSW; Gordon, 1972; Hoffmann, 1985). It is not present in Drake Passage (Orsi et al., 1995; Fig. 1.3). To the south of the SF, the Subantarctic Front (SAF) is characterized by a decrease in surface salinity to 34.5 ‰ in 100-400 m water depth and temperatures below 8°C (Burling, 1961). To the south the ACC is limited by the AD or Southern ACC Front.

1.2.3.2 Major Water Masses in Drake Passage and Bellingshausen Sea

Two surface and three subsurface and deep water masses are present in the Bellingshausen Sea and Drake Passage: Antarctic Surface Water (AASW) and Subantarctic Surface Water (SASW), and Antarctic Intermediate Water (AAIW), Circumpolar Deep Water (CDW) and Antarctic Bottom Water (AABW) (Fig. 1.1).

The AASW originates near the Antarctic continent and flows to the north until it encounters Subantarctic Surface Water of higher temperature and salinity (Tab. 1.1). Because the AASW is more dense than the SASW it begins to sink and mix with the underlying AAIW[4] (Tab. 1.1). The AAIW underlies several surface water masses in the north of the PF. It is formed by downwelling of surface waters between 55° and 60° S along the PF. Two bodies of AAIW can be distinguished: one is produced west of the Drake Passage and enters

[4] http//:glacier.rice.edu/oceans/4_antsurfwater.htlm.

the South Pacific subtropical gyre through subduction (Luyten et al., 1983), the other is produced East of the Drake Passage in the confluence of the Falkland and Brazil Currents (Talley, 1996). Its main characteristic in the world ocean is a subsurface salinity minimum, which appears immediately north of the PF (Sievers and Nowlin, 1984). CDW is a thick layer of warm, saline, oxygen-poor water. It is the most voluminous water mass of the Southern Ocean and incorporates North Atlantic Deep Water (NADW) formed in the Norwegian Greenland Sea (Sarnthein, 1994). It is the major water mass in the Drake Passage. At the northern end of the Drake Passage it reaches to the sea floor and has a thickness of 3000 m (Sievers and Nowlin, 1984). CDW is divided into Upper (UCDW) and Lower (LCDW) water masses. The LCDW is characterized by a salinity maximum and nutrient minimum at about 2900 m depth north of the SAF. The UCDW is recognized by its oxygen minimum in water depths between 1600 and 1800 m north of the PF (Armand, 1997). UCDW is only partly derived from NADW (for discussion see Armand, 1997).

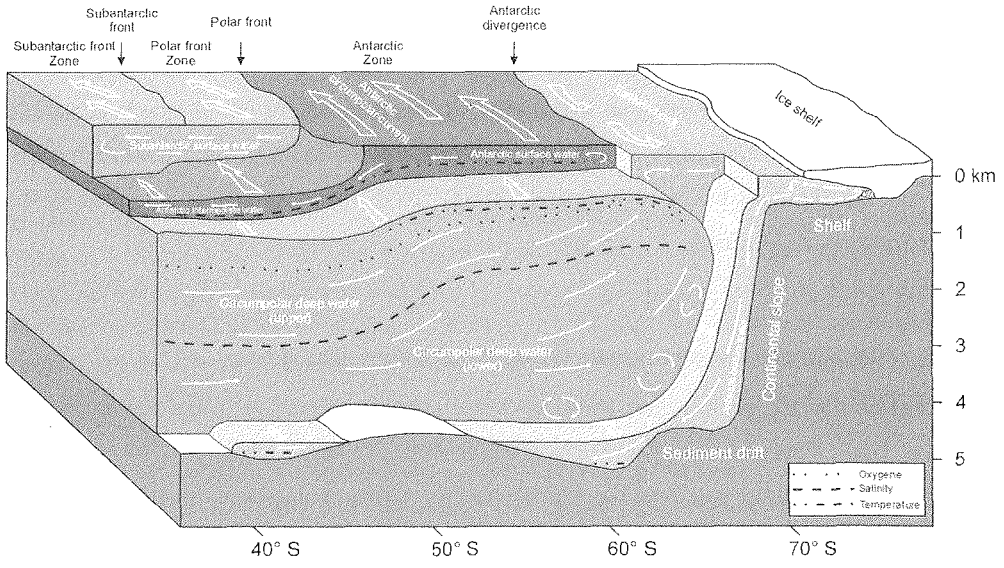

Fig. 1.1. Simplified sketch of water masses in Drake Passage. The sediment drifts of the Antarctic Peninsula are under the influence of a westward flowing counter-current within the Antarctic Bottom Water. Note that the Sub-Tropical Front is not present in Drake Pasage. Figure altered from a drawing of Thiede (1986), originally reproduced from Lutjeharms et al. (1985). The convection cell below the shelf ice is after a drawing of Hellmer (1989).

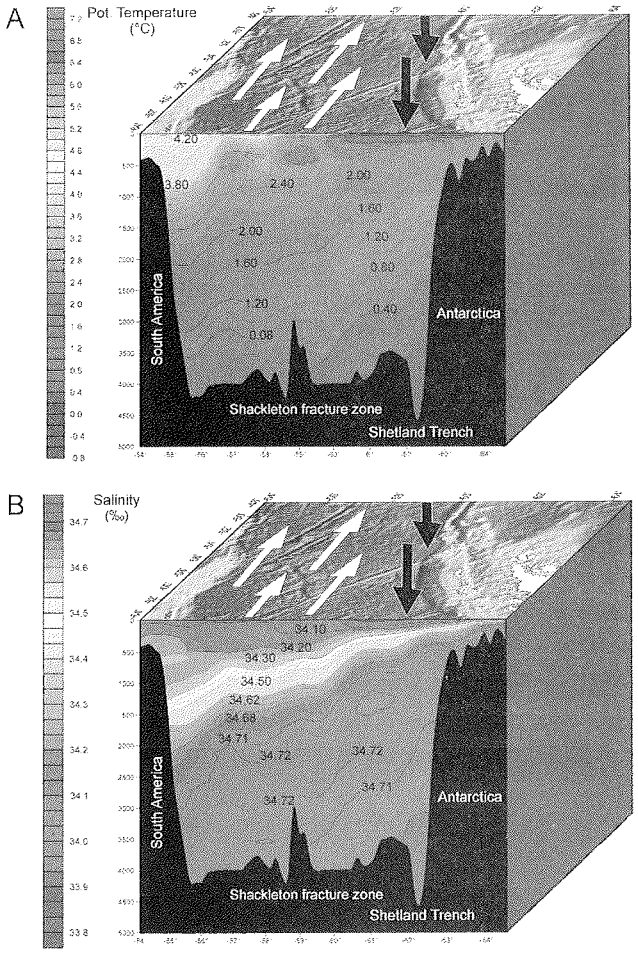

Fig. 1.2. Potential temperature **(A)** and salinity **(B)** across Drake Passage in January. 1990. Contours have been generated using a web based plotting algorithm (http://sam.ucsd.edu/vertical_sections/Atlantic.html). Data were acquired during METEOR cruise 23.01.-06.03.1990, Chief Scientist: W. Roether). The shallow part of the section is graphically interpolated.

The AABW originates through vertical convection along the Antarctic shelf. It gains its low temperature and high salinity by brine rejection of freezing surface water in direct contact with the shelf ice (Fig. 1.1). This highly oxygenated water is the most dense water in the ocean and hence occupies the depressions of the ocean basins. Its main areas of formation are the Weddell and Ross Seas (Pickard and Emery, 1982). On its way north AABW mixes with LCDW and can be traced into the North Atlantic. The westward flowing AABW, following the continental slope morphology, has a great influence on sediment erosion and redistribution (Thiede, 1986).

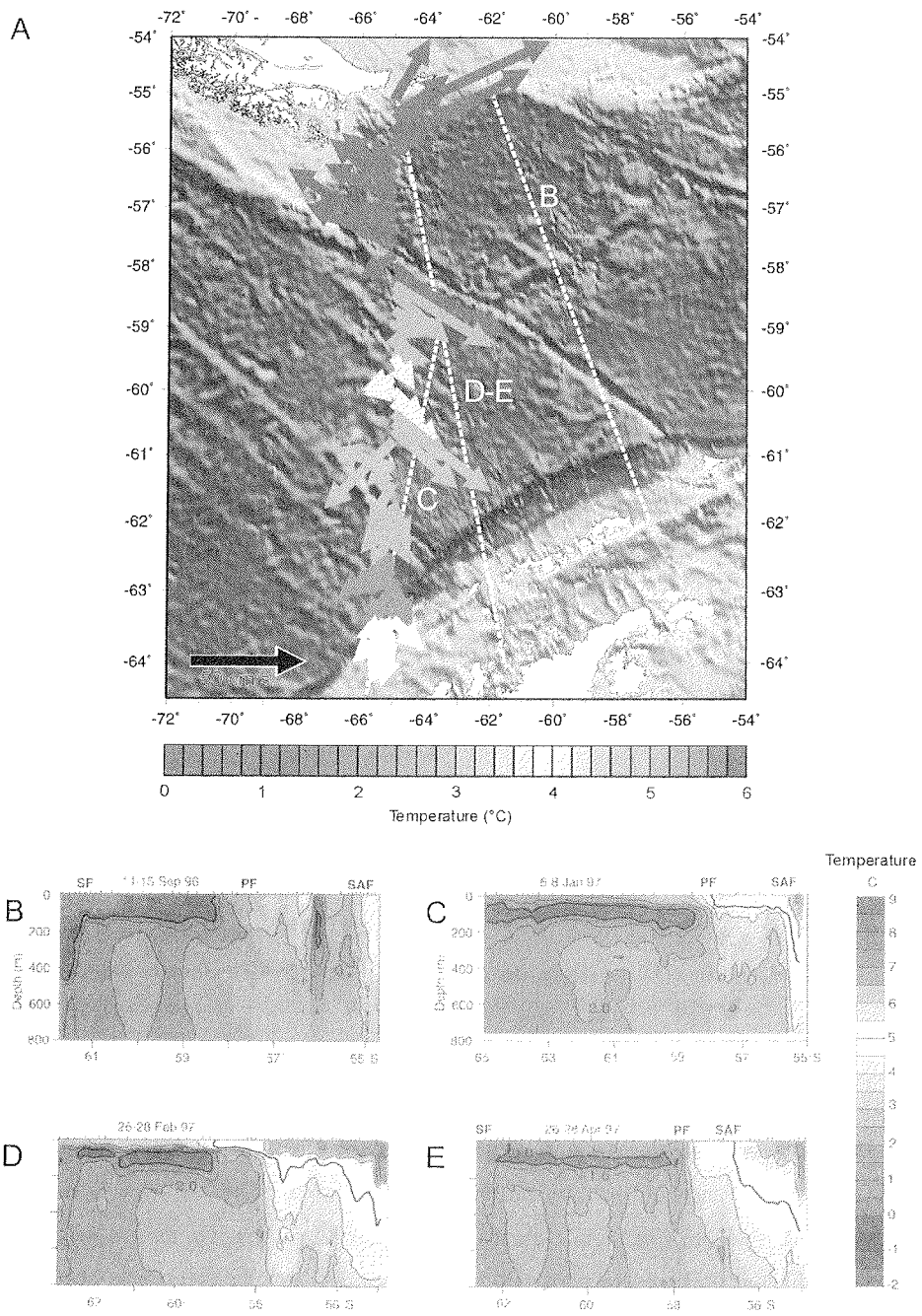

Fig. 1.3. (**A**) Complex subsurface 50 m depth water velocities across Drake Passage in April 2000 (redrawn from http://tryfan.uscd.edu/drake/; Sprintall, 2000). Note the cyclonic nature of the flow. (**B, C, D, E**) shallow temperature profiles across Drake Passage. (**B**) maximum extent of sea ice cover. (**C, D, E**) during decay of sea ice cover. The location of the oceanographic fronts is labeled on each section. ((**B-E**) Modified from Sprintall et al., 1997; see (**A**) for the location of profiles shown in (**B-E**)).

Water Mass	Abbr.	Depth (m) N-S	Salinity (‰)	Temperature (°C)	Oxygen (ml/l)
Antarctic Surface Water	AASW	0-250	33.80	<5.00	> 7.00
Subantarctic Surface Water	SASW	0-150	<34.00	<9.00	> 6.50
Antarctic Intermediate Water	AAIW	1450-600	34.50-34.36	3.20-7.00	3.20-4.70
Circumpolar Deep Water (Upper)	UCPDW	1800-1000	34.73	1.60-1.80	3.7-4.10
Circumpolar Deep Water (Lower)	LCPDW	2900-2000	34.71-34.73	0.90-1.60	3.45-3.63
Antarctic Bottom Water	AABW	>3500	34.66–34.69	-0.9-0.0	

Tab. 1.1. Characterization of major intermediate and deep waters around Antarctica (Armand, 1997; Sievers and Nowlin, 1984).

Shallow transects demonstrate the annual variability of the surface and subsurface water masses in Drake Passage (Fig. 1.3). More general, less detailed profiles, display the whole water column (Fig. 1.2). A velocity profile across the Drake Passage (Fig. 16 A) displays the complexities of the actual current situation.

1.2.3.3 Ice

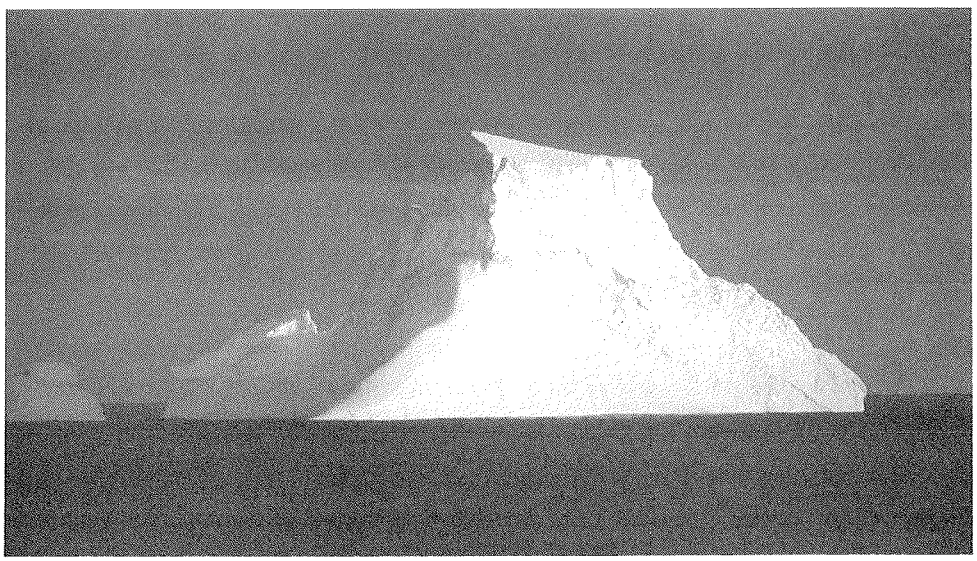

Fig. 1.1. Mature shelf iceberg, still recognizable by its originally flat top. Seen during ODP Leg 178, NW of Marguerite Bay.

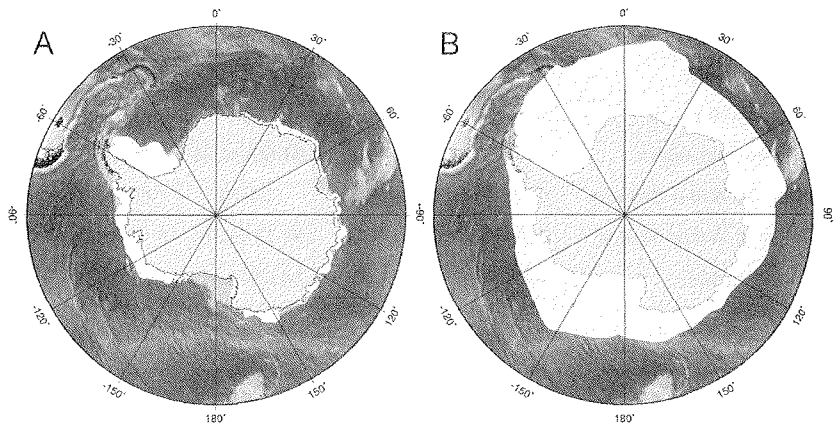

Fig. 1.2. Sea ice extent around Antarctica, **(A)** summer (February), **(B)** winter (September). Data from 13-year averaged satellite observations (Schweitzer, 1995).

Ice controls erosion, transport and redeposition on the Antarctic Peninsula continental margin. The shelf ice also controls the formation of the AABW, that under the influence of the AAC, erodes and redistributes sediments of the slope, rise and deep sea.

The Antarctic glacial ice cover is the largest connected ice mass on earth today. In contrast to the Arctic the Antarctic is surrounded by ice shelves having a total area of $1.4*10^6$ km^2). The Ross Ice Shelf ($0.526*10^6$ km^2) and the Filchner-Ronne Ice Shelf of the Weddell Sea ($0.474*10^6$ km^2) make up more than 71% of the total Antarctic shelf ice area (Robin, 1983, in Thiede, 1986). The ice of the ice shelves is either in direct contact with the rock (grounded shelf ice) or has a free floating tongue. All true shelf ice has its origin in the continental glaciers, which are up to several thousand meter thick (Fig. 1.1), flow at a rate of 200-600 m/y and thin seaward. The average shelf ice edge is 50 m above sea-level (Robin, 1983, in Thiede, 1986). The large ice shelves generate major icebergs characterized by flat tops.

In contrast to shelf ice, sea ice forms *in situ* on the water surface. March through May are the months of maximum sea ice growth. Sea ice forms first near the continent at a growth rate of 3 km/day (Cavalieri and Parkinson, 1981), and later gets dispersed to the north by the southern winds (Lemke et al., 1981). In September, at the end of the Antarctic winter, the "pack ice" has attained its maximum coverage of about 19 million km^2 and extends as far as 2,200 km from the coast[5] (Fig. 1.2B). Estimates from satellite data (Parkinson, 1992) show that the sea ice decay takes place between October and January at a rate of 20 km/day,

[5] http://www.antarctic.com.au/encyclopaedia/physical/IbergSI.html

considerably faster than sea ice growth in winter and summer (Fig. 1.2). Due to the strongly accelerated ocean current, the Drake Passage and the sea along the Antarctic Peninsula have only small pack ice belts in winter. Ice extent, wind and water temperature are all related. Fig. 1.3 shows the complex interaction.

Many authors (e.g. Rebesco et al., 1997) suggest a relation between the extent of sea ice and the location of AABW flow. At least in the Drake Passage the westward flowing AABW current has a strong influence on seabed morphology and sediment transport as a countercurrent. Possible geological proxy indicators for the link between sea ice and relative bottom current strength at sediment drifts will be identified and discussed below.

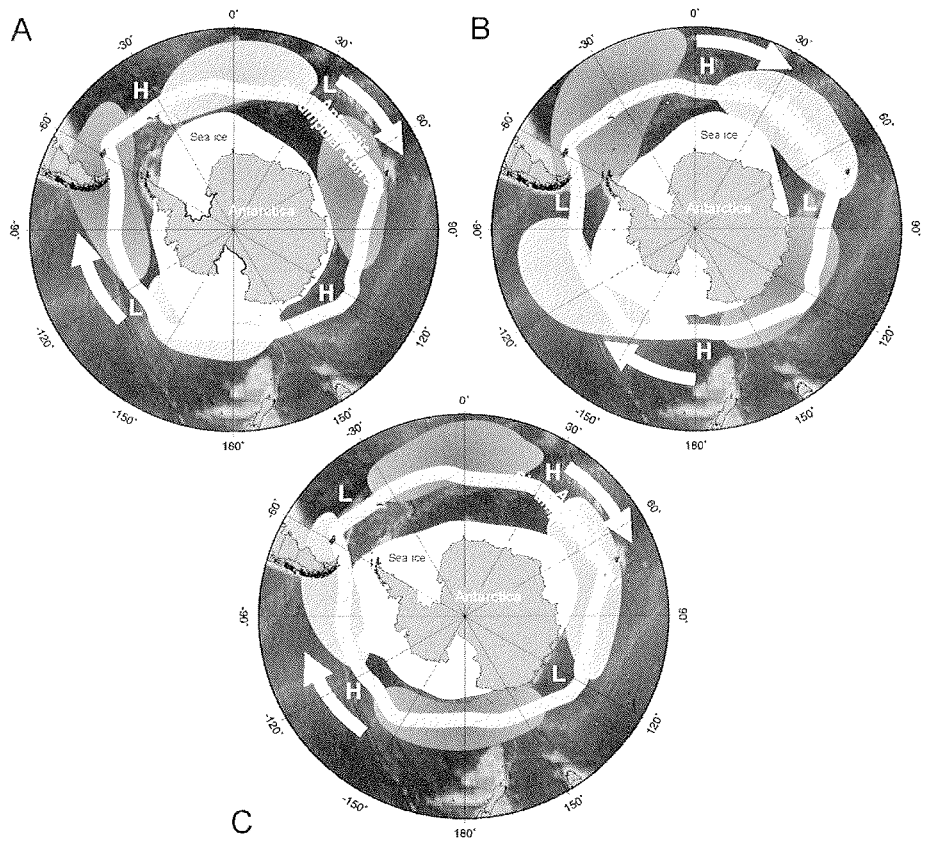

Fig. 1.3. Atmosphere-ocean interaction. Propelled by the ACC and atmospheric high and low pressure systems (H,L) – areas of relatively warmer (red) and colder (blue) water are driven around Antarctica. These anomalies propagade eastward with the circumpolar flow, with a period of 4-5 years and taking 8-10 years to encircle the pole. The system of coupled anomalies is called the Antarctic Circumpolar Wave and plays an important role in heat exchange beween the South Pacific and the South Atlantic and climate regulation and dynamics both within and beyond the Southern Ocean. (Courtesy: White and Peterson, 1996, Figure modified from National Geographic, October 2000: „*New Eyes on the Oceans*", p.94.)

1.3 Leg 178 "Antarctic Peninsula" Mission

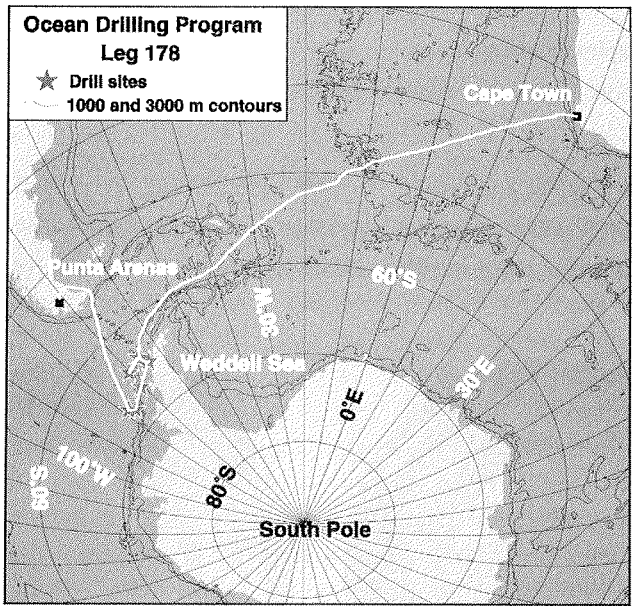

Fig. 1.1. General map of Leg 178 ship track with drill sites stared (Shipboard Scientific Party, 1999).

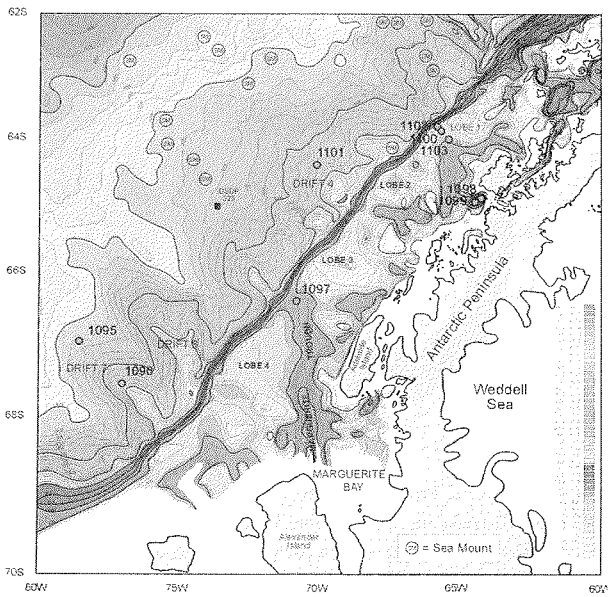

Fig. 1.2. Bathymetric map of the continental margin west of the Antarctic Peninsula (Rebesco et al., 1998) with ODP Leg 178 Site locations (SM = Sea mount).

Leg 178 "Antarctic Glacial History and Sea-Level Change" of the cruises of the drilling vessel JOIDES Resolution took place between the 5th of February and the 9th of April 1998. Guided by the Co-Chiefs Peter F. Barker, Angelo Camerlenghi and Gary D. Acton (Staff Scientist), the cruise started in Punta Arenas, Chile and ended in Cape Town, South Africa (Fig. 1.1). During Ocean Drilling Program (ODP) Leg 178, nine sites (1095-1103) were drilled on the Pacific continental margin of the Antarctic Peninsula (Fig. 1.2). These included a shelf site in a trough setting (1097), a transect of the outer continental shelf (1100, 1102, 1103) three sites on two hemipelagic drifts on the continental rise (1095, 1096 and 1101) extending back 6-10 m.y., and two shallow holes at two sites on the inner continental shelf (Palmer Deep, Sites 1098 and 1099) that provide an ultrahigh-resolution Holocene record. The „Antarctic Glacial History and Sea-Level Change" proposal and Leg 178 are the result of the ANTOSTRAT (Antarctic Offshore Stratigraphy Project) initiative. ANTOSTRAT aims to gain a better understanding of the Cenozoic glacial history of the Antarctic margin and provides site survey information through its data base collection (ANTOSTRAT Seismic Data Library System (SDLS)). Five circum-Antarctic drilling projects have been proposed to ODP. Two of these (ODP Legs 178 and 188) have been drilled. The Cape Roberts Project, associated with the ANTOSTRAT aims, is in its synthesis phase. Scientific objectives of Leg 178 were to [6]:

- extract and compare high-resolution records of the past 10 Ma of continental glaciation contained in topset beds (paleo shelf) of the glacial prograding wedge on the Antarctic Peninsula Pacific margin, in foreset beds (paleo slope) of the same sequence groups, and in hemipelagic sediment drifts on the continental rise;
- compile high-resolution history of grounded ice volume fluctuations for comparison with low-latitude records of sea-level change and isotopic estimates of ice volume change over the past 10 Ma;
- assess the main controls on sediment transport and deposition during glacial intervals and use the insights gained to optimize investigation of the longer, more complex record of glaciation and glacio-eustatic sea-level change in East Antarctic;

[6] Adapted from the ODP Leg 178, ANTARCTIC PENINSULA, Antarctic Glacial History and Sea-level Change, Scientific Prospectus (e.g.: http://www-odp.tamu.edu/publications)

- extract an ultra-high-resolution Holocene record from a protected basin on the inner continental shelf for comparison with similar records from ice cores and lower-latitude sediment sites.

1.4 Thesis Motivation and Organization

Invited as a "Joides Logger" for Leg 178, I worked in three science categories on board the ship (Seismic Stratigraphy, Downhole Measurements and Physical Properties). These diverse activities are reflected in this thesis. This work attempts to link the evolution of the passive continental margin shelf of the Western Antarctic Peninsula to the build-up of the sediment drifts on the continental rise. Rise sites accumulate sediment that can be dated – the shelves sites are riddled with hiatus.

This thesis is organized following the transport path of sediment from the shelf to the rise. Efforts have been made to:

- characterize the West Antarctic shelf at Site 1103 by its seismostratigraphy, physical properties and lithology.
- construct and validate a velocity profile from logs and laboratory data for Site 1103 (chapter 2.2, *paper in press*).
- develop a conceptual model of glacial and interglacial shelf sedimenation and compare West and East Antarctic shelves.
- model analog single channel reflection seismic data from Palmer Deep.
- develop software and configure hardware for the digitalization of analog single channel reflection seismic data.
- characterize the drift sediments of the rise with their seismostratigraphy, physical and chemical properties (logging data, grain-size data, pore space chemistry; chapter 4.3, *two reports* and *co-authored paper in press*).
- distinguish and characterize depositional processes by statistical treatment of grain-size data and compare the results to existing models of e.g. sequence stratigraphy or ice volume.
- link shelf and rise evolution over the last 10 Ma.
- develop software for acoustic core modelling and data clean-up (*Excursus* chapter 7)

2 The West Antarctic Shelf

2.1 Introduction

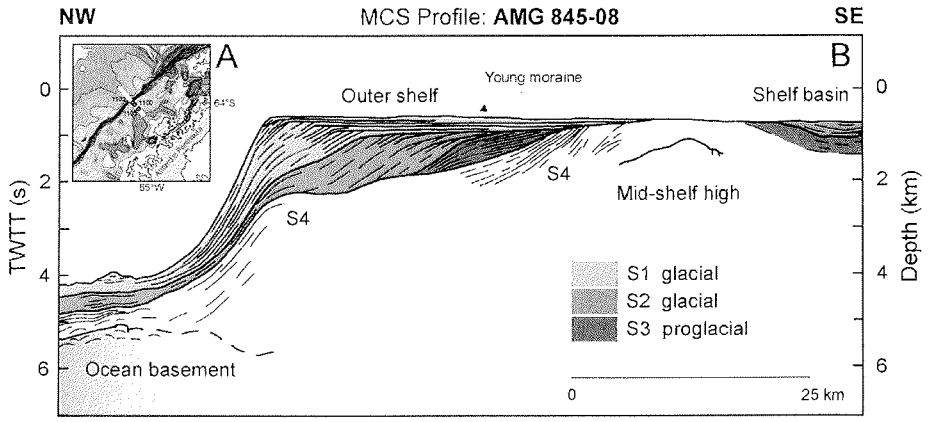

Fig. 2.1. Schematic line drawing of MCS profile AMG845-08 from the Pacific margin of Antarctic Peninsula, illustrating the unique overdeepened nature of the shelf and times of progradation (subhorizontal growth of the shelf e.g. S2, S3) and aggradation (subvertical growth of the shelf, S1). The depth scale is based on the assumption of average seismic velocities of 2000 m/s, hence the VE is 5:1. The figure is modified from Larter and Barker, 1991 and ODP Leg 178 Shipboard Scientific Party, 1999). Original correlations and interpretations assigned a glacial nature to sequences S1, S2 and a preglacial origin for the older sequence S3.

The abstract and introduction of the paper "Composite Velocity Profile of Shelf Site 1103 (ODP Leg 178, Western Antarctic Peninsula)" in chapter 2.2 present a detailed introduction to the goals of Leg 178 drilling on the shelf. To avoid duplication this introduction is focussed on the description of shelf morphology and deposits through their seismostratigraphic expression, using seismic profiles in the vicinity of Anvers Island as examples. The second part of this chapter presents the derivation of a new velocity profile for the shelf that is tested and validated in chapter 2.3 and used for core and logging data correlation with seismic units in part 2.4 of this chapter. A detailed "reflector-to-lithology" or "reflector-to-logging" data correlation and a summary interpretation of the reflection seismic data are given in chapter 2.5. A model of shelf deposition through a glacial cycle, with processes and parameters related to the unique nature of Antarctic shelves is presented in the last part of chapter 2.5. Finally a short discussion of other Antarctic shelves reveals striking similarities in shelf build-up since 3.2-2.3 Ma and discusses possible explanations for this synchronous evolution (chapter 2.6).

2.1.1 Inner Shelf

The inner shelf (to the E of the profile shown in Fig. 2.1), the area landward of the main shelf islands (e.g. Adelaide Island and Anvers Island, Fig. 1.2), is commonly shallower than 200 m, but also includes several deep and steep-sided troughs (e.g. Palmer Deep SW of Anvers Island). Due to the persistant ice-cover, only limited seismic and core information is available. The acoustic hard sea floor and the rugged irregular morphology suggest that Mesozoic and early Cenozoic volcanic and plutonic rocks, similar to those found on the islands, outcrop on the glacially eroded sea floor of this area (Larter et al., 1997). An example of the seismic character and lithology of the glaciomarine sediment fill of a Holocene inner shelf depression is given in chapter 3 "Palmer Deep".

2.1.2 Shelf Basins

Shelf basins to the SE of the mid-shelf high (Fig. 2.1B) have average depths of 500 m. Depths increase inshore, typical of the „reversed profile" of the overdeepened Antarctic shelf. It is likely that the seismostratigraphic sequences of the shelf basins are depositionally linked to sequences of the outer shelf. In general, the shelf basins have a simple internal synclinal architecture with a steeper side toward the mid shelf high compared to the landward side of the basin (Larter et al., 1997). The reflectors follow the form of the basin instead of lapping onto the basin outline; Larter et al. (1997) suggest postdepositional deformation as a possible cause.

2.1.3 Mid-Shelf High

The mid-shelf high (MSH)(Fig. 2.1B) forms the seaward border of the shelf basins. This structural high is either exposed on the sea floor or covered by sediment. The MSH is laterally extensive (see Fig. 1.1), following the general trend of the shelf. It is not intersected by transform faults (Larter and Barker, 1991). According to Larter et al. (1997) the MSH is the center of uplift following the arrival of ridge crest segments at the subduction zone (see also for detail chapter 1.1.2). A time delay of 1 to 4 my between arrival of the segment and start of the uplift is inferred from stratigraphic relations. Two interpretations for the origin and character of the MSH are found in the literature. Kimura (1982) and Gamboa and Maldonaldo (1990) refer to the MSH as a paleo-island arc and consequently to the shelf basin as a back arc setting, similar to the South Shetland Island and Bransfield Strait to the NE (see chapter 1.1.3).

Other authors (Larter and Barker, 1991; Bart and Anderson, 1995) consider the MSH to be an uplifted part of an accretionary prism. Recently it has been proposed, that serpentine driven diapirism is responsible for the MSH uplift (Larter et al., 1997).

2.1.4 Outer Shelf with the Drilled Seismic Units of Leg 178-Shelf Transect

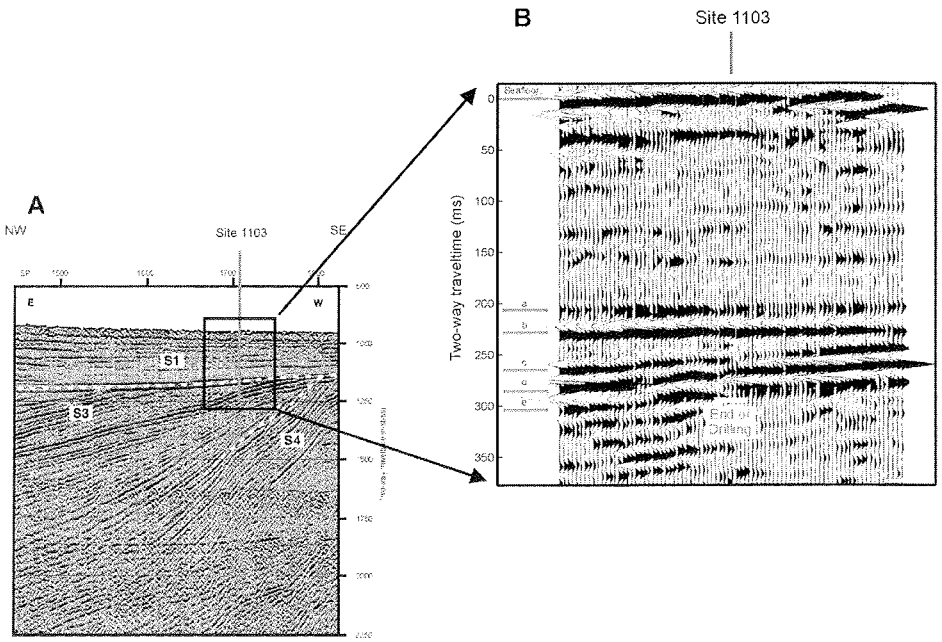

Fig. 2.1. (**A**) Part 1 of Multichannel seismic profile I95-152 across Site 1103. S.P. = shotpoint. Profile I95-152 gathered by the Programma Nazionale di Ricerche in Antarctica (Italy) (PNRA). Profile I95-152 (shelf transect, Sites 1100, 1102, and 1102) is a 30-fold stack of CDP gathers spaced 6.26 m apart with 2-ms sampling. Traces were deconvolved before stacking with an 80 ms operator and 4 ms predictive interval. Velocity analyses were performed every 2 km. The sea floor multiple reflection was attenuated by the application of a median filter to CDP gathers corrected for multiple velocity. The display section was produced with time variant three-trace lateral mix, deconvolution in the frequency domain, time-variant band-pass filter, and trace equalization using a variable window. Profile I95-152 provides a high-resolution image of the geometry of the glacial prograding wedge and of the "preglacial" structure of the continental shelf, complementary to that of profile AMG 845-08 (Fig. 2.1), which follows the same track. Boundaries of the major seismic Sequence Groups S1, S3 and S4 of Larter and Barker (1991), Larter and Cunningham (1993), and Larter et al. (1997) are shown. (**B**) Extraction of 40 traces around Site 1103 with marked prominent reflectors. The depth scale is preliminary and was revised in chapter 2.2.4. Refer to Fig. 2.1 of chapter 2.2.2 for the continuous profile. Courtesy: Barker, P.F., Camerlenghi, A., Acton, G.D., et al., 1999 *Proceedings of the Ocean Drilling Program, Initial Reports* Volume 178.

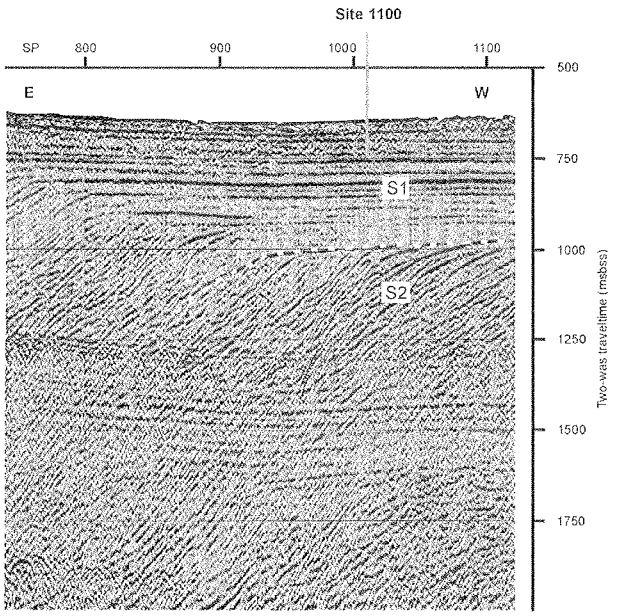

Fig. 2.2. Part 2 of Multichannel seismic profile I95-152 across Site 1100. S.P. = shotpoint The low-profile near-surface wedge of sediment landward of S.P. 950 (sampled at Site 1100) was interpreted by Vanneste and Larter (1995) as a prograding till body emplaced during the last glaciation, but not reaching the continental shelf edge at that location. See notes of Fig. 2.1 for processing details. Courtesy: Barker, P.F., Camerlenghi, A., Acton, G.D., et al., 1999 *Proceedings of the Ocean Drilling Program, Initial Reports* Volume 178.

The extensive (~30 km wide) outer shelf borders the MSH seaward[7]. The outer shelf consists of many stacked depositional sequences first described and labeled by Larter and Barker (1989). Larter et al. (1997) recognized 4 main units above and shortly below the sea floor multiple.

Reflectors in S4 (Fig. 2.1A) dip steeply seaward near the MSH and are erosionally truncated. Sequence Group S3 (Unit top: 247 mbsf, recovered to base of hole at 362.7 mbsf) is characterized by a series of reflectors that dip gently seaward from the MSH (Larter and Barker, 1989; 1991). Reflectors of Sequence Group S3 at Site 1103 are parallel or subparallel throughout the section. In tracing the reflectors away from the site, however, it is possible to

[7] Part of the section showing this is published in Shipboard Scientific Party, 1999. Shelf Transect (Sites 1100, 1102, and 1103, Seismic Stratigraphy). *In* Barker, P.F., Camerlenghi, A., Acton, G.D., et al., *Proc. ODP, Init. Repts.*, 178, 1–173 [CD-ROM]. Available from: Ocean Drilling Program, Texas A&M University, College Station, TX 77845-9547, U.S.A. Note: Authorship of sub-chapter „Seismic Stratigraphy": Escutia, C. and Moerz, T.

distinguish two reflector packages separated by a group of three high-amplitude reflectors (Reflectors c, d, and e in Fig. 2.1B). Above these three reflectors, S3 is characterized by parallel and subparallel gently dipping reflectors that are truncated landward by the unconformity between Sequence Group S1 and Sequence Group S3 (Fig. 2.1A and Reflectors a and b in Fig. 2.1B). Below the three high-amplitude reflectors, S3 reflectors diverge seaward and pinch out landward (Fig. 2A, B). The three strong reflectors (c, d, and e) separating the two reflector packages correspond to changes in the density and variations in the velocity of sedimentary formations (i.e., from 3300 to 2100 m/s between 270 and 285 mbsf, see chapter 2.2, Fig. 2.4). All reflector packages in S3 have lower amplitudes landward and increase in amplitude seaward of the site location.

Sequence Group S2 is typified by low-angle dipping reflectors, that steepen seaward (Fig. 2.2). Strata from S2 are truncated at the top by the erosional unconformity that marks the boundary between S1 and S2. At Site 1100, Sequence Group S2 consists of steeply dipping foreset reflectors that downlap onto a lower deeper reflector, indicating a prograding sequence. Internal truncations and downlap relationships in the foreset section are common, implying the existence of many individual prograding beds. Sequence Group S2 is not found at Site 1103, where an unconformity separates reflectors of Sequence Group S1 above from reflectors of Sequence Group S3 below (Fig. 2.1A, B).

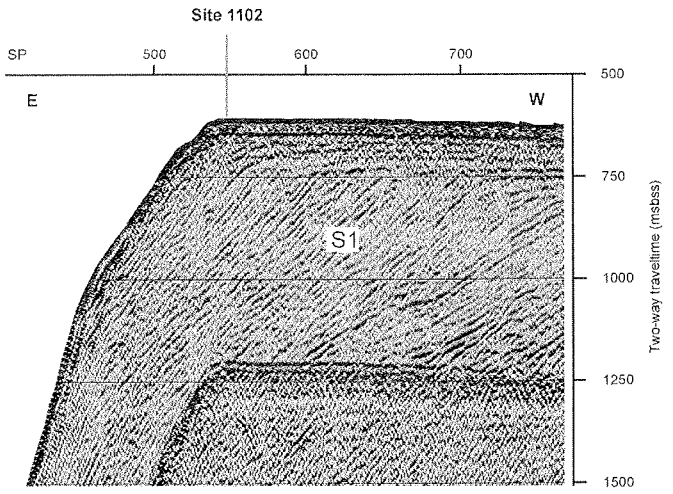

Fig. 2.3. Part 3 of Multichannel seismic profile I95-152 across Site 1100. S.P. = shotpoint. See notes of Fig. 2 for processing details. Courtesy: Barker, P.F., Camerlenghi, A., Acton, G.D., et al., 1999 *Proceedings of the Ocean Drilling Program, Initial Reports* Volume 178.

Sequence Group S1 is characterized by nearly flat-lying topset reflectors in the inner and middle shelf. To the seaward these become steeply dipping foreset reflectors (Fig. 2.3). Topset reflectors are marked by lateral changes in reflector amplitude (i.e., from high to moderate), whereas foreset reflectors have lower amplitudes. S1 has external wedge-like geometry, internally it consists of topsets that grade into foresets toward the shelf edge. The lower boundary of S1 is a high amplitude reflector that truncates reflectors from the underlying Sequence Groups S2 and S3 (Fig. 2.1 and Fig. 2.2). Sequence Group S1 at Site 1102 consists of an upper thin (~60 m) package of high-amplitude, flat-lying topset reflectors and a lower thick sequence of steeply dipping (foreset) reflectors (Fig. 2.3). Truncation and downlap relationships within the foresets suggest that S1 comprises several individual prograding sequences (Larter and Barker, 1989).

2.2 Composite Velocity Profile of Shelf Site 1103 (ODP Leg 178, Western Antarctic Peninsula)[8]

2.2.1 Abstract

Site 1103 was one of a transect of three sites drilled across the Antarctic Peninsula continental shelf during Leg 178. The aim of drilling on the shelf was to determine the age of the sedimentary sequences and to groundtruth previous interpretations of the depositional environment (i.e., topsets and foresets) of progradational seismostratigraphic sequences S1, S2, S3, and S4. The ultimate objective was to obtain a better understanding of the history of glacial advances and retreats in this west Antarctic margin. Drilling the topsets of the progradational wedge (0-247 meters below sea floor [mbsf]), which consist of unsorted and unconsolidated materials of seismic unit S1, was very unfavorable, resulting in very low (2.3%) core recovery. Recovery improved (34%) below 247 mbsf, corresponding with sediments of seismic unit S3, which have a consolidated matrix. Logs were only obtained from the interval between 75 and 244 mbsf, and inconsistencies on the automatic analog picking of the signals received from the sonic log at the array and at the two other receivers prevented accurate shipboard time-depth conversions. This in turn limited the capacity for making seismic stratigraphic interpretations at this site and regionally.

This study is an attempt to compile all available data sources, perform quality checks, and introduce nonstandard processing techniques for the logging data obtained to arrive at a

[8] Co-Authors: Laronga, R., Lauer-Leredde, C., Escutia, C., and Wolf-Welling, T.C.W. (Moerz et al., in press).

reliable and continuous depth vs. velocity profile. We defined 13 data categories using differential traveltime information. Polynomial exclusion techniques with various orders and low-pass filtering reduced the noise of the initial data pool and produced a definite velocity depth profile that is synchronous with the resistivity logging data. A comparison of the velocity profile produced with various other logs of Site 1103 further validates the data. All major logging units are expressed within the new velocity data. A depth-migrated section with the new velocity data is presented together with the original time section and initial depth estimates published within the Leg 178 Initial Reports Volume. The data presented confirm the location of the shelf unconformity at 222 ms two-way traveltime (TWTT) or 243 mbsf and allows its seismic identification as a strong negative and subsequent positive reflection.

2.2.2 Introduction

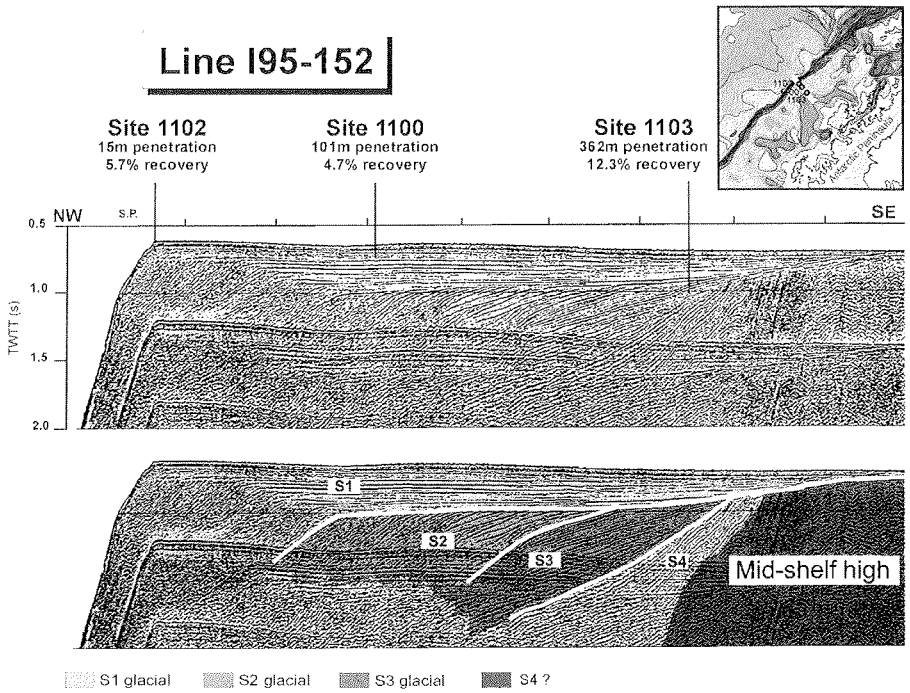

Fig. 2.1. Northwest-southeast air gun multichannel reflection seismic profile showing location of sites drilled along a shelf transect during ODP Leg 178 (Shipboard Scientific Party, 1999d). Hole 1103A recovered/penetrated sediments of the topsets (unit S1) and foresets (unit S3). Average recovery at Site 1103 is 12.3% but only 2.6% for unit S1. Note also the low recoveries at the other sites along the transect. The bathymetric map of the continental margin west of the Antarctic Peninsula (Rebesco et al., 1998a) indicates the location of the shelf transect sites and the approximate location of Seismic Line I95-152 (white line).

The Antarctic shelf differs in many ways from continental shelves of mid and low latitudes and even from the shelves of high northern latitudes. The Antarctic shelves are over-deepened with water depths between 300 and 1000 m and slope landward, principally because of the effect of glacial erosion and flexural loading by grounded ice (Ten Brink and Cooper, 1992; Barker et al., 1998). Sedimentary sequences exhibit two principal geometries in reflection seismic profiles collected across the West Antarctic Peninsula shelf: shelf topsets and slope foresets form the prograding wedge (Larter et al., 1994; Larter and Barker, 1989; 1991). In most areas of the middle and inner shelf, the topsets and underlying foresets are separated by a prominent regional unconformity (Larter et al., 1997). This unconformity marks a major change in the style of deposition from progradational to aggradational and progradational, adding large sediment-retaining capacities to the shelf (Fig. 2.1). Prograding sedimentary sequences on the continental shelf record changes in West Antarctic ice sheet volume, sea-level, climate, ice and sediment-induced isostatic change, and tectonic and thermal effects.

The aim of drilling the shelf-transect Sites 1100, 1102, and 1103 during Leg 178 was to characterize the age and depositional environment of seismostratigraphic units S1 (topsets), S2, S3, and S4 (foresets of the prograding wedge). Unfortunately, drilling through the topset sequences was very diffficult with the available rotary core barrel (RCB). Unsorted crystalline clasts (up to headsized) in an unindurated sand/silt/clay matrix prevented rapid penetration and resulted in minimal core recovery. This was primarily a result of clogging of the central opening of the rotary drill bit and the core catcher with stones. Despite drilling difficulties, Site 1103 penetrated to 362.7 mbsf with mixed recoveries. The upper 247 m of cored sediment, belonging for the most part to seismic unit S1, yielded only 2.3% recovery. The lower 116 m of cored material, with a cemented matrix, belonging to seismic unit S3, and yielded 34% recovery (Fig. 2.1). A hole blockage prevented the collection of logging data below 244 mbsf (Shipboard Scientific Party, 1999a). Thus, no or only very limited comparisons and cross checks of log and laboratory data are possible. In our investigation, we compiled all available data sources and performed quality checks and nonstandard processing techniques with the logging data obtained to arrive at a reliable and continuous depth velocity profile presented in this paper. Further characterizations of logging and seismostratigraphic units are the subject of Escutia et al. (in prep).

Reliable velocity profiles on the shelf for time-depth conversions of multichannel reflection seismic profiles (Camerlenghi et al., in press) are needed for all further geological interpretations and models of shelf sedimentation in seismic sections. Even though the shelf sediment record is less continuous and age constraints are less confined compared to the other

depositional environments drilled during Leg 178 (i.e., inner continental shelf deep basins and continental rise drift deposits), the best possible depth control of the shelf sequences is essential for regional stratigraphic correlations across the Antarctic Peninsula continental shelf and between the shelf and rise.

2.2.3 Data Resources and Methods

In the following chapter, the maximum drill depth of 367 mbsf reached in Hole 1103A is divided into three depth ranges: 0-70 mbsf, 70-244 mbsf, and 244-367 mbsf. The velocity information and processing techniques used for each depth interval is discussed separately.

2.2.3.1 Interval 0-70 mbsf

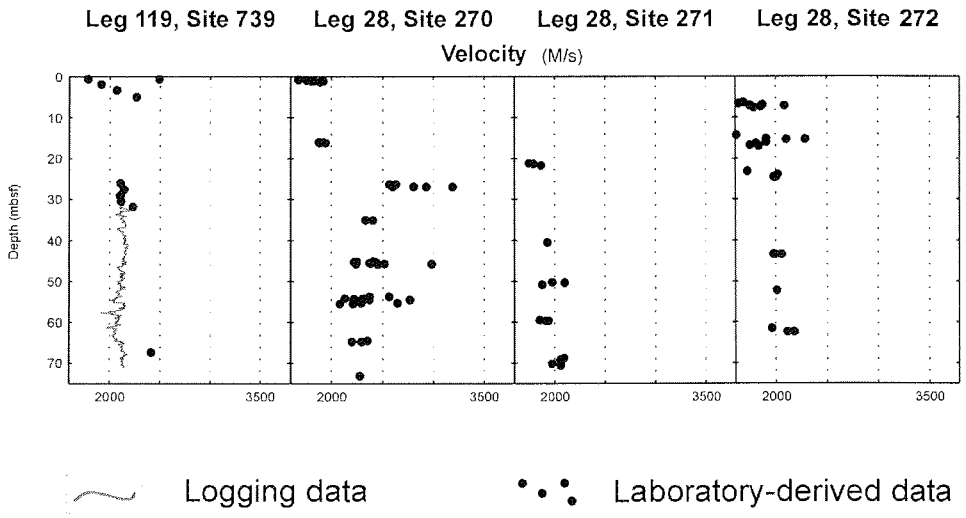

Fig. 2.1. Compilation of OPD/DSDP velocity data from topset environments in Prydz Bay and Ross Sea continental shelves. We used an average velocity calculated from logging data from Site 739, Leg 119 (Shipboard Scientific Party, 1989).

The depth interval between 0 and 70 mbsf is particularly limited with regard to available velocity information and is thus speculative. Unstable hole conditions caused the pipe to be pulled up only to 84 mbsf prior to logging. No useful logging data were obtained through the pipe over the first 75 m. Very low core recovery in this interval prevented the collection of velocity data in the laboratory. Based on laboratory measurements on core samples recovered from Hole 1100C of the shelf transect, we measured reasonable shipboard Hamilton frame

(PWS3) values of 1650-1700 m/s for the upper 0-3.5 mbsf (Shipboard Scientific Party, 1999b). In order to fill the remaining gap from 3.5 to 75 mbsf, all available Ocean Drilling Program and Deep Sea Drilling Project (ODP/DSDP) velocity information from Antarctic shelf topsets were compiled (Fig. 2.1).

For this study, we considered data from four prior drill sites depending on availability, shelf geometry, location on the shelf and reported lithology: Site 739, ODP Leg 119 in Prydz Bay and Sites 270-272, DSDP Leg 28 in the Ross Sea. Of all recorded shelf topset values between 5 and 75 mbsf, 92% are in the range of 1800 to 2500 m/s. The average of all recorded velocity values over this depth interval is 2172 m/s. Considering sediment descriptions and corresponding logging data given in the Initial Reports volume (Shipboard Scientific Party, 1989) and by Hambrey et al. (1991), sediments from Site 739 consist of dominantly uncemented diatom-rich diamictites with large igneous and metamorphic clasts in the upper 70 mbsf. Even though the degree of compaction may differ compared to sediments of the upper 70 mbsf of Site 1103, Leg 178, the recorded velocities are close to the overall topset values considered in our comparison (2112 m/s) .

In summary, we took three velocity values from Site 1100C of the shelf transect in the depth range of 0.7-3.5 mbsf and added a velocity value of 1630 m/s at the sediment/water-interface (0 mbsf). The sea floor value of 1630 m/s is based on extrapolation of the Site 1100C data mainly for ease of use in later calculations of depth-traveltime curves and synthetic seismograms. For the interval between 3.5 and 70 mbsf, we used the average velocity (2112 m/s) of Site 739 (5-75 mbsf), ODP Leg 119, Prydz Bay. Besides geological reasons, the decision to accept Site 739 velocity values is based on the availability of logging data and the good agreement between logging and laboratory derived data for this site. Considering the introduced error in velocity for the total profile, the assumptions are reasonably conservative, because all known mid- to outer-shelf Antarctic velocities of the upper 75 mbsf only show small acoustic velocity variations focused in the 1800 to 2500 m/s range.

2.2.3.2 Interval 70-244 mbsf

Three logging tool strings (triple combination [TC], geological high-resolution magnetic tool [GHMT], and the formation micro-scanner sonic tool [FMS]) were deployed at Hole 1103A. After completion of the triple combo logging descent, difficulties in reentering the base of the pipe resulted in the loss of the 1.5-m-long accelerator porosity sonde (APS) bow spring. In order to avoid complications with the missing parts still in the borehole, the FMS-sonic tool

was used without the three centralizing bow springs of the mechanical caliper device (MCD), Fig. 2.1. During two logging passes with the FMS-sonic tool (Fig. 2.1), transit-time and velocity information were obtained between 124 and 244 mbsf (during the first run, pass one) and from the sea floor to 243 mbsf (during the second run, pass two).

The Schlumberger sonic logging tool used at Site 1103A is commercially known as the array sonic or sonic digital tool (SDT, Fig. 2.2). It carries two piezoelectric ceramic monopole transmitters that are separated by 2 ft near the downhole end of the tool. The transmitted signals have a dominant frequency of 10 kHz with a fire rate of 7.5 Hz. Ten ceramic receivers are arranged at various spacings uphole with respect to the transmitters. Two of the receivers are located in the central part of the tool, at distances of 3 and 5 ft from the upper transmitter. The remaining eight wideband receivers are clustered 6 in. apart, forming an array near the top of the tool from 8 to 11.5 ft above the upper transmitter (Schlumberger, 1989). The various transmitter/receiver spacings allow the simultaneous recording of many different transit-times. Detection and recording of an 'analog transit-time' occur in each case when the signal level at the receiver crosses a fixed threshold. This may or may not occur on the true first arrival of the signal, depending on several circumstances, impacting the signal-to-noise ratio downhole. The standard output transit-times with their respective transmitter/receiver spacings are listed in Tab. 2.1. A graphic representation is given in Fig. 2.2.

Transmitter receiver pair	**TT1**	**TT2**	**TT3**	**TT4**	**LTT1**	**LTT2**	**LTT3**	**LTT4**
Transmitter spacing (ft)	5	3	7	5	10	8	12	10

Tab. 2.1. Transmitter/receiver spacings of the standard output of the SDT sonic velocity tool without the wideband ceramic receiver array (see Fig. 2.2 for a graphic representation and localisation).

Four differential time or ΔT outputs of the logging software (Delta-T [DT] computed from TT1, TT2, and TT4, Delta-T Long [DTL] computed from TT1, TT3, and TT4, Delta-T Long Near [DTLN] computed from LTT1, LTT2, and LTT4, and Delta-T Long Far [DTLF] computed from LTT1, LTT3, and LTT4) estimate the formation slowness (inverse of velocity). Each relies on a computation combining four individual transit-time outputs. This gives an answer that is compensated against small inaccuracies resulting from tool tilt, sudden changes in hole diameter, etc. However, should a single transit-time be detected incorrectly, any ΔT output that uses it is rendered completely invalid.

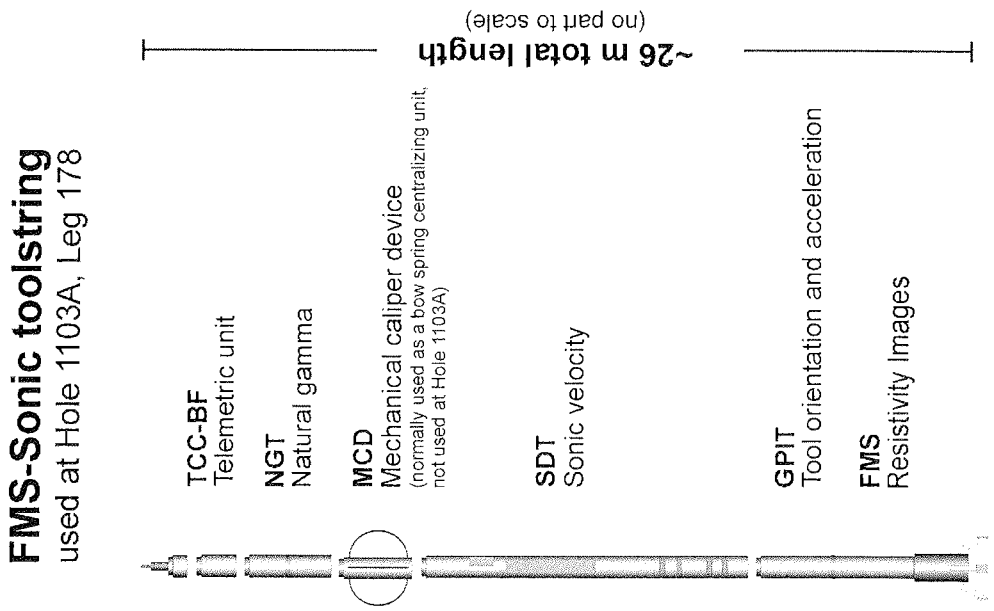

Fig. 2.1. Schematic drawing of the FMS-sonic toolstring used at Site 1103, Leg 178. Note that the MCD centralizer unit that is normally part of the assembly was not deployed at this site.

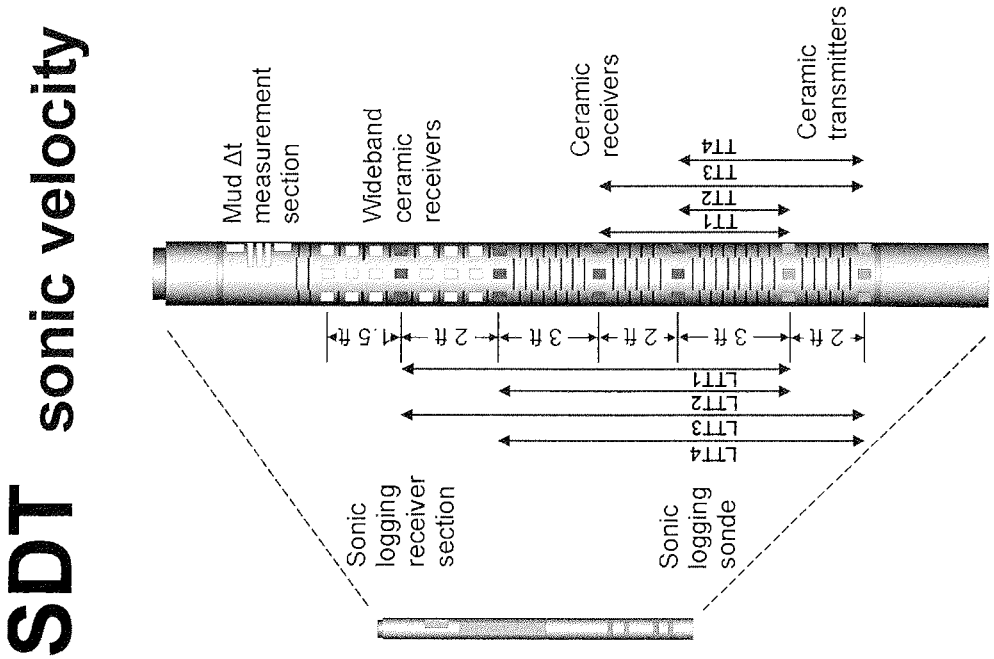

Fig. 2.2. Detailed drawing of the transmitter and receiver configuration of the SDT sonic velocity tool. The "mud" transmitter and receiver near the top of the tool are not used.

Nowhere in the logged interval were all transit-times simultaneously correct. Typically, four or five of the eight were wrong at any given depth, rendering the standard formation slowness estimates completely useless. There are several reasons why this might have occurred. In general, large boreholes (> 13 in.) and unconsolidated formations are challenging for sonic logging because the signal is attenuated by travel through fluid and slow formation. The fundamental problem with slow formations (< 2000 m/s) and the high fireing frequency of 10 kHz is the resulting long wavelength with the possibility of interference of subsequent wavelets at the receivers. Additionally, the lack of the upper centralizing unit (MCD, Fig. 2.1) resulted in the tool being off center, further attenuating the signal and causing additional acoustic noise generated by the tool touching the borehole wall. Consequently, the automatic detection of the signals received at the array and at the two other receivers was inconsistent over time and the signal was often picked within noise preceding the first true arrival (Shipboard Scientific Party, 1999b). Another reason for the recording of poor and inconsistent data could be due to strong velocity inhomogeneity within the logged formations. Tills with unlithified matrix and large clasts show large velocity differences within the measurement range of the tool. Matrix velocities may be in the range of 1800 m/s, whereas those of crystalline clasts can be as high as 5000 m/s (e.g., fig. F24, PWS3 data for Site 1103 in Shipboard Scientific Party, 1999b). Judging from Formation MicroScanner (FMS) image observation, large clasts of different sizes, embedded in a finer grained matrix, are unequally distributed around the borehole. Therefore, it seems possible that an emitted signal could take strongly contrasting travel paths on different sides of the borehole wall.

An additional ΔT output of the logging software (referred to herein as DC) is calculated using digital coherence mapping. At each 6-in. (~0.15 m) sample interval, the waveforms of the eight wideband array receivers are digitized and stacked with various time offsets that compensate for moveout. The correct moveout (and formation slowness) at each depth is recognized from the offset that produces the highest amplitude stack. The data obtained are self diagnostic to some degree in that the coherency of the eight waveforms is a quantifiable indicator of confidence in the data. This technique is more robust in the difficult conditions described above, but in this case only limited intervals featured coherent waveforms. Small-scale formation inhomogeneity may have contributed to the lack of a consistent moveout across the 3.5-ft array.

Remedial on board processing focused individually on the widely spaced receiver/transmitter geometries LTT1 (10 ft) and LTT2 (8 ft) that showed the most consistent transit-times. But this is a weak technique, considering that individual transit-times do not

account for traveltime within the drill slurry gap between tool and formation. A first attempt toward determining true formation velocities was to divide the transit-time by the transmitter-receiver spacing and to add 10% to the resulting velocity to correct for the acoustically slower gap between tool and formation (Shipboard Scientific Party, 1999b). This method is not capable of correcting for varying borehole diameters and varying densities of the slurry within the tool/borehole gap. Additionally, the method assumes that a signal recorded in acoustically faster formations will also pass the tool/borehole gap faster than a signal recorded within acoustically slower formations. These data also have inherently poor vertical resolution determined by the transmitter-receiver spacing used.

In contrast, the data processed postcruise and presented in this paper use exclusively differential times (ΔT), which automatically account for the tool-formation gap. Any pair of transit-times of different spacing can be used to estimate formation slowness, provided that they are of different transmitter-receiver spacings. Dividing the difference in transit-time by the difference in transmitter-receiver spacing, we obtain a ΔT:

$$\Delta T = (TTA\text{-}TTB) / (TRSA\text{-}TRSB) \qquad \text{(Eq. 2.1)}$$

ΔT: Differential traveltime
TTA: Traveltime of transmitter A
TTB: Traveltime of transmitter B
TRSA: Transmitter-receiver spacing A
TRSB: Transmitter-receiver spacing B

The pitfall of this method is that all errors in transit-time detection result in large velocity errors and only small sections of the record therefore contain useful velocity information. Our method is less elegant than Schlumberger's default computation, which uses four transit-times per ΔT; however, by relying on only two transit-times simultaneously, we greatly improved our chance of obtaining valid slowness/velocity data. In order to discern these valuable velocity data, we compared results of one processing technique using data from the two different logging passes and also compared the results of the same pass using different techniques.

Two of the total of 13 incorporated data categories and processing techniques described below are subject to human judgement and experience. Some of the data categories use information twice - all of those instances are noted.

2.2.3.3 Logging Velocity Data Categories

In this section we briefly introduce and discuss the different data categories. To make the abbreviations chosen for the data categories more transparent, two examples are given. The data category "AFA2/1(LTT1+2) match av" is composed of "AFA", for analog first arrival, "2/1" comparing pass one and two of transmitter receiver spacing "LTT1" and "LTT2". The additional abbreviation "match av" indicates that matching velocity values of both passes of the same depth have been used to calculate a mean or average value (av) representative for this data category and depth. Data category "2DC2a/DC2 match av" for example is based on velocity values obtained by digital coherency mapping (DC) of wavelets collected during run 2. The abbreviation "a" indicates special processing parameters, explained in detail in the section of the "DC2a/DC2 match av" data category. The abbreviation "match av" again indicates that matching velocity values of both processing types (DC2a and DC2) of the same depth have been used to calculate a mean value representative for this data category and depth.

AFA2/1(LTT1+2) match av

This category uses transit-times LTT1 (10-ft spacing) and LTT2 (8-ft spacing). Calculated velocities of the first and second passes are compared. Using 300 m/s quality criteria, all data that exceed this velocity difference are excluded from passes one and two. Data within this range are included using an average velocity of the first and second passes. Long-spaced transmitter and receiver pairs may be favorable in lithologic units with strong velocity inhomogeneities within the depth resolution of the tool, because they integrate over a larger rock volume.

AFA1(LTT1+2), and AFA2(LTT1+2) picked by log character

This graphical method uses the two transit-time plots of the two receiver/transmitter pairs LTT1 and LTT2 and the resulting velocity plot of each pass without comparing the two passes with each other and without looking at absolute velocity values. We believe that the ΔT calculated from these two transit-times merits special attention; of all the transit-times recorded, LTT1 and LTT2 performed best. This is based on the subjective experience of the logging engineer, observation of the waveforms during acquisition, and log quality control standards set forth by Schlumberger (Bateman 1985). Admitting that this method is largely subjective, it is nevertheless an independent approach to extract useful data. The major advantage of this method compared to the previous category (AFA2/1[LTT1+2] match av) is

that it is entirely focused on repeatability. Tool position, noise level, and a number of other variables can cause differences in quality and lack of repeatability between passes. In this category, valuable information from one pass that has no counterpart in the other pass can be included.

AFA1(LTT1,-2,-3,-4, TT1,-2,-3,-4) and AFA1(LTT1,-2,-3,-4, TT1,-2,-3,-4) high, AFA2(LTT1,-2,-3,-4) and AFA2(LTT1,-2,-3,-4) high

These data categories are the result of an unusual statistic and combinatorial processing approach. We computed differential transit-times for all available transmitter and receiver spacings (LTT1,-2,-3,-4 and TT1,-2,-3,-4). For n number of initial transit-times it is possible to generate q number of combinations.

$$q = \tfrac{1}{2}(n^2-n) \qquad \text{(Eq. 2.1)}$$

Using all recorded transit-times with their respective geometries, besides the six values of the wideband receiver array (Fig. 2.2), there are 28 possible and 26 actual resulting velocities for the first pass, as two transmitter/receiver pairs have the same spacing (LTT1/LTT4 and TT1/TT4). Unfortunately, TT1,-2,-3,-4 transit-times were not recorded for the second logging pass. Consequently, only five velocity combinations are possible. The resulting velocities for each pass were then compared (Eq. 2.2), leading to 325 combinations for the first pass and 10 combinations for the second pass. The confidence level was again $\leq$ 300 m/s difference in velocity. Additionally, all average resulting velocities < 1500 m/s (water velocity) or > 6000 m/s have been excluded.

For logging pass two, with 10 possible average velocities for each depth interval, the values were mostly within a narrow range and a simple average was calculated as a result for this pass and category. In the case of two distinct populations, the higher value in the AFA2(LTT -1,-2,-3,-4) high category was saved. Only 159 out of 1050 possible values in the depth interval 85-243 mbsf met the criteria.

For logging pass one, with 325 possible average velocities for each depth interval, up to 117 actual values were received using the 300 m/s confidence interval and the plausibility range of 1500-6000 m/s. As a guide for decision making, the values of the first pass were sorted in descending order and small graphs were plotted for most of the depth intervals (Fig. 2.1). Four cases are common. Typically, the values have a stable plateau at the high-velocity side (Fig. 2.1A) and only some anomalies at the low side of the values.

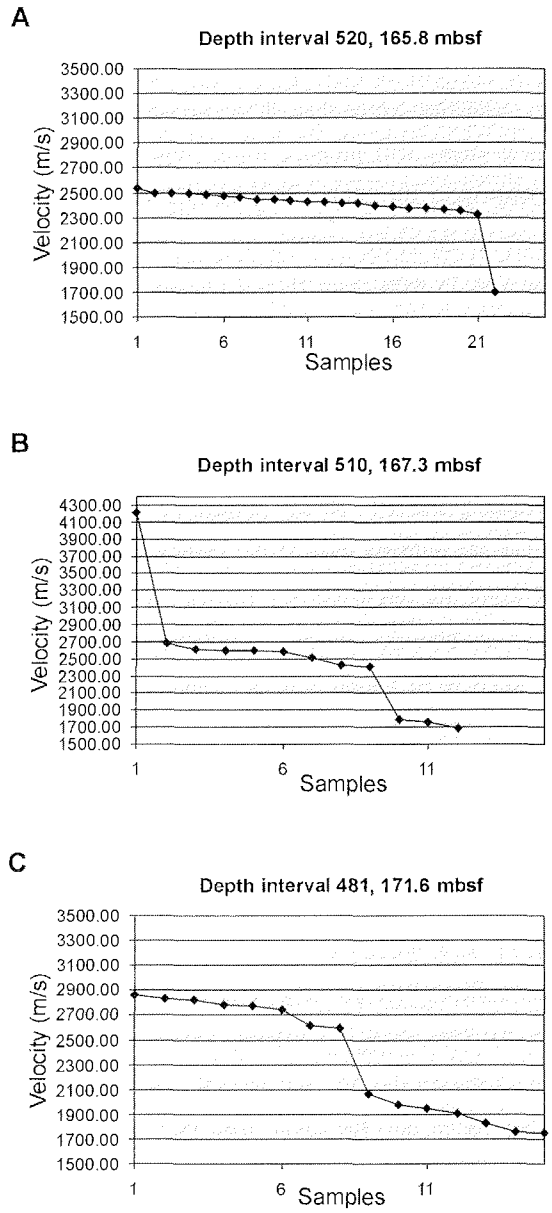

Fig. 2.1. The data categories AFA1(LTT1,-2,-3,-4, TT1,-2,-3,-4), AFA1(LTT1,-2,-3,-4, TT1,-2,-3,-4) high, as well as AFA2(LTT1,-2,-3,-4) and AFA2(LTT1,-2,-3,-4) high, are the result of a statistical and combinatorial processing approach. We calculated differential transit-times for all available transmitter and receiver spacings (LTT1,-2,-3,-4 and TT1,-2,-3,-4) based on analog picked first arrivals. As a guide for decision making all resulting velocity combinations were sorted in descending order and plotted into small graphs for most of the depth intervals. Four cases are common: A. Typically, the values have a stable plateau at the high-velocity side and only some anomalies at the low side of the values. B. In several depth intervals, we also observed erratic velocities at the high end of the velocity spectrum. C. However, depth intervals with two distinct bimodal velocity populations and depth intervals with no velocities within the plausibility range of 1500-6000 m/s (case 4) were also observed.

The choice of high velocities for a final value for this depth interval and category is based on the observation that analog picking in noisy, highly attenuated signals of our log commonly resulted in velocities lower than those expected. Additionally, all signals that travel only through drill slurry will produce lower velocities. However, at several depth intervals, erratic velocities were also observed at the high end of the velocity spectrum (Fig. 2.1B). These values may be the result of cable noise, malfunctioning transducers, or waves traveling alongside the tool. In both cases (Fig. 2.1A and Fig. 2.1B), the erratic values are relatively easy to detect. Their number is commonly small compared to the population of reasonable values, and usually the erratic values differ significantly from the majority of the values for the same depth interval and values of preceding and subsequent depth intervals. Since the aperture of measurement with this technique (equal to the distance between the two receivers used) is between 2 and 9 ft, abrupt changes in measured velocity from one 6-in. depth interval to another are unlikely even if the geological profile contains sudden major impedance changes. During the semiautomatic sorting and evaluation of the values, depth intervals with two distinct bimodal velocity populations were also evident (Fig. 2.1C). Because decisions are likely to be biased in those instances, the higher values were included in a separate category (AFA1[LTT1,-2,-3,-4, TT1,-2,-3,-4] high), similar to the high values of the second logging pass. A total of 751 out of 793 possible values in the depth interval 124-244 m meet the criteria for category AFA1(LTT1,-2,-3,-4, TT1,-2,-3,-4). Nonconclusive velocities were found for 5% of the depth intervals for this category and pass.

AFA1/2(LTT1,-2,-3,-4TT1,-2,-3,-4)mach av

This category compares values of the previous categories AFA1(LTT1,-2,-3,-4, TT1,-2,-3,-4) and AFA2(LTT1,-2,-3,-4). The average of velocity values of the same depth interval with a difference of $\leq$ 300 m/s between the first and second pass were incorporated. Although this category introduces data twice into the initial data pool without utilizing new processing aspects, it seemed especially important to emphasize agreeing results of the first and second pass. More than 80% of the few values (112) in the depth interval 124 –243 mbsf found in pass one (category AFA2[LTT1,-2,-3,-4]) matched their depth counterparts in logging pass two (category AFA1[LTT1,-2,-3,-4, TT1,-2,-3,-4]).

DC1/2 match av

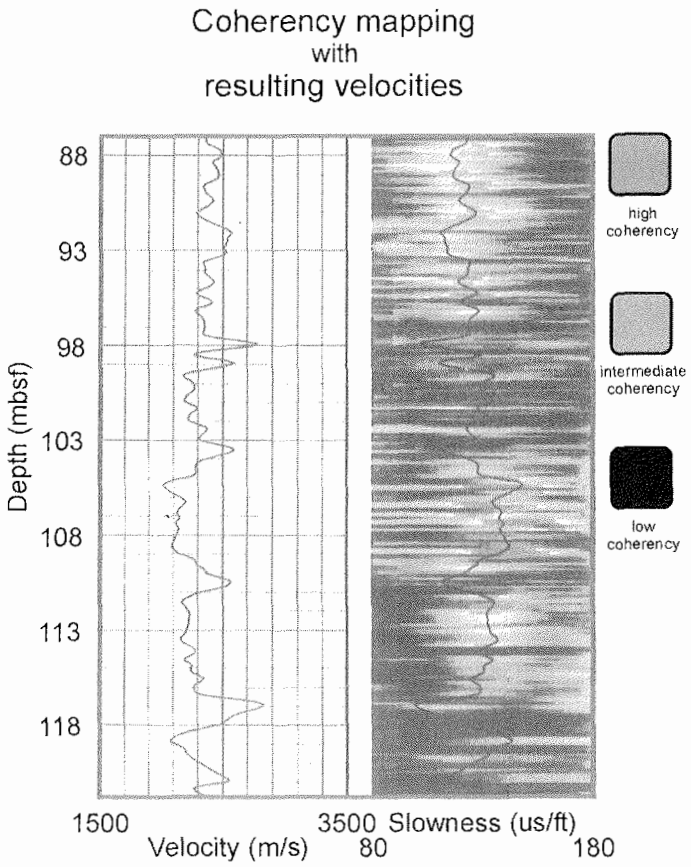

Fig. 2.2. Example of digital coherency mapping performed with data of logging run two, based on the tracking of highly coherent velocity values. The coherency values within the slowness range (80 –180 µs) are color coded (right side). The resulting velocity values are shown on the left side.

Digital coherency mapping output is based on the eight digitized wavelets received at the wideband receiver array (Fig. 2.2) as described above. In depth intervals with low coherency and disturbed signals, the coherency mapping technique has a tendency to produce significantly higher velocities than the velocities derived by analog picking. The category DC1/2 match av contains average velocity values of the first and second pass (see Fig. 2.2) for an example of data of the second logging run) calculated from values with a difference of 300 m/s or less for a specific depth interval. Of the 783 velocities acquired in both logging runs for the same depth intervals, 518 meet the 300 m/s criteria (66%).

DC2 high coherency

This category represents velocity values derived by coherency mapping of the recorded wideband receiver array of the second logging pass. Only depth intervals with excellent coherency values, indicating stable receiver signals, were included. This category may contain information that has already been used within the previous category. Nevertheless, it is important to regard additional valuable data which is only present within the second pass. Of the 1599 velocity values (depth interval 0- 243 mbsf) acquired in logging run two, only 270 meet the high coherency criteria (~17%).

DC2a/DC2 match av, DC2a/DC1 match av

The digital coherency mapping and subsequent tracking of coherent velocities across a certain depth interval is dependent on user-defined boundary parameters. For DC2a processing, we limited the portion of the waveform included in each stack with respect to the moveout applied. The aim was to filter out spurious coherency peaks that might be due to the arrival of slow compressional waves traveling strictly through a single medium (either the slurry or the tool housing). The resulting velocities are compared with the velocities from the DC1 and DC2 processing. Again, averages are calculated for velocities with a difference of 300 m/s or less. We introduced 1242 velocity values (78%) from data category "DC2a/DC2" and only 450 (57% out of 783) from category "DC2a/DC1 match av" to the final data pool. The high quantity of data introduced from category "DC2a/DC"2 into the data pool, is based on the fact, that category "DC2a/DC2 match av" contains velocity comparisons of the same original data and logging run with only modified recalculation parameters for the digital coherency mapping.

Pipe values 0-84 mbsf, (DC2, DC2a/DC2 match av, AFA2(LTT1,-2,-3,-4)

Acoustic data recorded within the drillpipe may carry no, or only limited, information concerning the geological formation. Numerous wave types with different transit times occur in closed forms with a low velocity center (e.g., love, raleigh, and tube waves) (Dresen, 1985). In general, the data should be neglected or treated with extraordinary care. Only a few recorded pipe values are incorporated into the data pool (Fig. 2.3).

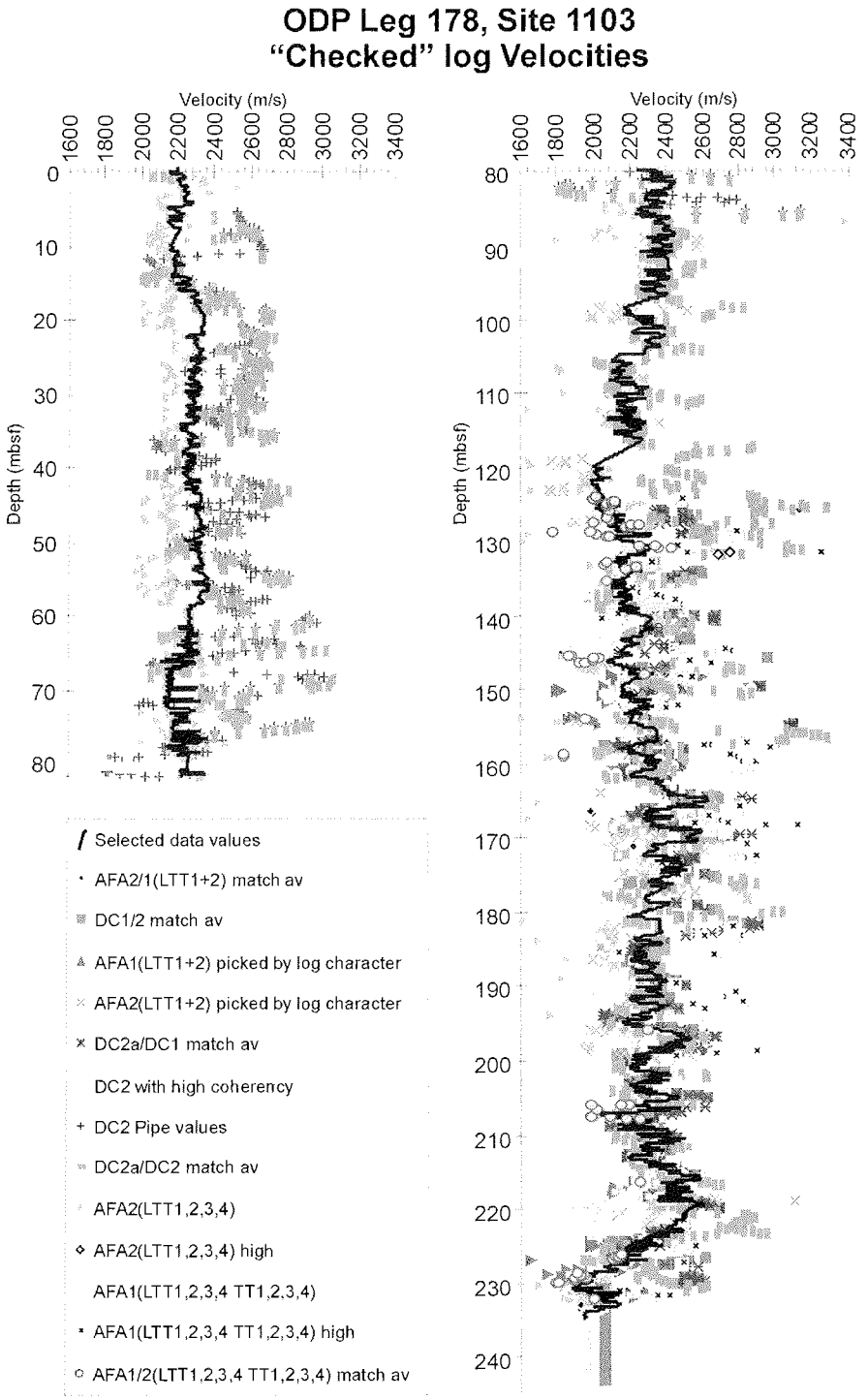

Fig. 2.3. Summary plot of all data categories before data reduction and filtering.

During different coherency mapping approaches and statistical analog-picked analyses (AFA2[LTT1,-2,-3,-4]), several velocity classes were observed. Three of these will be mentioned here. Velocities around 1600 m/s are probable from signals traveling within the water and mudfilled gap between tool and pipe. Velocities around 3500 m/s may result from waves that travel along the pipe/water interface (refraction waves). Some processing categories show values around 2250 m/s. Those values are close to the suspected formation velocity and also occur in the statistically treated category AFA1(LTT1,-2,-3,-4). However, we rejected most of the pipe data and included only about 9 m of it (75-84 mbsf) into our data pool. Within this depth range, the pipe data are in good agreement with laboratory determined velocities (Fig. 2.3).

2.2.3.4 Interval 244-360 mbsf

Below the S1/S3 (Fig. 2.1) unconformity, core recovery improved from 2.3% to 34% because of a change in matrix induration. We measured laboratory compressional wave velocity data on board ship using the PWS3 contact probe system for specimens and split cores (Fig. 2.3; Shipboard Scientific Party, 1999b: fig. F24, PWS3 data for Site 1103).

Preliminary comparisons of velocity data and lithological descriptions (Eyles et al., 2001) suggest that all recovered lithological changes are represented within the velocity data measured. We still have no information for 60% of the core. In order to produce a continuous velocity log for subsequent users, we made, the following assumptions based on the available data: The lab velocity (Fig. 2.3) and density data (Shipboard Scientific Party, 1999b), indicate that low-recovery zones are commonly located at acoustic impedance changes. We therefore assume that all major impedance changes are represented within the available data. Furthermore, in order to reduce data gaps by two thirds of their depth interval, we added artificial data points at both ends of the gap (Fig. 2.3).

This measure is supported by the observation of discrete changes in sedimentology within the cores recovered (interchange of clast-rich structureless diamictite with more sorted sands and silts). Using a simple interpolation technique to fill the data gaps would have caused unrealistic continuous transitions within the velocity profile that are also unfavourable for later seimic modelling (e.g. the calculation of synthetic seismograms).

2.2.4 Results and Discussion

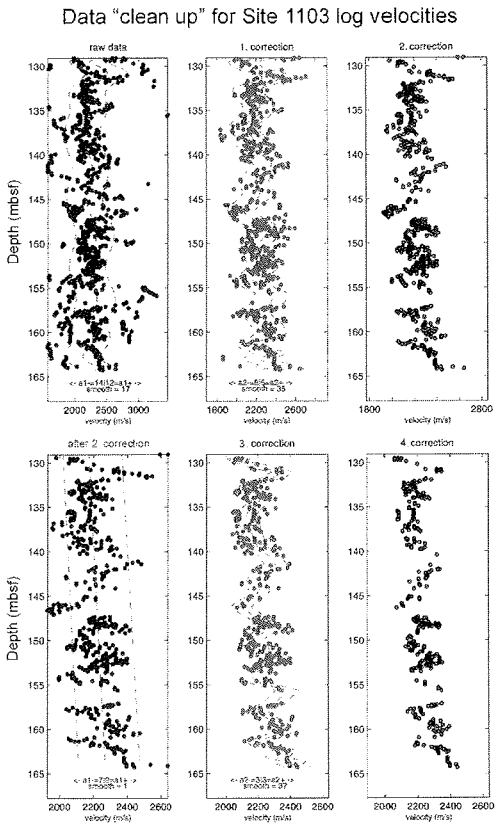

Fig. 2.1. Example of data reduction using polynomial fitting with cut-off limits of various orders. For a detailed description of the techniques refer to Shipboard Scientific Party, 1999a.

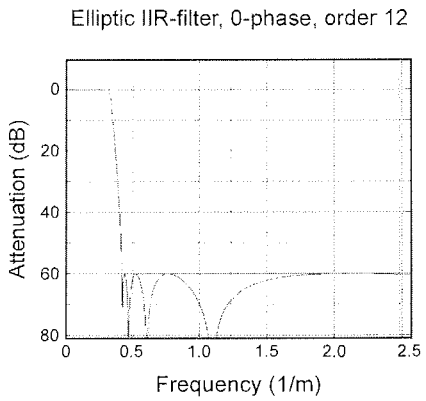

Fig. 2.2. A specially designed low-pass filter is used to remove short-wavelength variations. As a consequence, the depth resolution is reduced to ~ 2 m.

BRG-LDEO Depth Scale	Depth Scale of Unsynchronized Data	Absolute Depth Shift
87.630	81.865	5.765
102.413	98.915	3.498
108.052	106.515	1.537
131.826	130.965	0.861
142.037	141.315	0.722
162.763	165.065	2.302
165.354	167.465	2.111
167.335	169.715	2.38
195.986	197.515	1.529
207.569	210.565	2.996
210.007	216.115	6.108
212.598	220.365	7.767
229.819	230.065	0.246
233.934	232.665	1.269

Tab. 2.1. To synchronize the new velocity data to other logging data of the Borehole Research Group at Lamont-Doherty Earth Observatory (BRG-LDEO), we used 14 prominent features of the IMPH resistivity log. The synchronization was achieved with the linear mode of AnalySeries 1.2 (Paillard et al., 1996).

All the data derived from the previously described 13 categories of processing techniques (without the laboratory-derived velocities) incorporated into the initial data pool from 0 to 244 mbsf are shown in Fig. 2.3. The data are also given in Tab. 2.3. We merged all data categories, with a total of 5400 values into a single depth/velocity matrix by offsetting the depth of the individual velocity categories by 5 mm. Looking at the hole section in a compressed representation, it is difficult to detect well-supported trends (Fig. 2.3). Although only data that passed several quality criteria were included, the data set remains extremely spiky and velocity variations of 1600 to 2800 m/s for the same depth interval are common. Based on the large standard deviation of the data, we rejected a simple smoothing of the values. Our first step toward simplifying the data was carried out in 25-m sections. We used our own method as described in ODP Leg 178, Initial Reports, Seismic Stratigraphy,

"Explanatory Notes" (Shipboard Scientific Party, 1999a). This method is based on individual polynomial fittings of variable orders and uses selectable confidence intervals around the polynomial fit. An example of a six-step clean up is given in Fig. 2.1. An interpolated trendline connecting values chosen is shown together with the initial data pool in Fig. 2.3 (blue line). It has to be noted that the polynomial fitting and exclusion technique will always prefer incorporating regions with high data density. In most cases this is an improvement over simple averaging since outliers are completely removed and do not affect the resulting data. On the other hand, this method by no means ensures the extraction of only good data out of clusters in case the majority of the data for one depth interval is erroneous and the described data separation technique fails.

Subsequently, the data were filtered with a low-pass filter (Fig. 2.2) designed to exclude short wavelength variations. The frequency range of the pass band is set to reduce the vertical resolution of the filtered velocity log to approximately 2 m. The final representation of our approach is given in Fig. 2.3. Since all data processing within this study is based on raw unsynchronized data with respect to depth shifts between logging runs and with respect to the different transmitter receiver pairs used for the different data categories a final depth match was necessary. To achieve a profile comparable to other depth-shifted logging data processed by the Borehole Research Group at Lamont-Doherty Earth Observatory (BRG-LDEO), the resulting plots were graphically fitted with the IMPH resistivity data. The program used is AnalySeries 1.2 (Paillard et al., 1996), and the 14 matchpoints and resulting depth) (shifts are given in Tab. 2.1 and Fig. 2.3. The resulting depth shifts are larger near the drill pipe, between 87 and 100 mbsf according to the BRG-LDEO depth scale, very reasonable in the intervals 100 to 207 mbsf and 230-244 mbsf and unrealisticly high in the short interval between 207 and 212 mbsf. The higher shift values at the base of the drill pipe may be due to problems encountered during the process of reentering the tools after the logging run (Shipboard Scientific Party, 1999b).

Variable shift values between 0 and 3 m can be easily explained with a combination of three effects:

1) During the data processing at BRG-LDEO the GHMT log was used as the reference for depth-matching. The maximum depth shift of the Triple Combo (including the resistivity log) relative to the reference log was between 1 and 2 m. The maximum shift applied to the two FMS-sonic logging runs was an additional 0.6 m.

2) The maximum receiver transmitter spacing on the sonic tool is 13.5 ft (~4.1 m). During data processing the traveltime information of different transmitter receiver pairs with different spacings and effective integrative depth range was brought together without calibrating the sensor-pairs to their effective depth and without synchronizing the two logging runs individually beforehand.
3) The low pass filtering of the data is accompanied by a reduction of the depth resolution to 2 m.

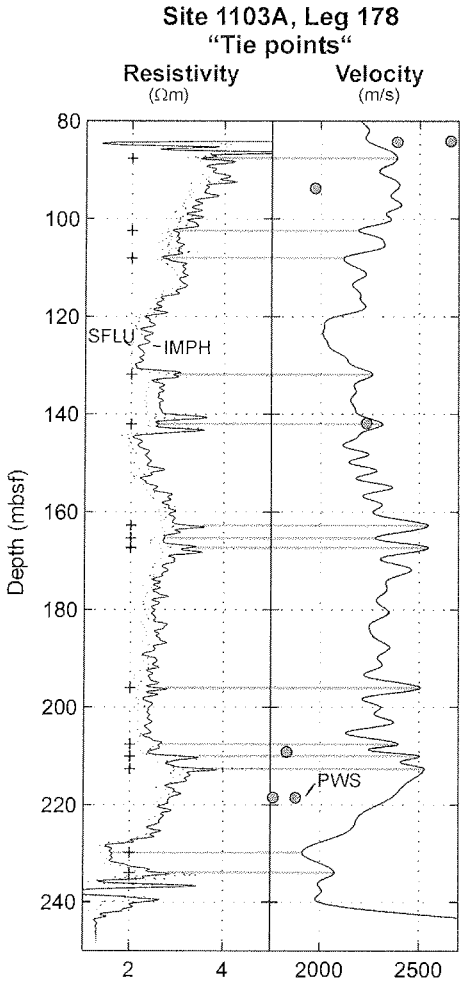

Fig. 2.3. Composite velocity profile of Site 1103, Leg 178. The different data resources are indicated. A digital version of the composite data can be found in Tab. 2.4.

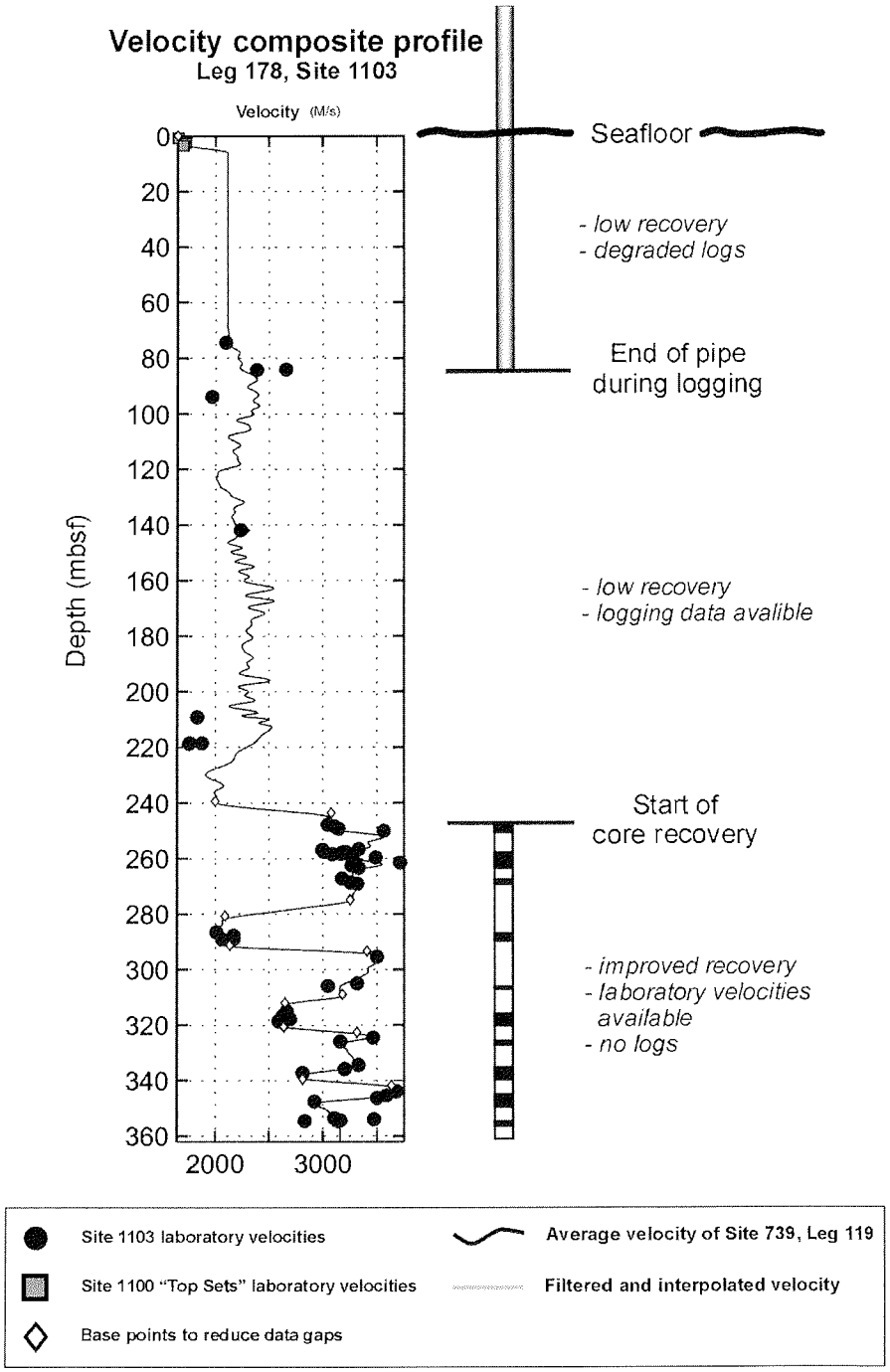

Fig. 2.4. The reduced and filtered logging velocity data synchronized with the depth-shifted resistivity data (integrated resistivity [IMPH] and self focusing resistivity [SFLU] processed by the Borehole Research Group at Lamont-Doherty Earth Observatory (BRG-LDEO). Tie points are marked with crosses. Absolute shifts are given in Tab. 2.1.

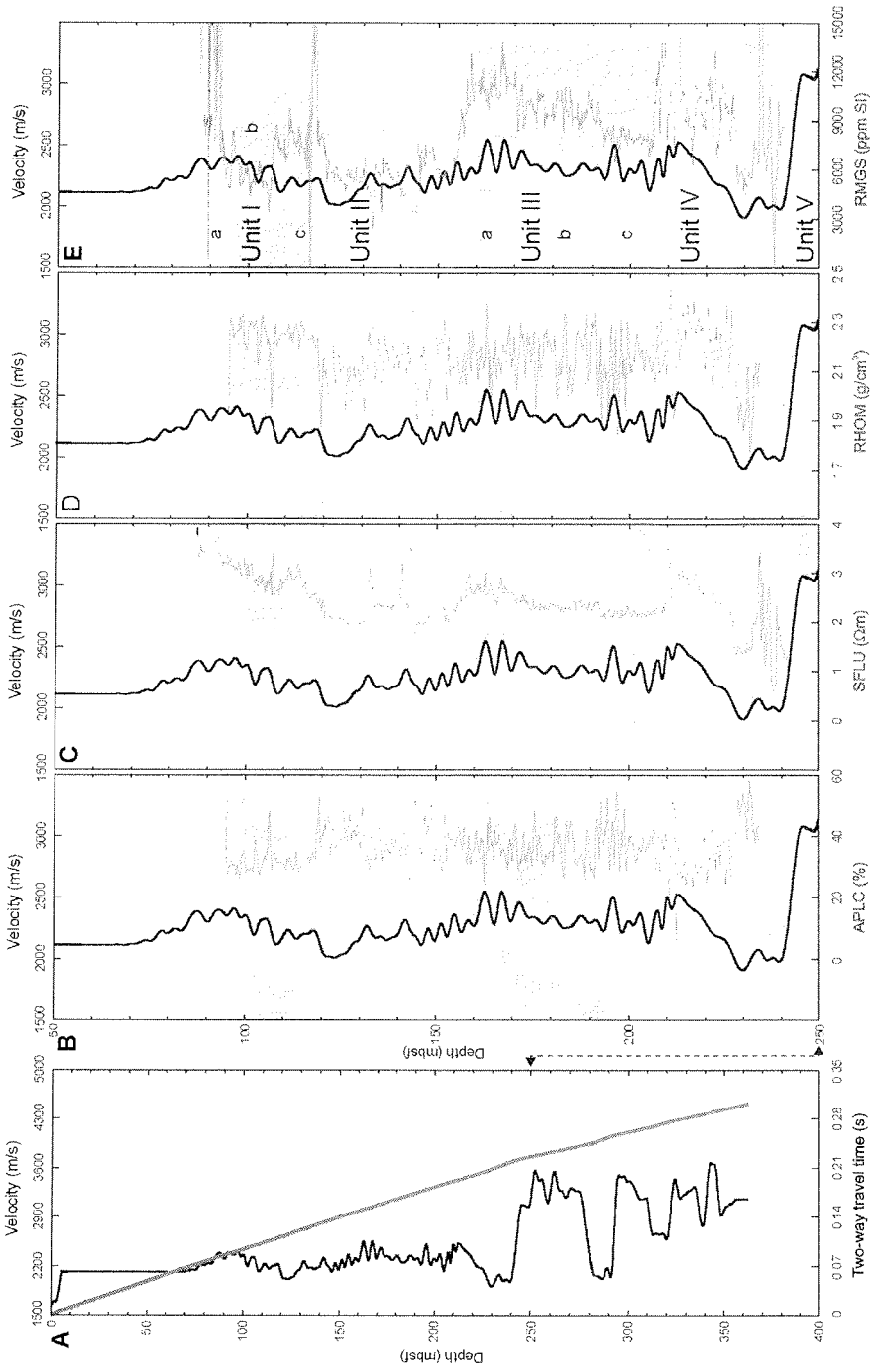

Fig. 2.5. Comparisons of the **(A)** new velocity data and representative downhole logs: **(B)** APLC (neutron porosity), **(C)** SFLU (electrical resistivity), **(D)** RHOM (bulk density), and **(E)** RMGS (magnetic susceptibility). The logging units I-V as defined by the Shipboard Scientific Party (1999b) are outlined **(E)**. Note the difference in depth for Fig. 2.6A and Fig. 2.6B-E.

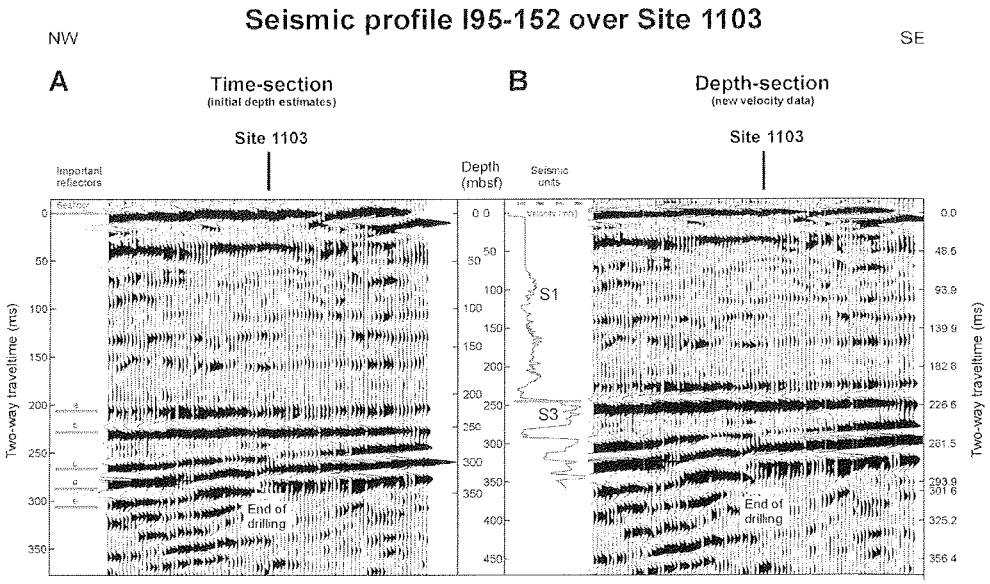

Fig. 2.6. Comparisons of the (**A**) time and (**B**) depth sections of line I95-152 in the vicinity of Site 1103 (Shipboard Scientific Party, 1999b). The depth migration is based on the new velocity data. Note the differences in depth scale and apparent S1/S3 geometry between (**A**) the time section of the Initial Reports volume with an approximate depth annotation, and (**B**) the depth migrated section presented by this study. The presented data confirms the location of the shelf unconformity S1/S3 at 222 ms TWTT or 243 mbsf. The unconformity is seismically expressed by a strong negative and subsequent positive reflection. Refer to Shipboard Scientific Party (1999b) for a detailed description of seismic units and major reflectors (a-e) shown in (**A**).

In the final velocity profile the effect of these three factors is combined, depending on the importance of each data category for a specific depth interval to the finally chosen data. However, the large shifts in the depth interval 207 to 212 mbsf are probably unrealistic and the result of a missmatch or incorporation of erratic data into the final velocity data selection. The correlation is based entirely on graphical correlation with the same systematics for the whole section (matching regional highs and lows of the reference with regional highs and lows of the filtered data curve). Given that the erroneous interval is very short, we decided accept the correlation and accepted its limitations in the mentioned depth interval 207-212 mbsf.

Finally, after compiling the data from all depth sections (0-75, 75-244, and 244-360 mbsf), the contacts were smoothed, resulting in a continuous profile displayed together with the laboratory velocity data values in Fig. 2.4.

The computed velocity curve can be compared for validation to the other representative downhole logs obtained at Site 1103 (Shipboard Scientific Party, 1999b): the neutron porosity (APLC), the bulk density (RHOM), the electrical self-focusing resistivity (SFLU), and the

magnetic susceptibility (RMGS) (Fig. 2.5). The chosen logs show reliable values, except the anomalies in the RMGS log at ~117 mbsf, caused by the APS bow spring lost in the hole.

The velocity curve is generally correlated with the RHOM, RMGS, and SFLU logs, and anti-correlated with the APLC log. The velocity curve shows the same features as the other logs that are divided in five units (Fig. 2.5). The first unit is characterized by low porosity and high resistivity, density, and velocity values. The second unit exhibits porosity values between 25% and 50% and lower susceptibility, density, velocity, and resistivity values. The two thin beds (~132 and ~142 mbsf) seen in all the logs (high SFLU and RHOM values; low NPHI and RMGS values) are also found in the velocity curve. In the third unit, the resistivity, susceptibility, and velocity logs all show higher values at the top with a slight tendency to decrease down the hole. The fourth unit is characterized by a sharp reduction of the logged values and a sharp increase in the porosity. In the last unit, we note a distinct jump to lower density, resistivity, susceptibility, and velocity values and higher porosity. The high variability of the logs in this part of the section is not seen in the velocity curve, probably because of the smoothing method used to reconstruct it.

Fig. 2.6 shows a comparison of the original seismic data and a depth-migrated section generated by using the new velocity data. The original time section already published in the Initial Reports Volume, ODP Leg 178 (Shipboard Scientific Party, 1999). The log data confirm the location of the major shelf unconformity at 222 ms two-way traveltime (TWTT) or 243 mbsf (see Escutia et. al., in prep., for a thorough discussion of the nature and history of the unconformity). The unconformity between seismostratigraphic units S1 and S3 (Shipboard Scientific Party, 1999b) is seismically expressed by a strong negative and subsequent positive reflection arround 222 ms TWTT below sea floor (Fig. 2.6A). The decline and rise in acoustic impedance (acoustic impedance = velocity x density) within the depth interval 220 to 245 mbsf seen in the velocity and density data of Fig. 2.5D are most likely the cause of this reflector. The positive reflection around 206 ms TWTT, is probably still part of the S1 topset package.

2.2.5 Conclusions

Starting with nonconclusive velocity logs caused by a slow formation with extremely high internal velocity contrasts, and an uncentered logging toolstring without bow springs, we improved the quality of the data and evaluated data previously unavalible with standard processing techniques. The velocity profile we produced correlates well with the other logs obtained (neutron porosity, bulk density, self-focusing electrical resistivity data, and magnetic

susceptibility; Fig. 2.5) and offers a reasonable estimate for the location of a prominent shelf unconformity. However, we must emphasize the limitations of the data. Errors may be introduced by:

- a bias in choosing and defining the data categories
- the possibility of exclusion of rare good data in a given interval where misleading values represent the majority of the data
- uncertainity of the precise depth of data from transmitter and receiver spacings collecting different regions along the toolstring for a given tool position
- mixing of the non depth-shifted raw data of logging runs one and two
- bias in the final correlation by assuming that low resistivity zones are most commonly denser and therefore acoustically faster

Nevertheless in contrast to seismically derived velocity information (Tinivella et al., 2001, see chapter 2.3). The velocity information presented here is more detailed and allows the investigation of the seismic character at least on the scale of the defined logging units (Fig. 2.5). We hope that the new velocity model will help seismostratigraphers, modelers, and sedimentologists to understand complexities of the Antarctic shelf. The new information is utilized in the paper by Escutia, et al. (in prep.).

2.3 Validation and Application of the new Velocity Data

2.3.1 Comparisons of the new velocity data with other velocity information

Prior to Leg 178, as part of the site survey and requested by the ODP Site Survey Panel, the Programma Nazionale di Ricerche in Antartica provided *P*-wave interval velocities for all drill sites. These stacking velocities have been supplemented post cruise by tomographically derived velocities and submitted to the ODP Leg 178 Scientific Results Volume (Tinivella et al., 2001).

Thanks to the authors (Tinivella et al., 2001) who provided the data for profile I95-152 prior to publication, it is possible to compare the velocities based on logging and lab measurements developed in this thesis with the velocities derived from multichannel seismic survey (MCS) data processing. Interval velocities derived from stacking velocity information via Dick's formula using root mean square velocity information constitute the prime seismic

velocity information obtainable from MCS. Tinivella et al. (2001) describe the disadvantages of using stacking derived interval velocities for target reflector depth determination:

- short streamer length compared to target depth reduces available offset and decreases data quality
- the assumption of horizontal layered reflectors with no lateral velocity variation is commonly not attained in reality

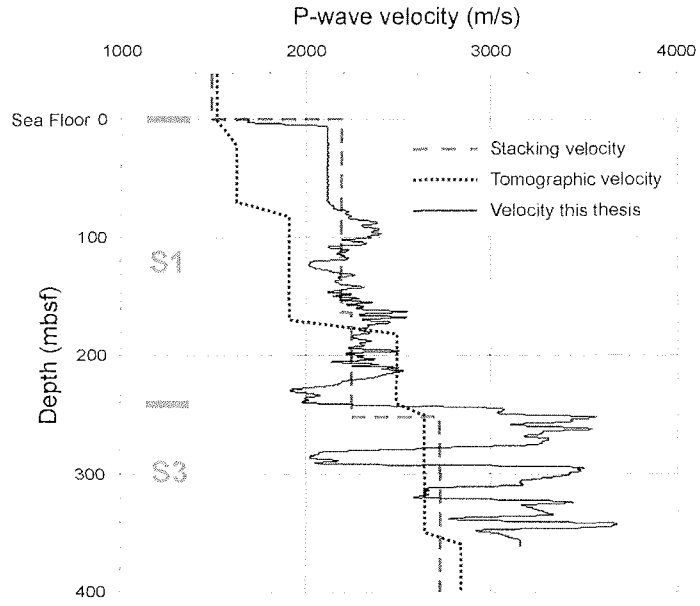

Fig. 2.1. Comparison of different *P*-wave velocities available at Site 1103. Stacking and tomographic velocities are adapted from Tinivella et al. (2001).

To obtain additional independent velocity information Tinivella et al. (2001) use iterative modelling based on ray tracing (seismic tomography). Semi-manually picked reflectors define a starting velocity model; this is then varied in geometry and velocity until lateral dispersion of resulting reflectors is brought to a minimum. This type of modelling also considers lateral velocity variations along reflector packages. The resolution of a velocity profile derived by tomography may be of the order of the trace spacing (12.5 m for profile I95-152).

The velocities for Site 1103 are illustrated in Fig. 2.1. In case of the tomography velocity (TV), the topset Unit S1 (Fig. 2.1 and Fig. 2.1) is divided into 3 layers of increasing velocity with depth. No sharp increase in TV is found at the lower boundary of the topset Unit

S1. TV velocities for Unit S3 have averages of 2600 m/s and show no internal velocity inversions. The stacking velocity (SV) is less detailed in depth resolution but does show a sharp increase in velocity at the S1/S3 unconformity. For Unit S1, the TV is notably smaller than the SV from 0-180 mbsf. For Unit S3, TV and SV are in the same range with absolute differences smaller than 200 m/s.

In comparison with the velocity profile derived in this thesis (chapter 2.2) TV values are dramatically lower in Unit S1. The SV velocities seem to represent a running average for Unit S1 and S3. Neither TV nor SV is able to represent velocity inversions in the 20-30 m range, notably the velocity inversion below the shelf topsets Unit S1.

Tinivella et al. (2001) describe one case (a location midway between Site 1100 and Site 1103, Fig. 2.1), where an inversion in the tomographic velocities occurs at the S2/S3 boundary. They attribute this inversion to ice load induced overcompaction of S1 and S2 compared to a normally compacted S3. The fact, that no inversion occurs in the tomographic velocities at Site 1103 is attributed to the nature of the contact (near-conformable Site 1103 vs. erosional at the 1100/1103 midway position).

One can disagree with this interpretation since the new velocity profile for Site 1103 shows a clear inversion at the top of S3. Seismic tomography is not detailed enough to show small-scale variations in the 20-30 m range. Also, the link between overcompaction and seismic velocity is weak, since lithological changes within Unit S3 (see chapter 2.4) are able to produce velocity variations exceeding those suspected from compaction history differences. Unit S3 is lithologically different from Unit S1, which consists of loose gravel in a clay/sand matrix, and the sediments of Unit S3 are diagenetically cemented. For acoustic behaviour the presence of cement in the porespace is more relevant than the compaction history. The velocity inversion (also seen as a density inversion in the logs, Fig. 2.5 and Fig. 2.1) at the top of Unit S3 seems to be a random feature of the stratal location of the unconformity separating S1 and S2 from the underlying Unit S3. Along the seismic profile, there are locations where S1 or S2 are in unconformable contact with a high velocity layer of S3 (cemented diamicts), which result in a positive velocity step. Another possible explanation for a velocity inversion could be the presence of a reworked high porosity horizon at the base of Unit S1 or S2, consisting of unrecovered, reworked, cemented older strata, (Fig. 2.1). In the later case the inversion zone should be restricted to the overlaying strata.

Overall, the SV seem to be much more reliable than TV in indicating absolute vertical velocity distributions. This is especially true where the streamer had a length of 1500 m and the target reflector depth was between 500 and 800 m.

2.3.2 Site 1103 Synthetic Seismogram

2.3.2.1 Background

As a quality check of the new velocity profile derived with unusual processing techniques of logs and lab data, Trevor Williams of the Borehole Research Group at Lamont-Doherty Earth Observatory calculated a synthetic seismogram on the base of this new velocity information. The figures shown will be published in a joint paper with Escutia and Lauer-Larede outside ODP.

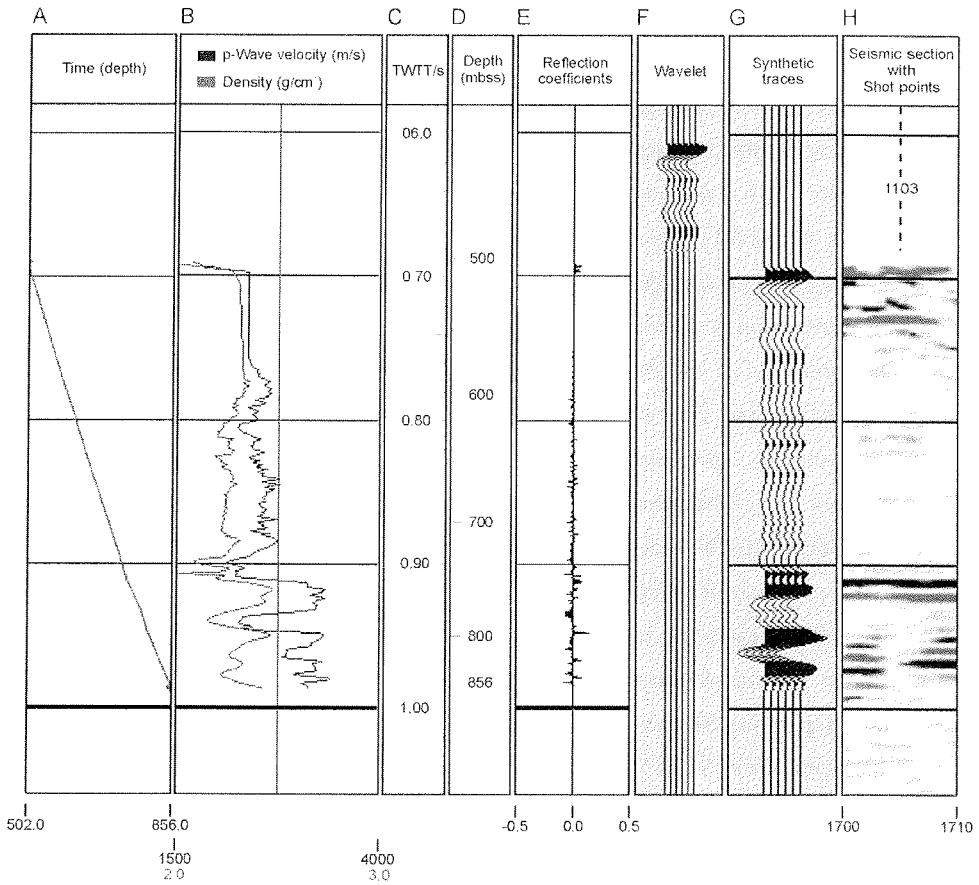

Fig. 2.1. Input variables and processing steps of a synthetic seismogram for Site 1103. Note that TWTT is given starting from the seasurface compared to Fig. 2.1 and Fig. 2.6 where the timescale starts at the sea floor offset ~ 700 ms). See text for details. Figure received and modified from Trevor Williams of the Borehole Research Group at Lamont-Doherty Earth Observatory (LDEO).

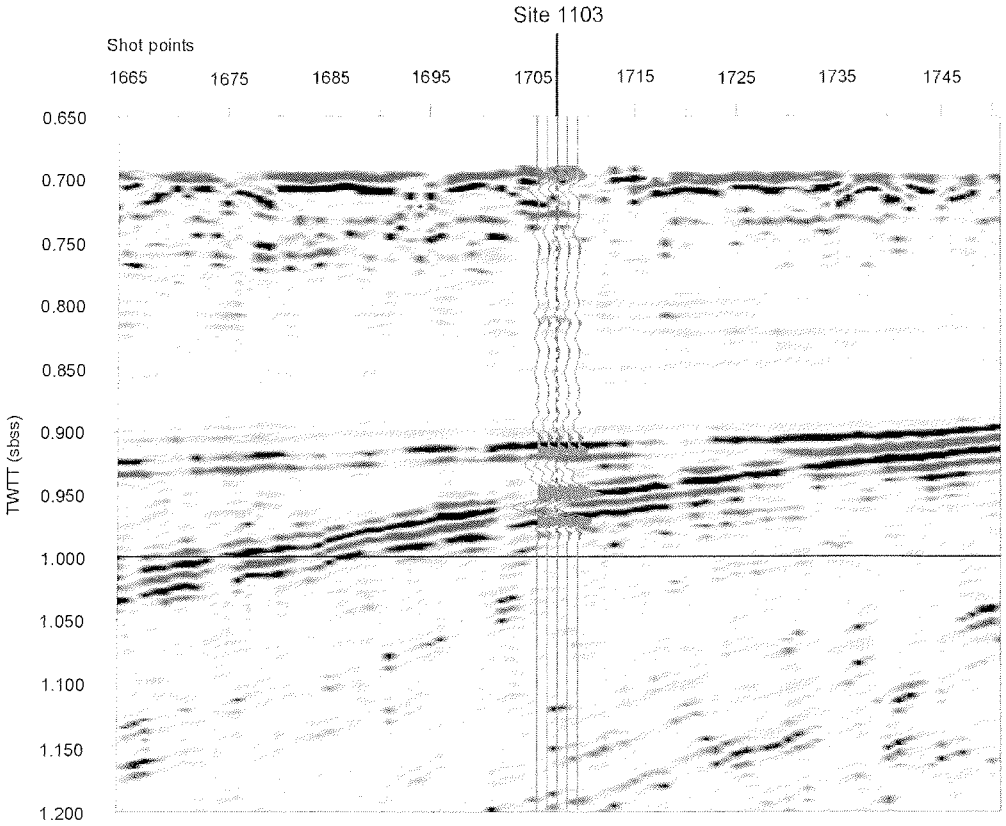

Fig. 2.2. The new synthetic traces overlain on part of MCS line I95-152. The major reflectors are in place – indicating an overall correct velocity model. Note that TWTT is given in sbss (seconds below sea surface), see notes Fig. 2.1. See text for detailed discussion of the comparison. Figure received and modified from Trevor Williams of the Borehole Research Group at Lamont-Doherty Earth Observatory.

The synthetic traces are calculated with a professional Schlumberger package (ESX of GEOQUEST) and not with the software synseis described in the "Excursus" (chapter 7.1.7). Starting parameters for the calculation (see the "Excursus", chapter 7.1.6 for mathematical and physical details) are the new velocity profile, a density profile (both shown in the second column from left (Fig. 2.1B) and a source wavelet (Fig. 2.1F).

Density values are empirically derived from deep penetrating resistivity data (SFLU, Fig. 2.3 and Fig. 2.5) and index properties of discrete samples (below 243 mbsf, when recovery started). The first step is an empiric conversion to porosity (Eq. 2.3, oral communication T. Williams, 2001) followd by a transformation to density using fixed density values for porewater (1.03 g/cm^3) and matrix (2.75 g/cm^3).

$$\text{Porosity} = \sqrt{\frac{0.28}{\text{SFLU Resistivity}}} \qquad \text{(Eq. 2.1)}$$

The wavelet is extracted via the ESX package from 20 neighbouring traces in the vicinity of Site 1103 using built-in deconvolution algorithms. Note the extreme length of the signal (0.06 sec or 90 meters in seawater). The resulting reflectivity coefficient profile (Fig. 2.1E), the synthetic traces after convolution (Fig. 2.1G) and adjacent traces from profile I95-152 are also given (Fig. 2.1H).

2.3.2.2 Discussion

The major reflectors start at about the correct depth (time /depth) e.g the unconformity between S1/S2 at 225 ms TWTT below sea floor or 243 mbsf and the seaward dipping reflectors below 260 ms TWTT below sea floor of Unit S3. The good representation of weaker reflectors is remarkable. This is the case even though the polarity is reversed in the horizontally stratified Unit S1 (e.g. the negative reflection around 50 ms TWTT below sea floor or several other reflectors below 75 ms TWTT below sea floor). As noted earlier, all S1 data are entirely log based, because recovery was poor in this interval.

Beside gaps in the data, there are some features in the seismic section that are not represented in the synthetic traces. For example the black reflector at about 220 ms TWTT below sea floor (920 ms below seasurface, within the seismic section) with a stronger red reflector immediately underneath. It may be a reversed polarity reflection, caused by a negative downhole impedance change. The velocity profile (Fig. 2.4 or Fig. 2.1B) does show a major velocity reversal at this depth and time (shortly above the S1/S2 unconformity). The match of the strong amplitude, seaward dipping reflectors of Unit S3 (around 250 ms below sea floor profile, Fig. 2.6 or 950 ms below sea surface Fig. 2.1 and Fig. 2.2) with the synthetic traces is not perfect (better vertical resolution on the seismic profile). Since the velocity and density profile are able to resolve these changes, it is likely that the long wavelet used for the convolution is responsible for the spread of details. Nevertheless these new synthetic traces are by far the best modelling results obtained and allow a confident interpretation of the reflectors and correlation with lithology interpretated from logging or observed by recovery (Chapter 2.4).

2.4 Linking Seismic Units to Lithology

2.4.1 Unit S1

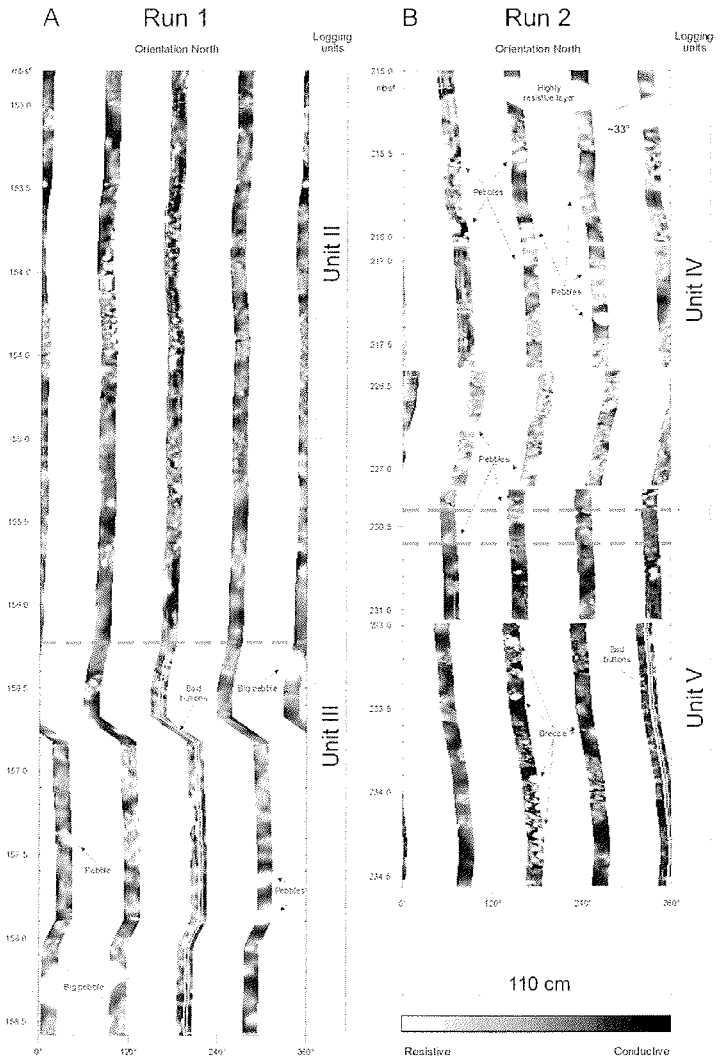

Fig. 2.1. Formation MicroScanner (FMS, see Fig. 2.1 for an image of the tool) resistivity images of selected intervals of logging run 1 and 2 of seismostratigraphic Unit S1. **(A)** contact of logging Units II and III. Logging Unit II has lower resistivity values (darker color coding) and fewer and smaller detectable gravel. Logging Unit III is generally lighter in FMS color (higher overall resistivity corresponding to fewer clays and silts) and contains abundant detectable gravel in various sizes. The visually detected start of significant gravel abundance is 1.25 m lower than the definition of the logging Unit II/III boundary. For our logging data this represents a tight fit since even after depth shifting of runs 1 and 2 by the BRG-LDEO large absolute depth errors remain in the data (Fig. 2.2). **(B)** Examples of gravel rich Unit IV (light colors -> high resisitivity) and transition to highly conductive Unit V with irregular shaped components in the lower part, see text for interpretation.

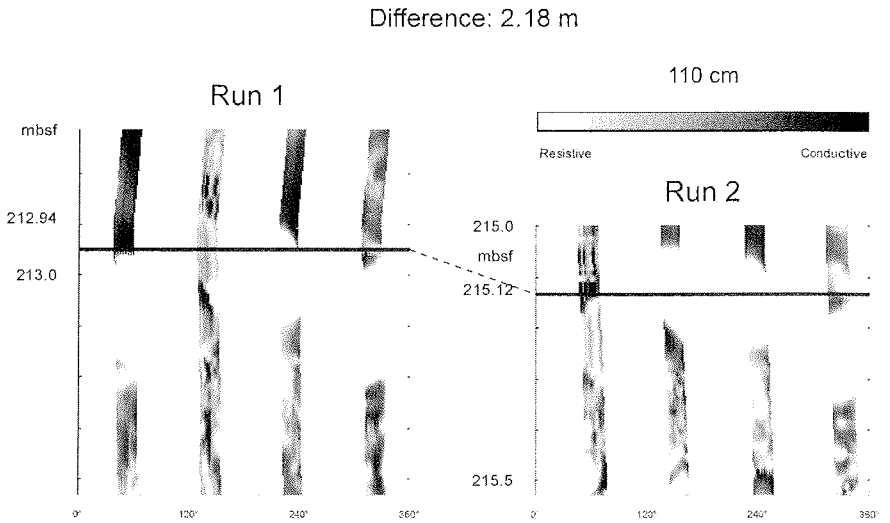

Fig. 2.2. A high resistivity layer, probably a large clast that has been perforated by the rotary drill bit, can be identified in both logging runs. Comparison of the figures illustrates the uncertainities in absolute depth remaining after correlation of the logging runs and application of depth shifts.

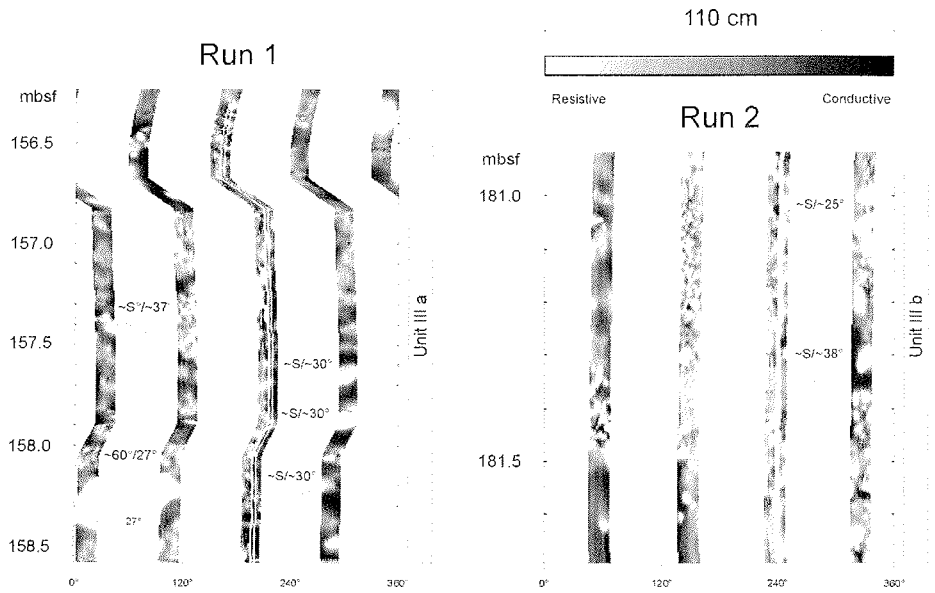

Fig. 2.3. Several clast-rich FMS logging units show oriented bright spots with southerly dip directions. This may be interpreted as imbricate fabric of basal moraines or lodgement tills. The observed dip directions of the clasts suggests an advance of the glacier from the south (in lodgement tills and basal moraines clasts dip up-glacier; Dreimanis, 1976; Compton, 1985). This is in good agreement with the orientation of a major shelf trough to be a major drainage channel for ice between Anvers and Hugo Island, Fig. 1.2).

Because cores were not recovered, the lithological description for seismostratigraphic unit S1is based on logging (e.g.: Fig. 2.5 and Fig. 2.1, Fig. 2.1. Sea floor images and resistivity images (FMS, Fig. 2.1-Fig. 2.3) together with clasts and matrix found in the core catcher, suggest matrix-supported coarse gravels with variations in the gravel abundance. The porosity correlates positively with the clay / silt / sand content of the matrix. Highs in the magnetic susceptibility correlate with clast-rich zones.

Logging Unit I: 84 (Base of Pipe)–118 mbsf[9]

Unit I is characterized by low (25%–35%) porosity and high resistivity, density, and velocity. Magnetic susceptibilities are variable. This unit seems to have a distinct lithologic character and may contain more chlorite than the underlying units (infered from natural gamma data and the photo electric effect; Shipboard Scientific Party, 1999). The distinct character of the magnetic susceptibility log justifies the division in three subunits: a, b and c (Fig. 2.5, Fig. 2.1, and Fig. 2.1)

Logging Unit II: 118–155 mbsf

Unit II generally has 35%–50% porosity but contains a subunit (130–145 mbsf) of lower porosity (25%–40%). Magnetic susceptibilities are low. The subunit is bounded at the top and bottom by thin (2 m) beds of distinctly higher resistivity and lower susceptibility.

Logging Unit III: 155–206 mbsf

Unit III has high magnetic susceptibilities, and the FMS images show that clasts are common in the upper part (Fig. 2.1). From about 170 mbsf to the end of Unit III clast occurrence decreases. This correlates with a reduction in magnetic susceptibility (two discrete steps are seen defining subunit a, b and c) and resistivity.

Logging Unit IV: 206–228 mbsf

Unit IV is similar to Unit III but with lower porosities and higher resistivities. A 30-cm-thick layer (or flat boulder?) of very low (0%–10%) porosity occurs at 212 mbsf, and a 1 m-thick layer of ~20% porosity lies at 210 mbsf, the only level in which layering is evident in the

[9] Part of this section is modified from Shipboard Scientific Party (1999). Note: the number of logging units has changed. Unit 3 and Unit 4 are now summarized in Unit 3. Authorship of sub-chapter „Downhole Measurements": Lauer-Larede, C., Moerz, T., Williams, T.

FMS images. Alternate explanation for this „layer" is a perforated low resistivity crystalline boulder (Fig. 2.1 and Fig. 2.2).

Logging Unit V: 228 mbsf–Base of Logging (242 mbsf)
Unit V is marked by a distinct jump to higher porosity (50%) and lower density, resistivity, and velocity. Porosity reaches 60% in a zone of highly variable log behavior (233–242 mbsf). The logs end at 242 mbsf, but Unit V cannot extend much deeper, as the first core with significant recovery (178-1103A-27R), characterized by a porosity of 20% and velocities of >3000 m/s, begins at 247 mbsf. The transition between the base of Unit V and the top of Core 178-1103A-27R thus represents the largest contrast in physical properties observed in the hole, probably caused by induration and cementation.

2.4.2 Unit S3

In the absence of a continuous sedimentary record (34% recovery) for seismostratigraphic Unit S3, stratigraphic subdivision is not possible. However, three lithofacies can be distinguished within in the interval 247-360 mbsf (Fig. 2.1):

Diamictites (lithified Diamict, Facies D)

The diamictities are poorly sorted mixtures of sand, mud and clasts, with clasts sizes larger than 2 mm in diameter. Clasts within the diamictites are matrix-supported following the classification of Flint et al. (1960). At Site 1103, diamictites have a distinctive gray-brown, asphalt-like appearance (Shipboard Scientific Party, 1999). Diamictites vary from clast rich (>20% clasts[10]) to clast poor (10-20% clasts). Clasts vary in size from 2 mm to larger than the core diameter. Most clasts are subangular but there is variation from well rounded to angular. Matrix composition varies between sand dominated (60% sand) and silt dominated (50 % silt) with clay contents between 20 and 30%.

Distinctive features of diamictites at Site 1103 are the mud and siltstone clasts (< 2 cm in diameter, e.g. in core 34R, Fig. 2.1 and Fig. 2.2B) and intervals of chaotically stratified zones (<30 cm thick), labeled as Facies Dms (Fig. 2.2C, D) separating massive diamictite units (Facies Dmm, Fig. 2.2A).

[10] All given % are % by volume.

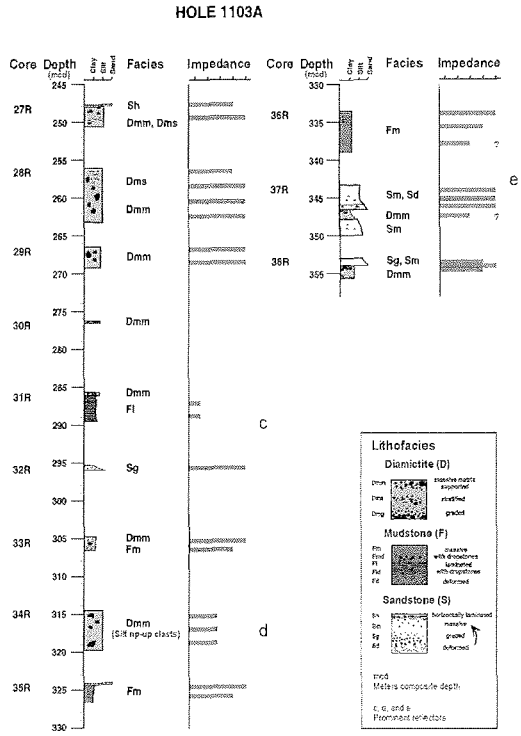

Fig. 2.1. Simplified lithostratigraphy showing lithofacies impedance indicators and possible reflector tops of the seismostratigraphic unit S3 below the major shelf unconformity at Site 1103 A. Refer to the text for characterization of the facies types. Modified from Shipboard Scientific Party (1999), the Figure has been rescaled to represent true thickness of recovered intervals and depth scale is converted to the mcd. Tentative impedance indicators have been added based on acoustic measurements on board the ship.

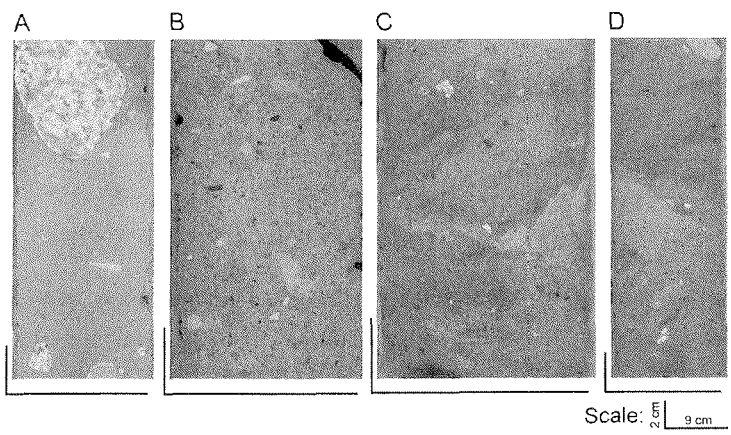

Fig. 2.2. (**A**) Example of massive diamict facies Dmm (interval 178-1103A-27R-2, 9–23 cm). (**B**) Massive diamict facies Dmm with numerous light-colored silt clasts (interval 178-1103A-34R-4, 43–53 cm). (**C,D**) Examples of chaotically stratified diamict facies Dms (**C**, interval 178-1103A-28R-2, 83–92 cm). (**D**, interval 178-1103A-28R-2, 24–41 cm). Modified from Shipboard Scientific Party (1999).

Sandstones (Facies S)

The sandstones are commonly massive (Facies Sm, Fig. 2.1) to chaotically stratified (Facies Sd, Fig. 2.1) and sometimes graded (Facies Sg, Fig. 2.1). The sandstones have the same color and grade of induration as the diamictites. They are very poorly sorted and have sharp erosive bed bases and tops (one bed top was recovered in core 37R, Fig. 2.1). Distinctive features of sandstones at Site 1103 include extensive soft sediment deformation, steep dipping beds within mudstone successions, and an abundance of floating gravel and mud clasts.

Mudstone (Facies F)

The mudstones are poorly sorted, gray (same color as sandstones and diamictites), massive mudstones. Facies Fm (Fig. 2.1) are the most abundant fine grained sediments at Site 1103. The distinction between Facies Fmd (massive mudstone with dropstones) and Facies Dmm (massive diamictite) is not always possible since the cores show gradational transitions between the two end member facies. Distinctive features of mudstones at Site 1103 include the absence of bioturbation, occurrence of weak laminae (Facies Fl), dewatering structures, pillow structures (load features) and core-scale normal faults.

Common to all facies at Site 1103 are shell fragments and reworked biogenic material of Miocene to Cretaceous age and the absence of bioturbation and *in situ* marine biota. Especially noteworthy is the presence of large numbers of light colored clasts of reworked marine mud (Fig. 2.2B) interpreted as so called rip up clasts (Pickering et al., 1989; Eyles, 1993). Their angular shape suggests a brecciation of consolidated sediment during the process of reworking. This is supported by well-preserved diatom assemblages found within the clasts but not within the matrix of the diamictite (Shipboard Scientific Party, 1999; Eyles et al., 2001).

2.4.3 Ages and Interpretation of the S3 Depositional Environment

Age assignments based on shipboard observations (smear slides of core-catcher sediment) are given in Fig. 2.1. Lithological features observed within the sediments recovered at Site 1103 (seismostratigraphic Unit S3) are consistent with an environment of very rapid deposition (dewatering structures in Fm and absence of bioturbation and insitu marine biota) on a glacially (poor sorting, size of clasts) influenced slope (tilt of beds, energy required to transport and support clasts). Transport mechanisms for the observed diamictites are debris flows and turbidites or muddy debris flows for the sand- and silt/mudstones. Common features within the matrix (e.g. colour) and clast types (e.g. the mud rip of clasts) suggest

differentiation of sand and mudstones out of the diamict facies during transport or a close-by common source for all three facies.

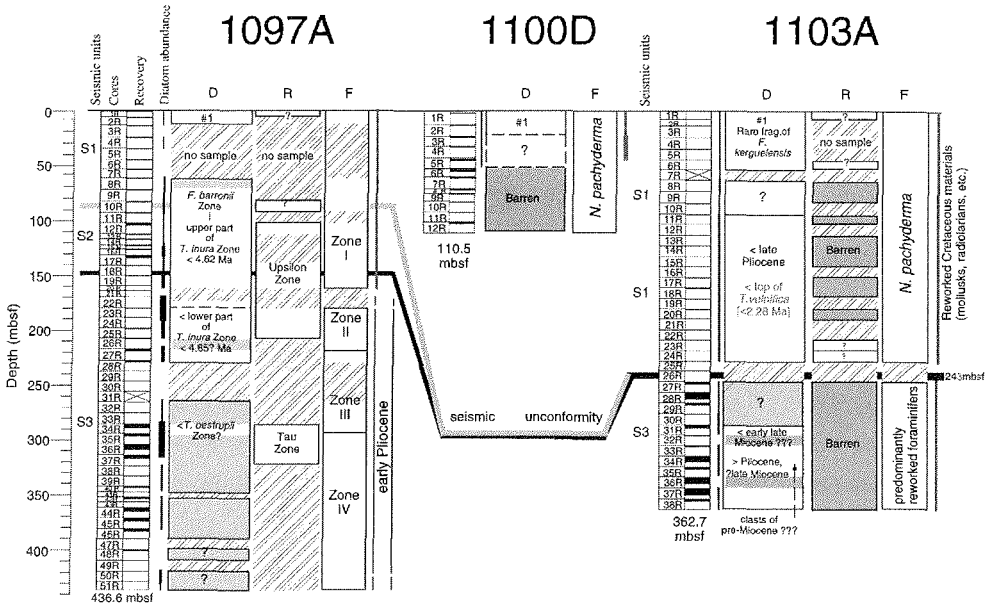

Fig. 2.1. Age constraints - Biostratigraphic summary of shelf sites (Holes 1097A (Fig. 1.2), 1100D, and 1103A (Fig. 2.1-Fig. 2.1)), based on shipboard observations and seismic correlation. Light gray horizons are material with very rare diatom occurrence. Age assignment of S3 (4.5-4.6 Ma, Camerlenghi et al., in press) at Hole 1097A is based on benthic foraminifers, diatoms, and radiolarian biostratigraphy. Age assignment of the base of S1 at Hole 1103A is based on diatom biostratigraphy. Dark gray horizons show intervals barren of microfossils. Note seismic unit S2 is missing at Site 1103 and the top of S3 at Site 1103 (early late Miocene) may be older than at Site 1097 (4.5-4.6 Ma). Noteworthy for later considerations: sediments above the unconformity S1/S3 contain the top of *Thalassiosira vulnifica* giving a minimum time constraint for the age of the unconformity.

The relative dominance of diamicts vs. muds and sands may be an indicator of the proximity of the source or of the higher potential for this facies to be preserved. Muds were probably deposited on diamict bed tops between flow events and were subsequently reworked and incorporated in successive flows (Eyles et al., 2001). Mud and silt clasts were imported from lower energy marine settings with high biological productivity. The induration of these clasts (angular shape) indicates that their source was stable over a considerable time (e.g. an interglacial). Two specific scenarios have been proposed by Eyles et al. (2001) and the ODP Leg 178 Shipboard Scientific Party (1999):

- Unit S3 may represent the upper continental slope forsets of the prograding shelf with a paleo shelf edge close to the midshelf high (see chapter 2.1).

- Alternatively, the facies of Unit S3 may be representatives of the „till deltas" argued to be forming at the grounding line of ice streams (described for the Ross Ice Shelf by Alley et al., 1989). Similar features have been proposed for the shelf of the Antarctic Peninsula based on deep-tow boomer data (Vanneste and Larter, 1995).

2.5 Seismostratigraphic Correlation, Interpretation (S1-S3) and Shelf Model

2.5.1 Log to Seismic Correlation (S1, S3) and Seismostratigraphic Interpretation (S1-S3)

Even though these are no samples of topset Unit 1, FMS images and the logging data (e.g. the magnetic susceptibility log of the GHMT Tool) allow evaluation of downhole clast distribution and some information on the orientation of single larger clasts. Igneous rock fragments have high magnetic susceptibility values due to the magnetic minerals they carry, and they have low electrical resistivity due to the lack of pore-space with free movable ions (bright spots in the FMS record). In our logs high magnetic susceptibility (magsus) values correspond to FMS intervals with abundant clearly detectable clasts (Fig. 2.1-Fig. 2.3). Therefore the magsus profile will be used for an attempt to identify lithological introduced amplitude variations in the seismic record of S1.

For direct comparison the magnetic susceptibility values have been converted to time using the time-depth function established in chapter 2.2 and plotted at the same scale as part of line I95-152 (Fig. 2.1). Logging units with high magnetic suceptibility values are marked with yellow, lower susceptibility units with light gray (Fig. 2.1). The apparently weak impedance contrast between the gravel rich and gravel poor units (the latter possibly related to interglacials) is represented in the seismic section by low amplitude, discontinuous reflectors (Fig. 2.1, Fig. 2.1, and Fig. 2.2). Commonly changes from high to low (Ic-II, IIIb-IIIc and IV-V) and low to high impedance contrasts (Ia-Ib, II-IIIa and within the upper third of Unit V) start with a positive reflector. However, the low to high impedance change between Unit IIIc and IV correlates within a weak negative reflector. The last „regular", gravel rich lodgement till deposit of the topsets (seismic unit S1, logging unit IV, Fig. 2.5, Fig. 2.1, and Fig. 2.1) rests on a thin low magnetic susceptibility zone followed by a section with the irregular high magnetic susceptibility values of logging unit V. Together with other logging data and the FMS images (Fig. 2.1B) this zone may represent a clay rich „gouge" type layer on top of a brecciated reworking horizon. No imbricate fabric has been found within this layer, and the clasts are small and oriented horizontally. Very high resistivity changes at the clast borders may be attributed to the angular shape of these components. As discussed earlier (chapter 2.2

and 2.3) the strong black reflector (negative amplitude) is the seismic representation of the shelfwide S1/S3 or S1/S2 unconformity (Fig. 2.1). Overall, the match between logging units, subunits and reflector packages is excellent and will improve other seismostratigraphic studies and depositional interpretations.

The sediment recovered from Sequence Group S1 at Sites 1100 and 1103 (Leg 178 Shipboard Scientific Party, 1999), logging data, resistivity images, and the detailed correlation agree with the scenario that a grounded ice sheet regularly extended across the continental shelf during the development of S1. Individual prograding sequences, recognized by truncation and downlap of reflectors in sequence Group S1, also suggest repeated episodes of ice advance and retreat. The internal discontinuity of reflectors within S1 represents erosional removal of a formerly continuous till or interglacial biogenic deposit. Logging Units III a and b at Site 1103 consist of two gravel rich tills. The depositional model presented in Chapter 2.5.2 assumes that a glacial cycle deposit consists of a basal till layer with "iceberg-turbated" and IRD-rich finer interglacial on top, however here this interglacial layer is missing. Further seaward in the seismic record (Fig. 2.1A) a new reflector package appears at the proper seismostratigraphic location. It may be speculated that prior to deposition of Unit Ia (and related erosion during ice advance) this „interglacial" layer might also have been present at Site 1103. Alternatively to the interpretation of the low magnetic susceptibility layers as being associated to interglacials, the topsets could consist of stacked lodgement tills with interglacial deposits having been removed or being too thin to be detected as independent seismic packages.

The top of sequence group S3 corresponds roughly to an improvement in sediment core recovery at 247 mbsf. The upper part of S3, above the three strong reflectors c, d, and e (Fig. 2.1 and Fig. 2.1), consists dominantly of massive diamict with low internal impedance contrasts (Fig. 2.1). Below these weak reflectors the strong seaward dipping reflectors (c, d, e) represent impedance contrasts within the slope-related diamict, sandstone, mudstone succession recovered in the cores 31R to 38R. The proper scaling and plotting of density and velocity derived impedance indicators reveal that previous ideas concerning the cause of acoustic impedance changes related to lithological changes used to explain the reflector origin are not entirely valid (Leg 178; Shipboard Scientific Party, 1999). The first strong acoustic contrast related to lithologic changes actually is seen recovered between the massive and stratified diamictite (~274- 286 mbsf) and laminated mudstone (Fl). Tentatively this impedance change is related to reflector c (Fig. 2.1, Fig. 2.1, and Fig. 2.1). The next major impedance change occurs within a diamictite unit, where diamictites with dominantly

crystalline clasts (33R) overlie a diamictite unit containing silt rip-up clasts. As described in chapter 2.2. large crystalline components are contribute significantly to the average *P*-wave velocity of a sediment. Tentatively this impedance change is related to reflector d (Fig. 2.1, Fig. 2.1, and Fig. 2.1). The lithological origin of the weakest of the three reflectors e (Fig. 2.1, Fig. 2.1, and Fig. 2.1) is less well constrained. Possible candidates for the reflector origin are a deformed till horizon with fewer clasts recovered in core 36R, or the thin sandlayers of core 37R (Fig. 2.1). The observed seaward increase in amplitudes of this reflector package (see seismostratigraphic description chapter 2.1.4) may be due to better preservation of interglacial related muds and sands further down the slope. Alternatively, if the idea of facies separation out of a single diamict during mass wasting is valid (see chapter 2.4.2), longer downslope transport would enhance the separation of the facies S and F. The transitions observed between the three facies are not gradual enough to support the theory that facies D, S, F originate from a single mass wasting event. In any case it must be recalled that only 34% of the Unit S3 record has been recovered.

Drilling results from Sites 1100, 1102, 1103 (Leg 178; Shipboard Scientific Party, 1999) indicate that the three Sequence Groups S1, S2, and S3 were deposited under a glacial regime. Foresets (S3) and topsets have their origin in a periodically advancing grounded ice sheet to reaches the shelf edge in some cycles. Previously the glacial section drilled in the shelf transect of the Antarctic Peninsula had been interpreted as changing upward from deposits representing a proximal glaciomarine environment (sequence group S3) to principally subglacial strata deposited beneath the base of a grounded ice sheet on the shelf (topsets of sequence group S1 and S2, Leg 178; Shipboard Scientific Party, 1999; Eyles et al., 2001). This interpretation is not entirely valid - conclusions regarding the depositional environment (more glacial, less glacial) should not be drawn across different settings (slope foresets, topsets). To observe changes in these settings time equivalent cores representing the seismostratigraphic packages of topsets and foresets of S1 and S2 would have been required. Leg 178 failed to provide these records.

During deposition of S2 and S1, glacial sequences are characterized by low-angle topsets and steepening foresets that prograde the margin by 20 km (along sesimic line I95-152 or AMG845-08) and aggradate the outer shelf by 200 to 300 m.

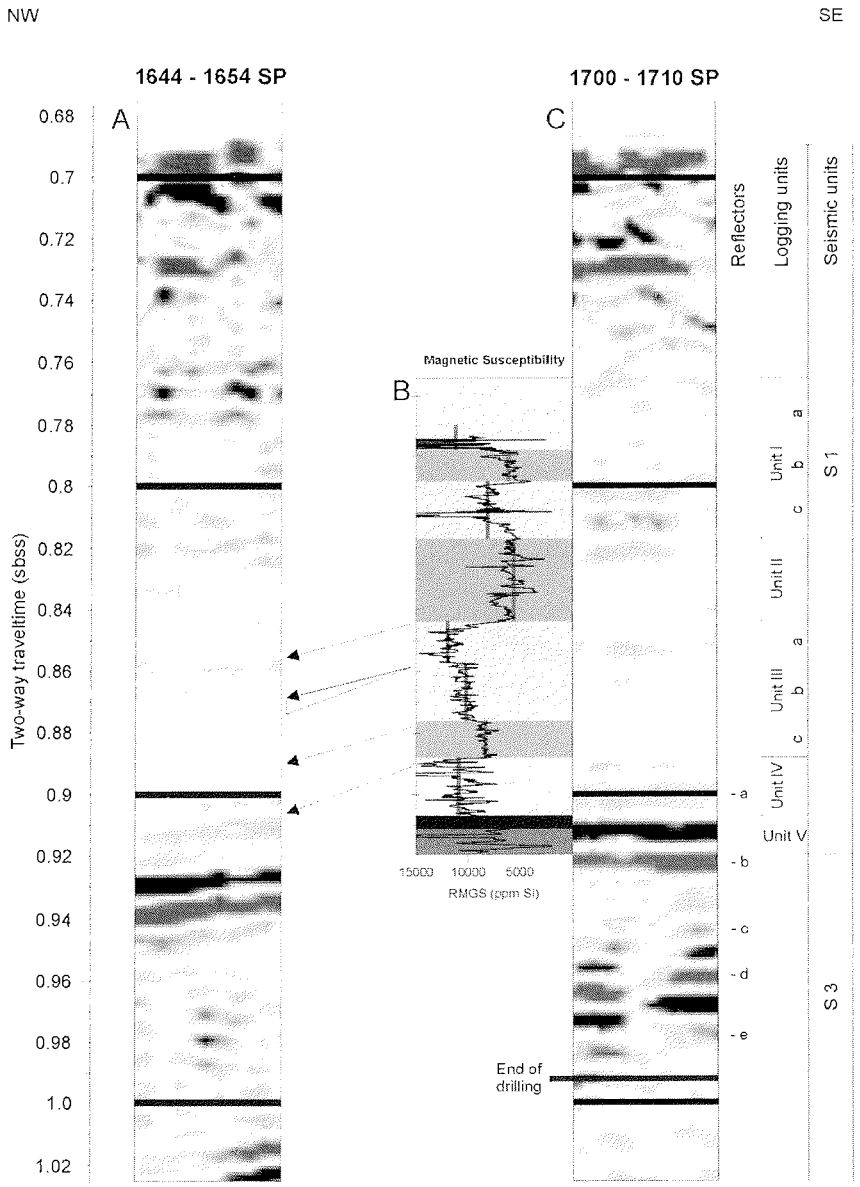

Fig. 2.1. Detailed graphic correlation of the time converted magnetic susceptibility profile (**B**, logging data) to reflector packages of the S1 topset Unit at Site 1103 (**C**, SP (shot points): 1700-1710). The section is composed of discrete intervals with higher (light gray) and lower (dark gray) gravel abundance. Within logging unit III, ontop of IIIb an interval of lower magnetic suceptibility is missing (due to erosion) further seaward of Site 1103 the missing section appears in the seismic profile (**A**). Anomalous values in the magnetic susceptibility log near 0.78 sbss (117 mbsf) may be caused by the APS bow spring, which had been lost in the hole during logging.

2.5.2 Shelf Model

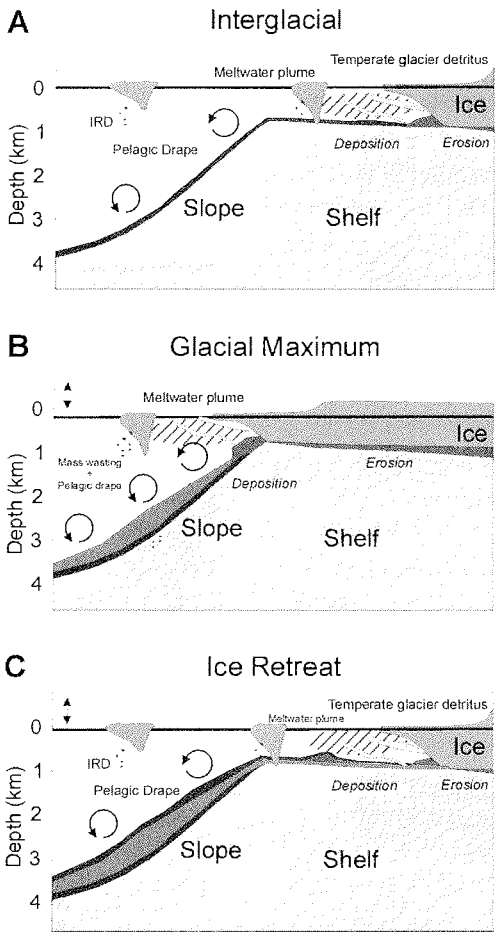

Fig. 2.1. Simplified sketches of the depositional and erosional processes during a glacial cycle. Starting in an interglacial (**A**) with drape sedimentation and erosion occurring at the inner shelf. (**B**) a glacial maximum where the ice extends to the shelf edge and erodes previously deposited material (**C**) ice retreat leaves a temporary till topset that is drape-covered during the following interglacial.

Like depositional processes on all shelves, deposition and erosion on the shelves of the Antarctic Peninsula are influenced by the external factors (Cooper et al., 1991):

- Sediment supply
- Tectonics
- Subsidence
- Eustatic sea-level change

Additionally the presence of ice introduces:

- Crustal flexure through ice loading
- Sediment erosion and redeposition by the ice sheet

During interglacials or glacials that do not produce an ice advance to the shelf edge, the grounding line is retreats toward the inner shelf. Pelagic or hemipelagic drape deposition takes place on the middle and outer shelf and slope (Larter and Barker 1989; 1991). Focal points of deposition are the ice front with meltwater plumes supplying temperate glacial outwash, and meltwater fines. Erosion takes place beneath the glacier. The shelf drape is subject to "iceberg-turbation" and IRD input. Some minor mass wasting removes sediment from the slope. Most sediment is kept on the overdeepened shelf and only minor export occurs through currents. Only thin foresets form (Fig. 2.1A).

During ice advance, inner shelf end moraine material, together with interglacial fines, are pushed towards the shelf edge in front of the advancing grounding line. Interglacial deposits are redistributed and additional erosion occurs beneath the shelf ice. Material transported to the shelf edge feeds larger scale mass wasting processes (debris flows for the upper slope and turbidites on the middle and lower slope). Thicker foresets develop, and the shelf progrades (Fig. 2.1B).

A grounding line moraine (produced by an ice advance that failed to reach the shelf edge, see also Fig. 2.1 and Fig. 2.2 in the introduction part chapter 2.1) and lodgement tills are left on the shelf after a retreat of the glacier. New drapes develop on top of this deposit. Erosion of the shelf takes place dominantly at the inner part during interglacials and glacials (ice is thicker toward the continent, Fig. 2.1). Repeated ice advances and retreats therefore automatically lead to overdeepened, inward sloping shelf geometry.

Except within shelf depressions there is no short-term preservation potential for lodgement tills or interglacial drapes on the shelf after repreated advances of grounded ice to the shelf edge in glacials.The best preservation potential for interglacial drapes is in the foresets on the slope.

Ten Brink et al. (1995) used numerical models to study behaviour of the shelf under varying conditions. They concluded that neither the eustatic curve by Haq et al. (1988) nor isotope data can be correlated with the position of the grounding line. According to their study, processes internal to the system can explain most of the phenomena. The transition from progradation to aggradation is dependent on:

- width of the shelf (longer distance from glacier source area to the shelf edge)
- amount of sediment input flux (decrease in sediment input results in an enhanced aggradation)
- probability that a glacial advance of grounded ice will reach the shelf edge (a lower probability overdeepens the inner shelf faster and increases the likelihood of preservation of deposits on the outer shelf)

2.6 Similarities and Differences - Other Antarctic Shelf Records

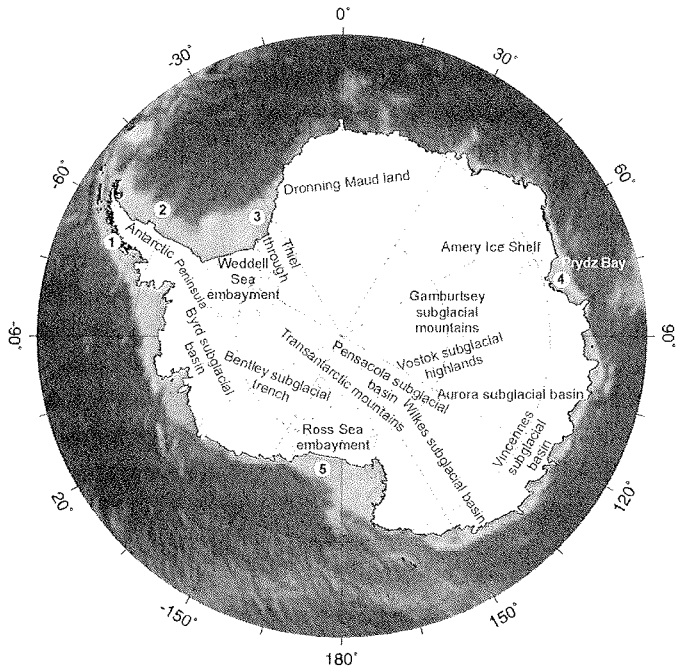

Fig. 2.1. Location of Antarctic shelf seismic profiles with distinct change from progradation to aggradation and consequent topset preservation: (1) Antarctic Peninsula, (2, 3) Weddell Sea, (4) Prydz Bay, (5) Ross Sea.

Many Antarctic seismic shelf profiles display a sudden change from progradation to aggradation and consequent topset preservation: (1) Antarctic Peninsula, (2, 3) Weddell Sea (Kuvaas and Kristoffersen, 1991; Hinz and Block, 1983), (4) Prydz Bay (Cooper et al., 1991b), (5) Ross Sea (Alonso et al., 1992; Anderson and Bartek, 1992). The boundary between topsets and the underlying strata is commonly unconformable toward the inner shelf, becoming gradually more conformable toward the outer shelf. As discussed in chapter 2.5,

shelf topsets are highly vulnerable to complete erosion in the subsequent glacial cycle of ice readvance. The change toward top section preservation of younger strata all around Antarctica implies a synchronous mechanism.

A detailed correlation of all other available Antarctic shelf records is beyond the scope of this thesis – and additionally would be incomplete since most of the data consists either of seismic lines with no or poor age estimates or only shallow piston and gravity cores too short to be correlated with the seismic profiles.

However, ODP Leg 188 Prydz Bay, Site 1166 provided both detailed seimic records, excellent core recovery and excellent logs supplemented in the upper part with Logging-While-Drilling (LWD) data. The results show striking similarities in the logging, lithological and fossil record with the Antarctic Peninsula at Site 1103.

It is believed that the East Antarctic ice sheet has a different and longer history than the West Antarctic ice sheet (Zachos et al., 2001; Barker, 1995). The West Antarctic passive margin is relatively young. The conversion from active subduction to passive margin is not older than 11.2 Ma at the location of the shelf transect (chapter 1.1.2, Fig. 1.1). The East Antarctic passive margin is much older, with sediment records extending back to the Turonian (O'Brien et al., 2000; Leg 188; Shipboard Scientific Party, 2000). Therefore the thermal history and present thermal subsidence behavior of the West and East Antarctic shelf should be fundamentally different (Barker, 1995). Nevertheless both records show that preservation of topsets began around 3.2 to 2.3 Ma, when the large-scale northern hemisphere glaciation was initiated. Low sea-levels, in combination with a global cooling trend resulting in thicker shelf ice, would normally prevent topset preservation and consequent shelf build-up.

A possible explanation is that isostatic response of the Antarctic continent as a whole may have led to higher subsidence on all circum-Antarctic shelves simultaneously. However, the differences in nature of the crust and their behaviour under flexual stress and loading makes this scenario highly speculative. Another explanation would be a rise in sea-level to provide accomodation space on the shelf – but this is highly unlikely for this time (Haq et al., 1988).

2.6.1 Comparison of Records: Prydz Bay (PB) and West Antarctic Peninsula (WAP)

Glacial topset preservation started above an unconformity that can be traced along the Antarctic Peninsula Margin (Larter et. al, 1994). Apparently this unconformity is also present in Prydz Bay, East Antarctica. At the unconformity there is a narrow zone of abnormally low densities, magnetic susceptibilities and resistivities (BB, WAP) interpreted as possibly fluid

rich deposit resulting from a single or several episodes of ice erosion of lithified strata (see chapter 2.5). At site 1103 (WAP) this „gouge zone" is accompanied by a coarser brecciated zone, apparently missing at Site 1166 (PB). Above the unconformity Lithological Unit Id, which is equivalent to logging unit 2c (PB) seems to be time equivalent to logging unit V (WAP, Site 1103). Both intervals have been dated with diatoms and contain the upper boundary of the *Thalassiosira vulnifica* Zone (Leg 178; Shipboard Scientific Party, 1999; Fig. 2.1) the lower boundary was not recovered. According to O'Brien et al. (2000) Leg 188 might have recovered the lower extent of the *T. vulnifica* zone. A recovery would date the unconformity at 3.2 MA whereas an unrecovered lower boundary would leave a uncertainity of 0.9 Ma and a minimum age of 2.3 Ma. Both units 2c (PB) and V (WAP) are almost identical in their logging expressiou,. displaying high density, resistivity and velocity values. Additionaly fms images of Site 1166 show high concentrations of larger clasts similar to the fms record of Site 1103 (WAP). Another striking feature is that both units have simular thicknesses (~ 20 m, Fig. 2.1). This till zone is overlain in both records by a lower density, lower resistivity layer (upper part of logging unit 2b (Site 1166) and Unit IIIc Site 1103). This zone is thicker at Site 1103, contains interbedded clay lenses and fewer clasts (Site 1166, ODP Leg 188, Shipboard Scientific Party, 2000). For the rest of the succession the similarities include low variability in acoustic velocities and similar alternations in magnetic susceptibility with the number and relative thicknesses of highs and lows correlating. However, the magnitude of magnetic susceptibility variation at Site 1103 is higher, indicating a more variable depositional environment (greater contrast in gravel size and abundance in each moraine deposit) that could be linked to the more dynamic nature of the West Antartic ice sheet (northerly location, more vulnerable to decay etc...).

2.6.2 Conclusion

The records at both sites indicate simultaneous glacial erosion of preexisting strata (3.2-2.3 Ma) and development of accomodation space adequate to preserve subsequent lodgement tills and interglacial fines resulting from the advance and retreat of ice sheets. Although Barker (1995) argued against time equivalence of the unconformities observed in Prydz Bay and West Antarctic Penisula records, the new data demonstrate at least a synchronous start of deposition after the erosive event. Te question arises, whether similar topsets above pronounced unconformities observed around Antarctica may also be time equivalent despite the differences in shelf history, sediment supply, proximity to the ice source, ice flow velocity.

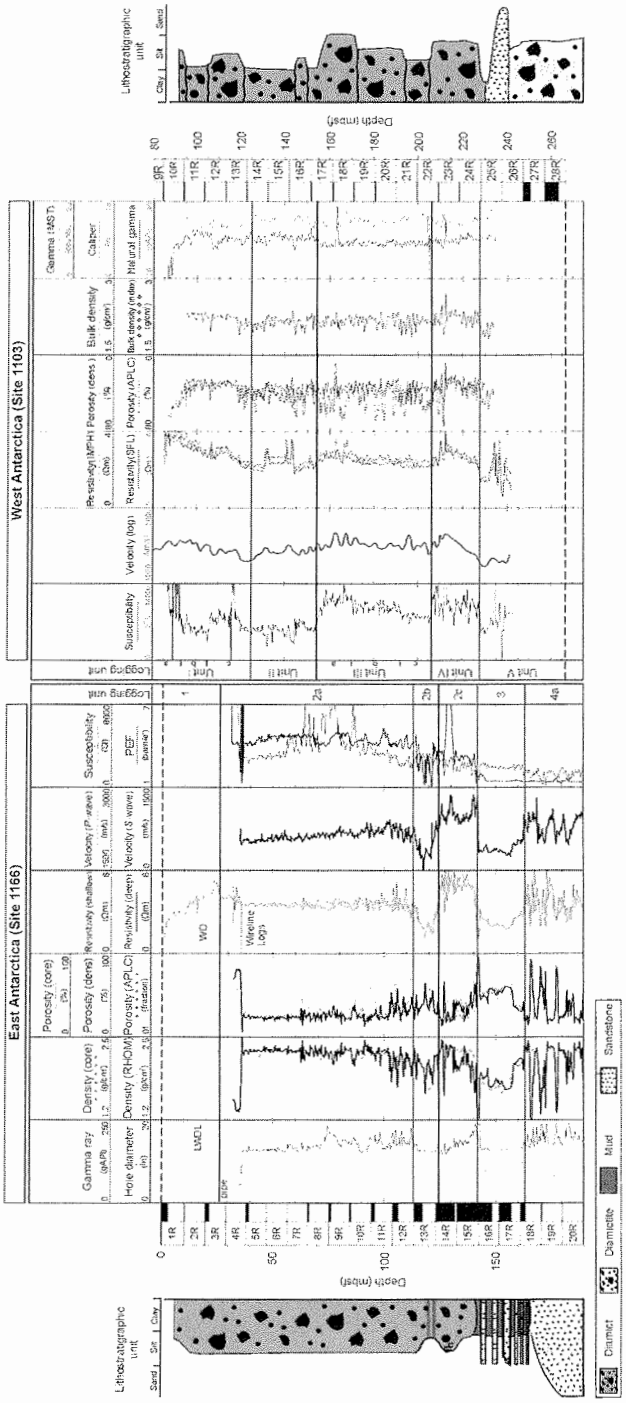

Fig. 2.1. Logging data comparison of East and West Antarctic shelf records (Antarctic Peninsula (Leg 178; Shipboard Scientific Party, 1999) and Prydz Bay (Leg 188; Shipboard Scientific Party, 2000)).

2.7 Summary of Chapter 2 "The West Antarctic Shelf"

Antarctic shelves are unique in many ways. The shelf of the West Antarctic Peninsula can be morphologically divided into the inner shelf with sediment traps (e.g. Palmer Deep), the shelf basins (bearing the glacial troughs) representing areas where ice was present more frequently and longer than the younger outer shelf or the mid shelf high.

With good acoustic velocity control it is possible to correlate logging and core data to seismic units and single reflectors. The logging and core derived velocity profile established for this thesis allows modelling of the shelf profile with synthetic seismograms and tying logging units of S1 on a reflector to reflector basis to the seismic section.

Seismostratigraphic Unit S1 at Site 1103 consists of a series of stacked lodgement tills deposited as basal moraines by advancing and retreating ice sheets, interrupted by finer, less clast-rich intervals possibly associated with interglacials. Imbricated fabric in ~200 mbsf (~2 Ma) with pebbles dipping to the S demonstrate deposition below a S-N oriented ice stream (consistent with the S-N oriented of a modern outlet-trough on the shelf west of Anvers Island) and witness the longevity of glacial outlet troughs on the shelf.

Seismostratigraphic Unit S3 at Site 1103 contains a diamictite / fines succession that represents upper slope deposits with a distal moraine-like source. The alternations of diamicts and fines may be related to advancing and retreating ice sheets with proximal sources in glacial times and more distal sources in interglacials. Topsets and foresets are linked to ice sheet advance and retreat; the preservation potential on the slope is higher since all deposits below the paleo shelf break are protected from direct ice erosion.

Many circum-Antarctic shelf records show an upsection trend toward shelf aggradation combined with better topset preservation. Logging data and FMS images in combination with lithological constraints allow a close correlation of WAP shelf records with EA shelf records (Legs 178 and 188). Since 3.2 Ma or latest 2.3 Ma both shelves have evolved in a similar way despite the many differences in margin type and overall setting (e.g. ice proximity and sediment supply).

Local and shelf processes are unable to explain these similarities. A strong external forcing factor is needed. Sealevel fall and increased isostatic subsidence due to ice build-up that affected the whole continent are one possibility. The alternative, a rise in sealevel during this time is highly unlikely.

3 Palmer Deep – Ultra High Resolution Holocene Record of the Inner-Shelf

3.1 Introduction

Palmer Deep is located 30 km southwest of Anvers Island on the inner portion of the Antarctic Peninsula continental shelf (Fig. 3.1A, Fig. 3.1). Similar to other inner-coastal depressions found along the passive margins of the Antarctic continental shelf, Palmer Deep is thought to be overdeepened by glacial erosion (Domack and ODP Leg 178 Shipboard Scientific Party, 1998). The interconnected depression surrounded by steep slopes (16° to 26°) consists of three Sub-Basins (I-III), with a dominant W-E orientation (Fig. 3.1C). The basin is in water depth between 1012 m (Sub-Basin I) and 1400 m (Sub-Basin III) and has formed an efficient sediment trap for coastal productivity, continental derived background sedimentation, and occasional gravity driven flows since the end of the Last Glacial Maximum. The proximal location, combined with a relatively thick latest Pliocene to Holocene sediment fill, provides a unique, highly sensitive, high resolution record for the Antarctic shelf. Two sites were drilled during ODP Leg 178 using existing seismic lines (Fig. 3.1B, C). Site 1098, located at the southern end of Sub-Basin I, recovered a ~47 m thick continuous sediment succession and reached the base of the basin fill. Site 1099 was drilled in the deepest part of Sub-Basin III, yielding 107.5 m of continuous sediment representing appoximately the upper three quarters of the total basin fill at this location. Continuous Multi Sensor Track (MST) logging data for both sites provide closely spaced (2-15 cm) magnetic susceptibility, natural gamma radiation, density and *P*-wave velocity data.

This chapter discusses the origin and early evolution of the shelf depression, and relates the down core physical properties to existing high resolution single channel Huntec Deep Tow Boomer (HDTB) seismic lines using synthetic seismograms. It includes a seismostratigraphic interpretation of the observed seismic units and an accurate time to depth conversion. The final part of this chapter is related to the digitalization of the 1998 HDTB seismic data and gives a first example of improvements achieved with this effort.

Fig. 3.1 (see next page). (**A**) location of the Palmer Deep depression on the inner Antarctic Peninsula shelf (Rebesco et al., 1998b). (**B**) initially compiled bathymetry of the Palmer Deep depression with seismic lines available until 1997. Note: prior to the '99 multi beam survey the Palmer Deep depression was thought to consist of three basins (Basin I-III) separated by sills (Kirby et al., 1998). (**C**) new detailed multi beam bathymetry (system: SeaBeam) of Nathan B. Palmer cruise 99-03 (Domack et al., 1999). Superimposed are high resolution HDTB '98 (RV LAURENCE M. GOULD, Cruise: LMG-98002), air- and GI-gun seismic lines further discussed in this chapter.

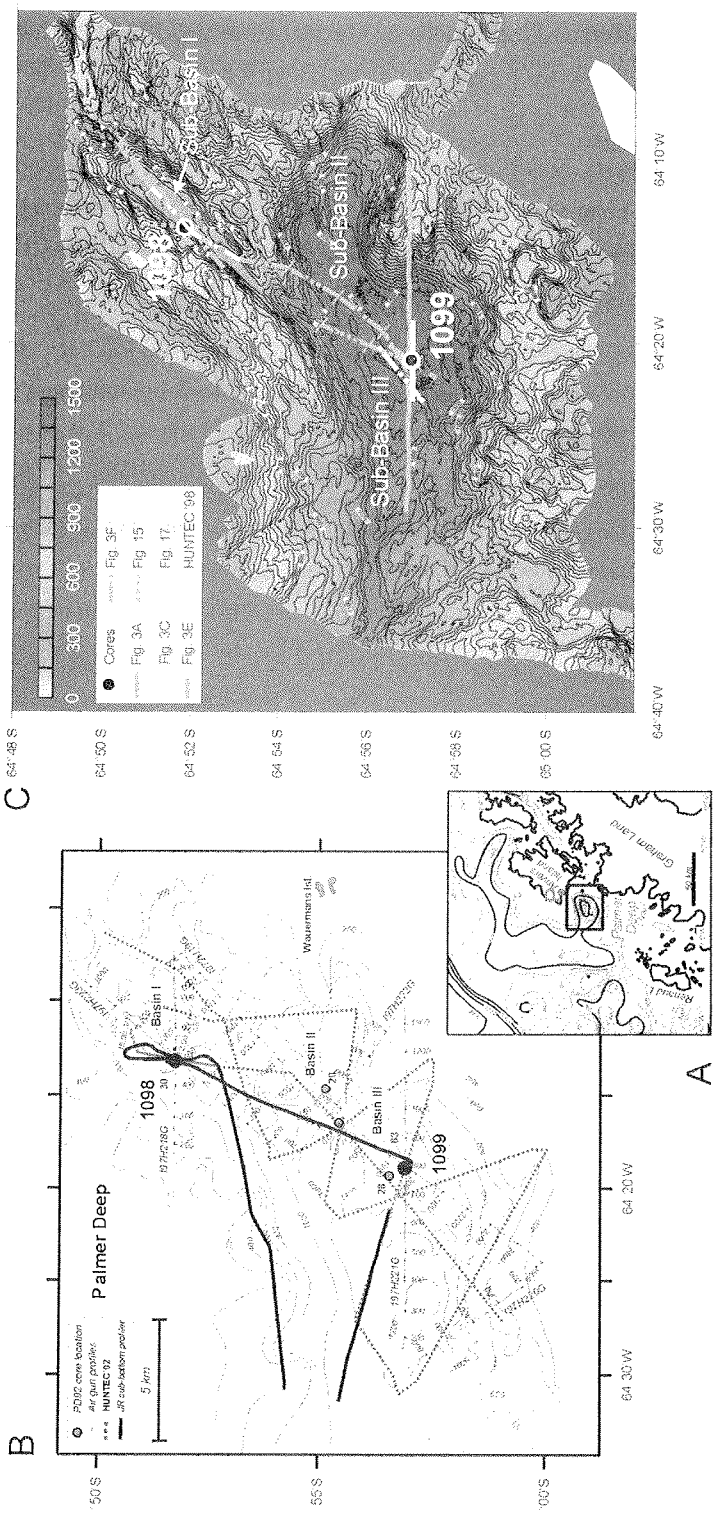
A
B
C
Palmer Deep
Basin I
Basin II
Basin III
Sub-Basin I
Sub-Basin II
Sub-Basin III
1098
1099
Wauwermans Id.
Graham Land
Rothschild I.
Cores
Fig. 3A
Fig. 3C
Fig. 3E
Fig. 3F
Fig. 15
Fig. 17
HUNTEC 98
0
300
600
900
1200
1500
64°48'S
64°50'S
64°52'S
64°54'S
64°56'S
64°58'S
65°00'S
64°40'W
64°30'W
64°20'W
64°10'W
64°30'W
64°20'W
64°10'W
65°S
65°S
65°00'S

3.2 Basin Origin and Early Basin Evolution

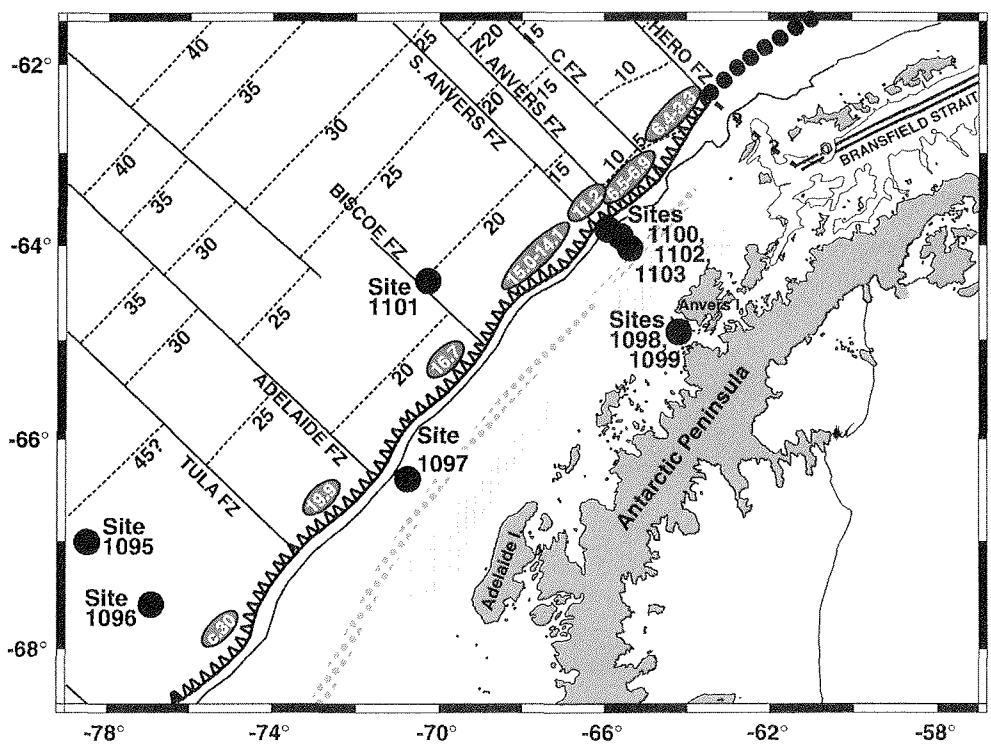

Fig. 3.1. Ages of ocean floor and ridge crest–trench collisions along the Antarctic Peninsula Pacific margin with drill sites marked (based on the time scale of Cande and Kent,1995). The mid-shelf high and the shelf basins are marked as dots and bars signatures respectively (Courtesy: ODP Leg 178 Shipboard Scientific Party, 1999).

Fig. 3.2 (see next page). (**A**) migrated (sea water velocity) GI gun single channel line I97H221G across Sub-Basin III. Survey speed is ~ 4 kt with a firing interval of 6s (12.5 m). Line and core locations are given in Fig. 3.1. (**B**) line drawing of A. The basin fill is seen as closely spaced horizontal reflectors. The side walls of the basin to the E can be interpreted as glacial moraine deposits. One major normal fault (detachment fault) is indicated (**F**). (**C**) close-up of Sub-Basin III sediment fill from airgun single channel section I97H228, 3.3 kt average survey speed, 5.3 s (9 m) firing rate. (**D**) line drawing of C with structural interpretation of the growth normal faulting within the basin fill. MBR (Midbasin Reflector) and seismic units 1 and 2 are explained further in the text. Line location is given in Fig. 3.1. (**E**) correlation of core derived synthetic traces and profile Iq7-219G, running SW-NE and crossing Profile I97H-228 at the location of Site 1099 (**C**). See text chapter 1.4 for details. (**F**) comparable low resolution single channel GI gun profile across Sub-Basin I. (Courtesy: Rebesco et al., 1998b; ODP Leg 178 Shipboard Scientific Party, 1999).

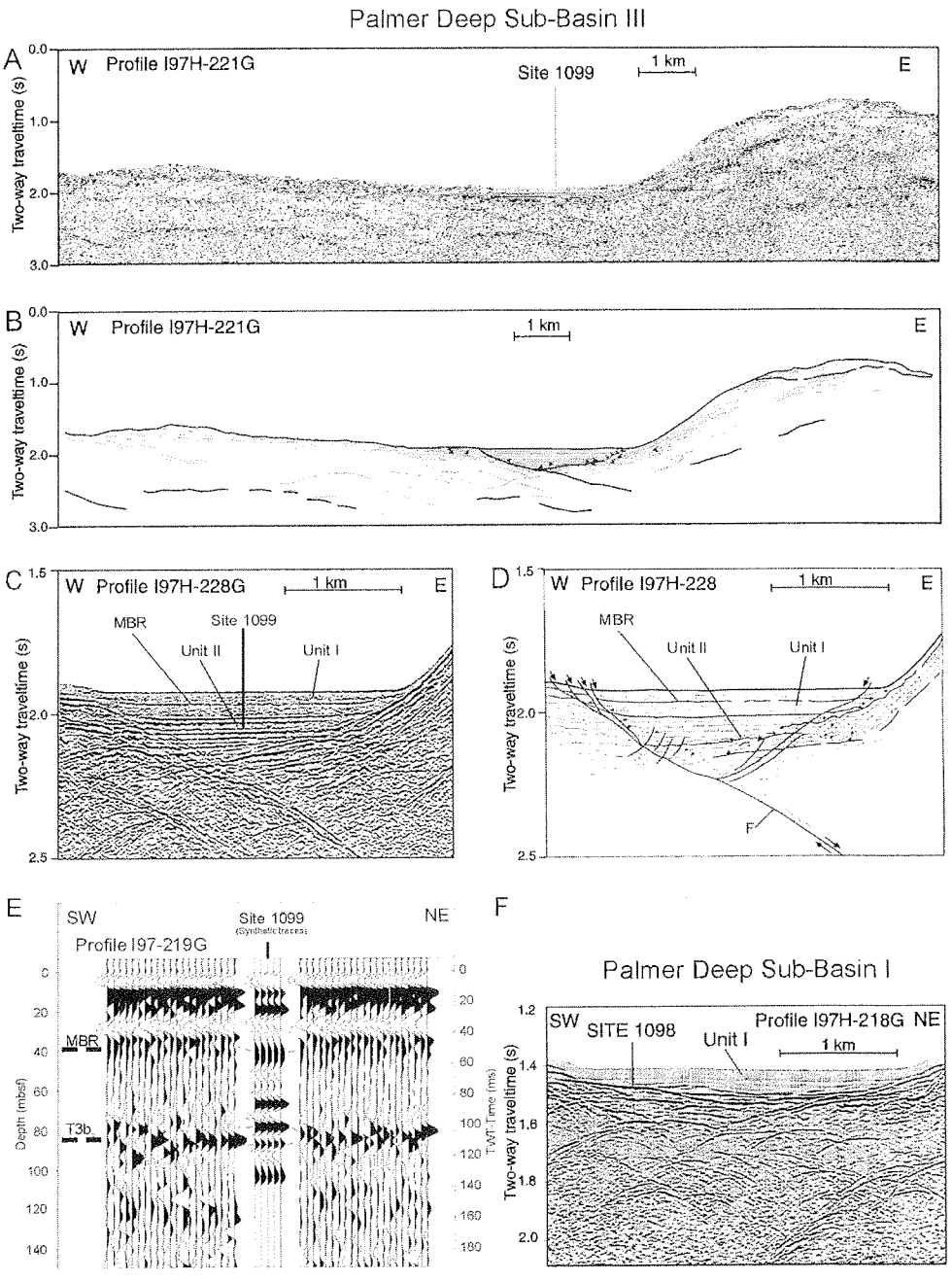
Palmer Deep Sub-Basin III
A
W Profile I97H-221G
Site 1099
1 km
E
Two-way traveltime (s)
B
W Profile I97H-221G
1 km
E
C
W Profile I97H-228G
1 km
E
MBR
Site 1099
Unit II
Unit I
D
W Profile I97H-228
1 km
E
MBR
Unit II
Unit I
F
E
SW
Site 1099
(Synthetic traces)
NE
Profile I97-219G
MBR
T3b
Depth (mbsf)
TWT Time (ms)
F
Palmer Deep Sub-Basin I
SW
SITE 1098
Unit I
Profile I97H-218G NE
1 km
Two-way traveltime (s)

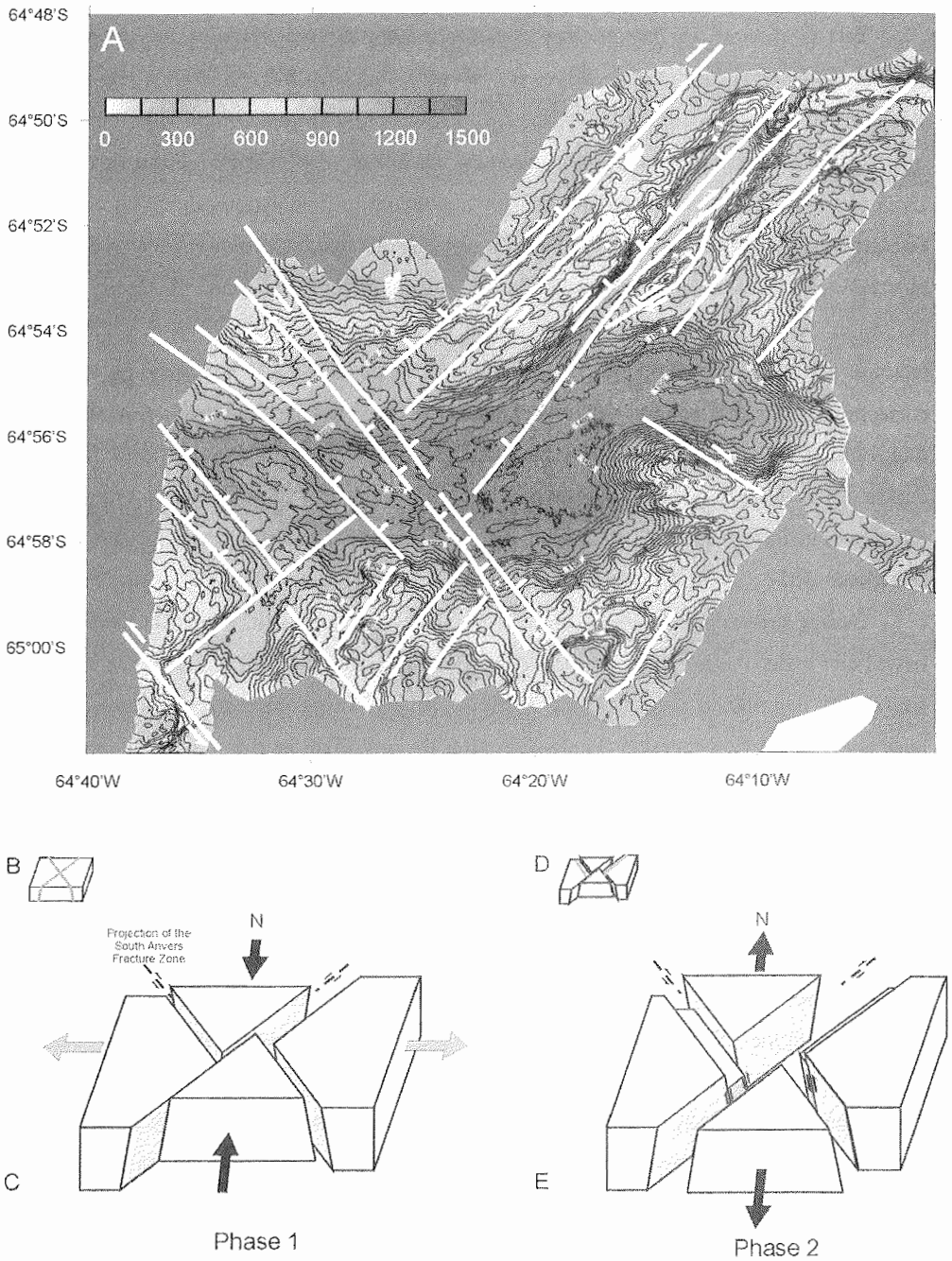

Fig. 3.3. **(A)** speculative tectonic interpretation based on morphological features, see text for discussion. **(B)** block model before deformation with initial location of conjugate fault set. **(C)** simplified block model of inferred initial compressive phase 1 with NS shortening and WE escape structures. **(D)** block model before deformation phase 2 with location of additional faults. **(E)** deformation phase 2 with NS extension and normal faulting.

The location of the Palmer Deep depression along the projection of the South Anvers Fracture Zone (Fig. 3.1) and the discovery of normal growth faults in seismic profiles (Fig. 3.2A-D; Rebesco et al., 1998b) has raised speculations of the tectonic origin of Palmer Deep.

Based on morphological features of a new multibeam map of Palmer Deep, provided by E. Domack's working group, and existing low resolution seismic data an attempt was made to establish a tectonic model in the context of the general margin evolution. Interpretation of morphological features of the basin walls and the basin fill surface indicates that there are two dominant sets of tectonic lineations separated by an angle of 70-85° (Fig. 3.3A). The two tectonic orientations are interpreted as conjugate sets of faults. The NW trending structures correspond to the orientation of the transform faults (in particular the Anvers Fracture Zone) that segment the sea floor west of the Antarctic Peninsula margin. These structures developed during the active phase of the margin evolution (chapter 1.1.3). Some authors believe these inactive transforms cause a tectonic segmentation of the Antarctic Peninsula and its shelf (Hawkes, 1981).

During a postulated initial stage of the Palmer Deep tectonic evolution the area may have been under the influence of North-South compression and left lateral strike slip, with lateral EW extensional escape (Phase 1; Fig. 3.3B, C). This compressive regime may have been succeeded by a general N-S extension after the arrival of the ridge segment around 11.2 Ma (Fig. 3.1). Modern N-S extension is suggested by the morphologically indicated left lateral movement on the NW trending faults (same as under the compressional conditions) and right lateral movement on the NE trending faults. This postulated extension could coincide with the extension in Bransfield Strait, to the NE. Both may be considered "back arc basins" in a plate tectonic context (chapter 1.1.3). The NE trending faults are morphologically best expressed in the narrow canyon of Sub-Basin I (Fig. 3.3A). The dip of the NE trending fault planes to the NW is indicated by the differences in canyon wall steepness. In addition to strike slip movements, recent extension (Phase 2; Fig. 3.3D, E) is accompanied by normal faults dipping to the NE. These become listric low angle detachment faults at depth (Fig. 3.2A-D; Rebesco et al., 1998b). The surface expression of these normal growth faults is seen in the step-like elevated basin fill surface to the west of 64°20' (Fig. 3.3A). It is interesting to note that the same tectonic orientations involved in strike slip movements during deformation 1 and 2 and are also observed in the recent normal faulting (Fig. 3.3E).

3.3 Core Data, Environmental Interpretation and Age Model

At Site 1098 (Fig. 3.1B, C) three holes (A-C) with 10 m horizontal offset and 3.5 m (1098 B) and 3 m (1098 C) vertical pipe offset were drilled with the Advanced Hydraulic Piston Corer (AHPC) to assure stratigraphic overlap. All three holes reached firm till below ~43 mbsf indicating the recovery of a complete sediment fill record of Sub-Basin I.

In contrast, at Site 1099, located in Sub-Basin III, only one record was recovered. Hole A was drilled to a depth of 62.3 mbsf and after an interruption caused by approaching icebergs drilling continued in Hole 1099 B where coring started at 60 mbsf and was terminated 107.5 mbsf. The cored record at Site 1099 does not represent the entire basin fill of Sub-Basin III since no tills of the basin floor were reached.

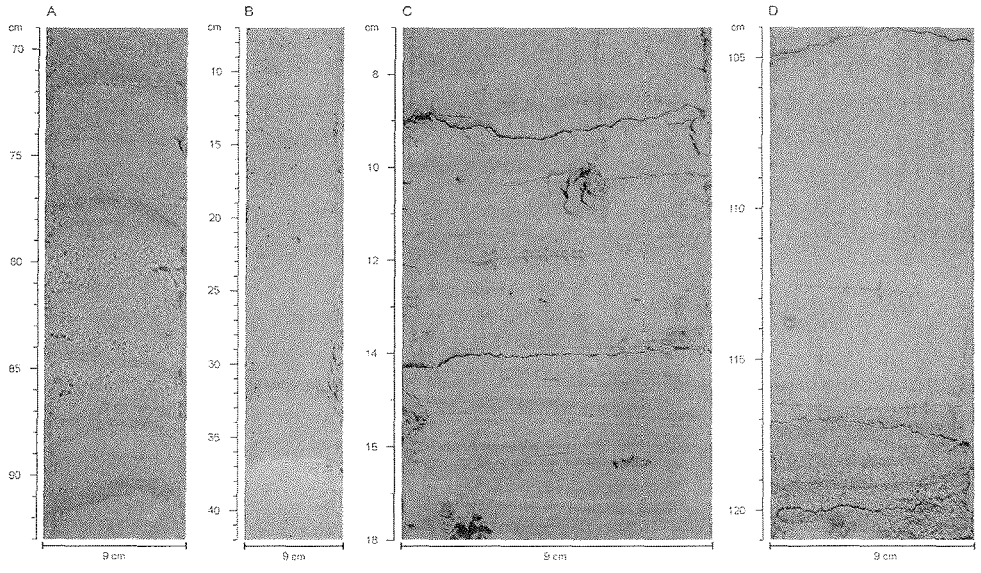

Fig. 3.1. **(A)** laminated diatom ooze rich in *Corethron criophilum* (pale layers) or *Chaetoceros* spp. spores (dark layers; interval 178-1098B-1H-3, 69–93 cm). **(B)** massive mud-bearing diatom ooze (top part) with one lamina in interval 178-1099A-2H-3, 31–32 cm, of *Chaetoceros* spp. spores, and the top part of a turbidite in interval 178-1099A-2H-3, 7–42 cm. **(C)** laminated diatom ooze showing millimeter-scale laminae in the lower part of interval 178-1099B-5H-5, 15–17 cm, and at 178-1099B-5H-5, 10–12 cm, with subhorizontal *Phycosiphon* burrows. **(D)** turbidite bed with medium sand base grading to mud (interval 178-1099B-4H-5, 104–121 cm) (Courtesy: ODP Leg 178 Shipboard Scientific Party, 1999).

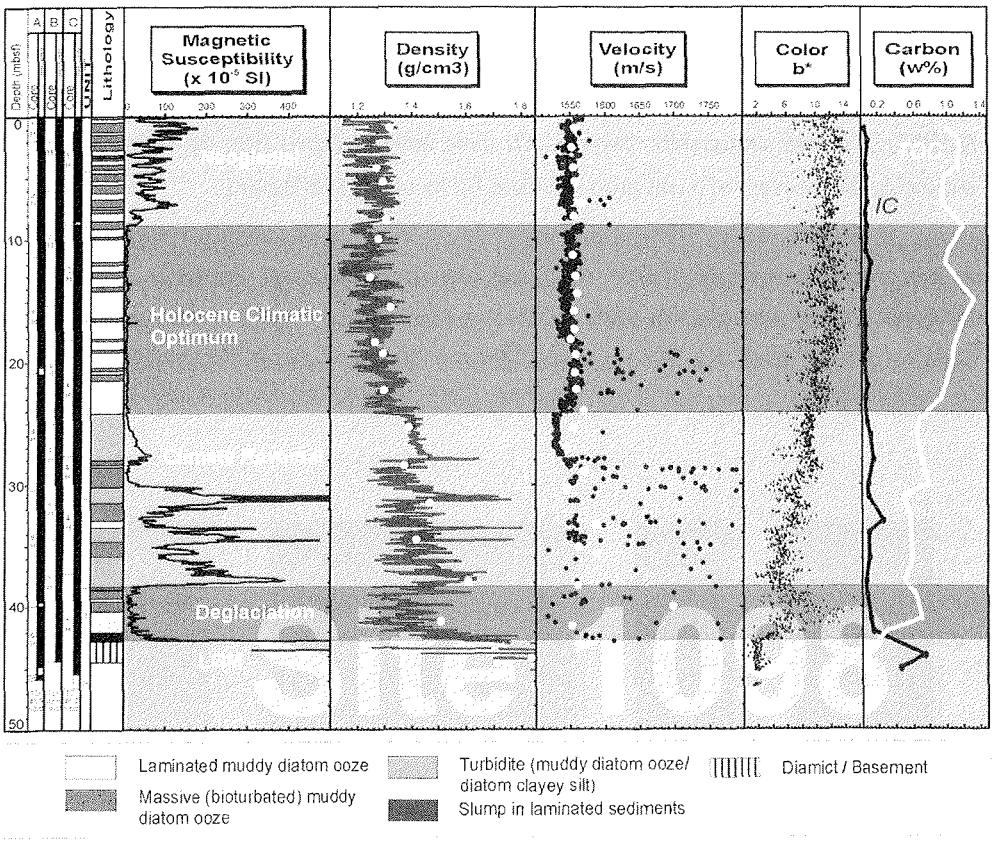

Fig. 3.2. Lithology summary chart of Site 1098. The magnetic susceptibility record is a key parameter in these organic rich sediments for detecting turbidites and evaluating the importance of IRD and continent derived sediments. Climatic zones (shaded horizontal sectons) and ages are indicated. See text for details.

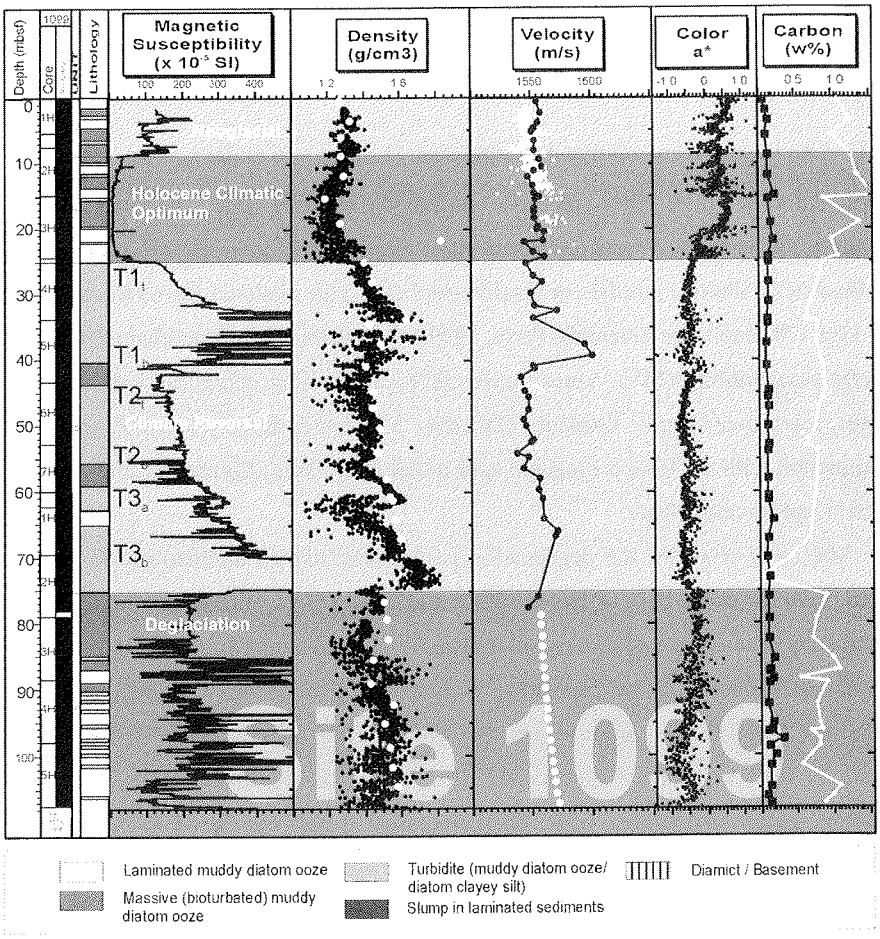

Fig. 3.3. Lithology summary chart of Site 1099. See Fig.1.6 for the lables of the climatic zones (colored horizontal sections). See text for details. Note the correlation of magnetic susceptibility highs with the base of turbidites, and corresponding highs in density and velocity (e.g. interval 25 to 40 mbsf). The velocity record below 75 meters was severely degraded due to close spaced horizontal gas expansion cracks within the core. A polynominal fit is used instead (light dots).

3.3.1 Lithostratigraphy and Environmental Interpretation at Site 1098 and 1099

The Palmer Deep sediments consist of olive-green homogeneous bioturbated to laminated diatom mud and ooze, rhythmically varve-like interbedded diatom ooze, pebbly mud, and muddy diamicton (Sjunnekog and Taylor, 2001). The laminations and diatom oozes vary in thickness from millimeter scale (interval 40-42 mbsf, core 5H, Site 1098, Fig. 3.1C and Fig. 3.2) to several centimeters (Fig. 3.1A and Fig. 3.3 interval below 87 mbsf). Five lithofacies

(see Fig. 3.2 and Fig. 3.3 legend) in five broad stratigraphic and climatic intervals have been distinguished at the two sites.

3.3.1.1 Last Glacial Maximum and Deglaciation (13.2 - 11.46 ka BP)

The deposition of tillites during the Last Glacial Maximum (LGM) shaped the Palmer Deep depression. Today the tills form the basement of Sub-Basin I (only reached at Site 1098). The grey „basement" diamict consists of massive silty clay with scattered ice-rafted debris pebbles (ODP Leg 178 Shipboard Scientific Party, 1999). The diamict is further characterized by high magnetic susceptibility (MS) values (attributed to larger lithic terrestrial components), high densities, low Total Organic Content (TOC; Fig. 3.2) and extremely low diatom abundances in conjunction with the lowest biogenic opal found in the hole (Sjunnekog and Taylor, 2001; Anderson and Ravelo, 2001).

The early phase of the deglaciation is characterized by inclined bedding and slump features observed at the base of Holes 1098B and C (Fig. 3.2). Diatoms found in this interval are indicative of a sub-ice shelf depositional environment (Sjunnekog and Taylor, 2001). The onset of more open marine deposition is marked by a decrease in MS and in gravel abundance. The sediment unit above the slump facies is rhythmically laminated, with alternations between pure diatomaceous ooze (*Chaetoceros* resting spores) and laminae containing greater terrigenous input. This alternation is also expressed in the MS record as small amplitude high frequency variations (Fig. 3.2). This interval indicates nutrient-rich stratified surface waters under proximal melt water influence (Sjunnekog and Taylor, 2001; Taylor and Sjunnekog, 2001). When comparing the records of Sites 1098 and 1098 based on the MS data and lithology it is obvious that the record of this time slice at Site 1099 is greatly expanded. This is probably caused by small turbidites that are much more pronounced in the 1099 record (Fig. 3.3).

Based on the Byrd ice core isotopic record (Sowers and Bender, 1995) warming started as early as 20 ka BP, well before the Northern Hemisphere deglaciation. Ice core records also suggest that warming halted between 14 ka BP and 12.5 ka BP. This so called Antarctic Cold Reversal (ACR) preceedes the Northern Hemisphere's Younger Dryas (YD) cold event although some authors correlate the ACR directly with the YD (Steig et al., 1998). This controversy has led to different interpretations of the diamicton and the turbidite rich intervals between 25 and 38 mbsf (Site 1098, Fig. 3.2) and 25 to 75 mbsf (Site 1099, Fig. 3.3). Domack et al. (1998) interpret the turbidite interval as linked to the YD, Sjunnekog and

Taylor (2001) suggest that the YD falls within the rhythmically laminated interval following the slump facies, and is not a pronounced event in the Palmer Deep area.

3.3.1.2 Climate Reversal (11.46 - 9.07 ka BP)

The deglaciation phase in Palmer Deep is replaced around 11.7 to 11.46 ka by a distinct „climatic reversal" marked by an increase in ice rafting, onset of major mass wasting, and reduced primary production (Taylor and Sjunnekog, 2001; Anderson and Ravelo, 2001). The precise timing of the onset of this reversal depends on the proxy used to recognized it. Taking the MS values indicative of IRD pebbles and the onset of the mass wasting (turbidite T3b, Fig. 3.3) the initiation of the reversal can be dated as 11.46 ka BP (Domack et al., 2001). Using the total diatom abundance as an indicator (Sjunnekog and Taylor, 2001) the start of the reversal is much earlier (11.7 ka, within the massive units below turbidite T3b, Fig. 3.2 and Fig. 3.3). Looking at changes in diatom assemblages, the transition to the reversal appears to be approximately 1000 yr later than indicated by the total diatom abundance record. It is characterized by a change from alternating *Thalssiosira antarctica* and *Rhizosolenia* deposits to associations dominated by *Rhizosolenia* (Taylor and Sjunnekog, 2001). The change in biogenic opal content in the profile of Anderson and Ravelo (2001), occurs at about 36 mbsf (corresponding to 10.6 ka BP) coincides with the diatom assemblage change. However, for practical seismostratigraphic purposes the start of the „climatic reversal" is set to base of turbidite 3b, following the suggestion of Domack et al. (2001) and the easy recognizable MS, bulk density and velocity increase (Fig. 3.2 and Fig. 3.3).

An explanation for the increase in terrestrial matter and IRD for this time may be the correlation with the YD event as discussed in the previous section (combined with a glacial shelf ice advance from the SE) or opening of the connection between Bransfield Strait to the NE and the Gerlach Strait (Sjunnekog and Taylor, 2001; Taylor and Sjunnekog, 2001). The later scenario would redefine the so called „climatic reversal" (Domack et al., 2001) to a time of continued warming with no shelf ice readvance but increased NS iceberg traffic and periodic grounding due to to the opening of the restriction between Bransfield- and Gerlach Strait. The high diatom abundance (Sjunnekog and Taylor, 2001) combined with the high organic opal (Anderson and Ravelo, 2001) content of the sediment along with diatom assemblages indicative of less ice and increased water circulation (Taylor and Sjunnekog, 2001) make this scenario attractive.

The major turbidites (T1-T3b) in the „climatic reversal" interval consist of a very thin coarse (sand to silt) base (Fig. 3.1E) and a very thick (up to 14 m, T1, Site 1099, Fig. 3.3)

faintly graded tail of massive silty to muddy diatom facies without major bioturbation. The 4 major turbidites of this interval are seismostratigraphically important and their basal density and velocity changes contribute significantly to the acoustic reflection seismic signal formation. At Site 1099 many smaller turbidites in the Neoglacial and the Deglaciation Phase contribute to the expansion of this section compared to Site 1098. This difference in section length may be explained by the depth difference between Sub-Basins I (Site 1098) and III (Site 1099) leading to higher basin walls with more material subject to slope failure.

3.3.1.3 Holocene Climate Optimum (9.07 – 3.36 ka BP)

A ~15 m thick sediment sequence above the top of turbidite 1 (~24 mbsf, Site 1098, Fig. 6 and Site 1099, Fig. 3.3) is dominated by laminated ooze and minor bioturbated massive diatom ooze in the upper part. The highest recorded total biogenic opal content (Anderson and Ravelo, 2001) in conjunction with diatom abundances higher than today suggest, that this period of the Holocene was a time of maximal primary production. Overall low MS values with low variability correlate with the highest recorded *Chaetoceros* resting spores (rs) vs vegetative cell ratios. Based on these observation and changes in faunal assemblages, Sjunnekog and Taylor (2001) suggest enhanced periods of upper water column melt-water stratification probably related to increased glacial run-off or earlier annual onset of sea ice melt. Other marine records of the Antarctic Peninsula (Pudsey et al., 1994; Leventer et al., 1996; Shevenell et al., 1996), the Ross Sea (Cunningham et al., 1999), and Prydz Bay (Taylor, 1999) do support a mid Holocene "warmer than today". Taylor and Sjunnekog (2001) describe the Holocene climate as bimodal, based on shifts in diatom assemblages. An expression of this bimodality is seen in the crude Shipboard TOC data set for Site 1098 (Fig. 3.2). The peak around 15 mbsf, corresponding to ~5.50 ka BP (Domack et al., 2001), correlates well with diatom abundance data and the begining of a relative climatic deterioration toward more ice influenced conditions (Taylor and Sjunnekog, 2001). This brief cool period is also suggested by Ingólfsson et al., (1998) based on a compilation of terrestrial Antarctic Holocene records. The subsequent upsection peak in TOC marks a second productivity high associated with diatom assemblages indicative of climatic warming and increased sea ice cover linked to the hypsithermal (Taylor and Sjunnekog, 2001; Domack et al., 1991) at the transition to the Neoglacial.

3.3.1.4 Neoglacial and Little Ice Age (3.70 - 0 ka BP)

The top 9 meters at both Sites (1098 and 1099) are characterized by increased MS signal amplitude and variability marking the widely recognized late Holocene rapid climate change from warm optimum conditions to the cool Neoglacial. The „cotton-like" textured cm-wide laminations of *Corethron criophilum* mats alternating with darker *Chaetoceros* resting spores layers are characteristic for this interval (ODP Leg 178 Shipboard Scientific Party, 1999; Fig. 3.1A).

High values of MS occur in massive bioturbated sediments which contain a lesser diatom abundance and a diatom assemblage indicative of reduced meltwater stratification (Ostermann et al., 2001). Preservation of benthic foraminifera is better in the massive units (Ostermann et al., 2001) indicating short periods of „unfriendly" bottom water conditions (pH, oxygen) during settling of diatoms as connected mats after bloom events. In general the MS signal correlates with relative strength of the terrestrial influx indicated by IRD and glacial debris. During the productivity highs the sedimentation rates were higher and the terrestrial input signal was diluted. In contrast, the massive bioturbated intervals represent times with low biogenic production and lower sedimentation rates, when the terrestrial influx accumulated. These alternations are also expressed in the bulk density (higher for the massive units) and velocity values that produce the impedance contrast within the Neoglacial section at Site 1098. Even though the thickness of the Neoglacial section at both Sites (1098, 1099) is identical, Site 1099 contains more turbidites in this interval, similar to the deglaciation record.

Starting about 700 yr BP a distinct MS high (2 mbsf, Site 1098, Fig. 3.2) associated with a decrease in diatom abundance (Sjunnekog and Taylor, 2001) may be related to the Little Ice Age, recognized as a bipolar cooling (600 to 100 yr BP; Kreutz et al., 1997).

3.3.2 Palmer Deep Age Model and the C^{14} Problem in Antarctic Waters

The chronology of Palmer Deep Hole 1098C is based on ^{14}C accelerator mass spectrometry (AMS) dating of bulk sediment organics and foraminifers from three sediment cores (Hole 1098C, core PD92-30, and core LMG98-02-KC1; for details see Domack et al., 2001). The AMS dates were corrected for reservoir effects of 1232.5 yr for the upper 28.77 m and 732 yr for the lower section. The two different reservoir ages are justified by radiocarbon ages of living marine invertebrates for the 1232.5 yr correction and an assumed change in bottom water composition with reduced CDW influence for the 732 yr correction (Domack et al., 2001; ODP Leg 178 Scientific Party, 1999). The reservoir corrected ages were subsequently

calibrated to account for atmospheric ^{14}C activity variations using the software INTCAL98 (Stuiver et al., 1998). Based on 54 corrected and calibrated ^{14}C dates a third-order polynomial regression is proposed as an age model for the upper 25 mbsf (Domack et al., 2001). Between the turbidites (Fig. 3.2 and Fig. 3.1) linear sedimentation rates have been proposed indicating no major loss in record below turbidite 1 but a loss of almost 1000 y at the base of turbidite 2 (Fig. 3.1; Domack et al., 2001). The chronology for the section below the third turbidite (below 40 mbsf) is vague (Domack et al., 2001) because the low sedimentation rate of 0.3 cm/yr is primarily the result of a sample within a slump unit above the tills that form the basement of the basin. It is also impossible to estimate the amount of erosion below turbidite 3b.

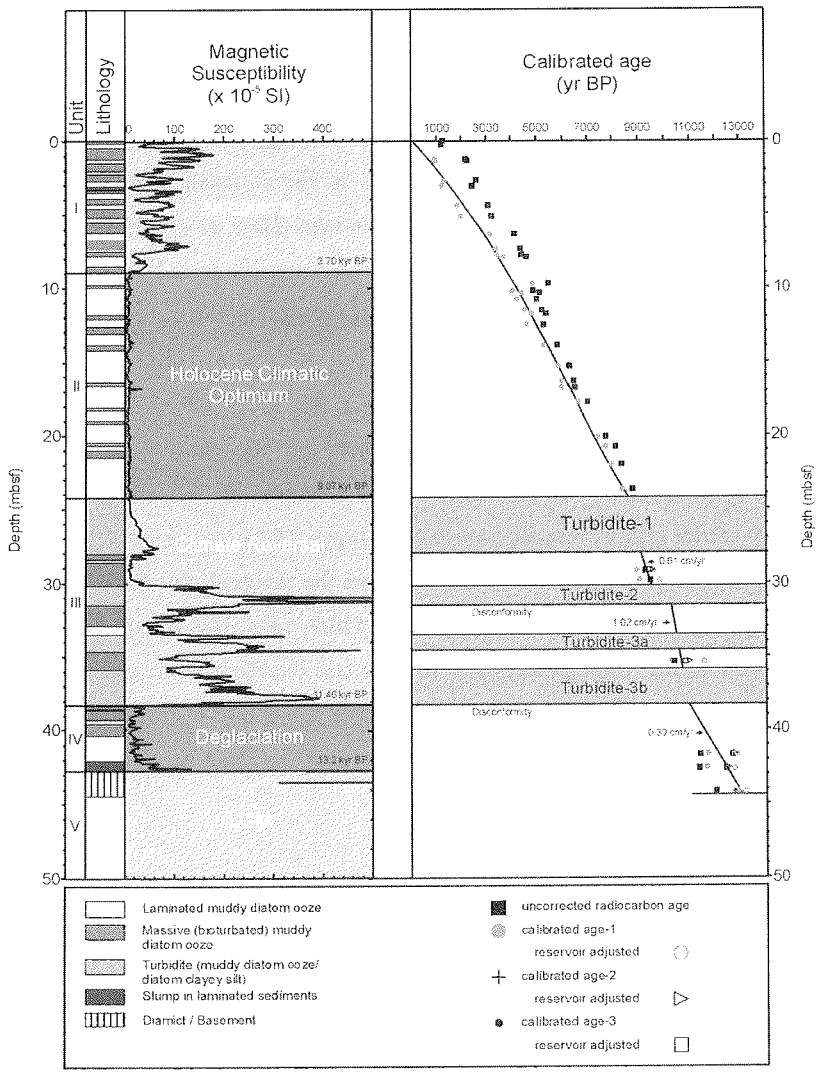

Fig. 3.1. Lithology, MS and time scale of Domack et al. (2001). Note that the original time depth conversion of Domack et al. (2001) is based on meters composite depth (mcd) and has been re-converted to mbsf (for details on the composite scale see Acton et al., 2001).

In general the radiocarbon dating in the Southern Ocean is challenging when using terrestrial radiocarbon calibration curves. Marine organisms living in both the surface and deep environments typically exhibit abnormally „old" radiocarbon ages with respect to terrestrial organic material (Gordon and Harkness, 1992; Bard, 1988; Bard et al., 1989; Domack et al., 1989). The Southern Ocean surface waters display the greatest offset between radiocarbon and calendar age. The following factors may contribute to the observed offset:

- Upwelling of „old" deep waters at the Antarctic Divergence and their mixing with local intermediate and surface waters
- The presence of sea ice temporarily restricting the surface water/atmosphere interaction, minimizing the amount of ^{14}C of the enriched atmosphere entering the surface waters during the windy winter months (Bard et al., 1989; Domack et al., 1989)
- Brine injection due to sea ice formation in the austral summer, bringing less dense old deep waters to the surface.

Therefore, the actual offset in absolute calendar age is dependent not only on the vital effects in the organic matter but also on the local reservoir of ^{14}C. Since the locations of oceanic fronts, water masses, sea ice patterns and brine formation vary over time, a reservoir age may only be valid for a short time period. Hence the timescale for Palmer Deep has to be treated with caution. The change of reservoir age within core 1098 is especially problematic. Age assignments in the lower part of Site 1098 should therefore be treated as best estimates (Domack et al., 2001).

3.4 Seismic Stratigraphy

3.4.1 The single channel HUNTEC Deep Tow Boomer (HDTB) Acquisition System

Seismic reflection profiles used in the Palmer Deep seismostratigraphic study for high resolution correlation were collected on board the *Polar Duke* (NSF-USAP, Antarctic Program, 1992; Fig. 3.1) and the *L. M. Gould* (NSF-USAP, Antarctic Program, 1998; Fig. 3.1). Both surveys used the HDTB system, contracting GEOFORCE Offshore Marine Services in Dartmouth NS, Canada to provide and operate the system. The 1998 survey in Palmer Deep took place during drilling of Leg 178.

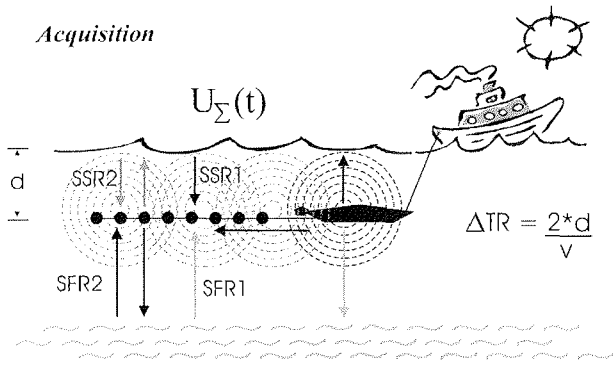

Fig. 3.1. Data acquisition with the HDTB System. The tow depth (d) of the fish and the sea water velocity (v) determine the maximum time window available for receiving data unaffected by the arrival of the sea surface return.

The HDTB System is designed to examine sub-seabottom marine sediments. It consists of the towed seismic source (the so called „fish" behind the ship, Fig. 3.2A.1, A.2 and Fig. 3.3), recording, processing and display units on board the ship (Fig. 3.2 B.1), a cable providing high current for signal generation, and data channels to receive signals and communicate with the fish. The fish is towed at a specific water depth chosen to avoid time overlap between the water surface to fish multiples and the sub-seabottom data return. The seismic source within the fish, the boomer, consists of an aluminum plate that is pushed outward and inward by the electromagnetic field of a copper coil behind it (Fig. 3.2 A.3, A.4). The high energy compressional signal is characterized by a wide frequency bandwidth (0-10 kHz) with dominant frequencies in the 0.5-5.5 kHz range. These are capable of penetrating more than 100 m of silty mud and up to 60 m of glacial tills. The high frequency broad band signal is well suited to detect a wide range of small scale impedance changes (resolution: < 30 cm). The fish is equipped with electronic and mechanical pressure (Fig. 3.2A.7) and tilt meters which locate the fish to specific water depth and upright position, and which can remove the effects of pitch. Changes in fish depth (heave, waves or change in survey speed) are corrected by advancing or delaying the triggering of the firing pulse that initiates the source wavelet (Fig. 3.3A). The outgoing wavelet, sub-seabottom seismic returns, and multiples are all recorded by an internal hydrophone (Fig. 3.2A.4) located within the fish and by an optional external streamer array towed behind the fish (Fig. 3.2A.1, A.6). The HDTB reflection seismic data used for this chapter were plotted on a EPC Recorder and stored on analog tape cassettes. Some institutions (e.g British Antarctic Survey and Bedford Institute of Oceanography) have equipped their systems with digital recording units.

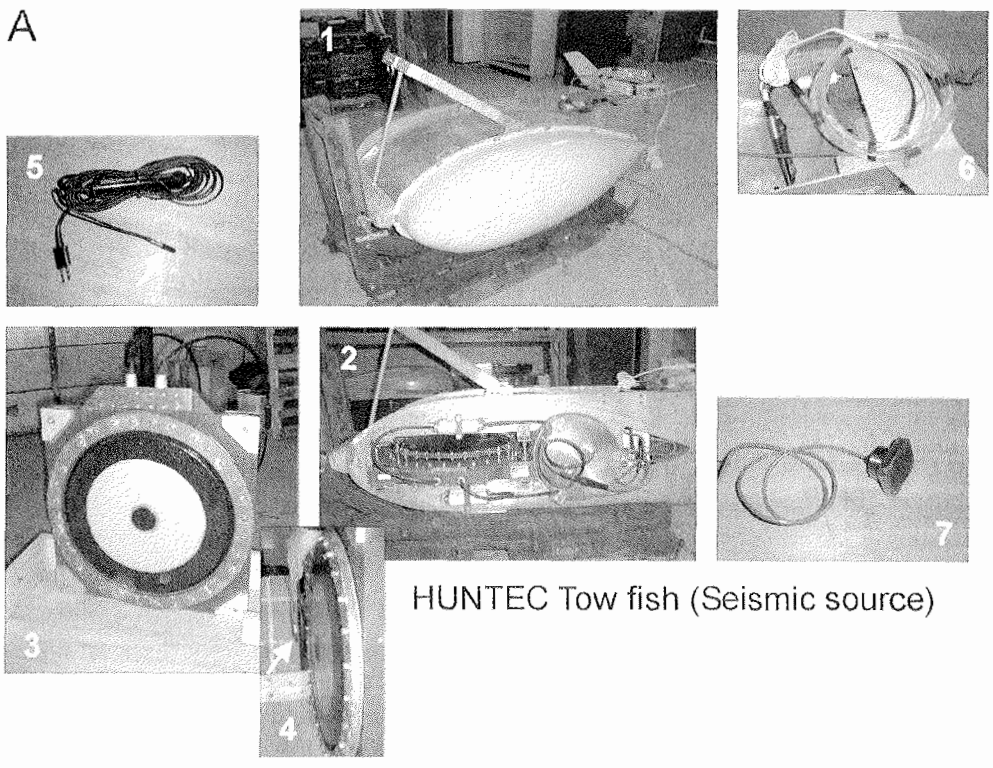

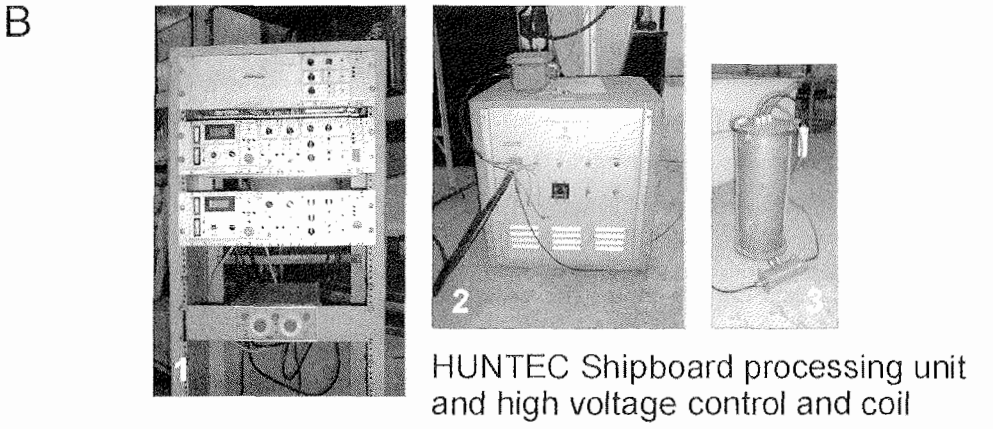

Fig. 3.2. (**A**) The tow fish and its main components: (**A.1**) Assembled tow fish. (**A.2**) Tow fish with left cover removed with the high voltage coil (see **B.3**) and the boomer plate (see **A.3, 4**) in place. (**A.3**) Boomer plate (acoustic source) with the movable aluminum disc sealed with a rubber membrane. (**A.4**) Side view of the boomer plate showing the location of the internal hydrophone (arrow). (**A.5**) Internal hydrophone (arrow). (**A.6**) External streamer. (**A.7**) Pressure transducer used for fish movement correction. (**B.1**) Analog shipboard based HUNTEC control panel, preprocessing, and recording unit. (**B2**) Shipboard-based high voltage control unit. (**B.3**) High voltage, high current coil feeding the boomer plate (part of the tow fish).

Even though the HDTB system was introduced in the early '70, many oceanographers prefer HDTB records over the newer subbottom profiling systems that commonly have much narrower sources (for additional HDTB information see Hutchins et al., 1976).

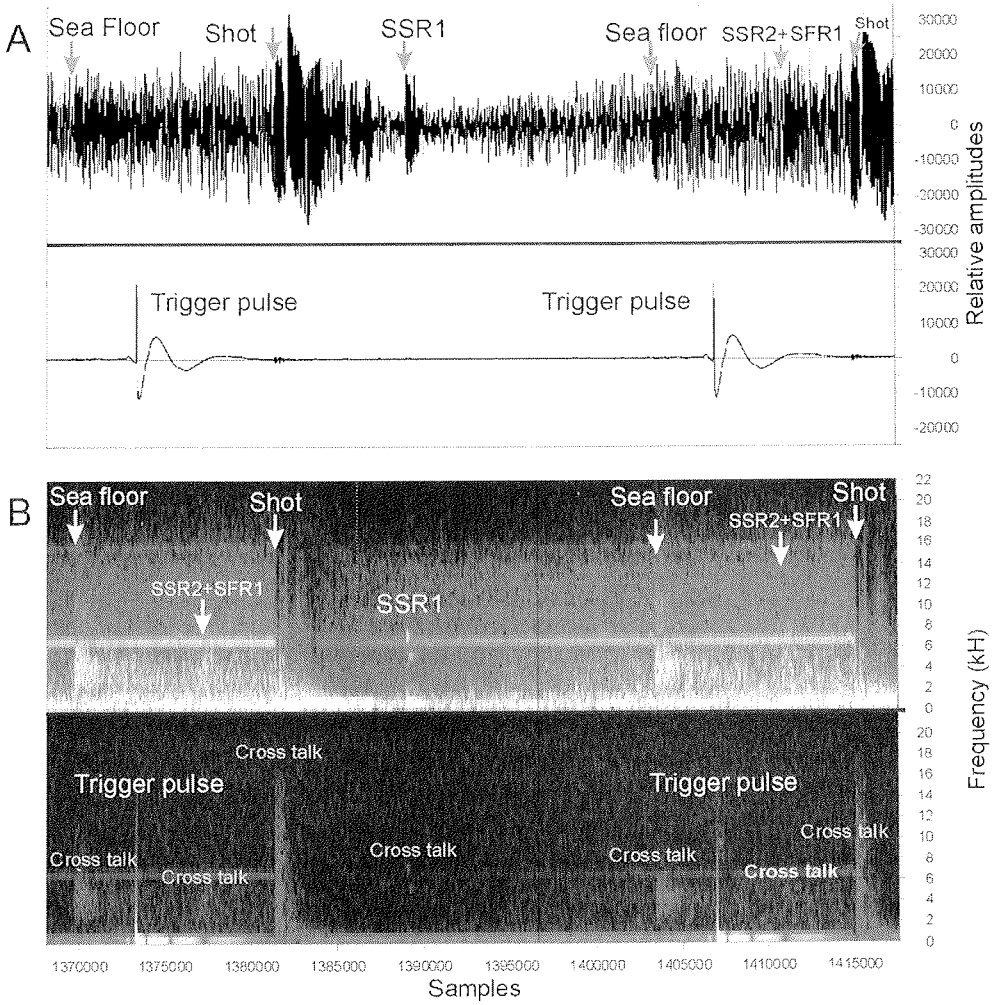

Fig. 3.3. **(A)** wave form and **(B)** spectral view of the data (top) and trigger (bottom) channel. **(A)** Note the linear time dependent gain, automatically applied by the HUNTEC unit to compensate for energy loss due to spheric spreading. A trigger pulse and onset of the shot (time of boomer plate outward movement) are separated by an adjustable delay (SSR1, sea surface return 1 (fish-sea surface-fish); SSR2 (fish-sea surface-fish); SFR1, sea floor return (fish-sea floor-fish). **(B)** considerable amplitudes are observed up to 10 kHz. Maximum frequency dispersion occurs at the sea floor. The cross-talk between data and trigger channel is best seen in the spectral view. Note the time window between trigger pulse and arrival of SSR2 and SFR1 cannot be displayed by trigger controlled systems (e.g. EPC-Recorders or the AGC Digitizers).

3.4.2 Seismic Models and Correlations

3.4.2.1 Density/Velocity Models

Bulk densities for the subsea formation were derived from MST (GRAPE) measurements (2-cm spatial resolution) and index property measurements (3.1-m spatial resolution, Site 1098; 3.5-m spatial resolution, Site 1099). Both Site 1098 and 1099 were cored using the APC, which provides undisturbed sediment that yields a high-quality MST (GRAPE) density record. Low GRAPE density values resulting from gas expansion gaps in the core from the lower part of Site 1099 were removed using methods described in the "Excursus" chapter 7.2. Spliced density and velocity data (see the Composite Depths chapter of the Palmer Deep section in ODP Leg 178 Shipboard Scientific Party, 1999) have been used for acoustic models at both sites (Site 1098, Fig. 3.2 and Fig. 3.1 and Site 1099, Fig. 3.3 and Fig. 3.2). Two differently derived velocities are available. The MST logger provided continuous data (4-cm spatial resolution) for all cores of Site 1098 and the upper 70 mbsf of Site 1099. Additionally, discrete PWS3 Hamilton Frame measurements with a lower spatial resolution (1.4–1.5 m) are available. The model for Site 1098 uses MST velocities, and PWS3 velocities are used for the Site 1099 model. High MST *P*-wave velocities below 35 mbsf at Site 1098 may be an artifact (they show no correlation with the density) and should be reevaluated (Fig. 3.2; Fig. 3.1). The lack of *P*-wave data below 77.5 mbsf at Site 1099, resulting from core disturbance by gas exsolution, has been compensated by extrapolation of data from higher in the section, using a third-order polynomial (Fig. 3.3; Fig. 3.2).

3.4.2.2 Source Signals

Three different source signals have been used for the seismic models at Sites 1098 and 1099: the far-field and sea floor signatures of the Generator Injector (GI) gun (as described in chapter 4.2.1.2) and a high-resolution digital recording of a HDTB farfield signal (P. Simptkon, pers. comm., 1997). The very short HDTB signal, with a length of 0.25 ms and a continuous energy spectrum up to 10,000 Hz, is displayed in Fig. 3.1. With a vertical resolution of 0.2 m (under optimal circumstances), the HDTB system is capable of producing ultrahigh-resolution records of non-indurated sediments.

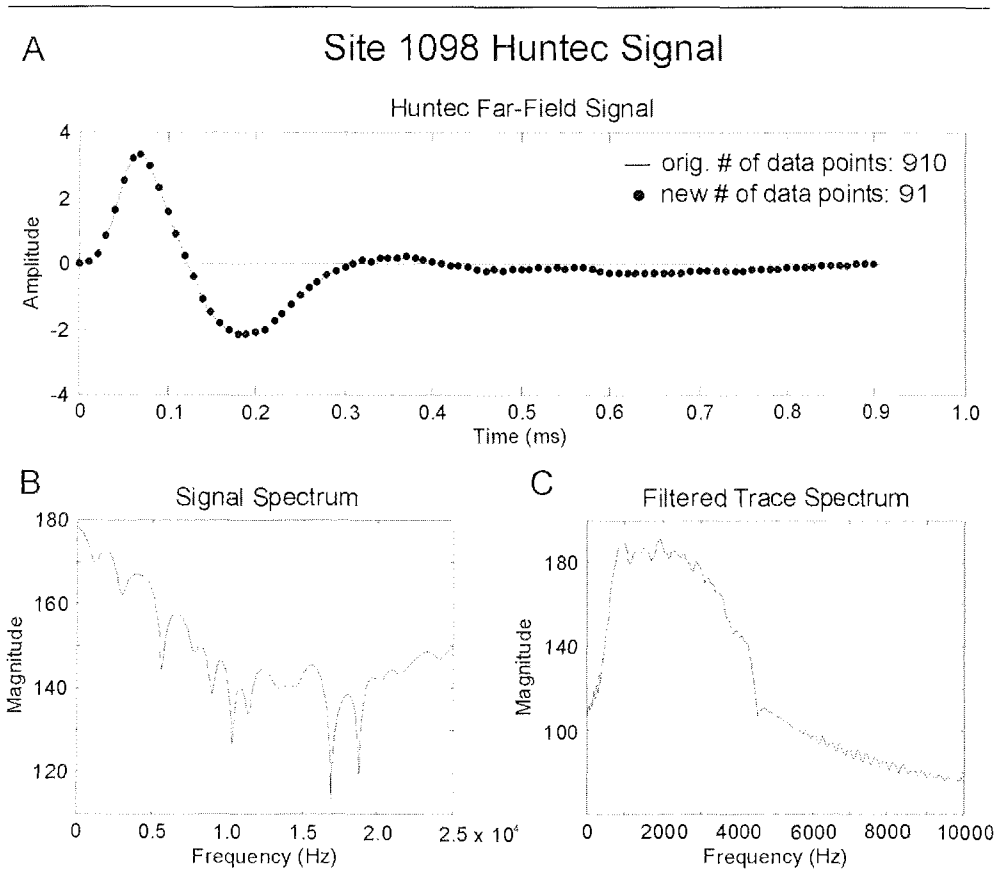

Fig. 3.1. (**A**) characteristics of the 540 J HDTB far field signal, provided by P.Simptkon. Note the fast onset (boomer plate moves outward) and termination (boomer plate moves inward) t of the signal and its short wave length. (**B**) signal spectrum. (**C**) frequency spectrum of the filtered synthetic trace. The filter is set up to simulate the analog Butterworth band pass used with the analog presentation of the data.

3.4.2.3 Time-Depth Models

Depth/traveltime curves have been calculated using the velocity data. At both sites, the traveltime/depth relationship is close to linear (Fig. 3.1). Indicating no or only minor compaction of the sediment with depth. This is thought to be due to the rigidity of opal diatom skeletons. The steepening of the Site 1098 curve at depth may be the result of incautious use of MST *P*-wave data (Fig. 3.1).

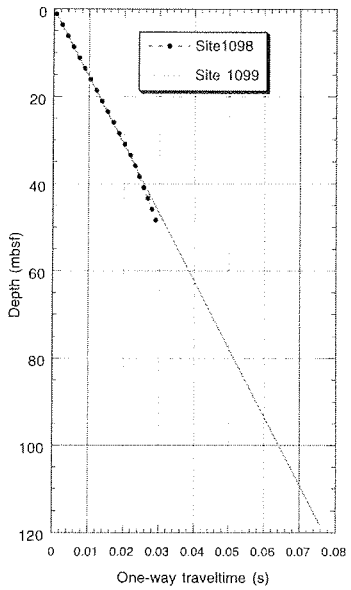

Fig. 3.1. Time/depth relationships at Sites 1098 and 1099. The steepening of velocity values at the base of 1098 is probably caused by the incorporation of bad MST data.

3.4.2.4 Synthetic Seismograms

All seismic models presented in the Palmer Deep chapter have been calculated using the „synseis-software" described in the "Excursus" chapter 7.1.6.

The spliced and corrected velocity and density data were resampled at 0.2 m (Site 1098) and 0.15 m (Site 1099) resolution. Only the reflectivity series of Site 1098 was convolved with the Huntec signal because no profile taken over Basin I with any other acoustic source (air gun or GI gun) showed comparable detail within the shallow basin fill. The velocity/density data, impedance curve, reflectivity coefficients, and an unfiltered synthetic trace are displayed in Fig. 3.1.

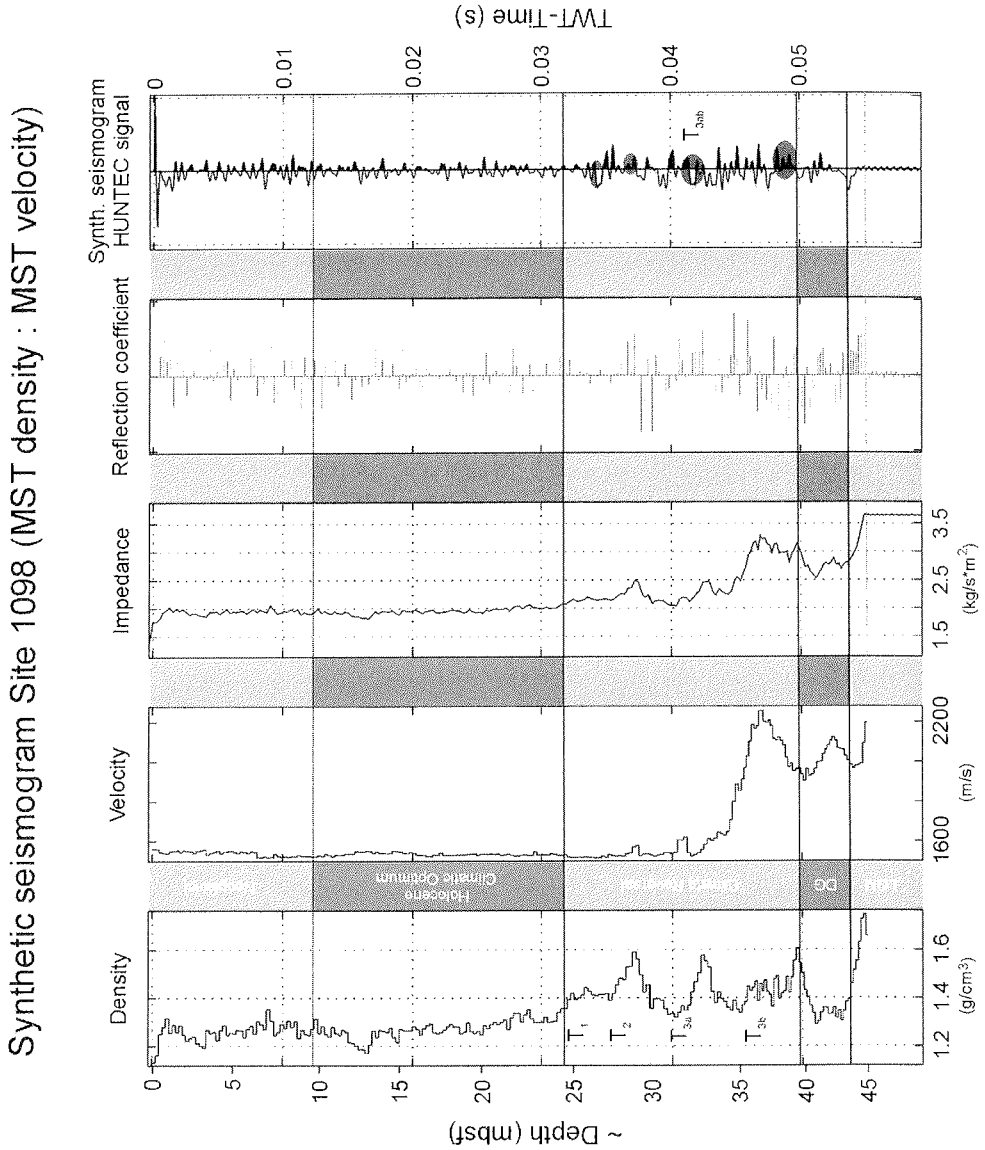

Fig. 3.1. Cleaned (see chapter 7.2) and resampled acoustic properties and the synthetic seismogram trace (calculated with the software "synseis", see chapter 7.1.7) of Site 1098 using the HUNTEC deep-tow boomer far field signal. Note that the data set is given in time domain, the depth scale therefore is only approximate. LGM, last glacial maximum; DG, deglaciation.

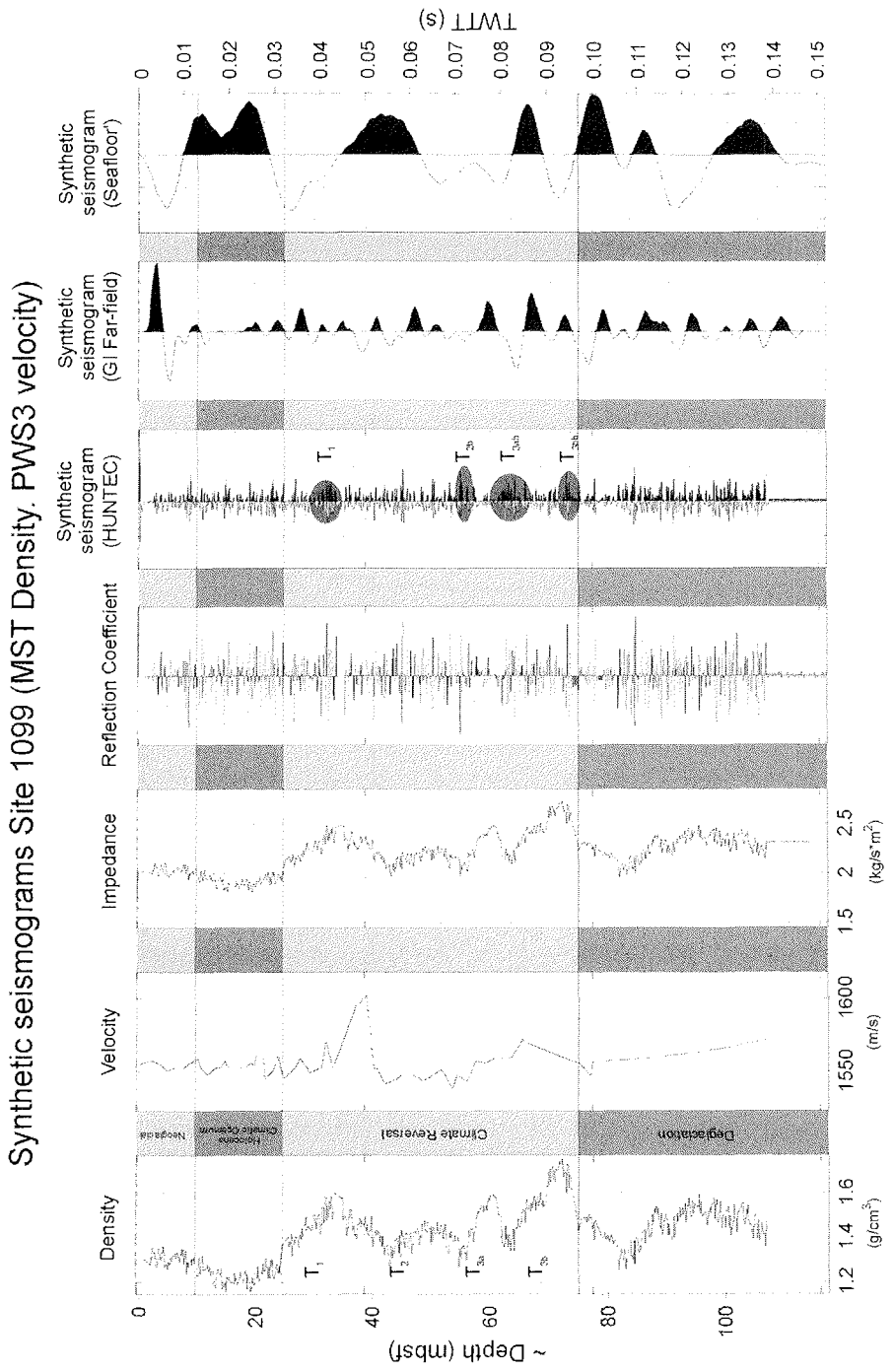

Fig. 3.2. Cleaned (see chapter 7.2) and resampled acoustic properties and the synthetic seismogram trace (calculated with the software "synseis", see chapter 7.1.7) of Site 1099. Three different source signals were used

to convolute the reflectivity series. Note that the data set is given in time domain, the depth scale therefore is only approximate.

For Site 1099, the acoustic impedance model was convolved with the GI gun far-field, the sea floor stack, and the HDTB signals (Fig. 3.2). An approximate depth scale is given in Figure 15. There are extreme frequency and resolution differences between the synthetic traces derived from the three different source signals at Site 1099. The time delay between an impedance contrast (e.g., at 0.043 s) and the corresponding reflection within the synthetic trace increases dramatically with the wave-length of the different signals. The response of the HDTB trace is close to "instant." The GI far-field response occurs at 0.048 s, and the GI sea-floor trace of 40 ms shows a response at 0.055 TWTT (s). To eliminate these effects, reflector depths must be measured with respect to the onset of the sea floor reflection. The Huntec traces for Sites 1098 and 1099 were resampled at 20,000 Hz and subsequently filtered using a zero-phase equi-ripple band-pass filter (pass band = 800–4500 Hz; attenuation = 40 dB; filter order) (40) to match their frequency content to a commonly used frequency range for the HDTB-record display (Fig. 3.1). As seen in Fig. 3.1, most of the prominent reflectors are represented within the synthetic traces for Site 1098 (chapter 3.4.3). At Site 1099, the synthetic trace shows all the important reflectors of the upper 40 ms of the HDTB profile (Fig. 3.1). For a detailed discussion and description of the seismic section see chapter 3.4.4. Additionally, the GI gun sea floor synthetic trace (based on the same impedance model) was filtered using a zero-phase equi-ripple band-pass filter (pass band = 30–110 Hz; attenuation = 35 dB; and filter order = 70) and processed to meet the processing specifications of seismic line I97H-219G which crossed Basin III (zero-phase Butterworth band-pass filter [pass band = 30–110 Hz], automatic-gain recovery window of 100 ms, static shift and cutting, and interpolation to 0.5-ms resolution). The only feature that can be identified with some confidence is a broad reflector at 50 ms TWTT (Fig. 3.2E).

3.4.3 Seismic Units at Site 1098[11]

At Site 1098, the till reached and sampled at ~43 mbsf represents the acoustic basement for all available reflection seismic records. In the single-channel air gun seismic profile I97H-218G

[11] Parts of this chapter are modified from: Shipboard Scientific Party, 1999. Palmer Deep (Sites 1098 and 1099, Seismic Stratigraphy). *In* Barker, P.F., Camerlenghi, A., Acton, G.D., et al., *Proc. ODP, Init. Repts.*, 178, 1–173 [CD-ROM]. Available from: Ocean Drilling Program, Texas A&M University, College Station, TX 77845-9547, U.S.A. Authorship of sub-chapter „Seismic Stratigraphy": Escutia, C. and Moerz, T.

(Fig. 3.2F), we identified one seismic unit above acoustic basement. Seismic Unit I (0–46.7 mbsf) is acoustically semitransparent, with some low-amplitude reflectors toward the base of the unit that onlap the irregularities of acoustic basement (Fig. 3.2F). High-resolution HDTB seismic profiles penetrate to >43 mbsf and allow division of seismic Unit I into three subunits (Fig. 3.1): (1) Subunit Ia (0–9 mbsf) is characterized by stratified continuous reflectors with a high-amplitude reflector at its base, (2) Subunit Ib (9–23 mbsf) consists of parallel reflectors at the top but becomes more transparent toward the bottom, and (3) Subunit Ic (23–43 mbsf) is mostly acoustically transparent but with high-amplitude reflectors at 30, 33, and 38 mbsf (T1, T2, and T3 in Fig. 3.1). The synthetic seismogram clearly reveals the high-amplitude reflections that occur at the base of Subunit Ia and the T1, T2, and T3a and T3b reflectors in Subunit Ic. Higher and lower amplitude reflection patterns in the synthetic traces can be correlated with acoustically stratified and semi-transparent acoustic facies, respectively, in the HDTB seismic profile (Fig. 3.1). Seismic Unit I has a drape geometry, indicated by uniform thickness of the unit in the central part of the basin and a bottom morphology that follows the irregularities of acoustic basement (Fig. 3.1).

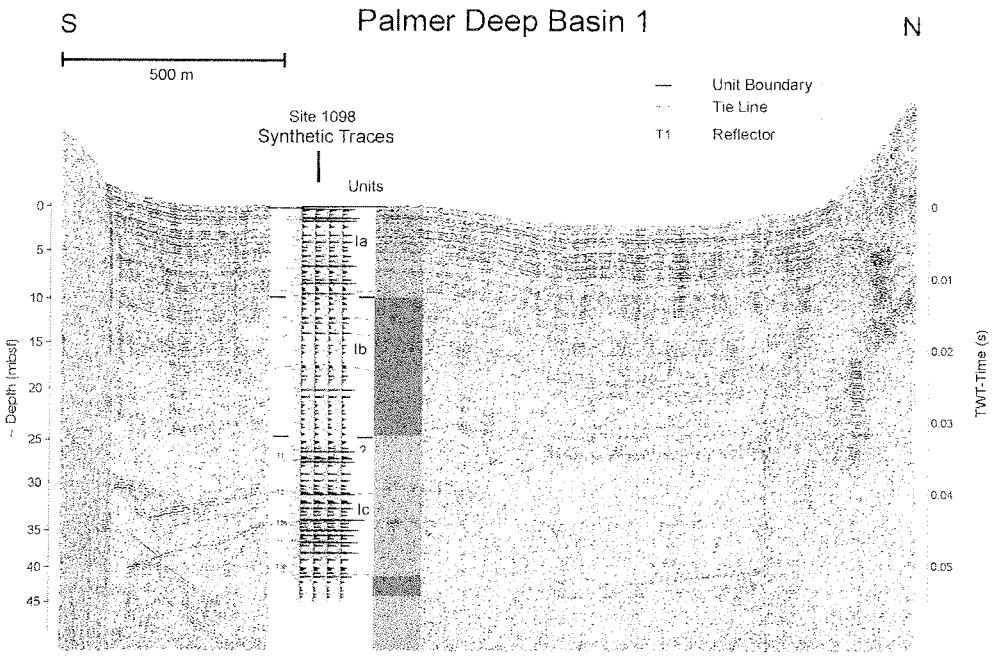

Fig. 3.1. HDTB '92 profile across Site 1098. Comparison of the seismic reflection profile with a synthetic seismogram. The acoustic Subunits Ia, Ib, and Ic roughly correspond to the climatic-lithological zones described in chapter 3.3.1 (for lables to these zones, represented by the color bar, see Fig. 3.2). Reflectors T1, T2, and T3a, T3b correspond to the base of the 4 major turbidite layers (for the lithology see Fig. 3.2).

3.4.4 Seismic Units Site 1099

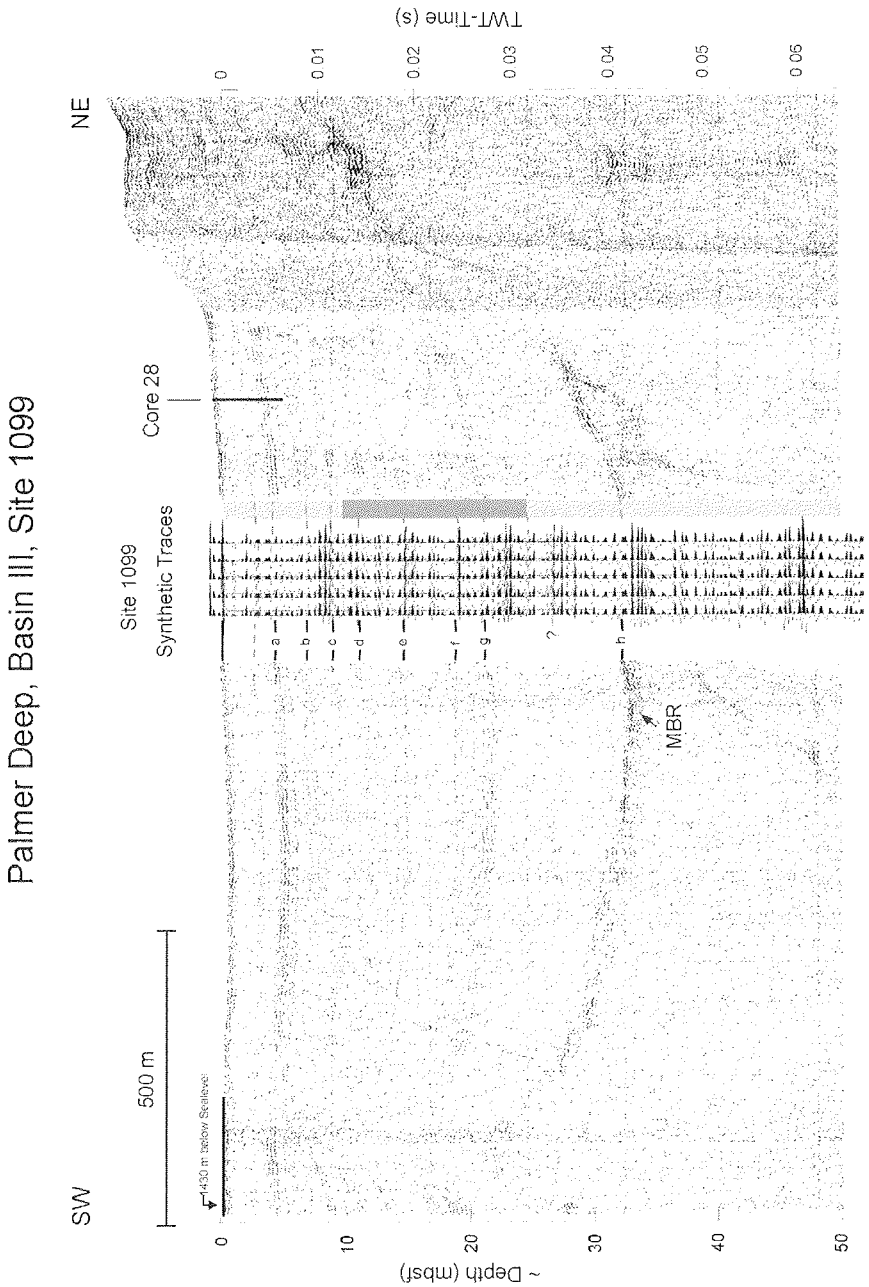

Fig. 3.1. HDTB '92 profile across Site 1099. Comparison of the seismic reflection profile with a synthetic seismogram. Reflector h (the Mid Basin Reflector (MBR), Rebesco et al., 1998b) can be linked to the base of turbidite T1 (see Fig. 3.2 for the lithology). The synthetic seismogram is a good acoustic model for the stratified Neoglacial and Mid Holocene section (see Fig. 3.1 or Fig. 3.2 for lables to the lithological units).

Two main seismic units can be differentiated in the air gun profile (Fig. 3.2C, D). Seismic Unit I (0–76 mbsf) is acoustically semitransparent (I97H-228G; Fig. 3.2C). A high-amplitude reflector, previously referred to as the Mid Basin reflector (MBR; Kirby, 1993; Rebesco et al., 1998b), divides Unit I into two parts. The thickness of Unit I is uniform in the center of the basin and thins toward the edges of the basin. High-resolution HDTB profiles penetrate the upper 34 m of seismic Unit I to the MBR (Fig. 3.1). Acoustic character above the MBR in this high-resolution profile allows differentiation of seven acoustic packages characterized by low-amplitude reflectors at the top and parallel, higher amplitude reflectors at the bottom. In Fig. 3.1, we assign letters from *a* through *g* to the base of acoustic packages at 4.5, 8, 10, 12, 14, 19, and 21 mbsf, respectively. The synthetic seismogram at this site shows a good correlation between high-amplitude synthetic reflections and the base of the acoustic packages (Fig. 3.1). The deepest strong reflector in the HDTB profiles and a high-amplitude reflection in the synthetic seismogram are found at 34 mbsf and correspond to the MBR (named *h* in Fig. 3.1). The MBR (representing the base of T1; Fig. 3.2C, D) in the air gun seismic profile is a horizontal reflector that can be traced across the basin. In the middle of the basin, the MBR has a lower amplitude and an irregular surface. Toward the sides of the basin, it grades to a higher amplitude reflector that onlaps a more acoustically transparent and chaotic package of reflectors. The MBR in the HDTB profiles is a reflector that parallels the irregularities of the sea floor (Fig. 3.1, Fig. 3.2). Seismic Unit II (76–107.5 mbsf) in the air gun profiles is characterized by horizontally stratified high-amplitude continuous reflectors (Fig. 3.2C, D). Reflectors in the upper part of this unit are flat-lying in the center of the basin, "climb" up at its eastern edge, and terminate abruptly in the western part of the basin. Lower reflectors exhibit typical onlap fill geometry either against the acoustic basement or against a package of irregular and chaotic reflectors. The thickness of seismic Unit II varies across the basin because of irregularities in the acoustic basement.

Fig. 3.2 (see next page). HDTB '98 profile across Site 1099 and Site 1098, assembled from EPC-recorder printouts (see Fig. 3.1 for the profile location). Lithologic units are mapped across Sub-Basin I and III. An enlargement of Sub-Basin III is correlated with synthetic traces. Turbidites T1-T3b are marked in both basins. The greater thickness of turbidites in the „Climatic Reversal" Unit in Sub-Basin III compared to Sub-Basin I may be explained by the discharge of gravity flows from Sub-Basin I into Sub-Basin III. Refer to Fig. 3.1 for the profile location.

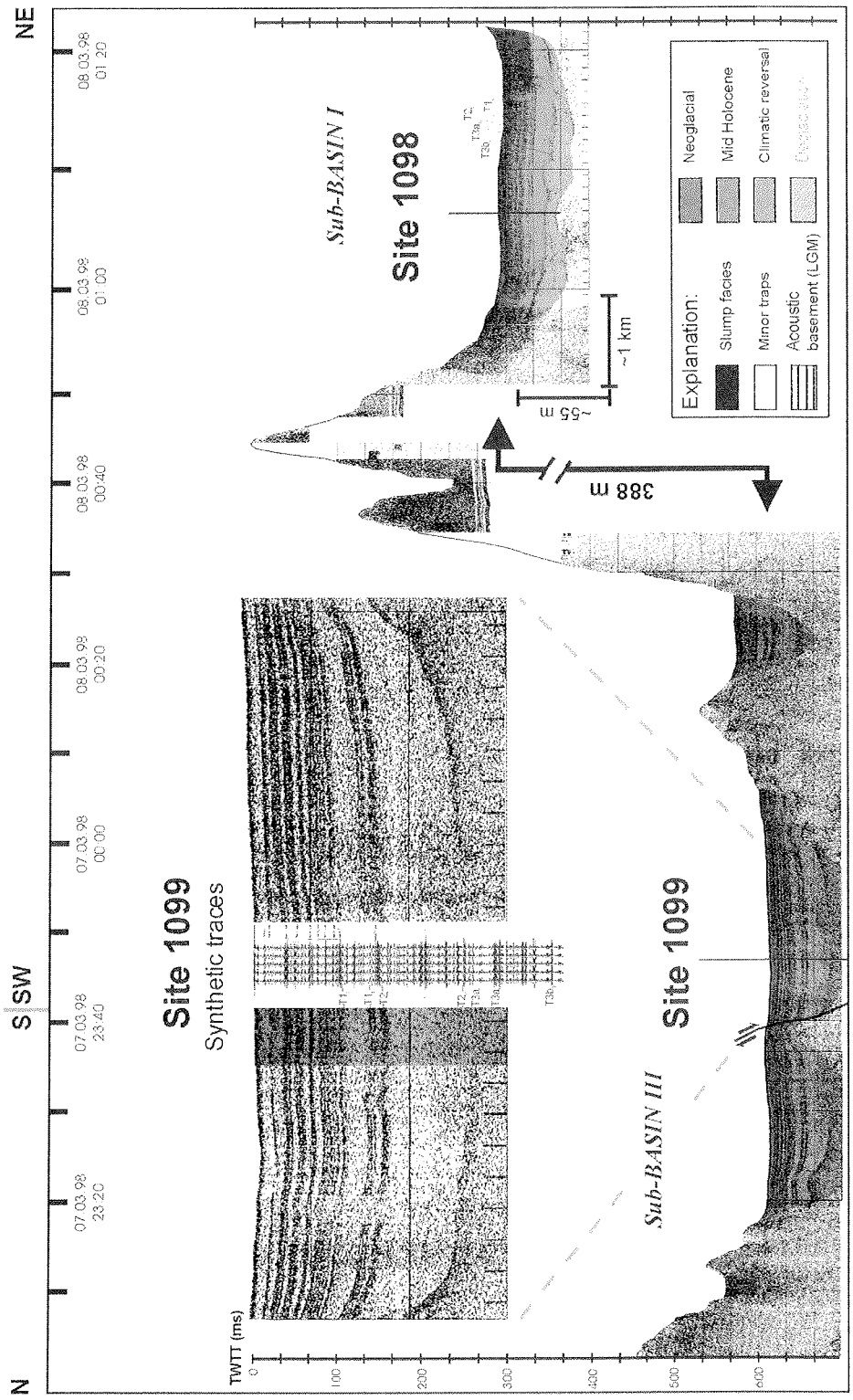
N
S SW
NE
07.03.98 23:20
07.03.98 23:40
07.03.98 00:00
08.03.98 00:20
08.03.98 00:40
08.03.98 01:00
08.03.98 01:20
Site 1099
Synthetic traces
TWTT (ms)
0
100
200
300
400
500
600
Sub-BASIN III
Site 1099
Sub-BASIN I
Site 1098
388 m
~55 m
~1 km
Explanation:
Slump facies
Minor traps
Acoustic basement (LGM)
Neoglacial
Mid Holocene
Climatic reversal

3.4.5 Interpretation and Seismic Mapping of Lithological Units

At Site 1098, parallel reflectors and sheet drape geometries in both air gun and HDTB seismic profiles are compatible. Sedimentation was dominated by hemipelagic/pelagic settling and low-density gravity flows. High-resolution HDTB profiles allow direct correlation between acoustic character, synthetic traces, and lithology (Fig. 3.1). The reflector marking the base of seismic Subunit Ia corresponds roughly to the base of a massive, bioturbated muddy diatom ooze (Fig. 3.2). Semitransparent and stratified reflectors of seismic Subunit Ib correspond to a 15-m interval where laminated sediments predominate. High-amplitude reflections in the synthetic traces of seismic Subunit Ic correspond to an acoustically semitransparent subunit in the HDTB profiles. This suggests that the acoustic character of this unit is the result of limitations in the penetration of the HDTB system and not a real representation of the stratigraphic and lithologic character of Subunit Ic. Three turbidite layers, T1 through T3, are correlated with high-amplitude reflectors at 30, 33, and 38 mbsf (Fig. 3.2, Fig. 3.1, Fig. 3.1).

At Site 1099, seismic Unit I above the MBR (the top 34 mbsf) is dominantly massive or laminated muddy diatom ooze. The higher amplitude reflectors (i.e., reflectors *a* through *g*) at the base of the seven acoustic packages identified in the HDTB seismic profiles correspond to seven thin turbidites in the upper 23 m of the core. Reflectors *c, e,* and *f* coincide with the base of Units Ia, Ib, and Ic, respectively, of Rebesco et al., 1998b. The MBR, apparent in both air gun and HDTB profiles at 34 mbsf, corresponds to a layer of coarse sand and pebbles interpreted as the basal unit of turbidite 1. The acoustically semitransparent Unit below the MBR corresponds roughly to a thick interval of massive, diatom clayey silt and muddy diatom ooze (Fig. 3.3). High-amplitude stratified reflectors of seismic Unit II (Fig. 3.2C, D) correspond to alternations of massive, bioturbated, muddy diatom ooze, laminated mud-bearing diatom ooze, and very fine-grained graded turbidites (Fig. 3.3). The overall onlapping character of the seismic units drilled in the Palmer Deep basins suggests that sedimentation was dominated by hemipelagic drape and infilling of the basins with sediment gravity flows, probably from a local source. The character of the MBR in the air gun seismic profile (grading into or onlapping more chaotic packages toward the sides of the basin) can be explained by its being the base of a mass flow unit originating from slope failures and slumps of the basin walls. An intrabasinal source for sediments is suggested by the irregular reflector packages on the sides of the basin (i.e., the western side in Fig. 3.2C, D).

The "climbing" reflectors of Unit I and the uppermost reflectors of Unit II at the edge of the basin (interpreted as growth faults) are most likely to be related to neotectonic activity in the basin (Fig. 3.2C, D; Rebesco et al., 1998b).

The HDTB profiles acquired in 1998 from the vessel L.M. Gould (cruise LMG 98-2) have been used as a base to map the lithological and climatic Units (see core interpretations, chapter 3.3). Compared to the focused internal hydrophone, the parallel wired streamer (Fig. 3.2A.6, all hydrophone signals are stacked) improves the detection of deeper reflectors (Fig. 3.2A.4, A.5) but reduces the lateral and vertical resolution of small scale features. As a consequence many sediment fill and acoustic basement features appear very smooth.

Prominent reflectors in the HDTB '92 profiles have been identified and correlated to lithology with the aid of synthetic traces. All of the previously named reflectors of Site 1099 are shown in Fig. 3.2 (enlargement), with additional reflectors are also labeled. The '98 streamer record penetrated deeper strata compared to that from '92. The lowest reflector identified at Site 1099 corresponds to the base of turbidite T3a (Fig. 3.2). At Site 1098 the lowest prominent reflector, previously thought to correlate with the base of turbidite T3a, has been identified as the top of the acoustic basement. A careful analysis and comparison of the two sub-basins revealed that the so called MBR in the papers of Rebesco et al., 1998b et al. (1998), identified as the prominent double reflector in the middle of the record at Sites 1099 and 1098 (Fig. 3.2) is not equivalent. Instead, this reflector corresponds to the the base of turbidite T3b in Sub-Basin I, marking the boundary between the deglaciation interval and the climatic reversal. At Site 1099 (Sub-Basin II) this reflector is in the upper quarter of the climatic reversal unit and represents the base of turbidite T1a. Nevertheless, all turbidites (T1, T2, T3a, T3b) previously described are present in both basins and are time equivalent. The reduced thickness of the turbidites in Sub-Basin I can be explained by the morphology of Sub-Basin I and its outlet to Sub-Basin III. Most of the mass gravity flows initiated by grounded ice advance or massive iceberg scouring near Sub-Basin I travelled through this canyon and discharged into Sub-Basins II and III (Fig. 3.1).

3.5 An Approach for Digitalization and Processing of Analog High Resolution Single Channel '98 HUNTEC Deep Tow Boomer Data

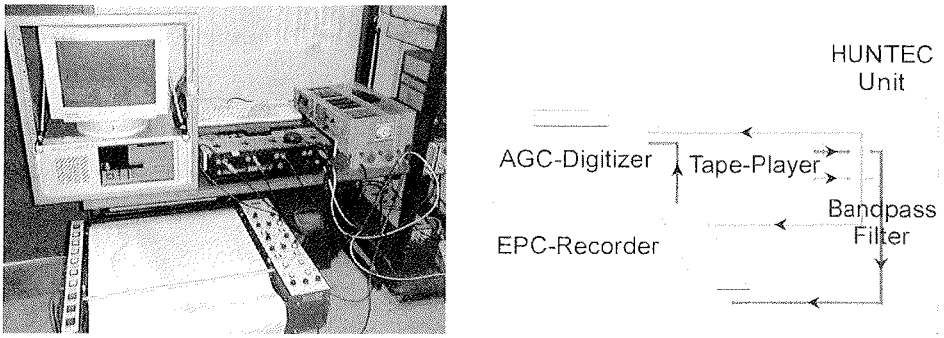

Fig. 3.1. Atlantic Geoscience Center (AGC) digitizing unit. The data on analog tape is played back and filtered. The trigger channel (dark gray lines, standardizing of the trigger pulse) and the data channel (light gray lines) are first fed into an EPC recorder (online display). The 12 bit AGC unit is working trace oriented with fixed samples in each trace and uses the trigger pulse for the start of a new trace. Data after the trigger pulse is lost due to a fixed delay set at the beginning of the trace to fade out most of the water column.

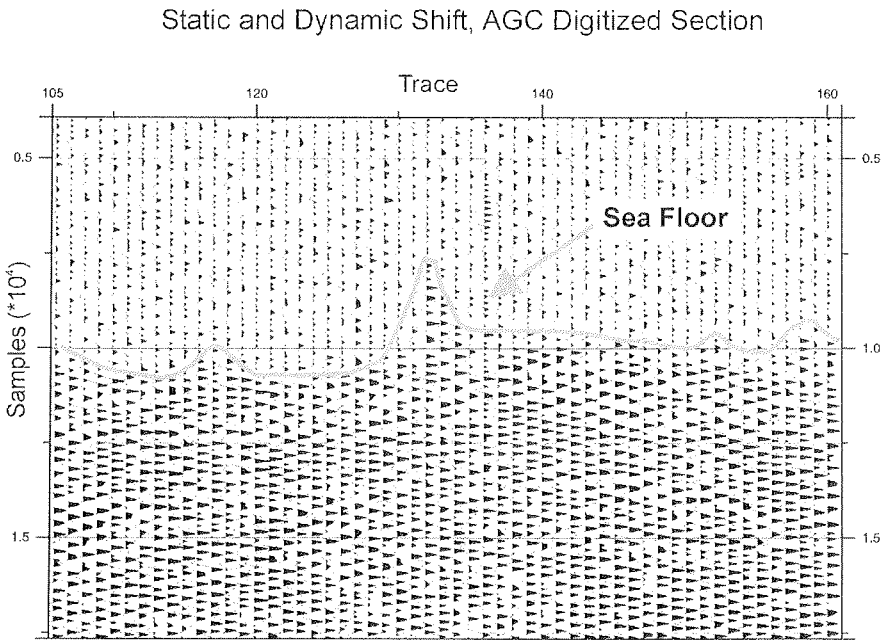

Fig. 3.2. Large static shifts distor the single channel record digitized with the AGC Unit. Most likely cause are poorly-detected trigger pulses.

In order to improve the vertical and horizontal resolution in this unique high resolution Holocene record, digital data must be processed. Fig. 3.1 shows the basic geometric arrangements for a Deep Tow Boomer survey. During the '98 Palmer Deep survey the source was towed between 100 and 140 m below the water surface and a parallel hydrophone streamer collected the signal, which was stored analog together with a time mark (Trigger) on normal cassette tape. Fig. 3.3 shows the two digitized channels in time and frequency domain. Note the adjustable delay between the trigger pulse and the actual firing of the boomer. Due to uncorrected high frequency fish movements, imprecise cassette tape mechanics, and nonlinear stretching of the tape itself, distances between time marks have different lengths. This leads to unpredictable dynamic and static noise between traces (Fig. 3.2). An initial attempt at correction was made using the single channel digitizing equipment of the Geological Survey Canada (Atlantic Geoscience Center, Fig. 3.1). Unfortunately, this highly specialized equipment works in a trace oriented mode, hence it is dependent on external triggering. Lateral coherency of the record is dependent on trigger quality and detection repeatability. Furthermore, this professional system is incapable of recording the the trigger channel, preventing subsequent processing and correction of the time base. To overcome this problem both hardware and software have been modified.

3.5.1 The Digitalization Hardware and Recording Software

A high quality SONY two motor cassette player with a ceramic casette holder was used to run the audio tapes. From there the two stereo channels were individually amplified by a KENWOOD amplifier (KAF-1010). The two channels were then fed into a TERRATEC Xlerate PCI Soundcard with a 16 bit 41 kHz front end digitizer. The primary recording software is a commercial version of CoolEdit v.6 (for the setup see Fig. 3.1A). Before starting the recording, the two channels are digitally amplitude adjusted to guarantee maximum usage of the 16 bit resolution. The endless stream of trigger channel and data channel data is saved as a binary audio .wave file (Microsoft .wave). To impress time stamps on the record, the HDTB system generates double triggers each minute, leading to two boomer signal releases within a short time interval. These data discontinuities have been removed manually, the ~1 minute data packages were then stored in individual files (1 minute = 10 Mb binary file size).

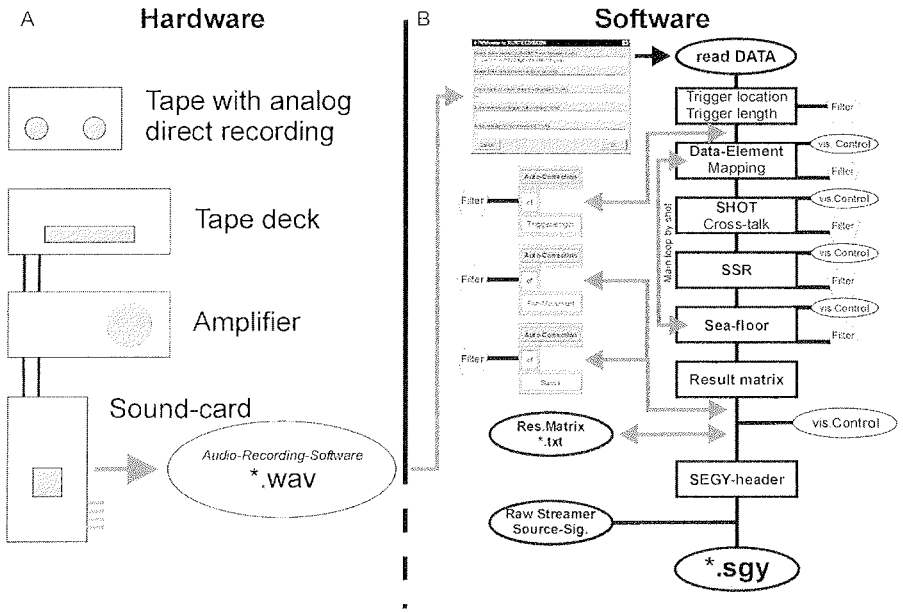

Fig. 3.1. Hard- and software configuration used in a low cost approach to digitize HDT data from analog audio tape: **(A)** hardware configuration, **(B)** processing software flow chart. Refer to the text for details.

3.5.2 The Interactive Processing Package "huntecdigcon"

A detailed description of the "huntecdigcon" software written in Matlab is beyond the scope of this thesis. Instead only a brief outline of the featues and procedures is given (see also Fig. 3.1B).

The one minute long files are read in as *.wave-files via a graphical user interface (file path, shot rate, type of correction). The first processing step is the trigger space detection. The trigger channel is low pass filtered and the trigger is detected by a combination of threshold and slope criteria. An optional subsequent trigger correction routine reduces or increases the number of samples of the data channel between trigger locations by means of interpolation of the shot and sampling rates. In the same interpolation step the trigger channel is also adjusted to a fixed spacing length. To map the three important features of each shot (time of firing, arrival of the sea surface return (~depth of the fish) and arrival of the sea floor return) an approximate location of these features is determined using polynominal techniques on filtered data segments between triggers (Fig. 3.1A).

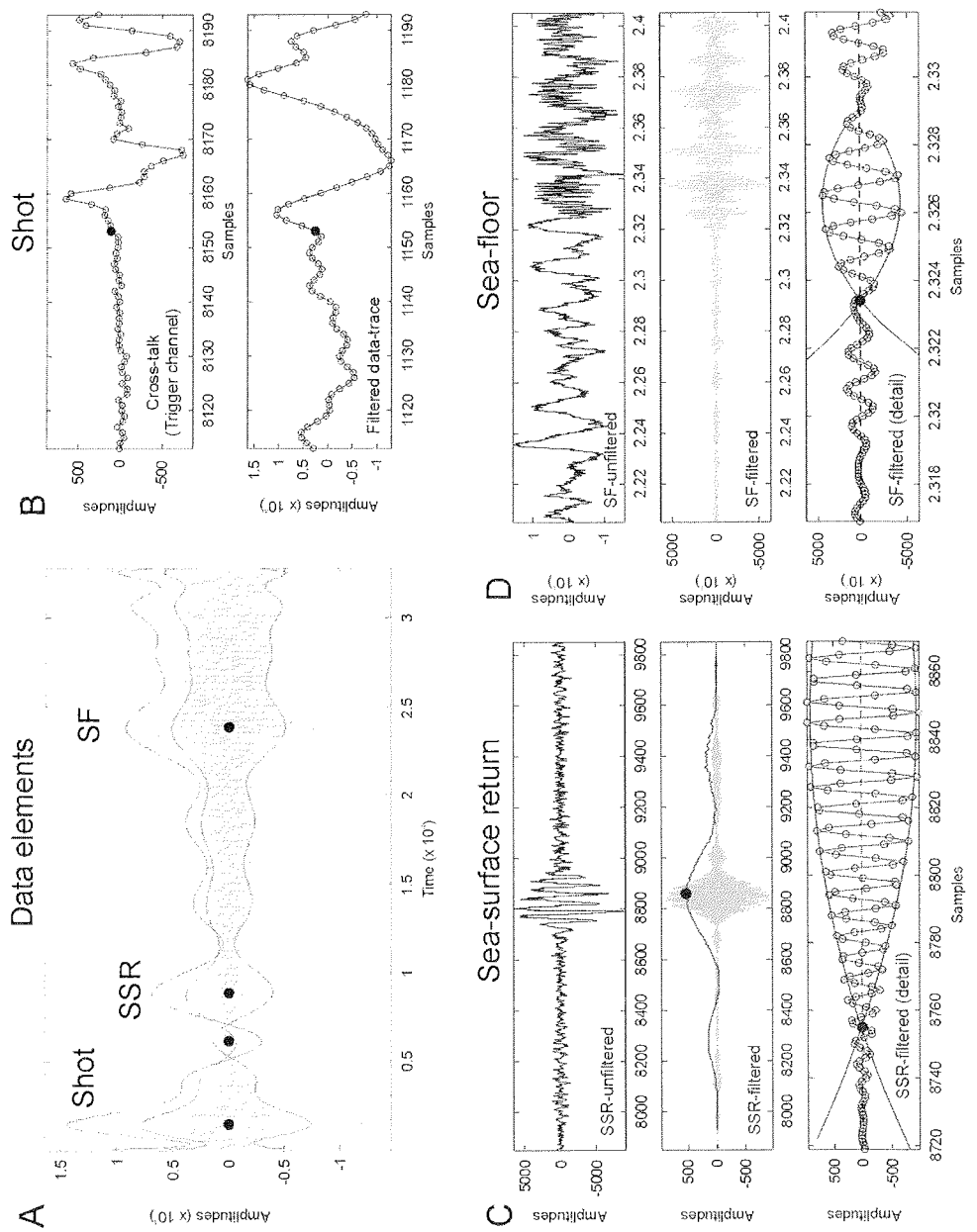

Fig. 3.1. **(A)** data element prelocation performed on a filtered trace using polynominal techniques (SSR, Sea surface return; SF, sea-floor). **(B)** the shot is detected using the cross-talk signal of the trigger channel. Note the clean signal structure before the shot in the trigger channel compared to the noise in the actual data channel. **(C)** picking of the sea-surface return on a filtered section. The initially picked location is extrapolated backward using polynomial based on amplitude maxima. **(D)** sea floor detection using routines similar to those for picking the sea-surface return.

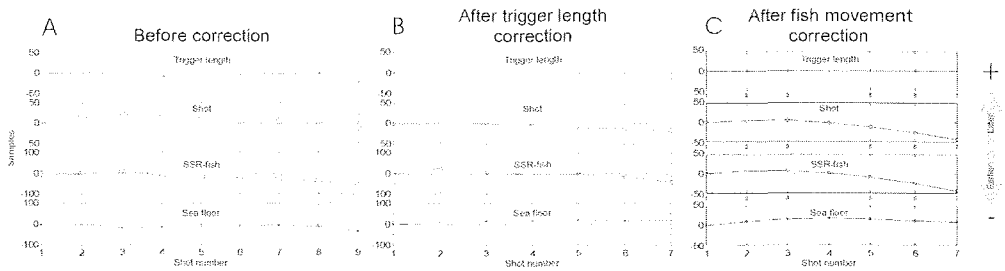

Fig. 3.2. (**A**) graphic representation of the result matrix before trigger length correction. Note that the irregular trigger spacing (line 1) is also seen in the timewise location of the sea floor (line 4). All picked times of the shot elements are expressed in samples relative to the detection of the element in shot one. (**B**) result matrix plot after trigger length equalization. Note the positive effect on the sea floor. (**C**) example of an approach to correct short-term fish movement (shot delay and fish depth are synchronized). Due to imprecise picking of the SSR this approach has not been used in the final processing.

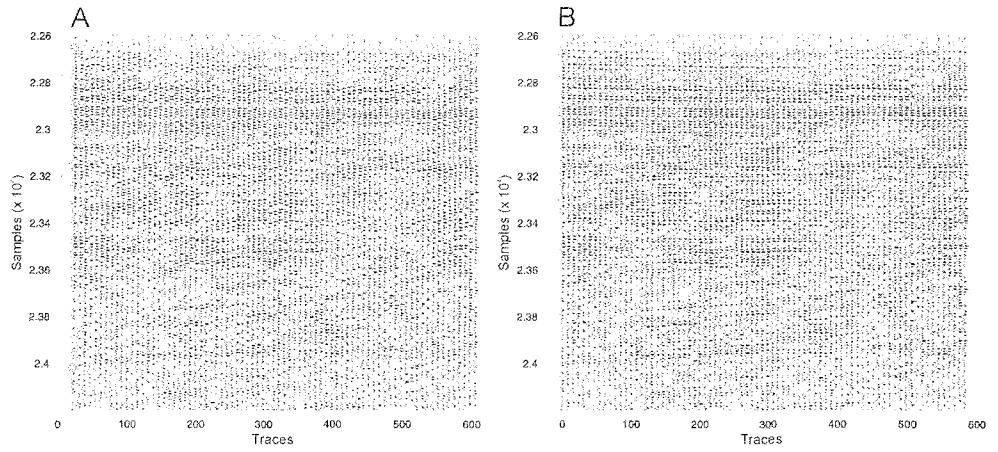

Fig. 3.3. The effect of the autocorrelation routine for minimizing residual static shifts on trigger length corrected traces (see Fig. 3.1, „Auto-correction of statics"). The correlation window is marked by rings: (**A**) one minute section before static correction. (**B**) the same section after static correction.

The data channel is too noisy to detect the actual time of boomer firing following the trigger. As seen in Fig. 3.3 the high voltage currents in the wires leading to the fish and within the fish itself create cross-talk between the data and trigger channel. However, detection of the shot onset can be achieved using the trigger channel data. The detection method used is a combination of time domain filtering, threshold, and slope criteria (Fig. 3.1B). The sea surface return and the sea floor are detected using high pass filters, threshold, and slope criteria, and complex backward polynominal extrapolation (Fig. 3.1C, D). Detection of the sea

floor is difficult in the Palmer Deep records since the transition between water column and sediment is continuous providing almost no impedance contrast even at high frequencies.

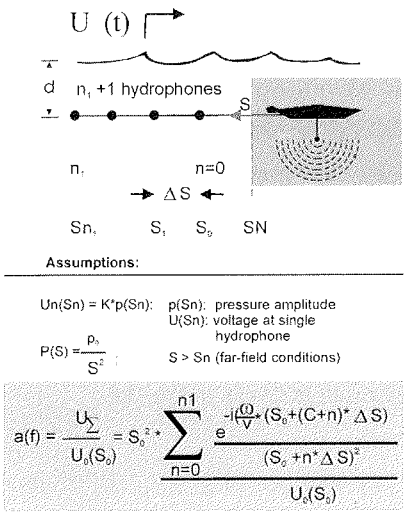

Fig. 3.4. Approach to restore the source signal from the 10 element streamer recording. A deconvolution function is defined allowing recalculation of the amplitudes for Hydrophone 1 ($U_0(S_0)$) when only the sum signal U_Σ is known. A source signal for each shot could be used in a shot by shot deconvolution.

The result of the detected shot elements is stored in a matrix and can be displayed for visual inspection of data quality and relative fish movement (Fig. 3.2). The greatest improvement of sea floor coherency is seen after the trigger correction (Fig. 3.2A). Efforts to correct short-frequency fish movements did not significantly improve the sea floor coherency (Fig. 3.2C). Therefore this part of the software was not generally used in the data processing, but an automated static noise reduction between traces was incorporated instead (Fig. 3.1B). This routine is called from the main program and performs windowed cross-correlation between low pass filtered traces. The width and timewise location of the correlation window can be selected via a user interface. The window is also capable of tracing climbing or descending reflectors linearly. This static treatment considerably improved cross-trace coherency (Fig. 3.3). Initial concerns that a purely successive autocorrelation function (starting with one trace and adjusting all following traces) would flattern all morphological features (personal communication A. Camerlenghi, 2000) have not been confirmed. A possible explanation is that even dominantly parallel stratified seismic sections have a certain degree of divergence. Finally the trigger corrected and statically corrected matrix is given

back to the main routine and a standard Seismic Unix header is created and saved together in *.SGY file format.

To summarize, the efforts of digital preprocessing are encouraging and unseen data (between trigger pulse and shot) may further extend the record. The resulting files can be fed into industrial packages (e.g.: SEISMOS) for further data processing. We have imported the one minute blocks into SEISMOS and applied an ascii trace header reconstruction, semimanual shifts of the blocks, band pass filtering, and spike deconvolution. All across-trace balancing and processing turned out to decrease lateral resolution. Improvements may be achieved by applying a true predictive shot by shot deconvolution using a reconstructed source signal from information provided by the direct arrival 10 hydrophone streamer signal. The required math has been made available in cooperation with G. Mörz (pers. communication 2000) and the result is shown in Fig. 3.4.

3.5.3 Example

To demonstrate the improvements of resolution achieved with the low cost digitizing and processing steps, a section of ~ 6 min lateral extent from the NE corner of Basin I is shown in Fig. 3.1A. The profile is located at the base of a steep canyon (Fig. 3.1, multibeam map). For comparison, the analog EPC record is shown in Fig. 3.1B: The well stratified basin fill to the SW of the profile displays better resolution than the analog section. Permitting reflectors spaced less than 40 cm apart to be distinguished within the top 5 ms below the sea floor.

In the middle of the section shown in Fig. 3.4, a slight elevated plateau a very faint tepee-like structure can be seen. The structure height is approximately 4 meters above the surrounding sea floor. The width of the structure is approximately 30 m. Below the structure a dike-like feature with weaker and irregular reflectors extends downward. The structure is interpreted as a miniature mud diapir with feeder channel. The geometry and feeder channel morphology are similar to those of mud volcanoes described by Brown and Westbrook (1988). From the cores it is known that the deeper sediments of Palmer Deep are very gas rich (ODP Leg 178 Shipboard Scientific Party, 1999, "Palmer Deep" chapter), and the origin of the mud diapir can be attributed to the overcompaction of fluid- and gas-rich sediment resulting from gravity flows from the steep basin sides. Fluid and gas escape in the middle of the Palmer Deep basin may be achieved by venting producing pockmarks. In the slump facies at the sides of the basin the buoyancy contrast introduced by mass flow may be large enough to initiate gas, fluid, and mud diapirism.

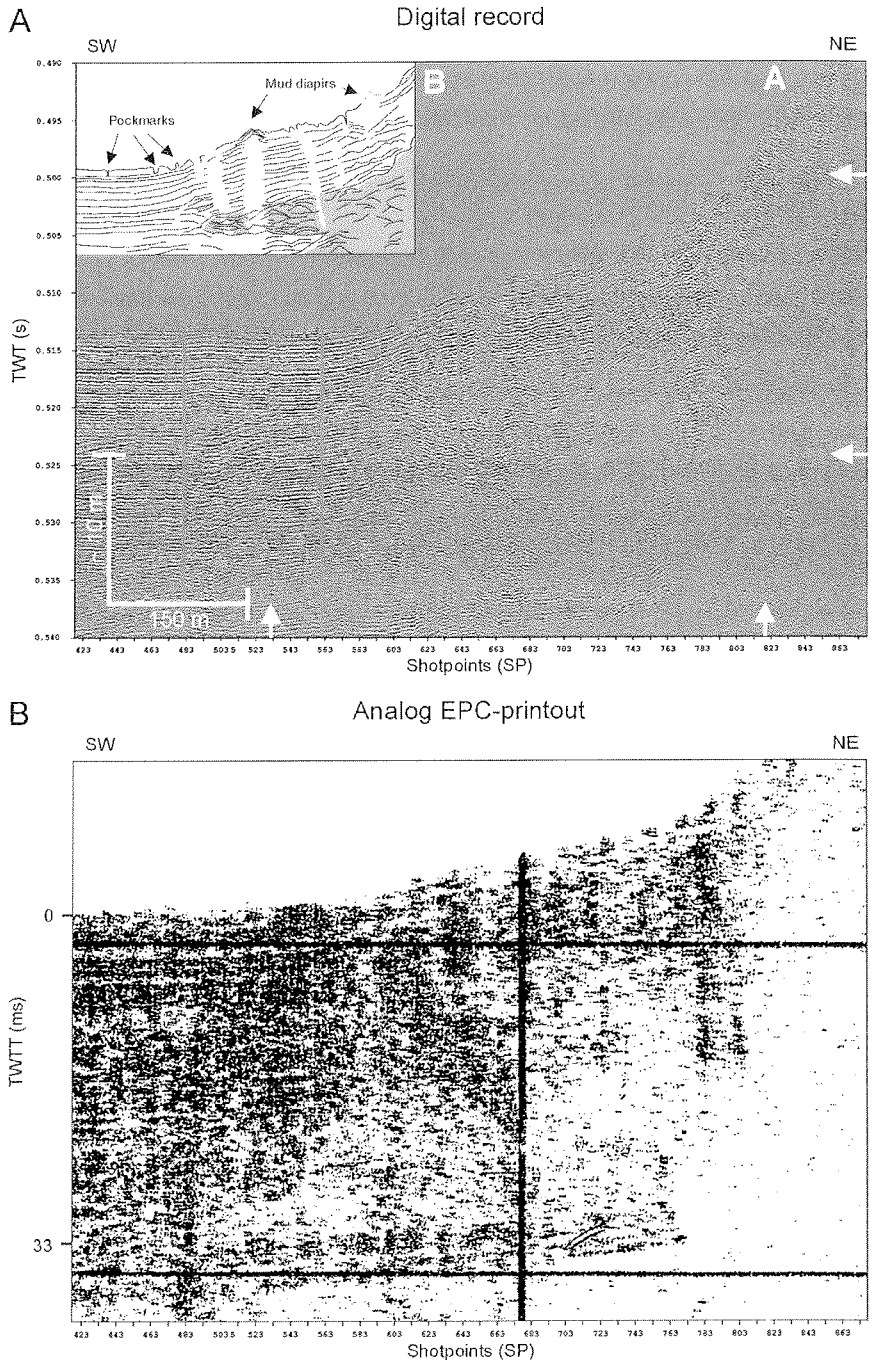

Fig. 3.1. (**A**) Example of digitized HDTB '98 data of the NE corner of Basin I, on the base of the basin wall. Note the improvements in resolution over the analog EPC-recorder printout shown in (**B**). The weak tepee structure above the sea floor is interpreted as a small mud volcano (height along section 4 m, width along section 30 m) with an underlying feeder channel.

3.6 Summary of Chapter 3 "Palmer Deep"

Palmer Deep provides a unique high resolution Holocene to latest Pleistocene record from the Antarctic Shelf. Sediments drilled on Site 1098 and 1099 can be divided into 5 climato-stratigraphic zones on the base of core logs and sedimentology. Core to seismic correlation is possible on the basis of single reflectors using synthetic seismograms and very high resolution single channel Deep Tow Boomer records. The strongest impedance contrasts are at the base of turbidites and at changes between massive, bioturbated and laminated units. The climato-stratigraphic zones have been mapped in profiles of Sub-Basins I and III (Fig. 3.2)

The digitization of the data significantly improved vertical (< 0.4 m) and horizontal resolution. The digitized data also yield information on the deeper units.

In a first digital processed section from Sub-Basin I a small scale mud diapir (4 m height, 30 m width, in ~1000 m water depth) with feeder dike, can be recognized in the slump and drape deposits at the base of the steep canyon slope.

The load of slumps and gravity flow deposits on the unconsolidated diatom ooze seems to be sufficient to overpressure the gas and fluid-rich sediment and to initiate diapirism. This process has never before described in extensional basins of the Antarctic shelf.

4 The West Antarctic Continental Rise

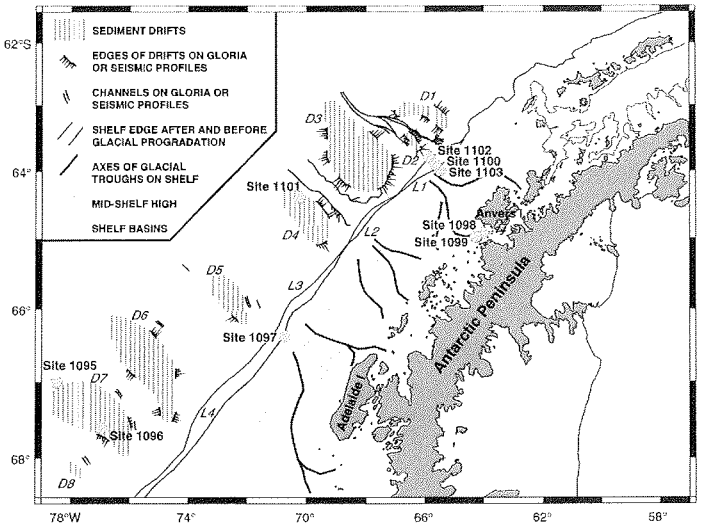

Fig. 4.1. Schematic figure of the hemipelagic sediment drift bodies along the West Antarctic Peninsula Margin and their relationship to glacial and tectonic elements on the West Antarctic Peninsula Shelf. Progradational lobes on the shelf represent areas of maximum sediment supply feeding small scale channels between drifts. These locations of focused sediment supply are a precondition for the drift growth on the rise below. Figure revised from Barker (1995).

4.1 Introduction

Drilling on the continental rise was conducted following the ANTOSTRAT approach that considers the rise sediments along the Antarctic Peninsula to be a distal but continuous recorder of ice sheet history and fine-grained equivalent of the slope foresets that are the direct product of ice advance and retreat on the shelf.

For further general information refer to the abstract and introduction of the accepted report (in press) „Fine-Fraction Grain-Size Distribution Data, Their Statistical Treatment and Relation to Processes, Site 1095 (ODP Leg 178, Western Antarctic Peninsula)" reproduced here as chapter 4.3.

The first part of this chapter provides a brief introduction to drift morphology and the sediments recovered at Site 1095 and Site 1096. The second part describes the internal drift architecture and its seismic sequences followed by physical data from the cores including the grain-size study. In the last part of the chapter new age and depositional models over time are presented and discussed in a paleo-oceanographic context.

4.1.1 Morphology and Oceanographic Setting

Large mounds on the continental rise along the Antarctic Peninsula Margin between 63°S and 69°S and within 200 km of the shelf break have been interpreted as sediment drifts, separated by turbidity current channels (Pudsey and Camerlenghi, 1998). The nine drift bodies are numbered progressively from NE to SW (Fig. 4.1). The average water depth of the drift crests lies between 2500 and 2800 mbsl. The channel systems separating the drifts are most likely connected to troughs between progradating depositional lobes on the shelf, even though no major deep sea canyons intersect the shelf edge and upper slope (Barker and Camerlenghi, 1999). Drifts 6 and 7 are the largest (SW corner of Fig. 4.1) and are located off Marguerite Bay. They attain elevations of 700 m above the surrounding sea floor and reach more than 130 km outward from the shelf edge. The width of a drift typically exceeds 50 km. With few exceptions the drift bodies are asymmetric along their SE-NW axis with a steeper and rougher side toward the shelf and a more gently dipping smooth side toward the ocean basin (Rebesco et al., 1997). Schematically, the SE-NW long axis cross-section can be seen as an elongated asymmetric triangle with the highest point ("drift-crest") toward the shelf (Fig. 4.2C, D). The gently dipping side merges gradually with the lower continental rise and the abyssal plain. The steeper side is always separated from the continental slope by a sea-floor trough or channel (Fig. 4.2C, D). The cross-sectional view of the modern drift bodies is also asymmetric (Fig. 4.1B, C, D and Fig. 4.2B). Seismic lines parallel to the margin and detailed topographic maps (Fig. 4.1) show a steeper side to the SW and a more gentle flank to the NE. This asymmetry is attributed to bottom currents with a net westward component. This is most likely the AABW (see chapter 1.2) which originates in the Weddell Sea and flows north through deep gaps in the South Scotia Ridge and then westwards along the Antarctic Peninsula Margin (Nowlin and Zenk, 1988; Pudsey and Camerlenghi, 1998). Recent one year lasting current measurements 8 m above the seabed on both sides of Drift 7 revealed SW directed bottom currents with average speeds around 6 cm/sec and maxima sometimes exceeding 14 cm/sec (Camerlenghi et al., 1997; ODP Leg 178 Shipboard Scientific Party, 1999). These modern currents are considered to be too weak to cause significant erosion of continental rise sediment, though they may hold fine silt and clay in suspension (Pudsey and Camerlenghi, 1998).

The size and seaward extent of the drift bodies in the study area increase toward the SW. This can be explained by three factors:

- The Antarctic Peninsula becomes broader toward the SW, hence the sediment supply for the rise increases.
- The margin is progressively older toward the SW (see chapter 3, Fig. 3.1), hence the time available for deposition on the rise has been longer in the SW.
- A predominantly SW directed current removes material from the NE and successively deposits it toward the SW. This, together with a decrease in current strength toward the SW due to growing distance from the Weddell Sea and widening of the Ocean Passage, could lead to thicker sediment accumulations over time.

The continental rise of the Antarctic Peninsula is affected by seasonal sea ice cover which restricts open-water conditions to austral spring and summer. The study area Drift 7 is, on average, ice free for about 8 months a year (Parkinson, 1994).

4.1.2 Drift Lithostratigraphy at Site 1095, Drift 7

Site 1095 lies in 3840 mbsl on the lower NE flank of Drift 7 and is the more distal of the two Sites (1095 and 1096) drilled (Fig. 4.1, Fig. 4.2C, Fig. 4.1). Lithologies are here described only for Site 1095. The stratigraphic units found there are also representative of the expanded sediment section cored at Site 1096,which is more proximal to the source. Refer to the Site 1095 and 1096 lithostratigraphy chapter for detailed core descriptions (ODP Leg 178 Shipboard Scientific Party, 1999).

Unit I (0-50 mbsf)

The upper 50 m of sediments at Site 1095 consist of alternations of laminated and extensively bioturbated brown diatom-bearing silty clays with gray less biogenic more terrigenous, massive sections typically richer in IRD. These alternations are seen as the stratigraphic expression of successive glacial and interglacial cycles (ODP Leg 178 Shipboard Scientific Party, 1999; Pudsey and Camerlenghi, 1998). The lower part of Unit I (also labeled Unit Ib, ODP Leg 178 Shipboard Scientific Party, 1999) is coarser; laminated silty clay layers together with IRD become more frequent. The shipboard biostratigraphy and magnetostratography indicate a Quaternary age for Unit I (ODP Leg 178 Shipboard Scientific Party, 1999). Sedimentation rates are low and average around 2.5 cm/ka.

Unit II (50-435 mbsf)

Unit II is of Pliocene to late Miocene age. It is characterized by sharp-based, graded, laminated fine sands and silts and laminated silty clays, interbedded with massive, structureless, intensely bioturbated zones. The IRD content is higher in the massive layers. Again the alternating nature of the sediments is interpreted as glacial and interglacial cycles. Sedimentation rates (5-7cm/ka) are higher than in Unit I. A coarse layer near the top of the unit is interpreted as a debris flow deposit (ODP Leg 178 Shipboard Scientific Party, 1999), which may have caused significant erosion of underlying stata (hiatus 1, see chapter 4.4 for a discussion of suggested age models).

Unit III (435mbsf to drilled depth)

Sediments below 435 m do not show the distinct cyclicity of Unit I and II. The nonbioturbated parallel laminated silt and claystones are interpreted as thin bedded turbidites. Unit III has a late to middle Miocene age with the highest average sedimentation rates of 12 cm/yr. Noteworthy are small cm thick zones of massive chert indicating the onset of opal dissolution and redistribution at the base of the hole.

4.2 Seismostratigraphy and Drift Architecture

The following summary of drift architecture and Leg 178 core-seismic correlation is based on surveys of the Programma Nazionale di Ricerche in Antartide (Italy) (PNRA) carried out in 1992 and 1995. Profiles for Drift 7 (Sites 1095 and 1096) are 60-fold (1992 survey: 30-fold) stacks of common depth point (CDP) gathers spaced 12.5 m (1992 survey: 25m) apart. Furthermore the following account draws heavily on work by Rebesco et al. (1996; 1997), Volpi et. al. (2001)[12] and the ODP Leg 178 Shipboard Scientific Party (1998) for seismostratigraphic unit names and interpretations of drift evolution.

[12] Volpi, V., Camerlenghi, A., Moerz, T., Corubolo, P., Rebesco, M., and Tinivella, U., in press. Data report: Physical properties relevant to seismic stratigraphic studies, continental rise Sites 1095, 1096, and 1101, ODP Leg 178, Antarctic Peninsula. *In* Barker, P.F., Camerlenghi, A., Acton, G.D., and Ramsay, A.T.S. (Eds.), *Proc. ODP, Sci. Results*, 178, College Station, TX (Ocean Drilling Program).

4.2.1 Core-Based Seismic Models[13]

4.2.1.1 Relevant Core and *In situ* Physical Data of Site 1095

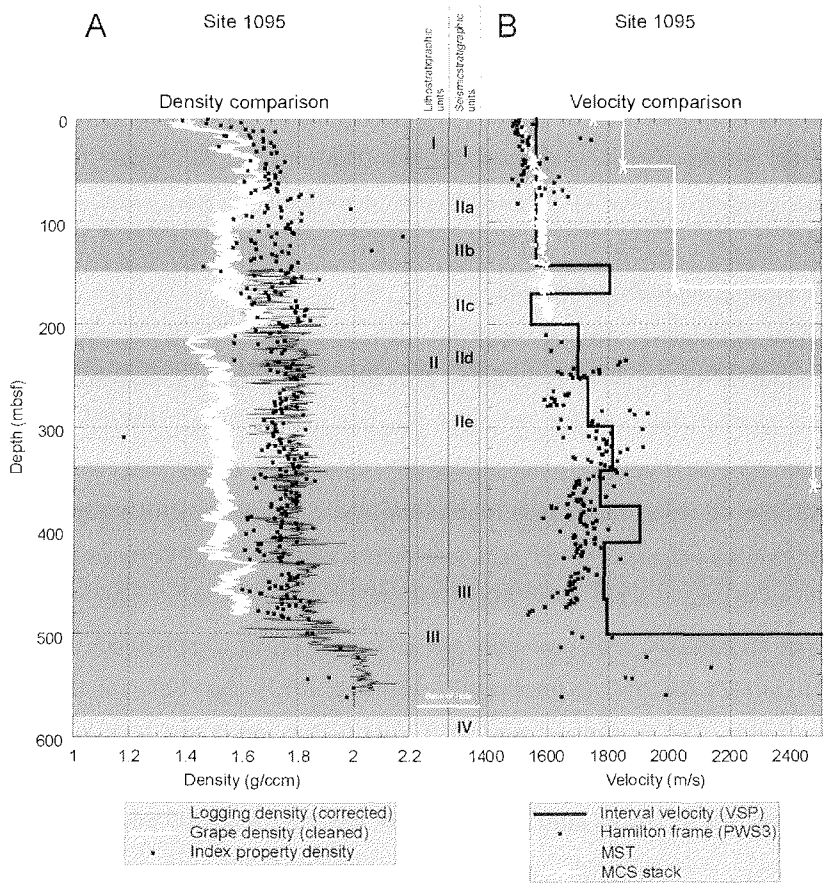

Fig. 4.1. (**A**) comparison of different density data sets for Site 1095. (**B**) compilation of MST, downhole (VSP), and stacking velocities (MCS; Volpi et al., 2001) velocities used for different modelling approaches, Site 1095. Lithological unit boundaries are marked according to the definitions in chapter 4.1.2 and Tab. 4.1. Note the increase of in-situ velocity (MCS and VSP) at ~160 mbsf that is not recorded in the laboratory data.

[13] Parts of this chapter are modified from: Shipboard Scientific Party, 1999. Site 1095 and Site 1096 (sub-chapter: „Seismic Stratigraphy"). *In* Barker, P.F., Camerlenghi, A., Acton, G.D., et al., *Proc. ODP, Init. Repts.*, 178, 1–173 [CD-ROM]. Available from: Ocean Drilling Program, Texas A&M University, College Station, TX 77845-9547, U.S.A. Authorship of sub-chapter „Seismic Stratigraphy": Escutia, C. & Moerz, T.

Bulk densities have been derived from MST GRAPE measurements with a 2 cm spatial resolution, index properties measurements (1.5 m spatial resolution), and lithodensity logging data (High Temperature Litho-Density Sonde, measurement separation ~15 cm, Fig. 4.1). The results from index properties measurements agree very well with the *in situ* properties from the downhole logs. Compared to these two data sets, the MST GRAPE densities generally show lower values. This difference increased dramatically (~0.3 g/cm 3) when the coring method changed from APC to XCB at 205 mbsf at the top of Core 1095B-14X, probably as a result of the larger air/water gap between liner and core and the higher degree of core disturbance produced by the XCB. Two different density models have been tested, using (1) only index properties data and (2) a combination of GRAPE density (0-150 mbsf) and downhole logging data (150-560 mbsf).

Three differently derived velocities are available. The MST logger provided continuous data at 4 cm spatial resolution to 200 mbsf, within the APC-cored part of the holes and sparse data between 200 and 280 mbsf. Single Hamilton Frame (PWS3) measurements (usually one per core section) provide high-quality data for the deeper parts of Site 1095. The MST data, interval velocities derived from a down-hole seismic experiment (using the WST and a 2500 cm^3 two-chamber GI air gun), and the Hamilton Frame (PWS3) measurements are plotted for comparison in Fig. 4.1B. Most of the MST-derived *P*-wave velocities are slightly higher than the interval velocities from the downhole seismic experiment. The latter are believed to provide the most accurate results (Hardage, 1985). Two different velocity models have been tested. The first model uses MST data (0-209 mbsf) and Hamilton Frame data (209-543 mbsf); the model also combines MST and Hamilton Frame data but from different depth intervals (PWS3 = 0-80 mbsf, 209-560 mbsf, and MST = 80-209 mbsf).

4.2.1.2 Source Signals

Two differently derived signals of the GI-gun used during the site survey were employed for the seismic models presented here. (1) Six randomly chosen traces were extracted from a digital far-field recording of multiple firing of the gun in water (recording distance ~300 m) (Fig. 4.1C). The signals were brought in phase, then stacked and resampled at 0.5 ms using a cubic interpolation function (Fig. 4.1A). The signal (wavelength ~ 10 ms) contains a continuous energy spectrum up to 350 Hz (Fig. 4.1B). (2) A second source signal was generated by extracting strong, coherent sea floor reflections from the MCS profile across the drill site. The signal is derived as for the far-field signature above. The sea floor signal has a much longer wavelength (40 ms) and consists of a negative onset followed by two positive

excursions and a final negative one (Fig. 4.1D). The derived signal has a dominant frequency range of 10 to 250 Hz (Fig. 4.1E). Differences between the frequency spectra of the signals can be explained by the low-pass filter effect of a long path through seawater and the uppermost sea floor sediments and by antialias filtering applied during data acquisition.

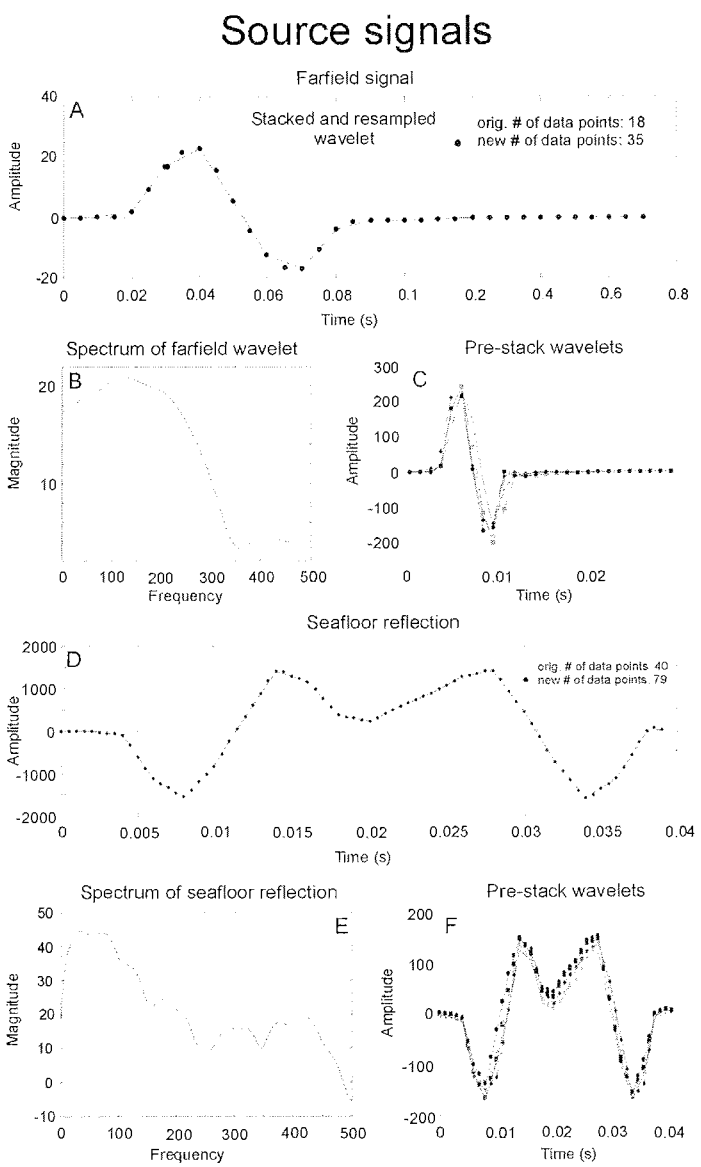

Fig. 4.1. Generator Injection gun (GI-gun) source signal characteristics. **(C)** matched far-field wavelets prior to stacking. **(A)** stacked and resampled far-field wavelet used for convolution. **(B)** spectrum of the far field source signal shown in **(A)**. **(D)** matched sea floor reflections prior to stacking. **(A)** stacked and resampled sea floor used for convolution. **(B)** spectrum of the sea floor source signal shown in **(A)**.

4.2.1.3 Vertical Seismic Profiling (VSP) and Traveltime Depth Models

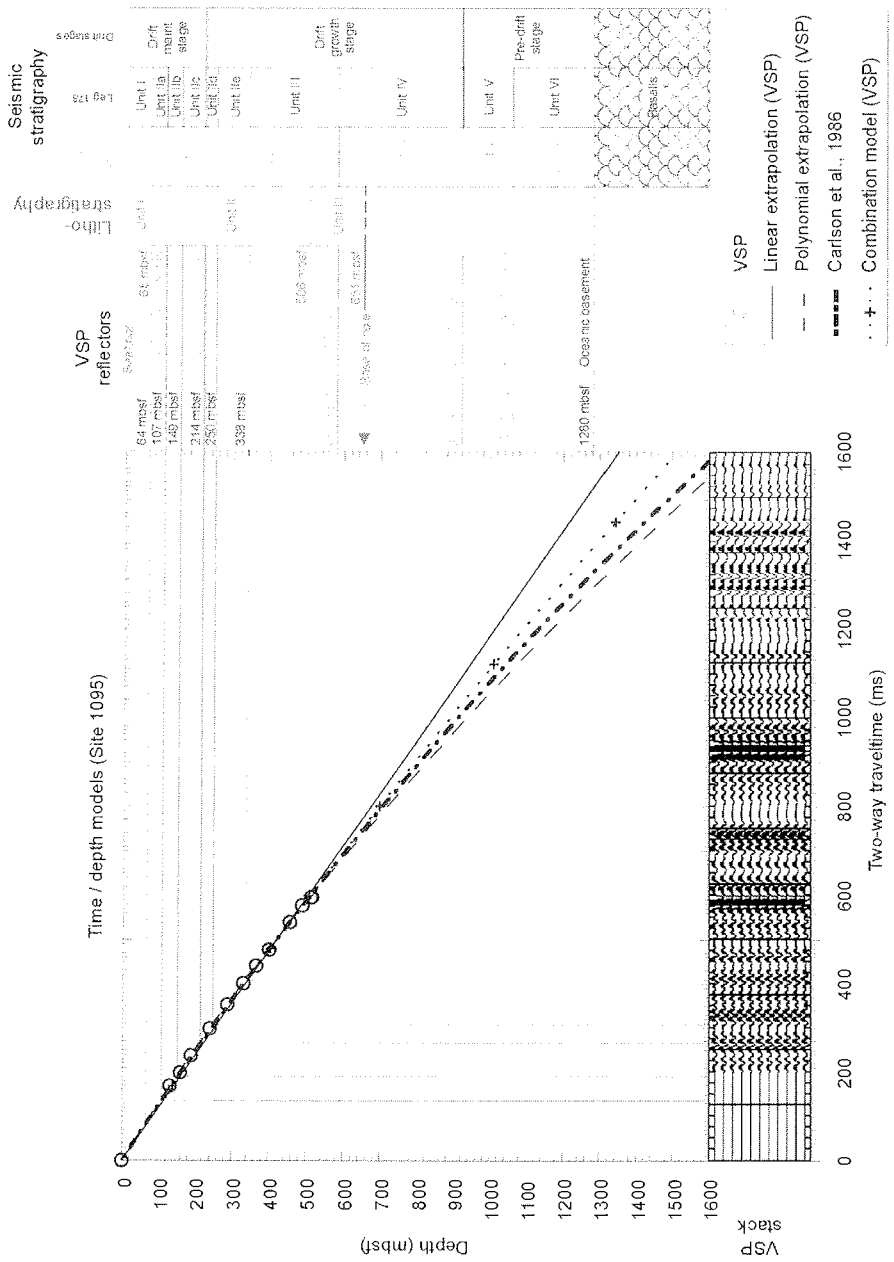

Fig. 4.1. VSP traces, major lithological and seismostratigraphic unit boundaries follow the definitions of ODP Leg 178 Shipboard Scientific Party (1999) and are compared to the units originally defined by Rebesco et al. (1997) and with traveltime depth models for Site 1095. The empirical approximation after Carlson et al. (1986) (Depth = -3.03*ln(1-0.52*(OWTT(ms)/1000))*1000) and the observed and extrapolated traveltimes from the VSP experiment (Depth = =745.97*(OWTT(ms)/1000)^2+1500.43*(OWTT(ms)/1000) are in good agreement.

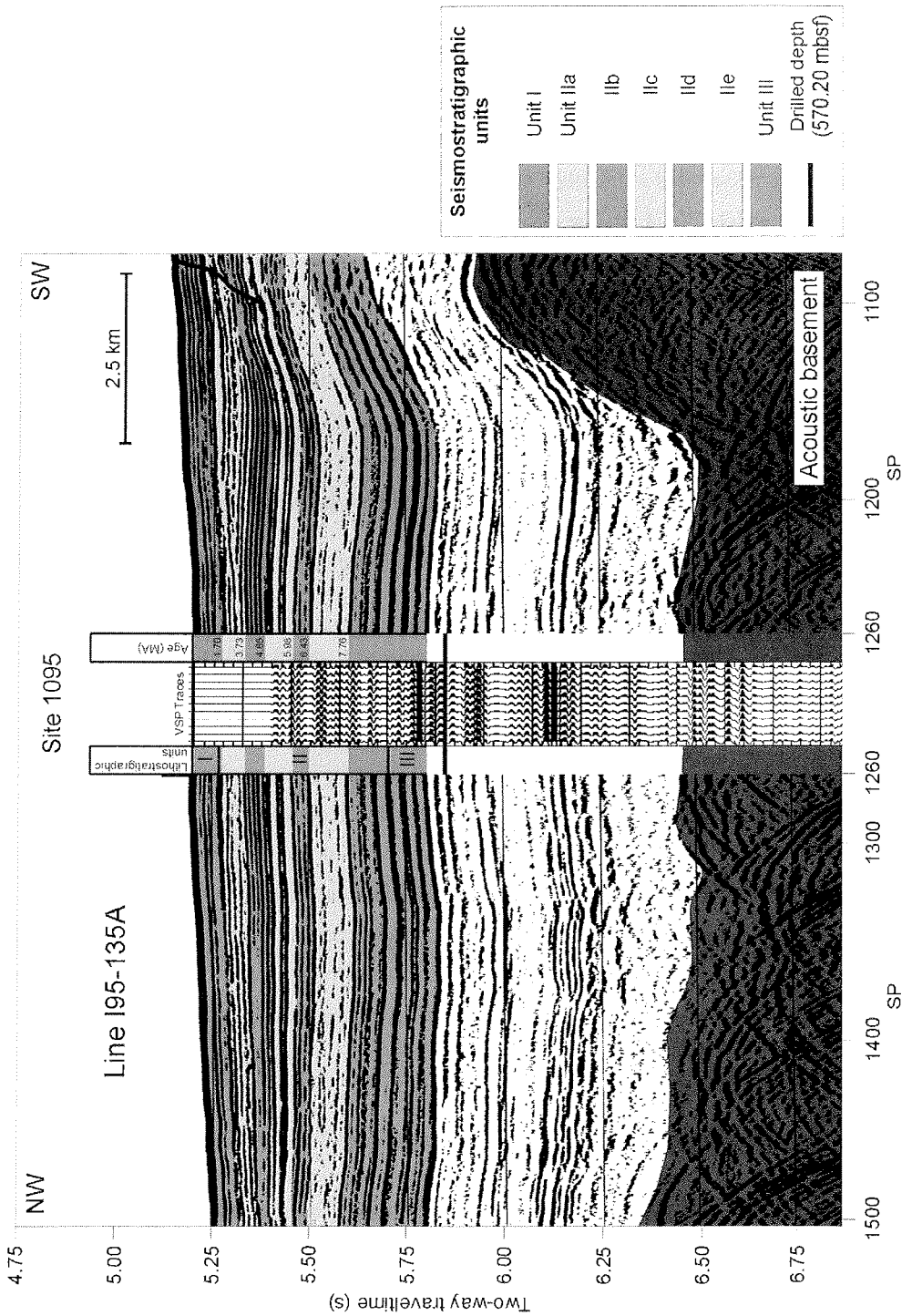

Fig. 4.2. Correlation between on-site multichannel seismic data (Line I95-135A) and the vertical seismic profile (Volpi et al., 2001) for Site 1095. The approximate location of the profile is given in Fig. 4.1A.

The results from 12 geophone *in situ* velocity checkshot stations of a downhole seismic experiment have been processed to a VSP section on board the ship. Later the recorded data were reprocessed and improved (Volpi et al., 2001). Additionally, the traveltime information was used to compare a standard traveltime/depth relationship (Carlson et al., 1986) to a second-order polynomial extrapolation, to a linear extrapolation, and to a combined linear-polynomial model (Fig. 4.1). The polynomial model, the Carlson et al. (1986) relationship, and the combined linear-polynomial model show good agreement and allow the time to depth conversion of seismostratographic unit boundaries and the oceanic basement reflectors at 1290 ms TWTT (corresponding to 1280 mbsf; Fig. 4.1). Furthermore the VSP reflectors (Volpi et al., 2001) have been compared to the multichannel profile. Even though the low number of stations (12) and their wide spacing (average: 33 m) prevented a correlation in the upper part of the section most of the stronger reflectors of Units II-VI and the basement reflectors are present and allow a tight VSP to profile correlation (Fig. 4.2).

4.2.1.4 Synthetic Seismograms

The raw velocity and density data were carefully evaluated and corrected for obvious artifacts. The 1.5 m core section edge effects (in *P*-wave velocity and density data) and density lows caused by core disturbance were removed from the MST data. The velocity and density data were preprocessed and cleaned in 20 m sections using the method described in the Excursus (chapter 7.2). Special care was taken with anomalous density values within the downhole logging data that were caused by overwidened hole sections which resulted in failure of the applied caliper correction. These artificial density lows were removed manually. Model A data (index properties density, PWS3 and MST velocity; Fig. 4.1) were resampled at a 0.8-m spatial resolution. For Model B (logging and MST density, PWS3 and MST velocity; Fig. 3.1), the data resolution was degraded to 0.6-m spacing. Each acoustic impedance model was convolved with the far-field and sea floor signals. Velocity/density data, impedance curve, reflectivity coefficients, two unfiltered synthetic seismograms are displayed for each model (Model A: Fig. 4.1; Model B: Fig. 3.1). An approximate depth axis is displayed next to the time scale to allow traveltime/depth conversions. The most striking differences between the synthetic traces were not caused by differences in the velocity and density data but by the different source signals used for the convolution. The higher frequency content of the far-field signal and its shorter signal length result in a higher frequency, more detailed synthetic trace. Fig. 4.3 depicts a comparison of the two trace spectra from Model A and the corresponding

spectra of the signals used. Since shape and frequency range are nearly identical, there was no major loss in information during data subsampling and interpolation.

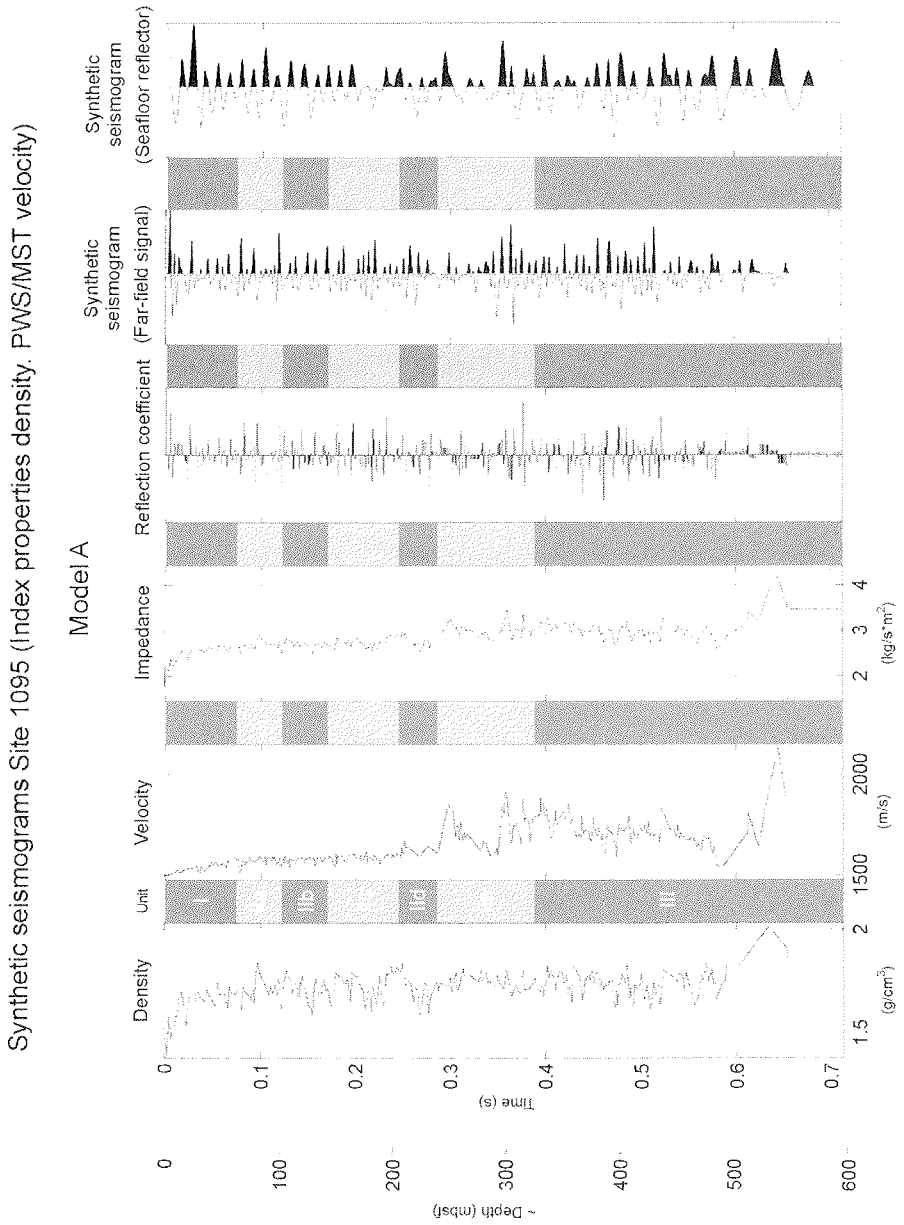

Fig. 4.1. Cleaned (see chapter 7.2) and resampled acoustic properties at Site 1095. Model A: Density: Index Properties, Velocity: MST (0-209 mbsf), PWS (209-543 mbsf) and the synthetic seismogram trace (calculated with the software "synseis", chapter 7.1.7) nsing the GI-gun far-field signal and the sea floor reflection. The data set is presented in the time domain; the depth scale is only approximate.

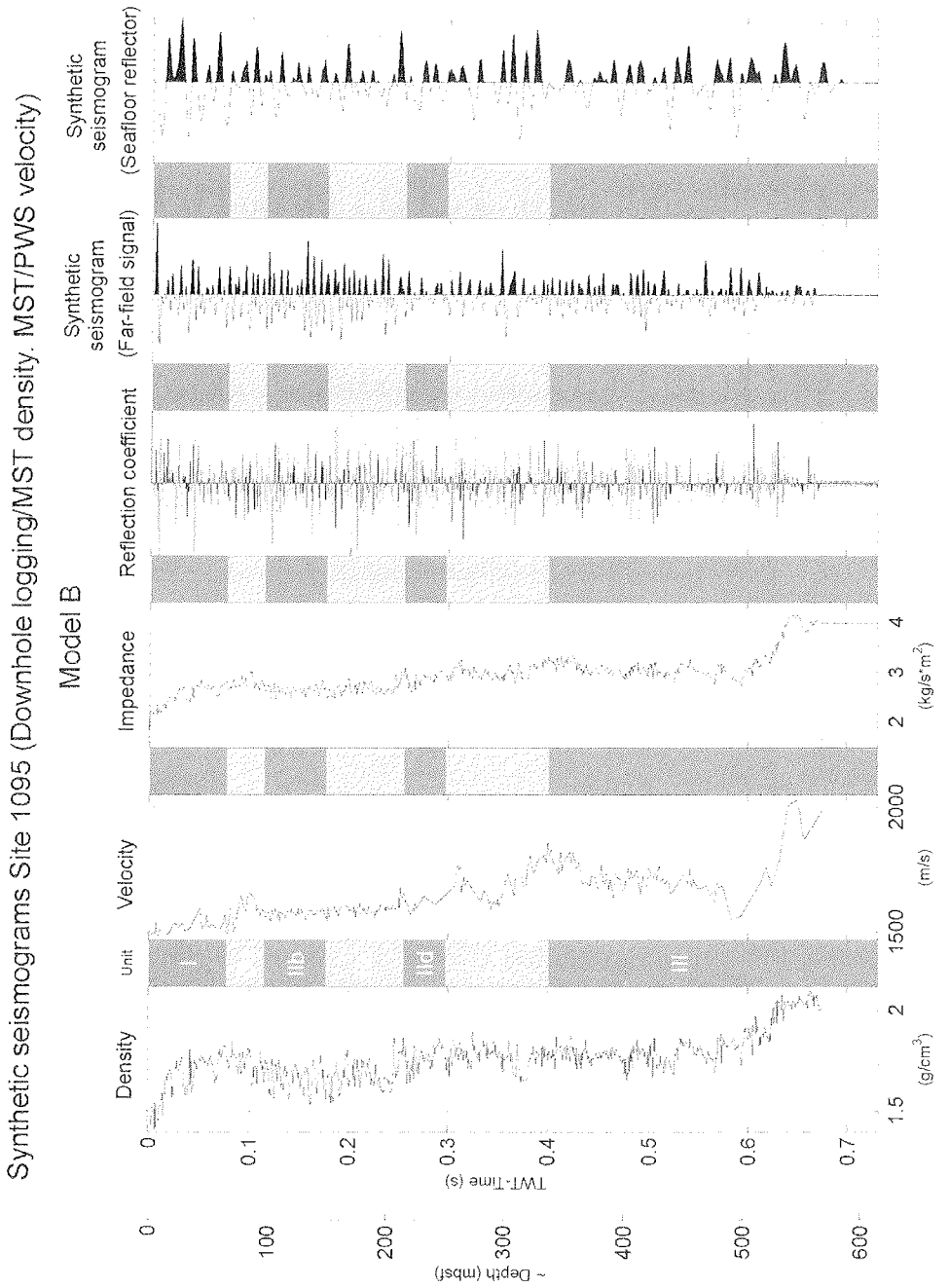

Fig. 4.2. Cleaned (see chapter 7.2) and resampled acoustic properties at Site 1095. Model B: Density: MST (0-150 mbsf), Downhole Logging (150-560 mbsf), Velocity: PWS(0-80 mbsf, 209-560 mbsf), MST (80-209 mbsf) and the synthetic seismogram trace (calculated with the software "synseis", see chapter 7.1.7) using the GI-gun far-field signal and the sea floor reflection. The data set is presented in time domain, the depth scale is only approximate.

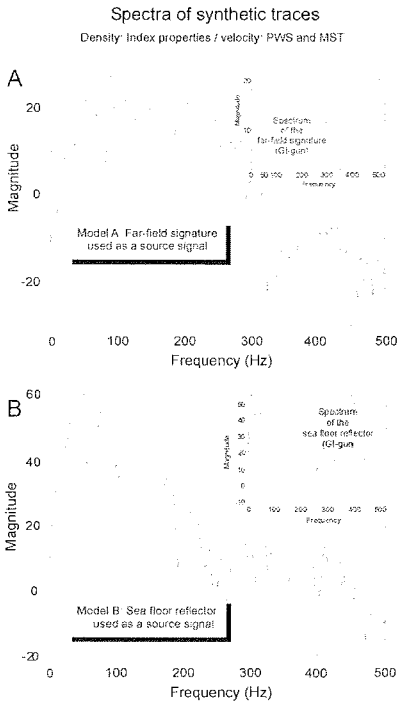

Fig. 4.3. Comparison of the input and output frequency spectra of Model A. **(A)** Frequency spectra of the unfiltered synthetic trace based on acoustic Model A and the GI-gun far field signature. Inset: frequency characteristic of the source signal (GI-gun). **(B)** Frequency spectra of the unfiltered synthetic trace based on acoustic Model A and the stacked sea floor signal. Inset: frequency characteristic of the stacked sea floor wavelet.

4.2.1.5 Evaluation of the Synthetic Models

All four calculated synthetic traces were interpolated to 1-ms resolution (1000 Hz) and then filtered using a high-order, zero-phase equiripple band-pass filter (pass band = 20-110 Hz, attenuation = 60-70 dB, filter order = 170-220; Fig. 4.1). Five of these traces are shown together with 42 traces of the field seismic profile (Fig. 4.2, Fig. 4.3). A zero-phase Butterworth band-pass filter (pass band = 10-110 Hz) and a 150-ms automatic gain recovery window were applied to the sorted and stacked data set. Additionally, the total time window and the delay were reduced, and the 2-ms data were interpolated to 1 ms to match the time resolution of the synthetic trace. The optimal filter parameters were adjusted to values used during processing of the precruise survey data. Different amounts of time-invariant gain were applied to equalize the overall amplitude appearance of the field and synthetic traces. Possible tie lines connect synthetic and survey reflectors. Because of polarity changes within the synthetic traces, correlation between positive and negative half-cycles are possible.

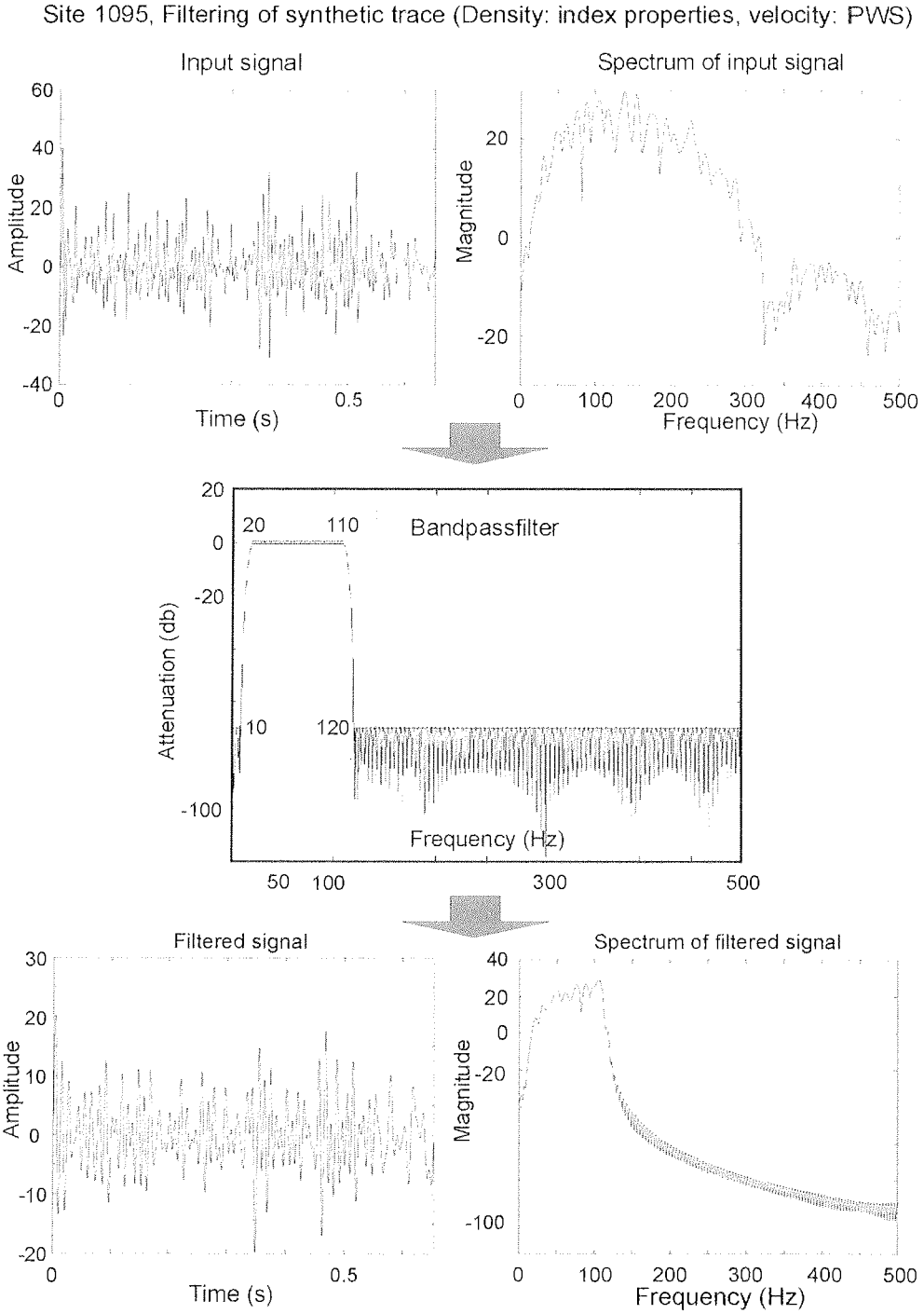

Fig. 4.1. Characteristics of the filter used on the synthetic trace of Model A (far-field source signal) to fit the average characteristics of the GI-gun multichannel profiles. Similar processing was done on the synthetic traces of Model B.

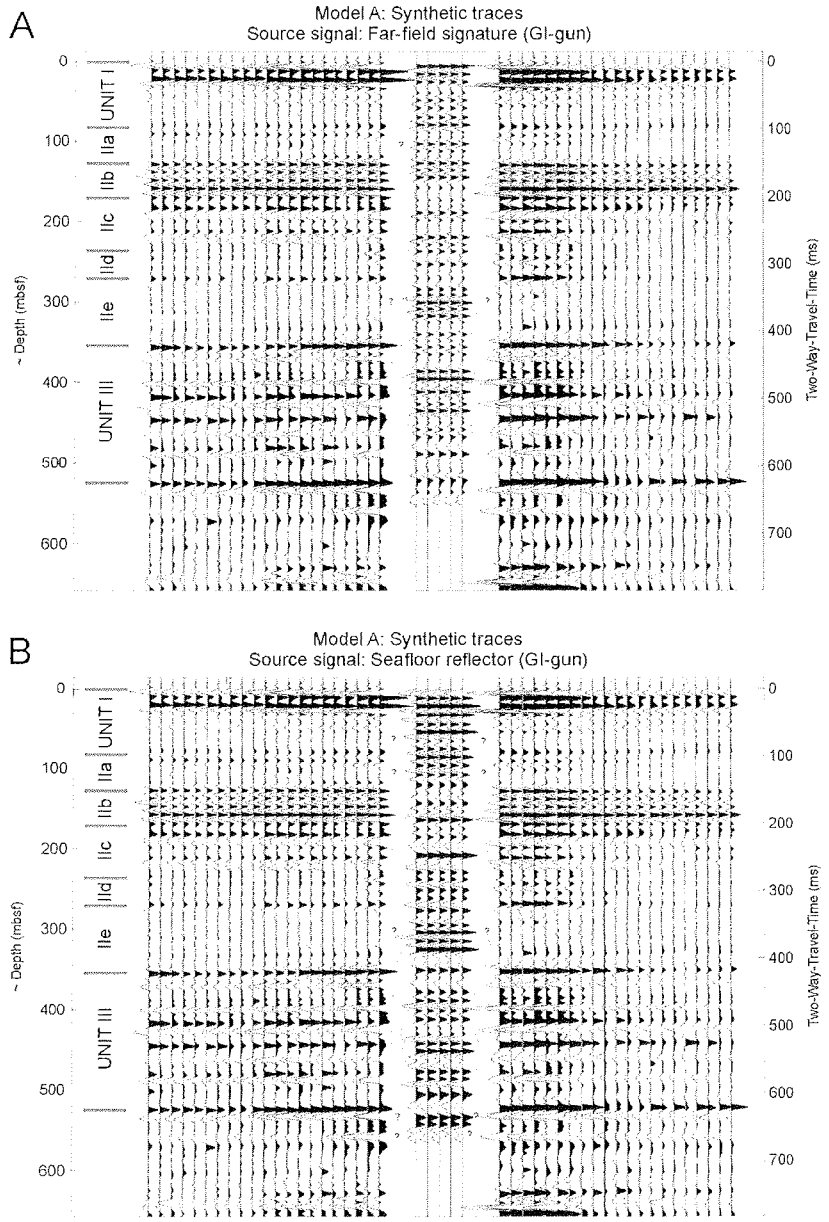

Fig. 4.2. Comparison and correlation of the synthetic and seismic traces for Model A (Density: Index Properties, Velocity: MST (0-209 mbsf), PWS (209-543 mbsf)) **(A)** far-field source signal, **(B)** sea floor reflector and digital data of survey line I95-135A. Model A using the sea floor reflection produces the best fit of synthetic traces to the seismic data.

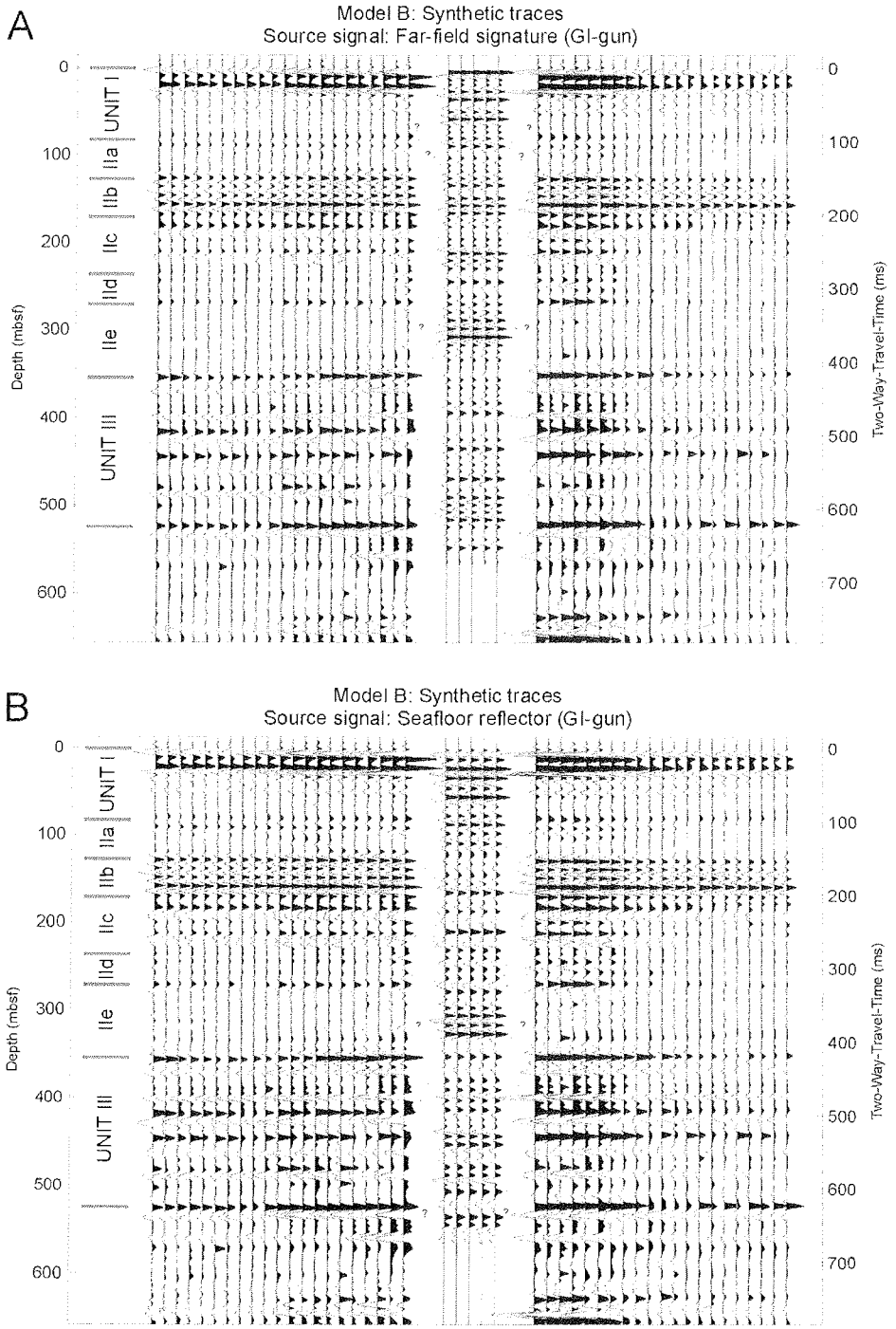

Fig. 4.3. Comparison and correlation of the synthetic and seismic traces for Model B (Density: MST (0-150 mbsf), Downhole Logging (150-560 mbsf), Velocity: PWS(0-80 mbsf, 209-560 mbsf), MST (80-209 mbsf)) **(A)** far-field source signal, **(B)** sea floor reflector and digital data of survey line I95-135A.

Each correlation approach has its own problems where there is poor or no correlation with the survey data. For example, a zone of strong reflections between 300 and 350 mbsf in all four synthetic runs does not fit the survey data.

Best fits have been found for earth Model A (index properties density and PWS3 velocity) in combination with the sea floor reflection as a source signal (Fig. 4.2B). Most of the important reflectors and seismostratigraphic boundaries show up within the synthetic seismograms. However, both velocity models (A, B) permit accurate time/depth conversion. The two-way traveltime to the base of Hole 1095B (~654 ms) is defined within 20 ms (Tab. 4.1).

Recent studies (Volpi et al., 2001) carefully reevaluated the density and velocity information and improved the resulting synthetic traces and their fit to the reflection data. Nevertheless significant misfits remain; the problems and a possible explanation are further discussed in chapter 4.5.

4.2.2 Drift Architecture, Seismic Data Integration and Interpretation

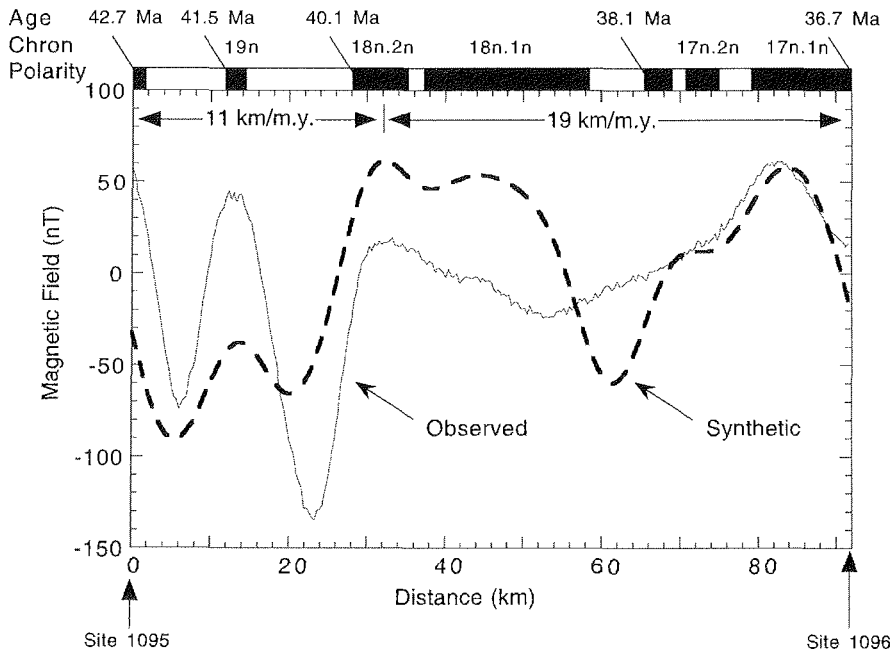

Fig. 4.1. Magnetic total-field profile collected during transit between Sites 1095 and 1096. Identified magnetic anomalies show that basement age at Site 1095 is 42.7 Ma and at Site 1096 is 36.7 Ma (time scale of Cande and Kent, 1995, courtesy: ODP Leg 178 Shipboard Scientific Party, 1999).

4.2.2.1 Basement and Pre-Drift Stage

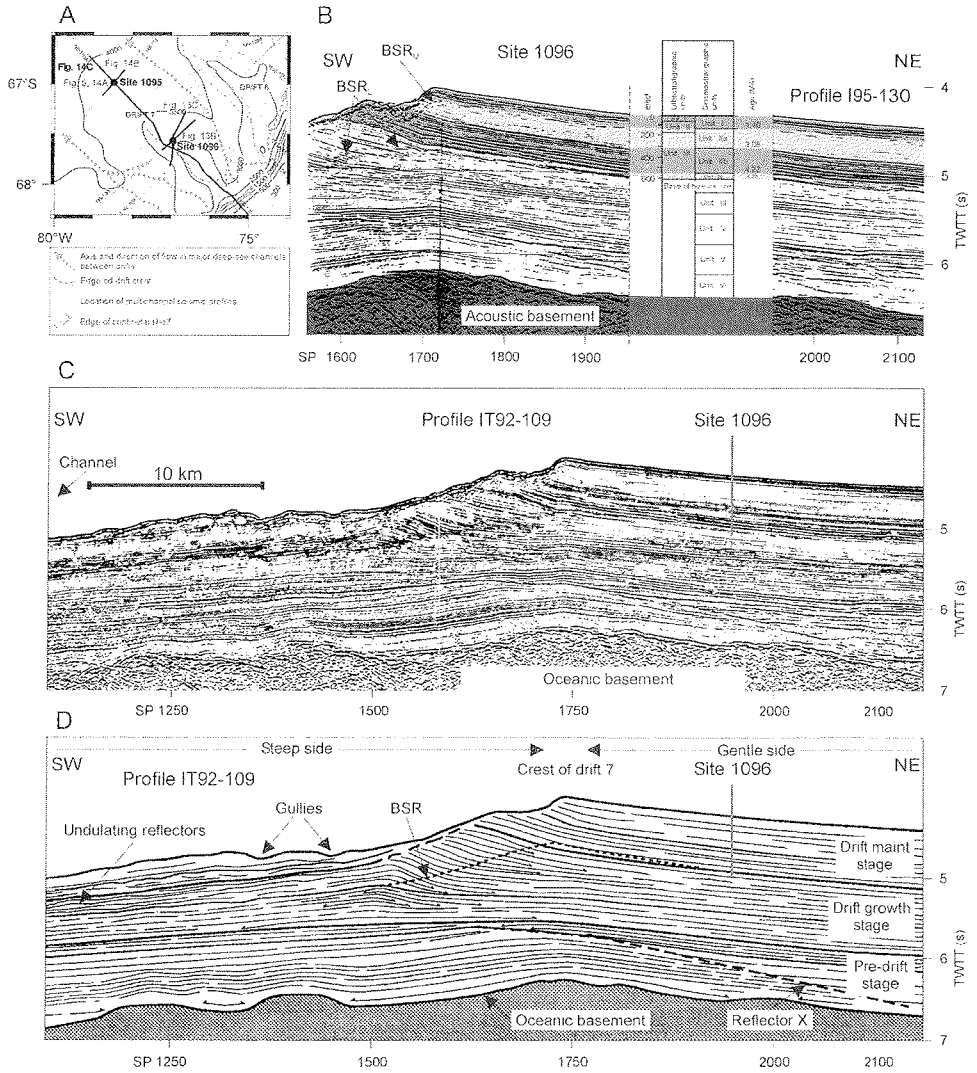

Fig. 4.1. Seismic profiles across Drift 7, parallel to the margin. **(A)** Location map of seismic profile sections. **(B)** Profile I95-130 across Site 1096, parallel to the margin. Lithostratigraphic and seimostratigraphic boundaries are shown together with an approximate depth and age scale. Note the upper and lower bottom simulating reflectors (BSR), The upper BSR was first noted by ODP Leg 178 Shipboard Scientific Party, 1999. It had not been identified on the 1992 profiles **(C,D)**. **(D)** schematic interpretive line drawing of C with the interpretation of various drift stages (Rebesco et al., 1997; 1996). Possible explanations for the origin of "Reflector X" are discussed in chapter 4.5.2.

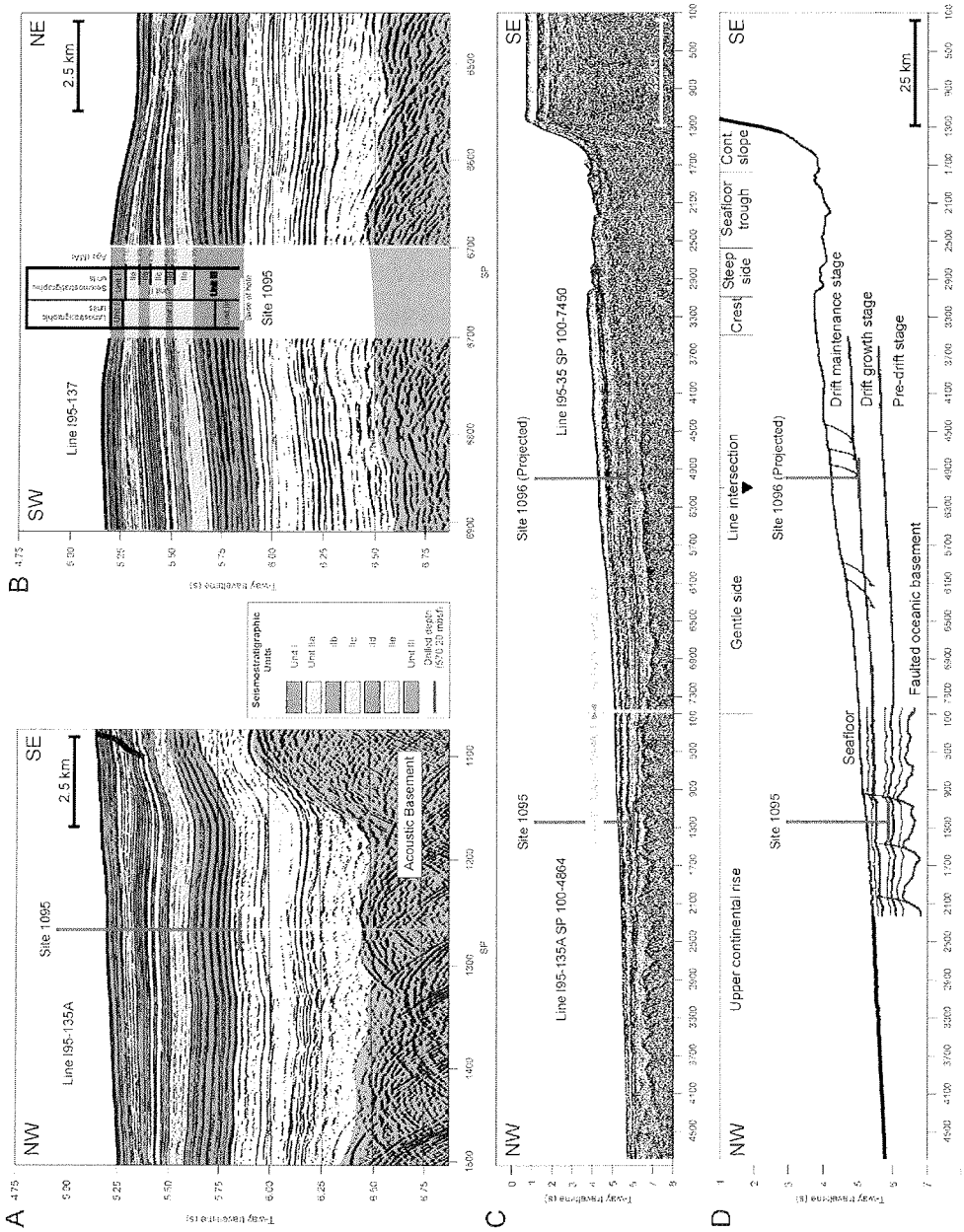

Fig. 4.2. Seismic profiles across Drift 7, parallel and perpendicular to the margin. See map Fig. 4.1A for locations. **(A)** NW-SE profile (seismic line I95-135A) across Site 1096, perpendicular to the margin. Seismostratigraphic packages are outlined in color (see text for descriptions and interpretation). **(B)** SW-NE profile (seismic line I95-137). Lithostratigraphic and seimostratigraphic boundaries are shown with an approximate age scale. **(C)** NW-SE seismic profile (line I95-135A) from the shelf across Drift 7. **(D)** Schematic interpretive line drawing of **C** with interpretation of various drift stages (Rebesco et al., 1997; Pudsey et al., 1998).

Sites 1095 and 1096 are approximately 90 km apart. Basement ages were established during Leg 178 with a magnetometer survey, indicating that the oceanic basement is 42.7 Ma below Site 1095 and 36.7 Ma at Site 1096 (Fig. 4.1). Basement roughness below the drifts and especially below the highest part of the drift crest toward the shelf (Fig. 4.1B, Fig. 4.1) suggests that the drift location may be predefined by basement heights (McGinnis and Hayes, 1995). Seismic profiles (Fig. 4.1, Fig. 4.2) show no evidence of mound formation in seismostratigraphic Units VI and V directly overlying the basement. Unit VI can be characterized as a drape and fill unit with respect to the basement. Unit V is essentially made up of planar reflectors thinning toward the abyssal plain and the shelf. None of these seismic Units was reached by coring during Leg 178.

A "Reflector X" (Fig. 4.1, Fig. 4.1; Rebesco et al., 1997) appears to cut across seismic Units VI and V at Site 1096 and to merge with the top of seismic Unit V. The origin of this reflector is uncertain (see chapter 4.5.2 for a discussion).

4.2.2.2 Drift Growth Stage

The initiation of drift growth is first seen in seismic Unit IV. Reflectors on top of Unit V are mound-shaped and downlap on both sides of the drift nuclei (e.g. at Site 1096; Fig. 4.1). Seismostratigraphic Unit III (338-580 mbsf) records the main phase of drift growth. Reflectors at the base of the unit downlap on both sides of the drift. The drift cross section asymmetry (parallel to the continental margin) develops, starting in the middle part of Unit III, with undulating internal reflections on the steeper side and lateral continuous reflectors on the gentle side (Fig. 4.1; Rebesco et al., 1997). In general seismic Unit III is typified by a sequence of reflectors with very high amplitude and continuity. The lowermost sampled part of seismic Unit III corresponds to a rapid increase in VSP velocity and downhole and laboratory densities (Fig. 4.1). This abrupt change is associated with the first appearance of chert layers in the cores and the traced location of the lower Bottom Simulating Reflector (BSR_L; Fig. 4.1B, C, D) in the '95 reflection seismic profiles (see chapter 4.5.1 for details). It also marks the lithological Unit II/III boundary. Seismostratigraphic Unit III has been modelled successfully using the earth model A and the sea floor reflection wavelet (Fig. 4.2B).

The lower subunits of seismostratigraphic Unit II (IId and IIe, not recovered at Site 1096) also belong to the drift maintenance stage (note differences in the Shipboard definition of the seismic units, also adapted in this thesis and initial seismic unit definitions given by Rebesco et al., 1997). Seismic Subunit IIe (~250-338 mbsf) is characterized by reflectors of

low amplitude and continuity, and has a patchy appearance (Fig. 4.2A, B). Strong reflectors seen in the synthetic seismogram (Fig. 4.2, Fig. 4.3) around 380 ms correspond to a velocity increase accompanied by a density decrease around 300 mbsf (Fig. 4.1). These reflectors are not seen in the reflection seismic and VSP section (Fig. 4.2, Fig. 4.2). Seismic Subunit IId (~214-250 mbsf) is characterized by continuous mid-amplitude reflectors that correspond to a coarsening upward section of lithological Unit II indicated by an increase in the mean grain-size (Fig. 4.3).

4.2.2.3 Drift Maintenance Stage

The drift maintenance stage consists of seismostratigraphic Subunits IIc-a and Unit I. It spans the last 5.31 Ma. The asymmetric shape of the drift during the drift growth stage, with discontinuous reflectors on the steep SW side and continuous reflections on the gentle side, is preserved in the drift maintenance stage. The lack of mound-shaped reflectors, that would indicate localized build-up in addition to drape growth, has been related to a shift from slope parallel to downslope sediment transport (Rebesco et al., 1997). This interpretation is supported by the presence of sharp-based, graded lamina thought to be distal turbidites in the upper part of lithological Unit II (see chapter 4.1.2 and ODP Leg 178 Shipboard Scientific Party, 1999).

The lowermost seismic unit of the drift maintenance stage, Subunit IIc (267-190 ms TWTT; 214-149 mbsf) is marked by very strong continuous couplets of high-amplitude reflectors, also found in synthetic traces (Fig. 4.2) and in the first part of the VSP traces (Fig. 4.1, Fig. 4.2). The strong reflectors have their origin in density and strong velocity increases (Fig. 4.1). The upper boundary coincides with an unusual reflector with up to three successive positive amplitude excursions (Fig. 4.2B), that can be traced with the upper bottom simulating reflector BSR_U (Fig. 4.1A). The BSR_U is only obvious on the SW side of the drift crest (Fig. 4.1A) on the '95 profiles. It merges otherwise with the parallel reflectors of the gentle side (see chapter 4.5.1 for a detailed discussion).

Subunit IIb (190-138 ms; 149-107 mbsf; 4.65-3.73 Ma) consists of high-amplitude reflectors that thin towards the abyssal plain to the NW and toward a deep sea channel system to the NE. They become thicker toward the base of the continental slope (Fig. 4.2C). Subunit IIa (394-84 ms; 107-64 mbsf) is similar in external geometry but contains local internal reflection truncations, lateral discontinuities and onlaps. This geometry is consistent with higher depositional energies, expressed as sharp facies changes. A major episode of non-deposition and erosion is suspected close to the top of the subunit (see chapter 4.4.1 for

further discussion). Laterally (e.g. parallel to the continental margin) Subunit IIa can be linked to overbank deposits of turbidite channels adjacent to drifts (ODP Leg 178 Shipboard Scientific Party, 1999), demonstrating the importance of turbidites for this subunit (see also the interpretation of the grain-size data, chapter 4.3.5).

Seismostratigraphic Subunits IIc-IIa are Messinian and Early Pliocene; the drift has a high opal content (Hillenbrand and Fütterer, in press) and lower input of continental sediment during this interval (see chapter 4.4.2.2).

		TWTT (ms)		Depth (mbsf)		Age (Ma) (SSP)		Age (Ma) (Revised)	
Seismic Unit	**Subunit**	1095	1096	1095	1096	1095	1096	1095	1096
I		84	140.6	64	110	1.7	1.4	2.5	2.1
II	IIa	138	394	107	316.5	3.73	3.08	3.83	3.28
	IIb	190	631.6	149	519	4.65	4.22	~4.82	~4.2
	IIc	267	-	214	-	5.98	-	~6.09	-
	IId	309	-	250	-	6.43	-	6.53	-
	IIe	409	-	338	-	7.76	-	~7.8	-
III		505	1100	~580	950	9.45	-	9.55	-
Base of Hole		652	732	570.2	606	9.88	4.7	9.88	4.85
IV		920	1440	852	1290	18-22	18-22	-	-
V		1060	1680	1012	1548	> 25	> 25	-	-
VI		1280	2180	1260	2154	42.7	36.7	-	-
Basement									
Litho-stratigraphic units									
I		60	82	49	63	1.77	-	2.5	-
II		506	219	436	173	8.9	-	9.0	-
III		647	729	570	608	>9.88	-	>9.88	-

Tab. 4.1. Seismostratigraphic summary of drift Sites 1095 and 1096: seismic units, their location in TWTT, with assigned depths and ages.

Seismic Unit I (84-0 ms; 64-0 mbsf) lies above a possible unconformity, as seen in seismic profiles parallel (Fig. 4.1, Fig. 4.2B) and perpendicular (Fig. 4.2A, C) to the margin. It consists of parallel and subparallel, intermediate–amplitude continuous and discontinuous reflectors (Fig. 4.2, Fig. 4.2). Its consistent thickness suggests a sheet drape geometry. Seismic Unit I correlates well with lithostratigraphic Unit I. Seismic resolution is around 15

m, glacial-interglacial cycles within the cores are in the 1 m range. The alternations in seismic reflectors may be a low resolution representation of major glacial–interglacial changes observed in the cores. None of the detailed studies (Wolf-Welling et al., in press; Hillenbrand and Fütterer, in press) support the idea that sedimentation dominated by slow hemipelagic settling of a biogenic-rich sediment, as suggested by the ODP Leg 178 Shipboard Scientific Party (1999). The opal (Hillenbrand and Fütterer, in press), $CaCO_3$ and TOC contents (Wolf-Welling et al., in press; Fig. 4.1A, B, C) of this interval are low compared to the rest of the core. The interval is characterized by low energy deposition, as indicated by small mean grain-sizes (Moerz and Wolf-Welling, in press). Three depositional mechanisms may act together to produce the sheet drape geometry:

- Turbidites feeding a nepheloid layer, resulting in deposition of low-energy distal overbank deposits (Rebesco et al., 1996).
- Bottom counter currents becomes less important upsection (within seismic Unit I)
- Organic hemipelagic settling during interglacials.

4.3 Fine-Fraction Grain-Size Distribution Data, Their Statistical Treatment and Relation to Processes, Site 1095 (ODP Leg 178, Western Antarctic Peninsula)[14]

4.3.1 Abstract

Fine-fraction (<63 µm) grain-size analyses of 530 samples from Holes 1095A, 1095B and 1095D allow assessment of the downhole grain-size distribution at Drift 7. A variety of methods of data processing, statistical treatment, and display techniques were used to describe this data set. The downhole fine-fraction grain-size distribution documents significant variations in the average grain-size composition and its cyclic pattern, revealed in five prominent intervals: (1) between 0 and 40 mcd (0 and 1.3 Ma), (2) between 40 and 80 mcd (1.3 and 2.4 Ma), (3) between 80 and 220 mcd (2.4 and 6 Ma), (4) between 220 and 360 mcd and (5) below 360 mcd (prior to 8.1 Ma).

[14] chapter 4.3 is a report in press:

Moerz, T., and Wolf-Welling, T.C.W., in press. Data report: Fine-fraction grain-size distribution data and their statistical treatment and relation to processes, Site 1095 (ODP Leg 178, western Antarctic Peninsula). In Barker, P.F., Camerlenghi, A., Acton, G.D., and Ramsay, A.T.S. (Eds.), Proc. ODP, Sci. Results, 178.

In an approach designed to characterize depositional processes from Drift 7, we used statistical parameters determined by the method of moments for the sortable silt fraction to distinguish groups in the grain-size data set. We found three distinct grain-size populations, used here for a tentative environmental interpretation. Population 1 is related to a process in which glacially eroded shelf material was redeposited by turbidites with ice-rafted debris (IRD) influence. Population 2 comprises interglacial turbidites. Population 3 is connected to depositional sequence tops linked to bioturbated sections that, in turn, are influenced by contourite currents and pelagic background sedimentation.

4.3.2 Introduction

The area west of the Antarctic Peninsula is a key region for studying and understanding the history of glaciation in the southern high latitudes during the Neogene. The area is critical for learning about variations in the western Antarctic continental ice sheet, the sea-ice cover, the induced eustatic sea-level change, and consequences for the global climatic system. Sites 1095, 1096, and 1101 (Fig. 4.15) were drilled on sediment drifts which form the continental rise in order to examine the nature and composition of sediments deposited under the influence of the fluctuating Antarctic Peninsula ice sheet. The ice sheet has repeatedly advanced to the shelf edge and subsequently released glacially eroded material onto the continental slope and rise (Barker, 1995; Barker et al., 1998; 1999). Mass wasting processes on the slope are responsible for downslope sediment transport by turbidity currents within a channel system between the drifts (Rebesco et al., 1998). Bottom currents redistribute the sediments, thus leading to the final build-up of drift bodies (Camerlenghi et al., 1997). The high-resolution sedimentary sequences on the continental rise can be used to document the variability of continental glaciation and, therefore, allow us to assess the main factors that control sediment transport and depositional processes during glacial periods and their relationship to glacio-eustatic sea-level changes.

This research was carried out on material from Site 1095, where coring recovered sediments as old as late Miocene (9.7 Ma). Site 1095 lies in 3840 m of water in a distal position on the northwestern lower flank of Drift 7 (Fig. 4.2). We measured the grain-size distribution of 530 samples from Holes 1095A, 1095B and 1095D in order to obtain a more detailed picture of three controlling factors: (1) the variability and magnitude of turbidites, (2) deep-oceanic currents (contourite currents), and (3) the ice-rafting component since the late Miocene.

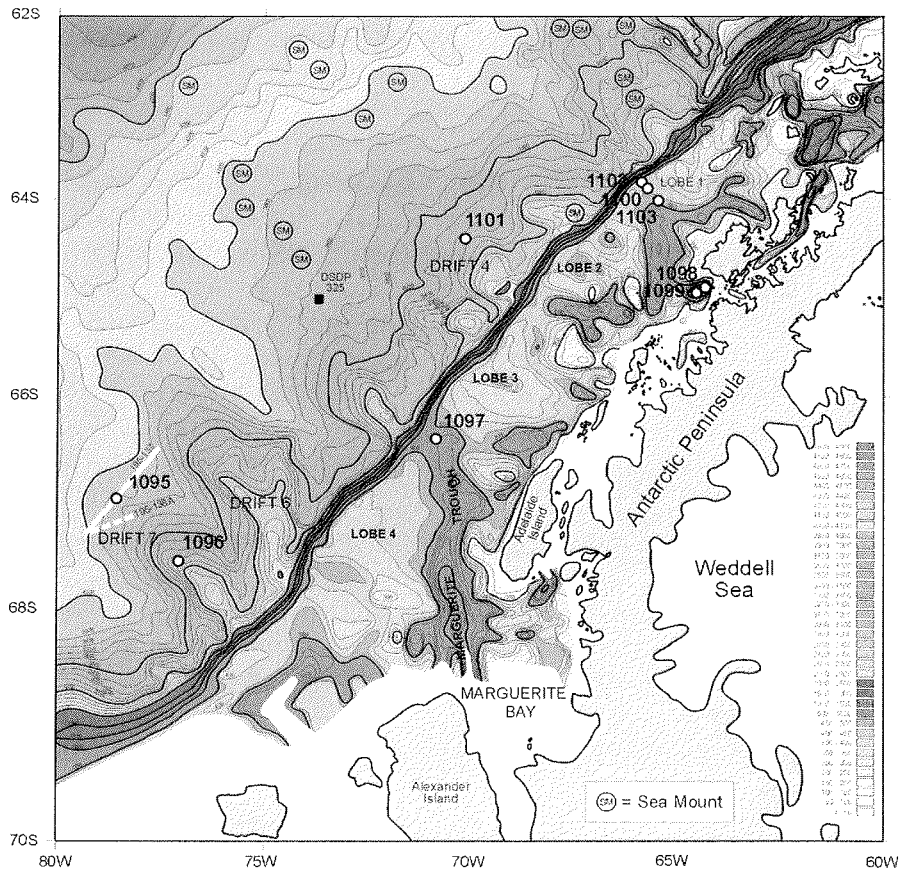

Fig. 4.1. Bathymetric map of the continental margin west of the Antarctic peninsula (Rebesco et al., 1998) with Leg 178, Sites 1095 and 1096 locations on Drift 7. The approximate location of seismic line I95-137 is also indicated (white line).

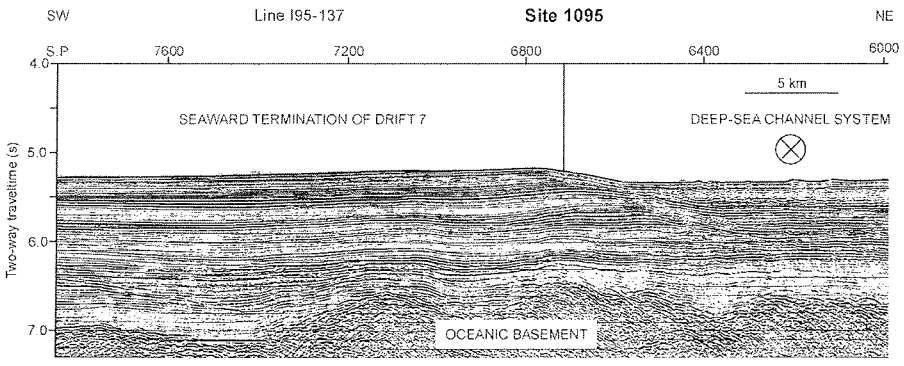

Fig. 4.2. Southwest-northeast air-gun multichannel reflection seismic profile across the seaward end of Drift 7 (for location see caption of Fig. 4.15; adapted from Shipboard Scientific Party, 1999b).

4.3.3 Methods

4.3.3.1 Sample Preparation

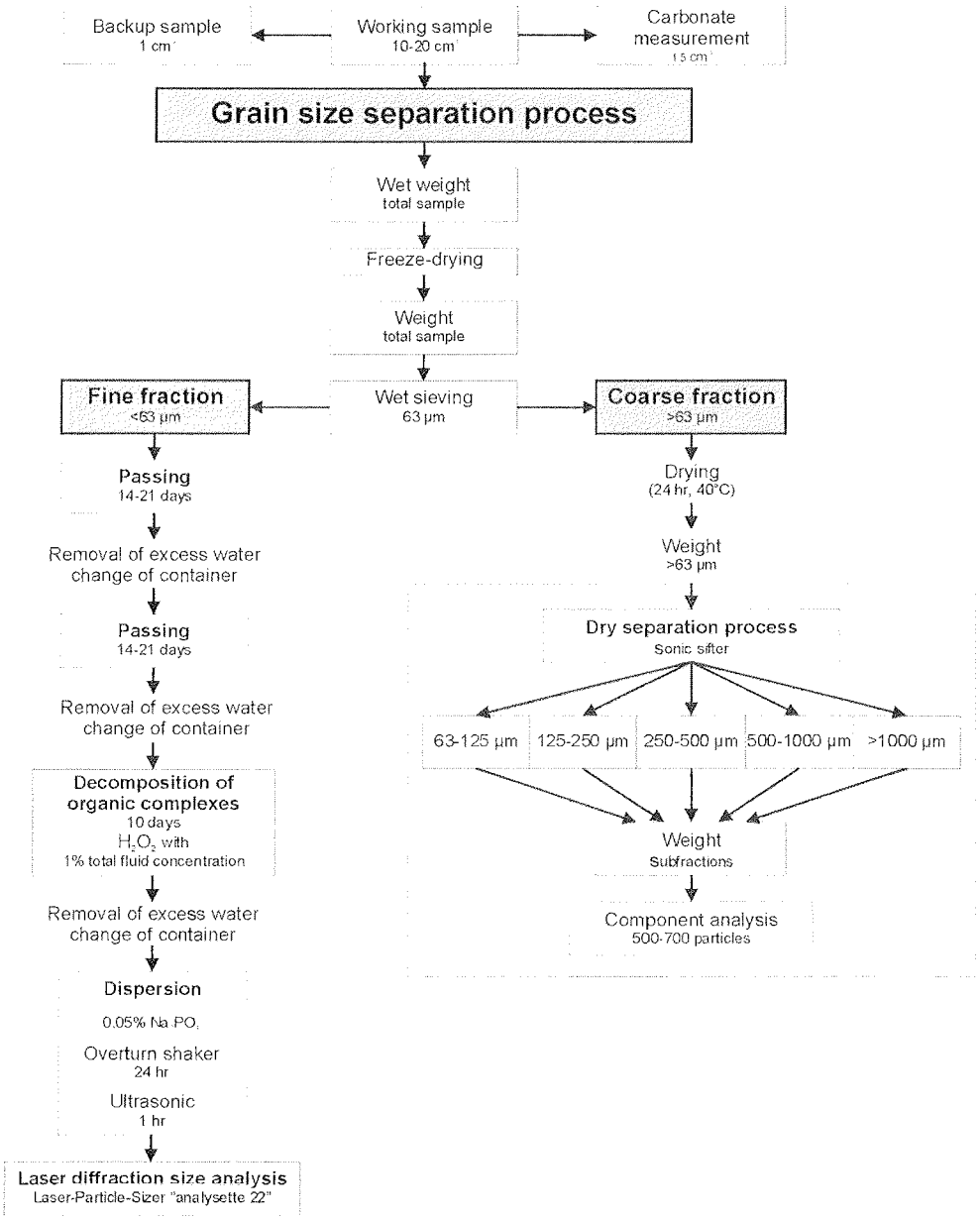

Fig. 4.1. Sample preparation scheme. Long passing times are due to an abundant very fine clay portion with slow settling velocities.

Sediment samples were taken from cores from Sites 1095 cores using a 10- to 20-cm^3 plugging device. After freeze-drying, the sample was split by wet sieving into the fine (<63 μm) and coarse (>63 μm) fractions. The coarse fraction was oven-dried, balanced, and set aside for further analysis (the results of the coarse-fraction analysis are given in the data report by Wolf-Welling et al., in press).

The water content of the suspended fine-fraction sample was reduced in two steps, by settling and the subsequent removal of excess water (vacuum pump). We added H_2O_2 to remove remaining organic complexes (Andersen, 1963; Matthews, 1991) and rinsed the fraction with distilled water before a final removal of excess water. Na_2PO_4 was used as a final dispersant to avoid fine-particle clogging (McCave, 1995a; McCave et al., 1986). The final preparation step included 24 hr shaking within an overturn shaker and 1 hr within an ultrasonic bath directly before sample analysis (Fig. 4.1).

4.3.3.2 Laser Diffraction Analysis

The fine fraction was subsequently analyzed by laser diffraction. Measurements were carried out using the Laser-Particle-Sizer "analysette 22"-Economy (Fritsch GmbH Laborgerätebau, 1994) (Fig. 4.1A). The unit is equipped with a 632.8-nm wave length, 3-mW helium-neon laser and handles suspensions with a particle size between 0.1 and 600 μm. The laser analyzer consists of four components: a dispersion unit, the measuring cell and laser, a multi-element detector, and a personal computer with software for recalculation and data display. The sample is fed into the dispersing and homogenization unit, which is equipped with an ultrasonic bath and a stirring compound. An interactive sample input, controlled by frequent absorption measurements, assures a certain grain-density range within the measuring cell. A centrifugal pump supports the transport of the sample to and from the measuring cell. After each measurement, the laser analyzer was set up to rinse and clean the cell four times with distilled water.

The laser measurement itself is based on the sensory interpretation of Fraunhofer interference images produced by the scattering of monochromatic light on spherical grain boundaries (Von Bernuth, 1988). The size of the grains is related to wavelength and frequency (f), a geometry factor k and the radius of the first-order Fraunhofer interference ring (R_o) (Fritsch GmbH Laborgerätebau, 1994).

$$\text{particle size} = \frac{k * f * \text{wavelength}}{R_o} \qquad \text{(Eq. 4.1)}$$

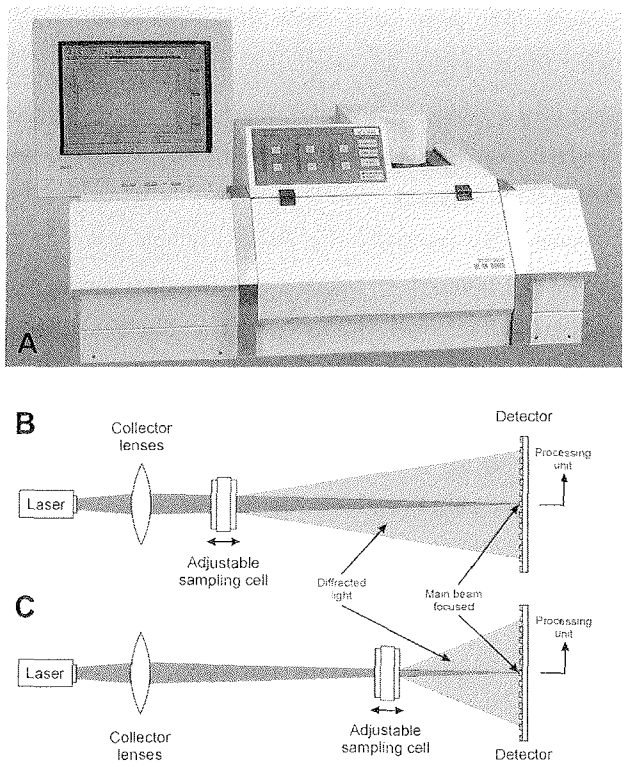

Fig. 4.1. (**A**) Layout of the Laser-Particle-Sizer "analysette 22"-Economy (Fritsch GmbH Laborgerätebau, 1994). The unit is equipped with a 632.8-nm wave length, 3-mW helium-neon laser and handles suspensions with a particle size between 0.1 and 600 µm. (**B, C**) The unique fixed-focus size analyzing system with particle size-range dependent cell shift. Shifting the sampling cell relative to the detector changes the diffraction angle and the size of the sensor area affected. A large distance between sampling cell and detector therefore permits the measurement of larger particles with a smaller diffraction angle, and short distances are used for small particles with a wide diffraction angle.

Particle sizes down to 0.02 µm can still be detected with sufficient accuracy using the Frauenhofer theorem (Von Bernuth, 1988). A special feature of this laser analyzing system is a fixed-focus optical setup with no focusing lenses behind the sampling cell, in contrast to other systems that use focusing lenses behind the sampling cell. In order to detect a wide range of particle sizes, the distance from the sampling cell to the multimeter detector is variable (Fig. 4.1B, C). Shifting the sampling cell relative to the detector changes the diffraction angle and the size of the affected sensor area. A large distance between the sampling cell and detector therefore permits the measurement of larger particles with a smaller diffraction angle, and short distances are used for small particles with a wide diffraction angle (Fig. 4.1B, C) (McCave et al., 1986). Our fine-fraction data set consists of 31 size classes ranging from 0.425 - 63.314 µm. The size classes are given in Tab. 4.1. The size

range of 0.4 to 63.3 µm was measured with a constant cell to detector spacing (single range measurement). Since some of the plots displayed in this report are given in linear scale and others (e.g. the statistical moment plots) in Φ units, we added a figure to demonstrate the relation between both scales (Fig. 4.2A) and the effects on the appearance of frequency distribution plots given in mm and Φ values (Fig. 4.2B, C).

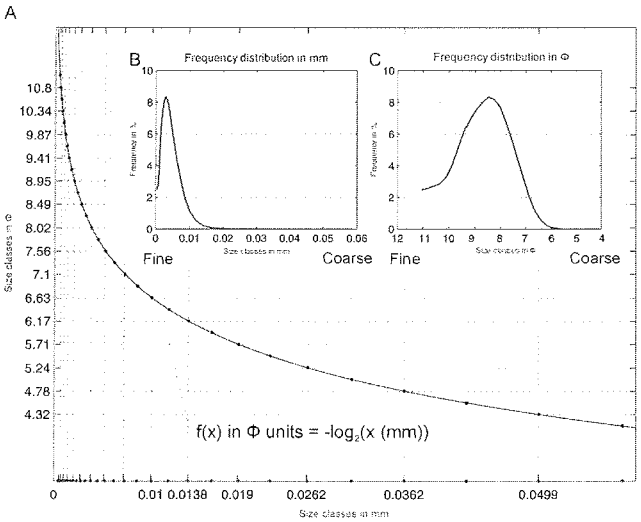

Fig. 4.2. (**A**) size classes in mm and Φ-values. (**B, C**) differences in frequency spectra plots given in mm and Φ-values.

Grain-size classes (µm)			
Midpoint (µm)	Midpoint (Φ)	Lower (µm)	Upper (µm)
0.47	11.055	0.425	0.514
0.559	10.805	0.514	0.604
0.656	10.574	0.604	0.709
0.771	10.341	0.709	0.832
0.905	10.110	0.832	0.977
1.062	9.879	0.977	1.147
1.247	9.647	1.147	1.347
1.464	9.416	1.347	1.581
1.719	9.184	1.581	1.856
2.018	8.953	1.856	2.179
2.369	8.722	2.179	2.559
2.781	8.490	2.559	3.004
3.265	8.259	3.004	3.527
3.834	8.027	3.527	4.14
4.501	7.796	4.14	4.861

Midpoint (µm)	Midpoint (Φ)	Lower (µm)	Upper (µm)
5.284	7.564	4.861	5.707
6.203	7.333	5.707	6.7
7.283	7.101	6.7	7.866
8.55	6.870	7.866	9.235
10.038	6.638	9.235	10.842
11.785	6.407	10.842	12.728
13.836	6.175	12.728	14.943
16.243	5.944	14.943	17.543
19.07	5.713	17.543	20.596
22.388	5.481	20.596	24.18
26.284	5.250	24.18	28.388
30.858	5.018	28.388	33.328
36.228	4.787	33.328	39.127
42.532	4.555	39.127	45.936
49.933	4.324	45.936	53.929
58.622	4.092	53.929	63.314

Tab. 4.1. Fine-fraction size classes mid points and ranges used within this study.

4.3.3.3 Stratigraphy and Age Model

The age model and stratigraphy for Site 1095 are based on the magnetostratigraphic results published by the Shipboard Scientific Party (1999c; see "Magnetostratigraphy").

We assigned ages for each sample assuming linear sedimentation rates between age dates. Even though depth below sea floor and recovery-corrected depth values do not differ significantly, we decided to work with meters composite depth (mcd). Because of the small overlap between Holes 1095A, 1095B and 1095D, we do not expect important changes for our model compared to stratigraphically spliced depth scales. We excluded two samples in the overlapping part of Holes 1095A and 1095B (between 83.0 and 87.3 meter below sea floor) to avoid assigning overlapping ages to samples.

The hiatus at ~60 mcd discussed by Hillenbrand and Ehrmann (2000) and in Shipboard Scientific Party (1999c; see "Magnetostratigraphy" and "Seismic Stratigraphy") has not been considered in our age model. Even so, the data presented support the ideas presented in Shipboard Scientific Party (1999c), and by Hillenbrand and Fütterer (2000).

4.3.4 Results

To provide a simplified overview of the fine-fraction grain-size frequency distribution of the data set, we have chosen a three-dimensional contour presentation that incorporates all samples with their individual frequency distributions (Fig. 4.1A, B). The original data set was gridded to a 1-m depth and 20-ka age grid resolution, with linear interpolated size classes of the original 31 channels in µm. We applied a true two-dimensional zero-phase filter algorithm to smooth the data (the moving average filter has a size of 5 data points for the age or depth axis and 3 points on the grain-size axis). The contour algorithm is linear and resolves six levels representing the percent of sediment found for each grain-size class. Percent values refer to the total sediment sample dry mass. The size fraction >63-µm was added as an undifferentiated two-dimensional summary curve at the right side of the graph. Single data values and a zero-phase filtered curve, obtained with an one dimensional filter (5 point) of the same size as for the fine fraction, are given. The fine-fraction and smoothed coarse-fraction data are therefore in phase and have identical interpolated depth resolutions.

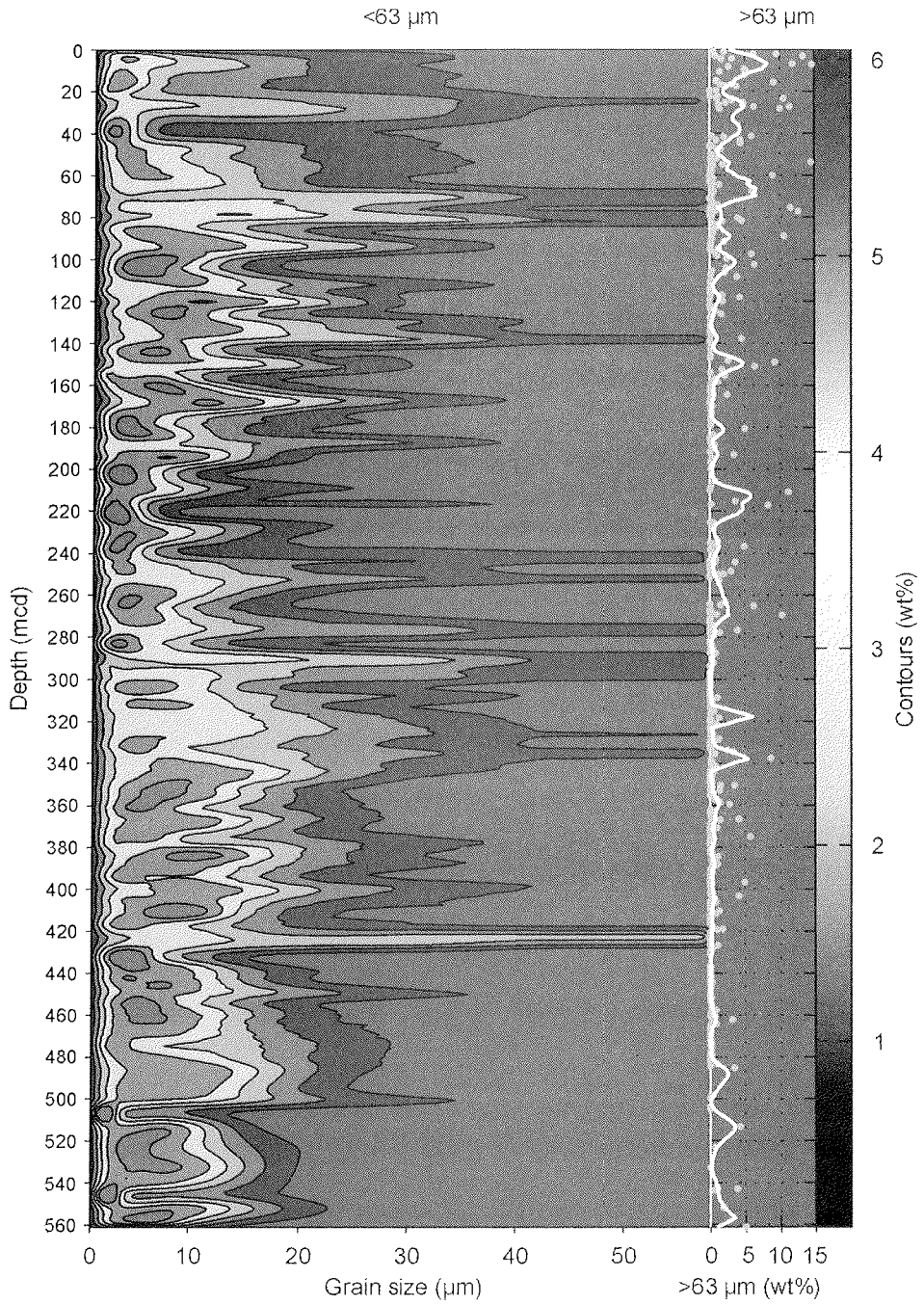

Fig. 4.1 Contour plots of the fine-fraction data vs. **(A)** depth and **(B, see next page)** age. The contour algorithm chosen is linear and resolves six contour levels representing the percent of sediment found for each grain-size class. Percent values refer to the total sediment sample dry mass. The size fraction >63 µm was added as an undifferentiated two-dimensional summary curve as a separate column at the right side of the graph. Single data values and a zero-phase filtered curve are given for the >63 µm fraction.

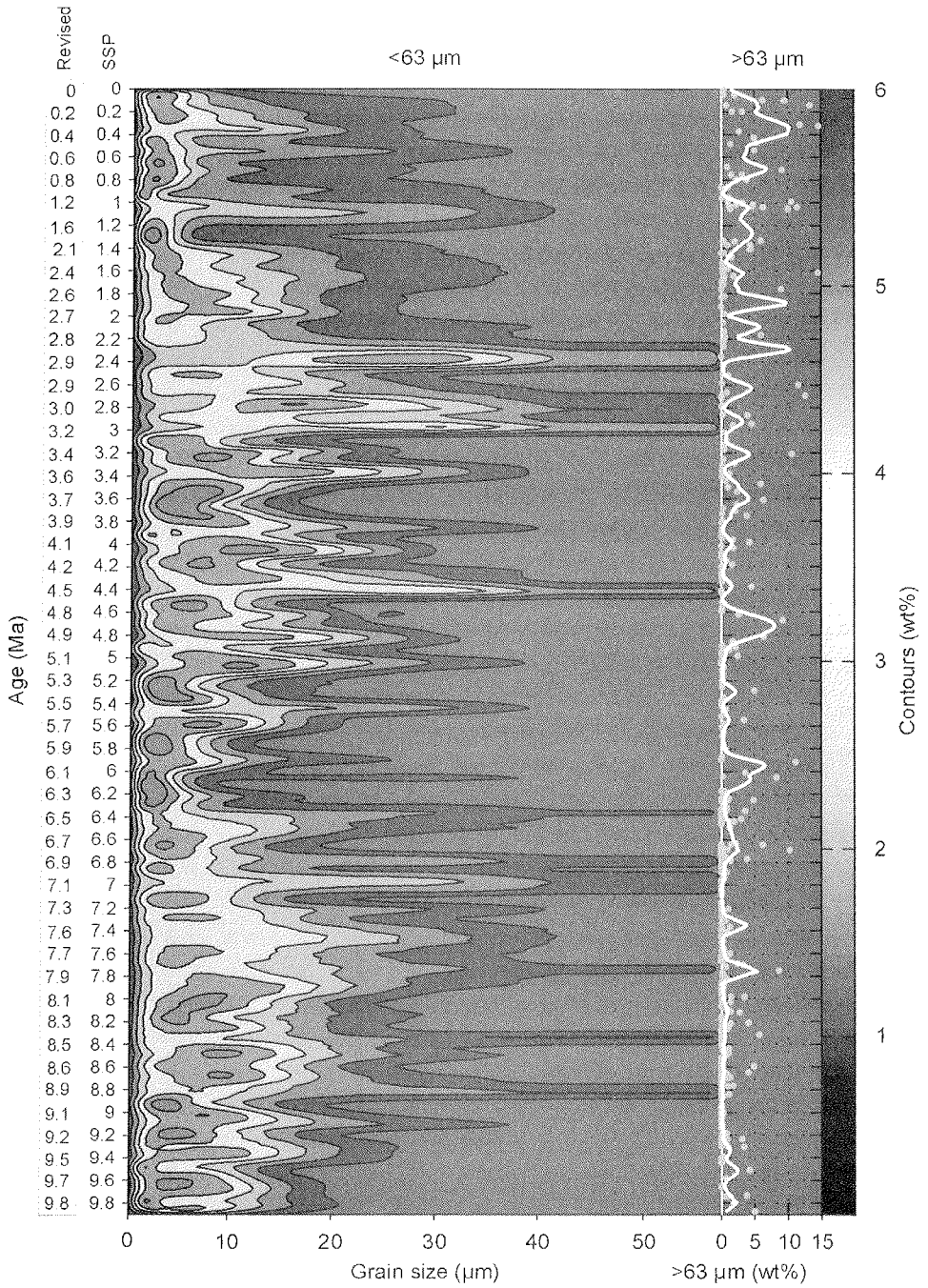

SSP = ODP Leg 178 Shipboard Scientific Party on board time scale; Revised = revised time scale this thesis (Chapter 4.4).

In general, the grain-size distribution down-core shows significant variations (Fig. 4.1A, B). There are five prominent intervals in which cyclicity and the clay/silt ratio change drastically: (1) between 0 and 40 mcd (0 and 1.3 Ma), (2) between 40 and 80 mcd (1.3 and 2.4 Ma), (3) between 80 and 220 mcd (2.4 and 6 Ma), (4) between 220 and 360 mcd and (5) below 360 mcd (prior to 8.1 Ma).

Interval 1 is characterized by small scale variations and a pronounced dominance of the 5 μm size class fraction compared to the other identified intervals. Even though the overall grain-size distribution within this interval is very fine, interval 1 is also associated with a continuous tail of 1% of the distribution reaching the 40 μm fraction.

Interval 2 shows a steady increase in the dominant grain-size class and only small amplitude cyclic variations. Interval 2 terminates with the highest dominant grain-size classes with 20 to 40 μm and 5% loading of our data set. The steady increase toward these highest recorded values seem to be interrupted between 60 and 70 mcd (~2.3 Ma). We attribute this gap in the temporal and spatial continuity of the grain-size distribution to the hiatus (discussed in: Hillenbrand and Ehrmann (2000).

Interval 3 is characterized by very high amplitude and frequency cyclic distribution changes and a more or less steady decline in the grain-size mode and overall amplitude. High loadings of up to 4 % for the 20 μm window are reached in the middle of this interval at 135 mcd or 4.3 Ma.

Interval 4 around 220 mcd or 6 Ma starts with a very narrow spectral distribution combined with high loadings of 6% in the size class below 5 μm. This nearly symmetrical upper zone of interval 4 has no tails into the coarser class fractions. The remaining lower part of the interval is characterized by a steady increase toward coarser size classes and moderately frequent but high amplitude variability, especially in the coarser tail (> 25 μm) of the grain-size spectra.

Interval 5 starting around 360 mcd or 8.1 Ma shows the same cyclic pattern as interval 4, but with a decreasing trend in the occupied size classes.

The plot (Fig. 4.1A, B) allows us to determine whether the fine fraction, <63 μm, is locally affected by IRD events. These are suspected where the < 63 μm fraction tails seem to be connected to peaks of the >63 μm fraction. For further IRD and coarse fraction data see Cowan and Wolf-Welling et al., 2000.

Mean (1^{st} moment)
$$\bar{x}_\phi = \frac{\Sigma fm}{n} \quad \text{(Eq. 4.1)}$$

Standard deviation (2^{nd} moment)
$$\sigma_\phi = \sqrt{\frac{\Sigma f (m - \bar{x}_\phi)^2}{100}} \quad \text{(Eq. 4.2)}$$

Skewness (3^{rd} moment)
$$Sk_\phi = \frac{\Sigma f (m - \bar{x}_\phi)^3}{100\sigma_\phi^3} \quad \text{(Eq. 4.3)}$$

Kurtosis (4^{th} moment)
$$K\phi = \frac{\Sigma f (m - \bar{x}_\phi)^4}{100\sigma_\phi^4} \quad \text{(Eq. 4.4)}$$

where f = weight percent (frequency) in each grain-size grade present
m = midpoint of each grain-size grade in ϕ units
n = total number in sample; 100 when f is in percent

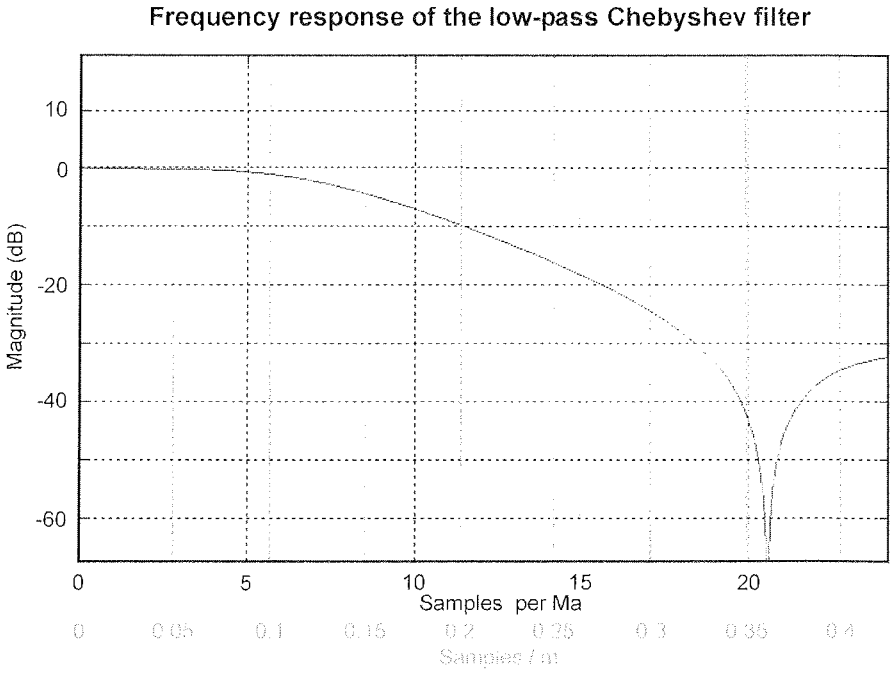

Fig. 4.2. Frequency response and the resolution in time and distance of the Chebyshev zero phase low-pass filter algorithm used to remove artificial high frequency patterns resulting from unequal sample spacing.

For further general investigations, we applied the method of moments for the <63-μm data set. The weight percent of the fine fraction was recalculated to 100%. The methods of moments is well established (Griffith, 1967; Folk, 1974; Boggs, 1987) and is the mathematical expression of four characteristics of a quasi-Gaussian distribution. In this case the moments are calculated using Φ values. The skewness (3rd monent) and the kurtosis (4^{th} moment) express the deviation of a grain-size frequency distribution from the general assumption of log normality to the base of 2 (Friedman, 1962). The results for the <63-μm range are given in a filtered (zero phase low-pass filter; Fig. 4.2) and discrete versions (Fig. 4.3A, B). The filter has been applied after interpolating the data to constant depth and age resolution. The aim of this filtering procedure was to reduce the effects of uneven sampling spacing. A documentation of the frequency response and the resolution in time and distance of the Chebyshev filter algorithm (Rabiner and Gold, 1975) used is given in Fig. 4.2.

Particle-size data are presented as downhole plots vs. depth and age of bulk <63-μm fraction in weight percent of the total dry sample mass, mean (1st moment), standard deviation (2nd moment), skewness (3rd moment), and kurtosis (4th moment). Bulk fine-fraction contents are generally high (>95 wt%). The mean of the bulk fine fraction (<63 μm) varies between 7 and 9.2 Φ units. There are some prominent maxima around 80 mcd (2.8 Ma), 138 mcd (4.4 Ma), 250 mcd (6.2 Ma), 290 mcd (6.8 Ma), 340 mcd (7.8 Ma), and 420 mcd (8.8 Ma). It appears that the mean of the fine fraction (<63 μm) is generally decoupled from the coarse fraction. Only in two cases, at 340 mcd (7.8 Ma) and 70 mcd (2.27 Ma), does a high mean of the coarse fraction correlate with a higher content of coarse fraction (>63 μm). Average standard deviation values above 1 Φ indicate poor sorting of the <63-μm fraction (Folk, 1974). The standard deviation and mean of the fine fraction in Φ units are inversely correlated throughout our data set. A decrease in degree of sorting is apparently coupled with higher mean grain-size values. The skewness values vary between -0.2 and >2. The skewness is, with a few exceptions, positive. This means that almost all samples analyzed have excess fine particles with respect to a log normal Gaussian distribution. There is a positive correlation between the skewness values and the kurtosis values. Fluctuations within the kurtosis values (measure of the peakness of a distribution) indicate highly variable depositional processes (Friedman, 1967).

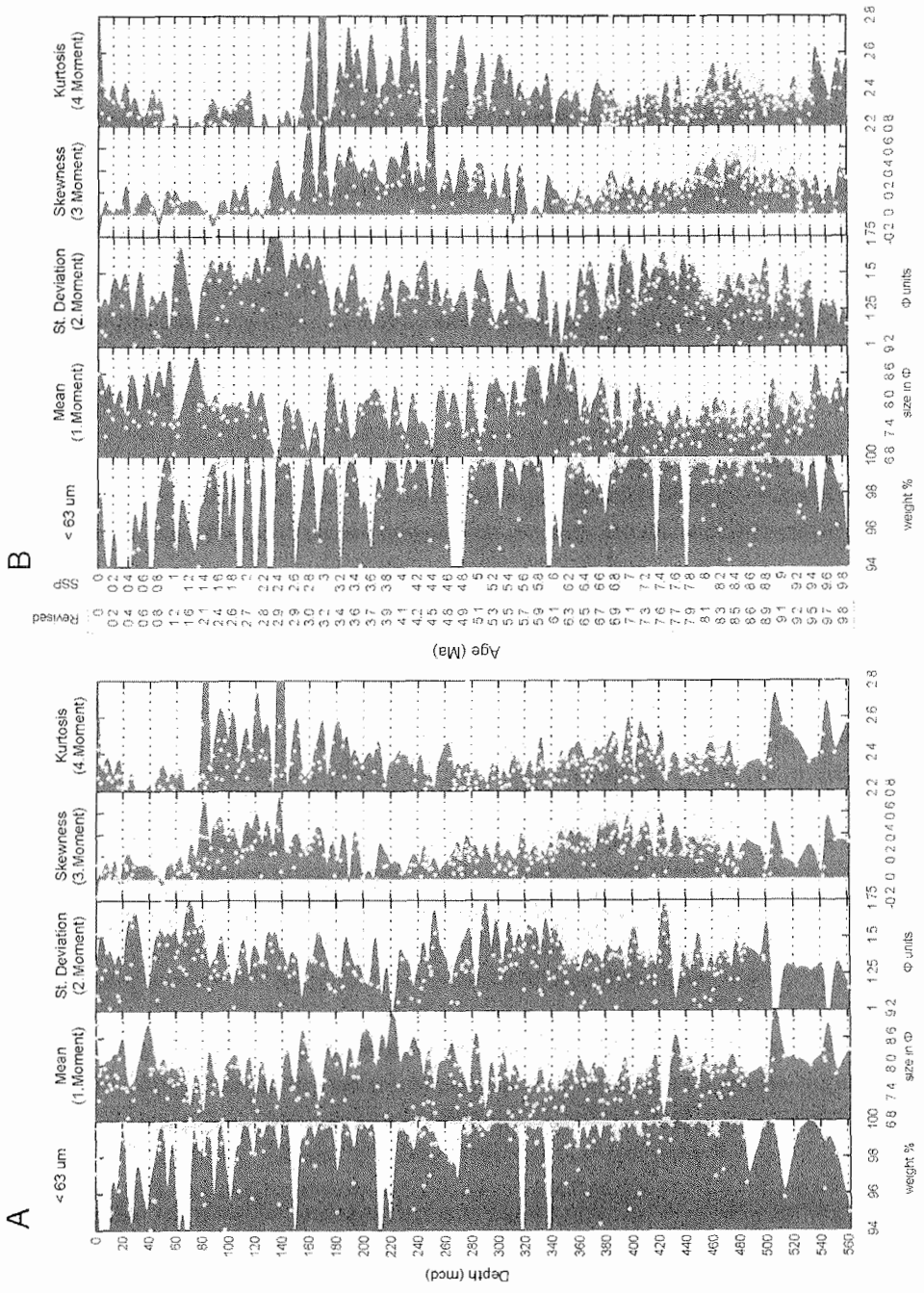

Fig. 4.3. Statistical grain-size data using the method of moments for all of the <63-µm data set. The results are given in a low-pass filtered and discrete version vs. **(A)** depth and **(B)** age. Bulk fine-fraction contents are generally high (>95 wt%). SSP = ODP Leg 178 Shipboard Scientific Party on board time scale; Revised = revised time scale this thesis (Chapter 4.4).

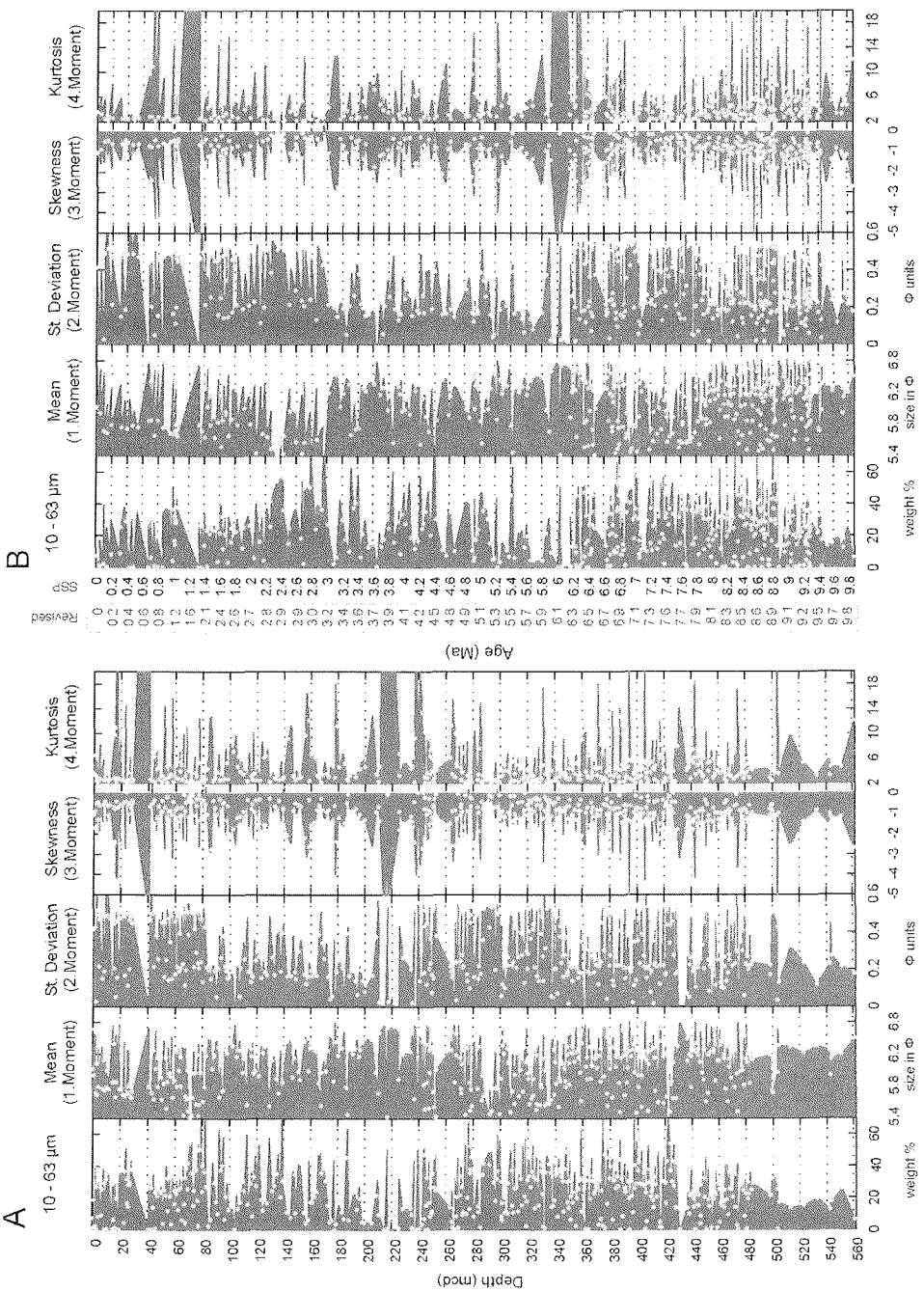

Fig. 4.4. Statistical grain-size data using the method of moments for the sortable silt fraction (10 to 63 µm) of our data set. The results are given uninterpolated in discrete samples vs. **(A)** depth and **(B)** age. The amplitude of fluctuation of the statistical parameters in the sortable silt fraction is more pronounced than in the bulk fine-fraction data set. Note the unequal spacing of our data coverage. SSP = ODP Leg 178 Shipboard Scientific Party on board time scale; Revised = revised time scale this thesis (Chapter 4.4).

The initially defined intervals based on the overall appearance of the grain-size distributions in contour representation also show distinguishing features in their moment representation. A detailed description is beyond the scope of this report but some marked changes are noteworth e.g. the change in skewness and kurtosis between interval 2 and 3 or the time around 6 Ma (end of interval 3, beginning of interval 4), where mean grain-sizes reach a minimum that is combined with moderate sorting and low skewness and kurtosis values. Not all of the <63-μm fraction is equally meaningful for the evaluation of depositional energy or paleo currents. The special importance of grain-size parameters such as the sortable silt fraction (10-63 μm) as a percentage of the fine fraction (McCave, 1995a; 1995b), and the mean of the 10 to 63-μm fraction (McCave, 1995a) are especially current sensitive. Therefore, we applied the same statistical treatment (method of moments) to the sortable silt fraction (10-63 μm). Sortable silt fraction, mean (1st moment), standard deviation (2nd moment), skewness (3rd moment), and kurtosis (4th moment) are presented as downhole plots vs. depth and age (Fig. 4.4A, B). The data presented are unfiltered and uninterpolated to give a better idea of data density and data gaps. Sortable silt-fraction values are generally much lower (average around 30 wt% of the fine fraction) than the bulk fine-fraction values, emphasizing the large fraction of <10 μm sediment not accounted for (Fig. 4.4A, B; left column). In addition, the amplitude of fluctuation in the sortable silt fraction (10 to 63 μm) appears to be much higher in older sediments [below 280 mcd (late Miocene)]. However this may be the effect of higher sample density in this interval. The mean of the sortable silt fraction indicates that most of the sortable silt fraction has a grain-size of around 6 Φ units (15 μm), whereas the minimal mean values range below 5.4 Φ units (25 μm). As a result of removing the fine grained tail below 10 μm, most of the skewness values turned negative in this statistic. After this modification frequency distributions which originally had a nearly symmetrical distribution appear to be coarse skewed.

4.3.4.1 Data Populations

Assuming that grain-size characteristics in the sortable silt range reflect conditions of the depositional process or environment, we used the statistical parameters determined by the methods of moments (Fig. 4.2A, B) to group our data set. In contrast to previous approaches (Friedman, 1961; 1967; 1979) that apply environmental statistical analyses to distinguish depositional settings (e.g., beach from river sand), we used bivariant plots to define depositional processes within a single depositional environment.

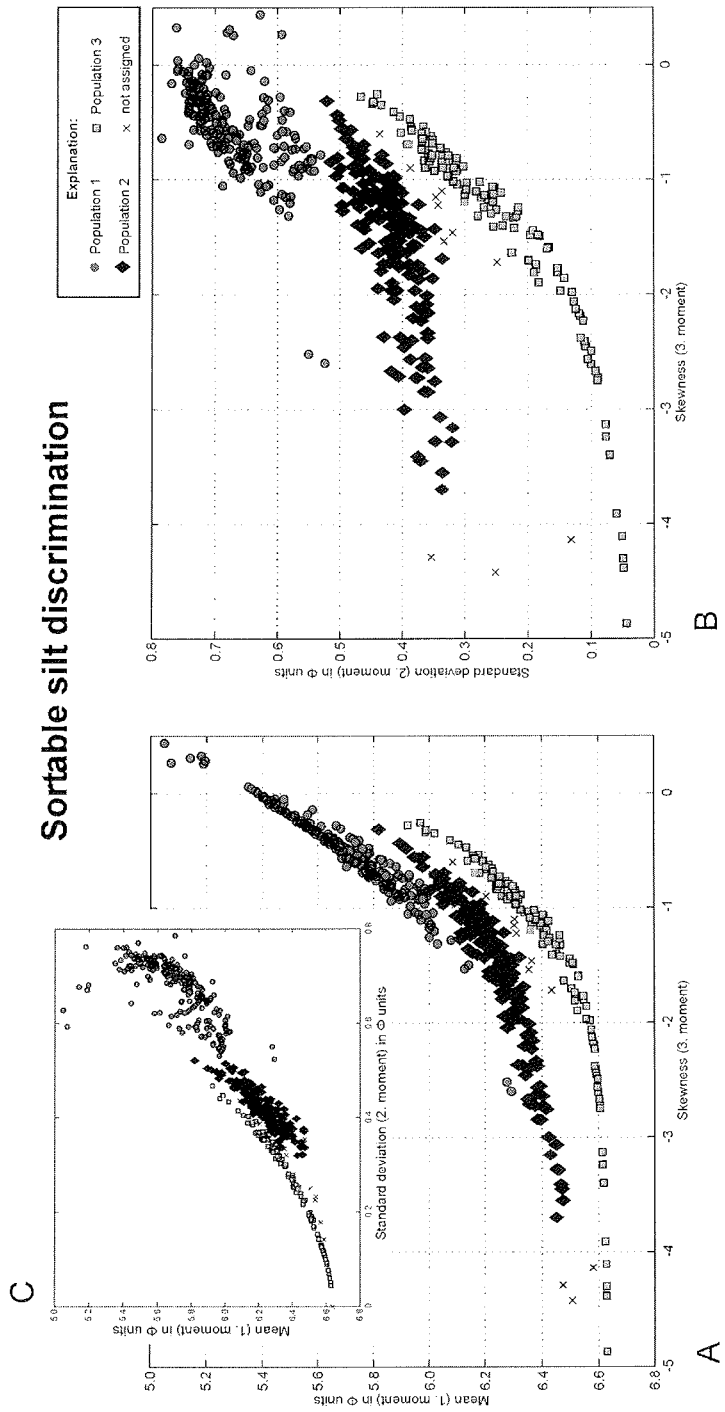

Fig. 4.1. Bivariant discrimination plots of the statistical parameters **(A)** mean vs. skewness, **(B)** standard deviation vs. skewness, and **(C)** mean vs. standard deviation skewness leading to the definition of three distinct populations.

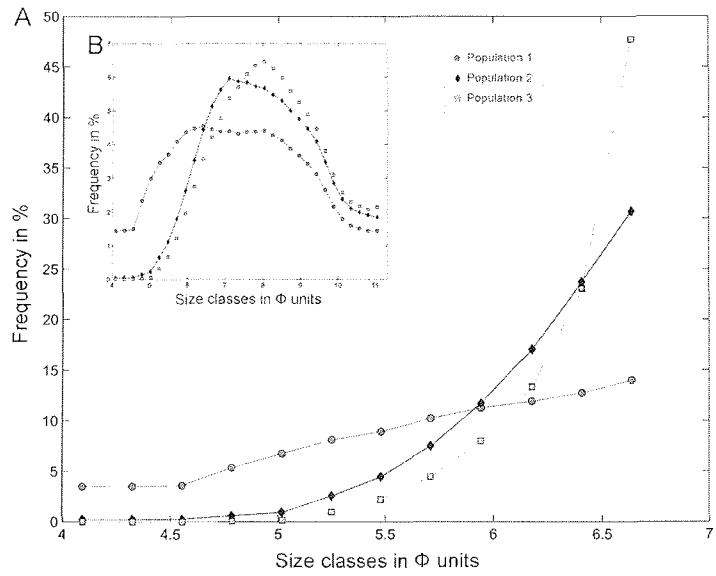

Fig. 4.2. Calculated average grain-size distributions for each population of the **(A)** sortable silt and **(B)** <63 μm fraction. Populations 2 and 3 follow a unimodal distribution. Population 1 has a bimodal distribution indicating that it may be further split into two subfractions.

The best spatial separation of our sediment drift data set is in the bivariant plots: mean vs. skewness (Fig. 4.1A) and standard deviation vs. skewness (Fig. 4.1B). Three clearly separated populations are seen. Population 1 is characterized by the highest absolute mean grain-sizes and standard deviation (Fig. 4.1C). Population 2 shows high variability in skewness and only small variations in mean grain-size and standard deviation (Fig. 4.1A, B). Population 3 is characterized by the lowest mean and standard deviation values but displays the highest combined variability for the parameters skewness and standard deviation within the bivariant field (Fig. 4.1B, C). In general, samples with larger mean grain-sizes have a higher standard deviation in our data set (Fig. 4.1C).

For a further visual inspection of the described populations we calculated average grain-size distributions for each population of the sortable silt (Fig. 4.2A), and for the <63 μm fraction (Fig. 4.2B). On average populations 2 and 3 follow a unimodal distribution. In contrast the average distribution of population 1 is very broad and bimodal. The average distribution plot for the sortable silt fraction (Fig. 4.2A) illustrates the characteristics of the 3 populations in a more graphical way.

4.3.5 Discussion

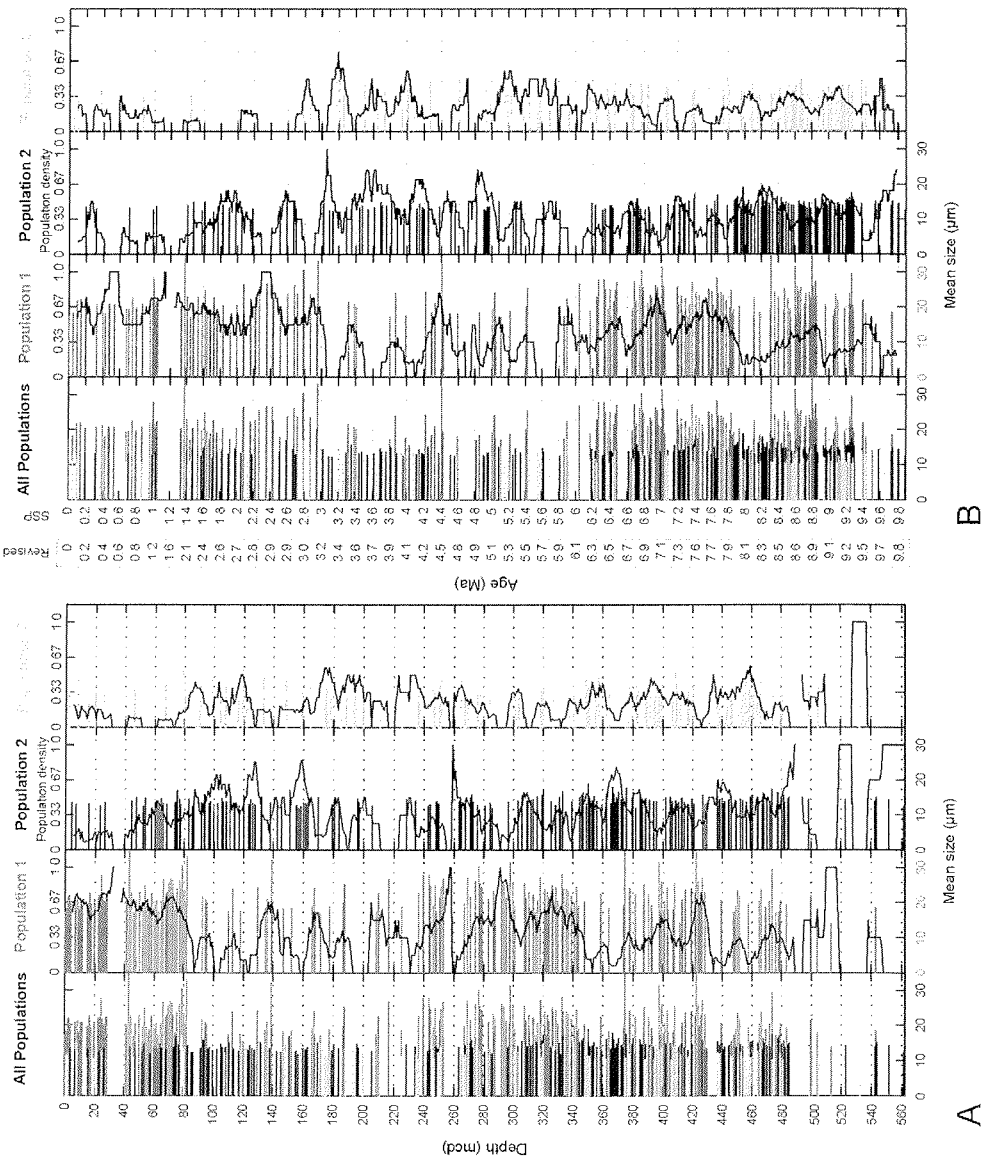

Fig. 4.1. Downhole plots of the three sortable silt populations vs. **(A)** depth and **(B)** age. The populations are color coded, and the amplitude refers to the mean grain-size. The black curves for each population represent the density of the occurrence of the specific population normalized to the total number of samples within a 10-m depth or 0.2-Ma time window. SSP = ODP Leg 178 Shipboard Scientific Party on board time scale; Revised = revised time scale this thesis (Chapter 4.4).

The bimodal distribution of population 1 may indicate that the group actually consists of two populations. Fig. 4.1B could be used to define a second population in this group. However, for the following discussion we use populations 1 to 3 as defined above.

In order to check the significance of the populations for interpretation in terms of depositional processes, we plotted the data groups with their mean grain-size against depth and age (Fig. 4.1A, B). Blank areas within the first column indicate areas of no sample coverage. The mean of the grain-size populations correlates in general with the depositional energy of a system or depositional process. An arbitrarily chosen definition of the populations leads to a random downhole distribution. Instead the populations show distinct groups of spatial and temporal occurrence and absence. Population 1 is most common in four distinct time/depth intervals (interval 1, 2, 4 and 5). Populations 2 and 3 are more continuous, except that population 3 is less common in younger/shallower deposits.

Our tentative correlation to depositional environments has been drawn from a comparison to a sequence stratigraphic model developed on board the ship (Shipboard Scientific Party, 1999c (see "Lithostratigraphy"). Population 3 is clearly related to bioturbated upper sequence boundaries that may be influenced by contourite currents. Population 1 is certainly glacial, with its maximum values correlating to ice-rafting events. However, most of population 1 may be indirectly ice-derived shelf material redeposited by turbidites. Especially noteworthy is the low number of population 1 events around the 3-6 Ma global warm period (starting with the Messinian salinity crisis and ending with the lower upper Pliocene).

The depositional significance of population 2 is less certain; we assume an interglacial turbiditic origin. The density curves in Fig. 4.1A and B represent counts of events at a certain depth and age ranges normalized to the total number of samples analyzed within this interval. The density curve of the glacial population 1 be linked to parameters such as ice volume, shelf ice extent or periods of advance and retreat of ice sheets.

4.3.6 Conclusions and Ongoing Work

This paper presents the laser diffraction derived fine fraction grain-size data for 530 samples from drift Site 1095. Contour techniques and the method of moments describe and characterize the frequency distribution data. The data set exhibits intervals of distinct changes in frequency, amplitude, spatial (downcore) and temporal occurrence.

On the basis of three statistical parameters (mean, standard deviation and skewness) calculated using the method of moments, it is possible to divide the data sets into at least three

populations. The downcore and temporal distributions of the populations may be linked to discrete depositional processes.

Further investigations and the incorporation of other data sets are needed for definition of a new sequence stratigraphic model for Drift 7. In our ongoing project the biavariant approach for discriminating the data set will be tested against multivariant factor- and cluster-analysis and complex physical property based depositional models.

4.4 Suggested Age Scales and Additional Environmental Sensitive Bulk Sediment Parameter of Site 1095

4.4.1 Time Scales

In addition to the previously published time scale (ODP Leg 178 Shipboard Scientific Party, 1999) other time scales have been proposed as a result of post-cruise studies. The different time scales and their consequences for the linear sedimentation rates are shown in Fig. 4.1. In general the shipboard biostratigraphy and magnetostratigraphic reversal time scales produce very similar age / depth relationships (Fig. 4.2A, B). The main differences occur within the interval between 180-280 mbsf and, less siginificantly, in an interval around 60 mbsf (Fig. 4.2A). In these intervals the biostratigraphic datums indicate initially steeper and subsequently gentler slopes (corresponding to higher and lower apparent sedimenation rates) compared to the magnetostratigraphy. Iwai (2001; personal communication) shifted the shipboard magnetic chronology to fit the diatom data (Fig. 4.2A,B) – the result is seen in Fig. 4.1B. This suggests two distinct long-lasting hiati (upper: ~60 mbsf, 1.25-2.53 Ma; lower: ~220 mbsf, 5.04 -6.14 Ma). Acton (2001; personal communication) also revised the shipboard magnetostratigraphic timescale, incorporated post cruise u-channel magnetic data. Magnetic u-channel data are thought to be better than split core data due to the removal of the drilling-disturbed outer part of the core. Overall, the revised age model appears to be designed to avoid short term changes in sedimentation rate (Fig. 4.1C). In the age / depth representation the revised Acton model is smoother than the shipboard time scale around 60 mbsf (Fig. 4.2B).

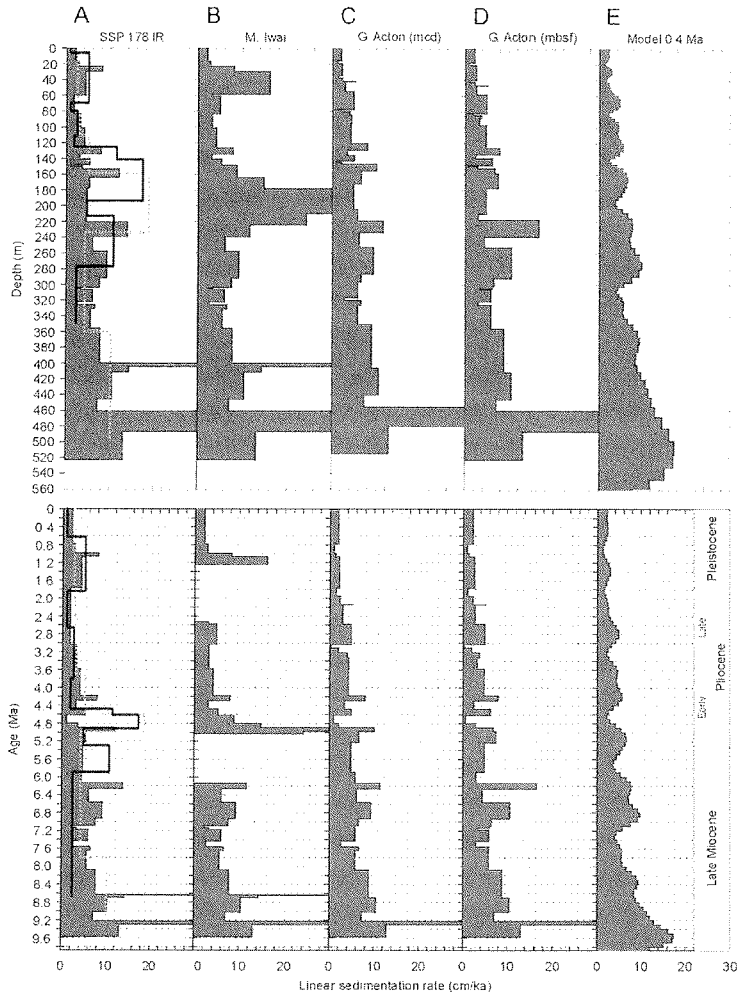

Fig. 4.1. Linear sedimentation rate (SR) models proposed for Site 1095 plotted against age and depth. (**A**) Shipboard Scientific Party (1999) sedimentation rate (cm/ka) vs. depth (mbsf) determined from geomagnetic polarity transitions and diatom and radiolarian datum. The filled bars represent paleomagnetic data from the combined core and Geological High-Resolution Magnetic Tool (GHMT logging tool) data sets, the dashed line indicates radiolarian data, and the solid line corresponds to diatom data. The abrupt spike in the paleomagnetic data at ~400 mbsf corresponds to an interval that has been interpreted as a cryptochron and whose absolute age and duration are not well known (see Initial Report Volume, ODP Leg 178 Shipboard Scientific Party, 1999). (**B**) Revised magnetic stratigraphy based on diatoms (personal communication Iwai, 2001). Note the two large hiati suggested by this model. (**C**) A revised magnetostratigraphic time scale incorporating u-channel magnetic data by Acton (2001; personal communication). The SR are based on the spliced composite depth scale (mcd) of Barker (2001). The main difference to the SSP time scale (SSP = ODP Leg 178 Shipboard Scientific Party on board time scale). (**A**) is the shift of the onset of Chron C2An.1n (3.040 Ma) from 82.22 mbsf to 58.88 mbsf (Hole1095D). (**D**) The revised time scale of Acton (2001; personal communication) converted to mbsf. (**E**) SR resulting from low pass filtering of the age depth relationship implied by (**C**). The filter (equiripple filter, bandpass) was applied in geological time domain and reduces time resolution to about 0.4 Ma. The „model 0.4" – timescale is used in other graphs and discussions and sometimes given as complementary information to figures still based on the Shipboard time scale (**A**).

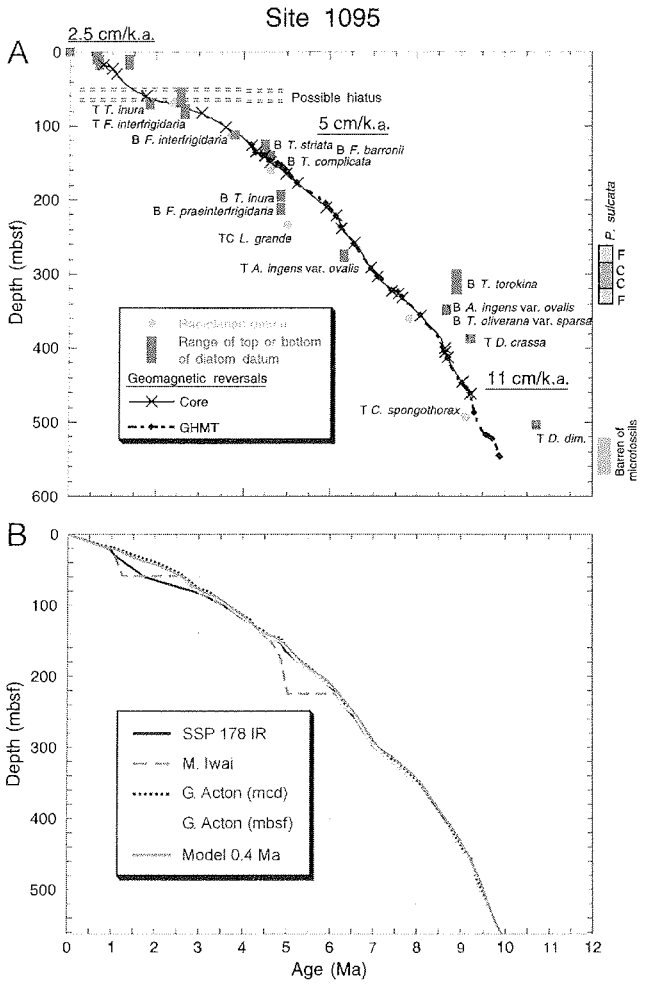

Fig. 4.2. Depth vs. age profiles for Site 1095. **(A)** Shipboard compilation of ages determined from geomagnetic reversals (interpolated) and diatom and radiolarian datums. Intervals of diatom datums are marked with a box indicating the distance between the samples used to define the first- or last occurrence interval. *P. sulcata* abundance is indicated by gray bars. Radiolarian datums are indicated by circles. In labels indicating species identity, T = last occurrence, B = first occurrence, and TC = top common occurrence. The hole is barren of microfossils below ~520 mbsf. Mean sedimentation rates (underlined) for three intervals show an uphole decrease. Refer to the ODP Leg 178 Shipboard Scientific Party (1999) for the full names of the biostratigraphic species. **(B)** depth vs. age plots of the magnetostratigraphic models presented in Fig. 4.1, see text for discussion.

Since the discussion between biostratigraphers and magnetostratigraphers regarding the time scale is ongoing, the revised magnetic time scale of Acton has been used in this thesis because it incorporates a larger number of datums. The original scale has been converted to mbsf and simplified by means of a low pass filter with a resolution of ~0.4 Ma. This removes short depth intervals with suspicious rapid increases and decreases in

sedimentation rates and also balances some of the differences in the various age models. The step back to mbsf (in this case almost identical with the recovery-corrected composite depth, mcd) allows direct comparison with previously published graphs and data. Futhermore, the two existing spliced tables by ODP Leg 178 Shipboard Scientific Party, 1999 and Barker, in press, can not be validated independently in the lower part of Site 1095 since no multiple cores are available for depths below ~90 mbsf.

The lower hiatus proposed by Iwai (2001, personal communication; Fig. 4.1B), based on diatom data, has not been confirmed by core or seismostratigraphic analysis. However, the upper hiatus falls within seismostratigraphic Subunit IIa with truncated reflectors (see chapter 4.2.2.3) and also correlates with an abrupt change in sediment fine fraction data around 60 mbsf (Fig. 4.1A,B). The duration of this hiatus may be not as long as proposed by Iwai (1.25-2.53 Ma) or suggested by Hillenbrand and Fütterer (1.77-2.581 Ma). Acton sees no evidence for a hiatus at this level. I estimate the maximum duration of the hiatus to be closer to 0.6 Ma, starting around 1.7 Ma. It probably eliminates the upper part of the *Thalassiosira vulnifica* zone (3.2-2.3 Ma)[15].

4.4.2 Environmentally Sensitive Bulk Sediment Parameters: Opal, $CaCO_3$, TOC

4.4.2.1 Parameters and Methods[16]

In order to supplement the grain-size information presented in Chapter 4.3 additional proxy parameters are discussed here. $CaCO_3$ and TOC (325 samples for site 1095) were determined using a LECO CS-125 analyser. In the first of two subsamples Total Carbon (TC) was directly measured. In the second subsample inorganic carbon (IC) was removed and TOC

[15] Note: In the first part of the thesis all ages (if note indicated otherwise) refer to the shipboard time scale ("SSP"). Starting from this point in the document all ages refer to the "Revised" time scale. For the purpose of convenient transformation refer to the age bars e.g. in Fig. 4.1, Fig. 4.3, Fig. 4.4.

[16] Some of the data presented data in this chapter have been published in:

Wolf-Welling, T.C.W., Moerz, T., Hillenbrand, C.-D., Pudsey, C.J., and Cowan, E.A., in press. Data report: Bulk sediment parameters (CaCO3, TOC, and >63 μm) of Sites 1095, 1096, and 1101, and coarse fraction analysis of Site 1095 (ODP Leg 178, western Antarctic Peninsula). In Barker, P.F., Camerlenghi, A., Acton, G.D., and Ramsay, A.T.S. (Eds.), Proc. ODP, Sci. Results, 178. and

Hillenbrand, C.-D., and Fütterer, D.K., in press. Neogene to Quaternary deposition of opal on the continental rise west of the Antarctic Peninsula, ODP Leg 178, Sites 1095, 1096, and 1101. In Barker, P.F., Camerlenghi, A., Acton, G.D., and Ramsay, A.T.S. (Eds.), Proc. ODP, Sci. Results, 178.

was measured analog to the first subsample. For further details see Wolf-Welling et al. (2001) and Wolf-Welling (1991).

$$IC(w\%) = TC(w\%) - TOC(w\%)$$

$$CaCO_3\ /w\%) = IC\ (w\%) * 8.333$$

The opal data have been made available by Hillenbrand (2001; personal communication). A total of 233 samples from sediment cores of Hole 1095A and B were analyzed, at an average sample interval of 2.4 meters. The weight % opal content has been analyzed by an automated leaching technique after Müller and Schneider (1993) with subsequent time dependent spectrophotometric analysis. Refer to Hillenbrand and Fütterer (2001) for details.

Bulk accumulation rates and accumulation rates for single parameters were calculated based on the new linear sedimentation rate shipboard index porosity and wet bulk density data, and averaged MST grape densities revised by Volpi et al. (2001). The following relations were applied (for an evaluation of the method see Wolf, 1991) for the derivation of accumulation rates:

$$AR_{Bulk} = LSR * Density_{DryBulk} \qquad \text{(Eq. 4.1)}$$

$$Density_{DryBulk} = Density_{WetBulk} - (k * Porosity\ (vol.\%) * 0.01)$$

$$AR_{X(w\%)} = AR_{Bulk} * X(w\%) * 0.01$$

AR_{Bulk}	=	Bulk accumulation rate or mass flux)
LSR	=	Linear Sedimentation Rate
$Density_{DryBulk}$	=	Dry Bulk Density
$Density_{WetBulk}$	=	Wet Bulk Density
k	=	Density correction for pore fluid salinity = 1.0363 (Boyce, 1976)
$AR_{X(w\%)}$	=	Accumulation Rate of Component X in weight %

4.4.2.2 Interpretive Data Description

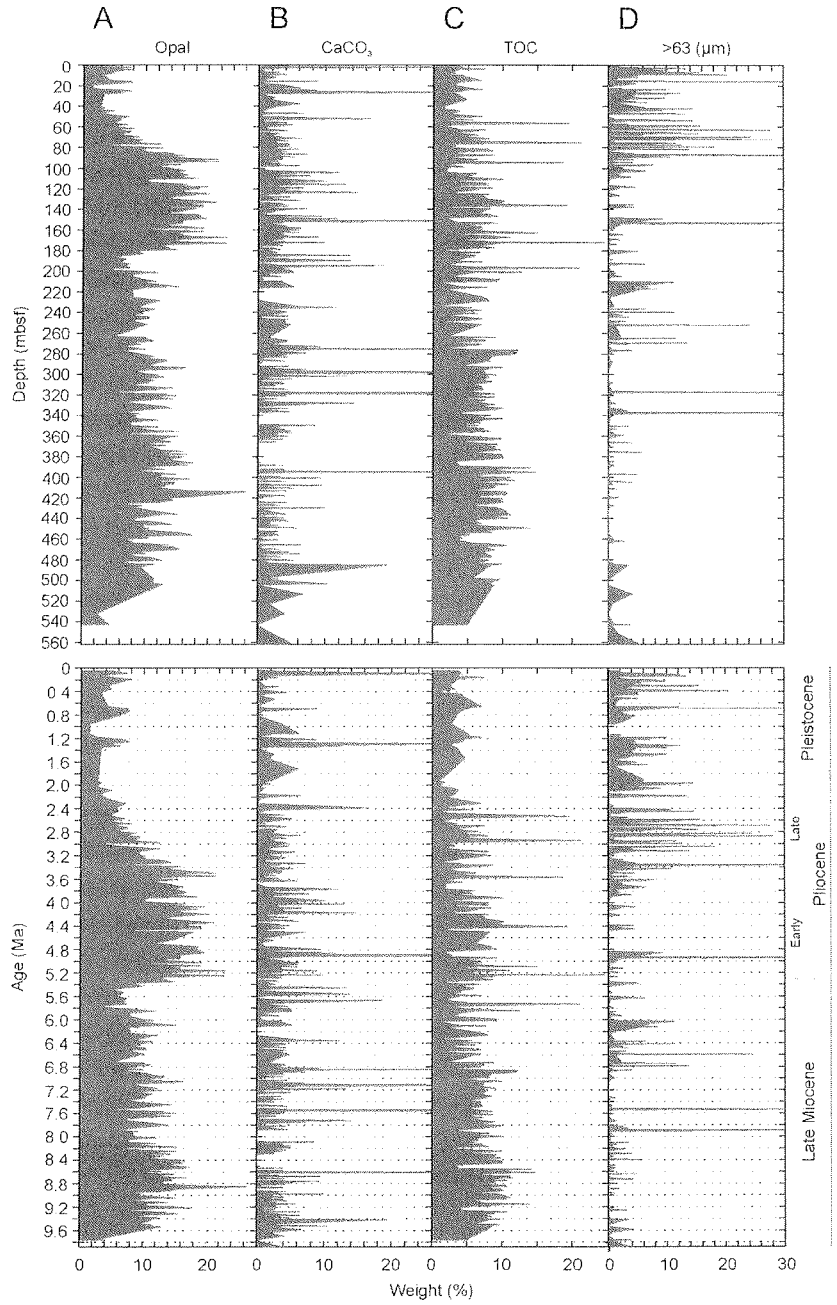

Fig. 4.1. Selected bulk sediment parameters at Site 1095, given in weight percent, plotted vs. depth and age. Note that the significant high in opal content between 180 and 80 mbsf (Early Pliocene) corresponds to an interval of reduced > 63 µm grain occurrence.

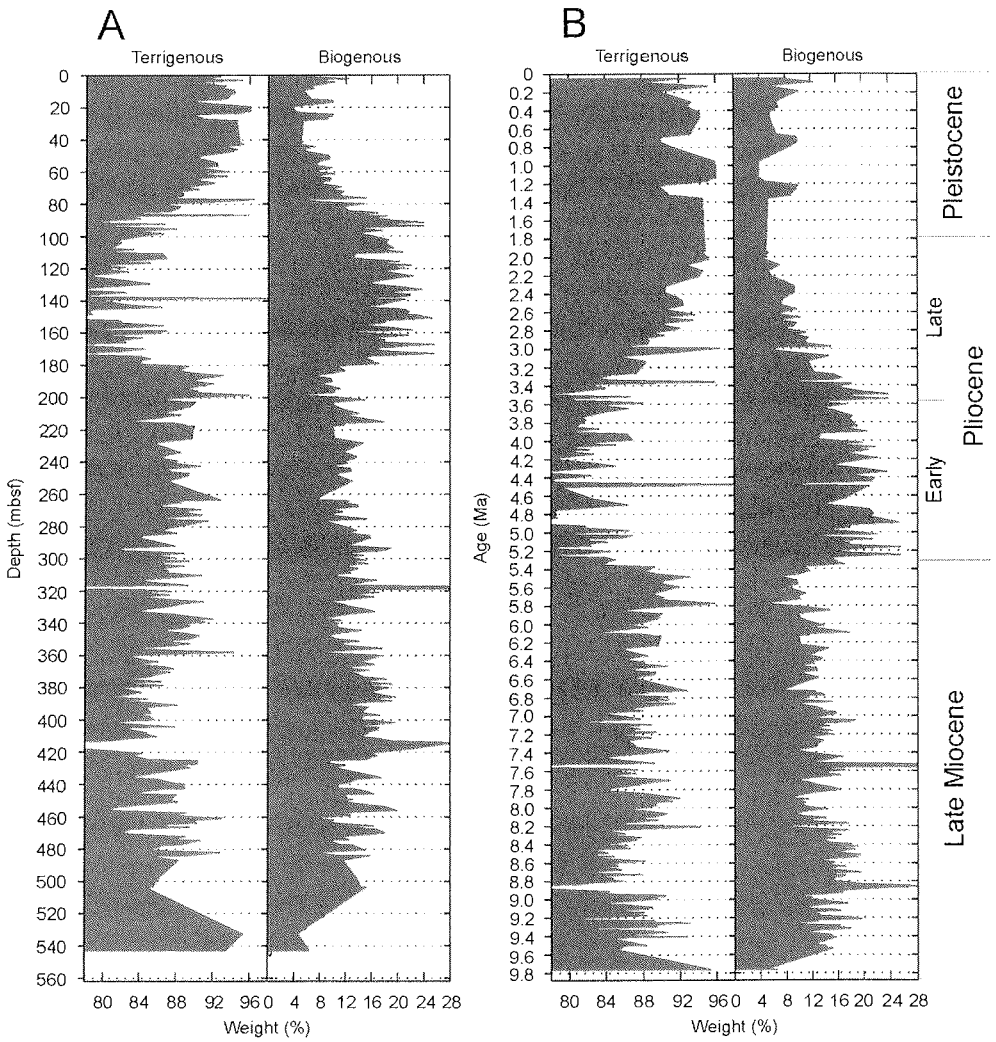

Fig. 4.2. Summary of terrigenous and biogenous weight percent data for samples from Site 1095, plotted vs. depth and age.

Instead of a parameter by parameter description of the following graphs only general trends are discussed and important links between parameters are indicated. A summary of all drift-related proxy parameters of the rise sediments in a time and process context follows in chapter 4.6.

As seen in Fig. 4.1, the opal and >63 μm grain-size data display high variability in both age and depth plots. They are generally accepted as paleoenvironment indicators. Opal content in sediments from the Bellingshausen Sea and Antarctic continental margin is regarded as a proxy for productivity changes in the surface waters (Hillenbrand and Fütterer,

in press). Since biological productivity in the Circumantarctic surface waters is not limited by nutrient supply (Defelice and Wise, 1981) or water temperature, the growth of planktonic algae (diatoms) is mainly controlled by the availability of light. Light intensity is a function of the presence or absence of sea ice. Hence, opal content is an indicator for the presence and duration of sea ice above Drift 7.

Except for the few low opal content values below 510 mbsf (Fig. 4.1A) that may reflect diagenetic processes (see chapter 4.5.1 for details) and the high values of the Early Pliocene, the general decline from late Miocene to Present is interpreted as reflecting a decrease in surface productivity and hence an intensification of sea ice cover. The abrupt high in opal content during the Early Pliocene (5.3-3-5 Ma) correlates with a low in >63 μm and may reflect a warm period with reduced or no sea ice cover. A summary of biogenic and terrigenous weight percents vs. depth and age is given in Fig. 4.2.

In interpretations accumulation rates are preferred to sedimentation rates since the effect of compaction with depth leads to artificially reduced sedimentation rates. Bulk accumulation rates, and the porosity and density data used for their generation, are shown in Fig. 4.3. Porosity and density values show an abnormal undercompacted trend with depth (see Brückmann, 1989). Below 500 mbsf density increases correspond to a strong decrease in porosity. This is indicative of diagenetic processes discussed further in chapter 4.5.1. The accumulation rate curve (Fig. 4.3) can be described as an exponential decay function with respect to depth and age. The curve shows no anomalies within the Early Pliocene that would support the WSI over the EPD theory. In contrast to Barker's (1995) prediction, a cyclic pattern with decreasing absolute amplitudes in bulk accumulation persists throughout this time. The sharp decrease in accumulation rate at 310 mbsf (7.4 Ma) corresponds to the lower part of seismostratigraphic Subunit IIe (Fig. 4.1, Fig. 4.2). This may be the termination of the drift growth stage (as defined by Rebesco et al., 1997; Fig. 4.1). The influence of glaciation on accumulation rates on the rise will be further discussed in chapter 5.

The conversion of component weight % to accumulation rates (Fig. 4.4, Fig. 4.5) for trace components (e.g. TOC or $CaCO_3$) does not provide new insights because the bulk accumulation rate overwhelms the trace component data. However, opal contents of up to 20 weight % may not suffer too much from this effect. Noteworthy is the continuous decline in the opal accumulation rates starting around 3 Ma (Fig. 4.4A) in conjunction with the onset of the Northern Hemnisphere Glaciation (NHG).

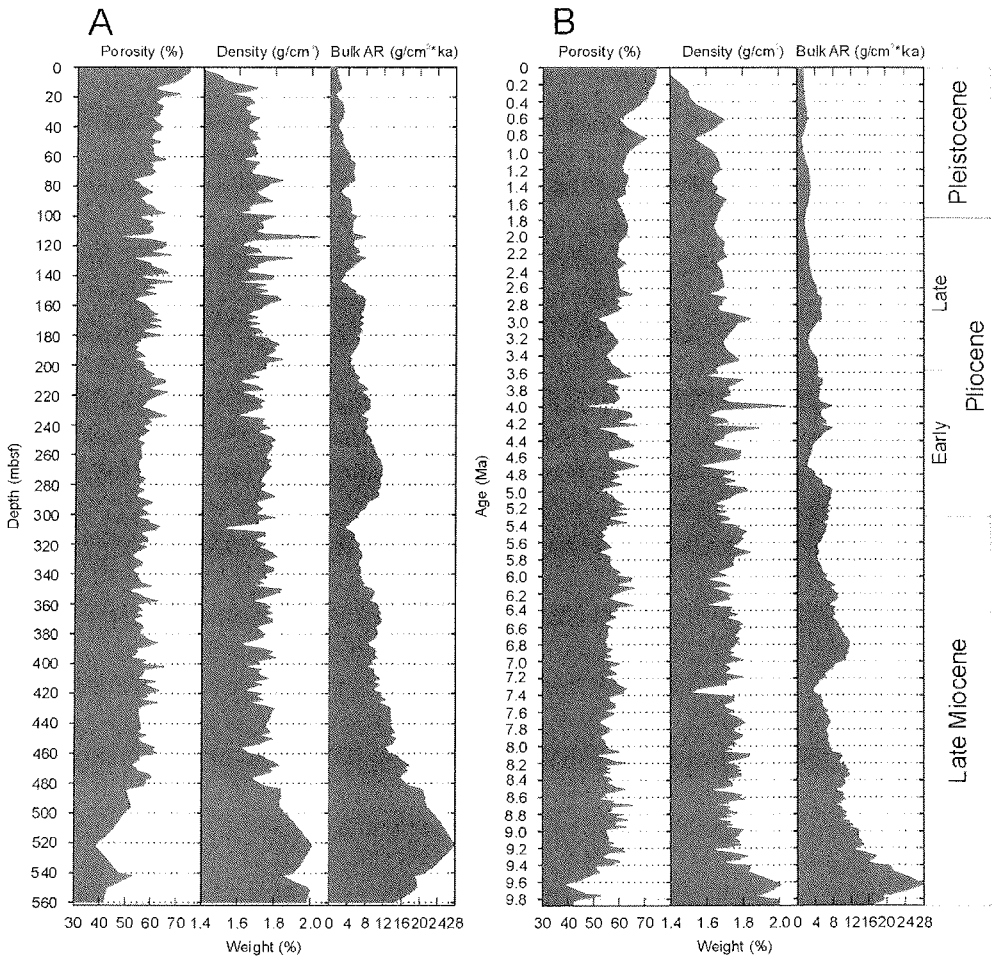

Fig. 4.3. Bulk accumulation rates (mass flux) of Site 1095 derived from the linear sedimentation rates of the „model 0.4" shown in Fig. 4.1E and the porosity and density compilations of Volpi et al. (2001). Even though the bulk accumulation rates are heavily dominated by the sedimentation rates, the intervals with slightly higher densities (probably linked to glacial debris input) agree well with intervals of higher sedimentation (Fig. 4.1) and accumulation rates.

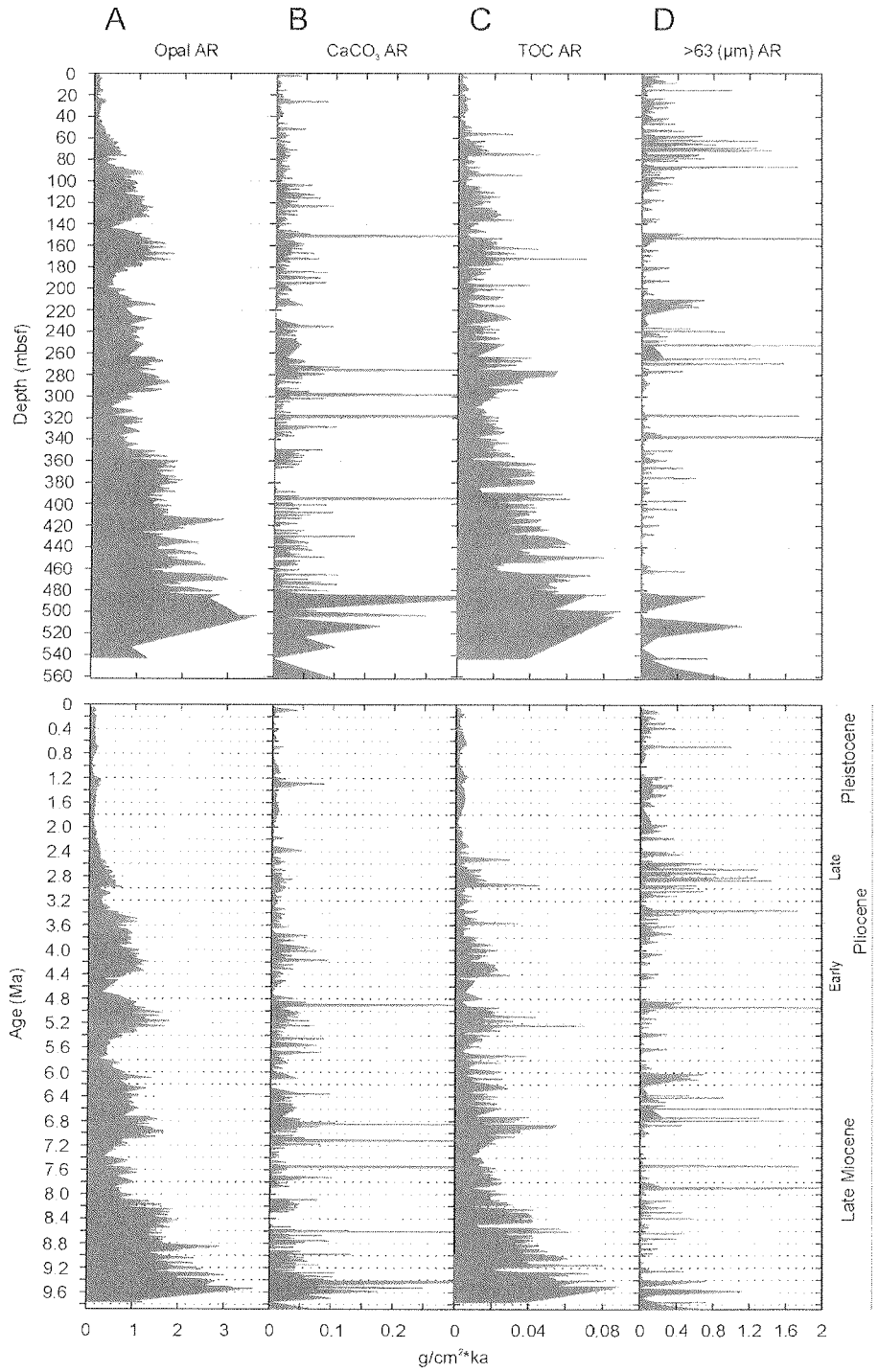

Fig. 4.4. Accumulation rates for selected sediment parameters at Site 1095. The calculations are based on the total bulk accumulation rate (Fig. 4.3) and the weight percent of the individual parameters (Fig. 4.1).

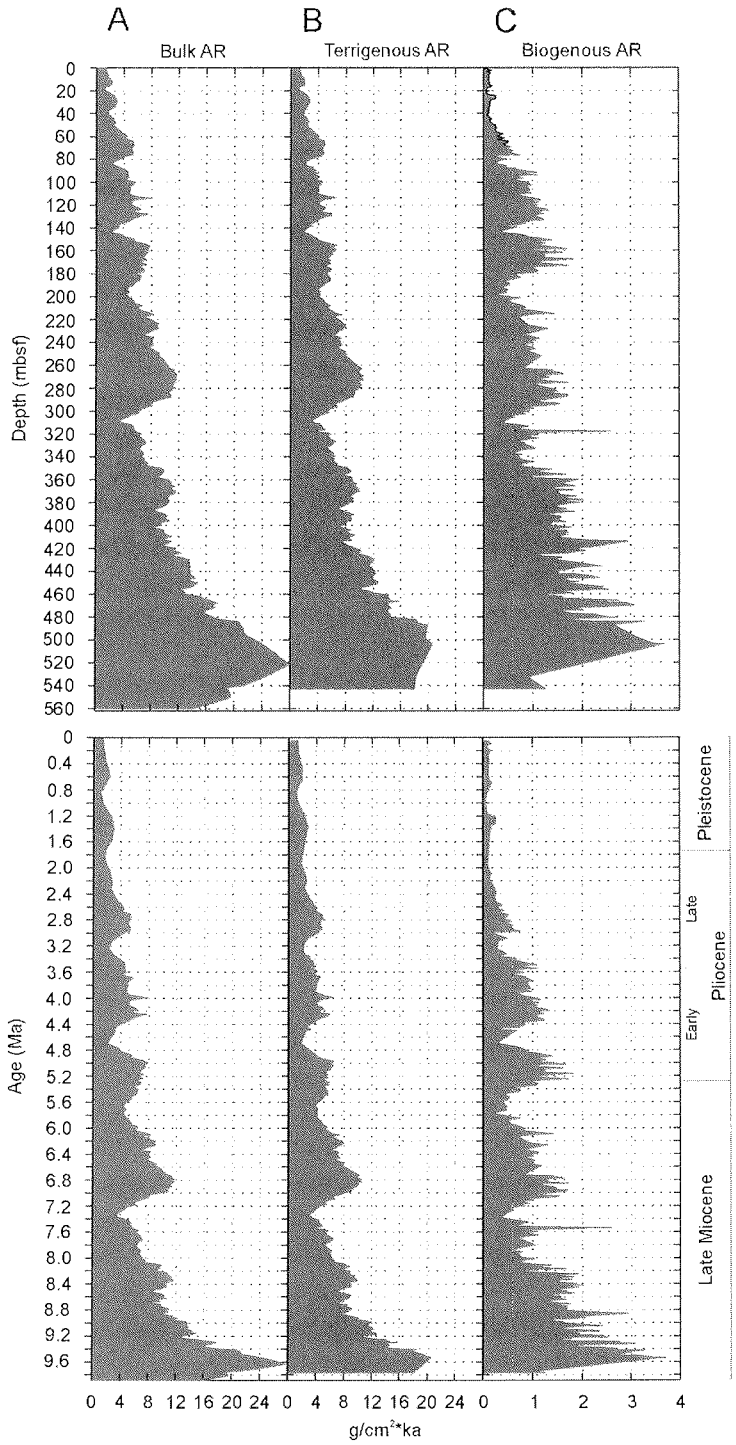

Fig. 4.5. Summary of terrigenous and biogenous accumulation rates compared to the bulk accumulation rate for samples of Site 1095 plotted vs. depth and age.

4.5 Peculiar Reflectors

4.5.1 The Double BSR Enigma – Diagenetic vs. Hydrate Origin

A strong deep bottom-simulating reflector (BSR_L) is seen in seismic profiles along the continental rise at 550 to 600 mbsf (corresponding to ~650 ms TWTT below sea floor at Site 1095; Fig. 4.1). This BSR_L is most obvious beneath the elevated parts of the drifts, especially at the steep SW sides close to the ridge crests (Fig. 4.1). Beneath the gentler flanks it merges gradually with the sea floor-parallel lithological bedding reflectors and hence is more difficult to detect. This lower BSR is regional and has been observed in Drifts 7, 6a, 6b (following Rebesco et. al., 1997). A BSR that is similar with respect to character and location in TWTT below the sea floor has been described in the southwestern part of the Scotia Basin (Tanahashi, 2001). In recent literature there is a consensus for linking the BSR_L to a diagenetic front (Opal A to CT transition) and for rejecting the idea of a hydrate origin (Camerlenghi et al., in press; Rebesco et al., 1997; Barker and Camerlenghi, 1999; Lodolo and Camerlenghi, 2000). The following arguments support the diagenetic nature of the BSR_L:

- A tentative positive polarity associated with the BSR_L (Barker and Camerlenghi, 1999).
- The diffuse nature of the BSR_L compared to a discrete reflector thought to be characteristic of a Hydrate BSR.
- The predicted geothermal gradient over the 43-37 Ma old crust and *in situ* thermal data collected at Site 1096 and evaluated by Barker (ODP Leg 178 Shipboard Scientific Party, 1999) suggest that a Hydrate BSR might exist 200 m above the observed BSR_L.
- Centimeter-size, fully indurated cherts have been found in the lowermost part of the section at Site 1095B.
- The porosity decrease and density increase in this core interval (below 500 mbsf), combined with a sharp increase in seismic velocity (Fig. 4.3, Fig. 4.1 starting 510 mbsf at Site 1095) is attributed to biogenic opal dissolution and reprecipitation (chapter 4.1.2 and Camerlenghi et al., in press)
- Biostratigraphic samples below 510 mbsf at Site 1095 are barren of siliceous microfossils, supporting the idea that diagenesis is important below this depth.

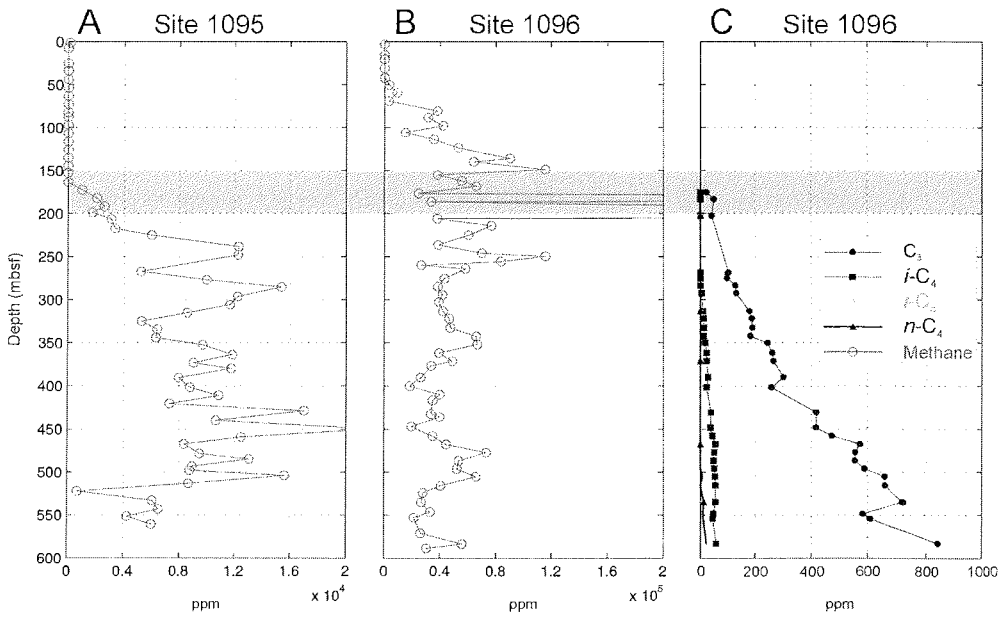

Fig. 4.1. Hydrocarbon pore space volatiles at Site 1095 and 1096. (**A**) Methane concentration from headspace samples at Site 1095 (Scale is in 10^4 * ppm). (**B**) Methane concentration from headspace samples at Site 1096 (Scale is in 10^5 * ppm). (**C**) C^{3+} hydrocarbon concentrations measured in vacutainer samples extracted from gas pockets. Data from: ODP Leg 178, Shipboard Scientific Party (1999).

The identification of a second, upper BSR (BSR_U) during intense seismostratigraphic studies on board the ship during Leg 178 (Fig. 4.2) requires reappraisal of the arguments for a purely diagenetic nature of the BSR_L. This upper BSR has not been described previously and is not seen on the lower resolution 1992 seismic profiles (compare the 1995 Fig. 4.1B profile with the 1992 Fig. 4.1C profile). BSR_U is at as depth of approximately 150-180 mbsf, corresponding to 200 ms TWTT below sea floor, at Sites 1095 (Fig. 4.2) and 1096. As with BSR_L the upper BSR is best seen on the steep SW side of Drift 7. On the more gentle dipping NW side of the drifts the BSR_U is not obvious but may blend in to sea floor parallel lithological reflectors. The BSR_U as well as the BSR_L cut across lithologies and time lines and roughly follow the sea floor morphology. The following arguments support a possible hydrate origin of both the lower and upper BSR:

- The upper limit of hydrate occurrence is not physically defined. At Drift 7 the pressure / temperature stability field of hydrates should reach the sea floor (bottom-water temperature ~ 0°C, depth = 3152 mbsf (Site 1096) and 3840 mbsf (Site 1095). A second limiting factor, the occurrence of volatile hydrocarbons (methane) in the pore

space, controls the upper boundary of hydrate formation. At the base of the sulfur reduction zone (the sulfate-methane transition zone) hydrocarbons (methane) are oxidized by anaerobic microrganisms (Kasten and Joergensen, 2000). At Drift 7 the BSR_U occurs at the base of the sulfate reduction zone where methane and higher hydrocarbons become abundant (Fig. 4.1A, C) or are already present in considerable concentrations (Fig. 4.1B).

- The BSR_U lies in a zone of abnormal *in situ* acoustic velocity not found by laboratory measurements (Fig. 4.1B). An increase in velocity is suspected when entering a hydrate-bearing zone.
- A short abrupt increase in formation resistivity (between 180 mbsf and 200 mbsf, ODP Leg 178, Site 1095, Shipboard Scientific Party, 1999) seen in the downhole logs could correlate with hydrate at the depth of the BSR_U.
- The polarity of an upper hydrate BSR should be positive since hydrate-filled pore space provides a higher impedance than the overlying fluid/gas filed pore space. The observed polarity of the BSR_U is positive with respect to the main sea floor reflection (Fig. 4.2).
- The anomalous, underconsolidated porosity and density profiles previously explained by variations in density, porosity and rigidity of diatom frustules forming the biogenic opal (Camerlenghi et al., in press) may actually reflect hydrate stabilization of the pore space.
- Published *in situ* geothermal gradients for Site 1095 and 1096 vary considerably. Logging temperature profiles indicate a minimum geothermal gradient of 24°C/km at Site 1096 and 33°C for Site 1095. However, shipboard Adara- and Davis-Villinger Temperature Probe analyses by Barker (ODP Leg 178 Shipboard Scientific Party, 1999) indicate a geothermal gradient of ~80 °C/km. A recent ODP heatflow report (Pribnow et al., 2000) based on the same Adara- and Davis-Villinger Temperature Probe data come up with a geothermal gradient of only ~52 °C/km for Site 1096.

  A hydrate stability curve was calculated based on pore gas composition and pore water salinity using the thermodynamic modelling software EQUIPHASE HYDRATE V. 5.0[17]. According to this calculation the BSR_L is stable at Site 1096 for a geothermal gradient of around 50°C/km.

[17] EQUIPHASE HYDRATE, from D.B. Robinson & Associates, Edmonton, Alberta, Canada

This is one of the few locations where two BSR can be observed (Posewang and Mienert, 1999). Arguments can be made for a diagenetic and hydrate related origin of BSR_L and a top of hydrate explanation for the BSR_U. It is possible that hydrates define zones of restricted pore fluid movement, inhibiting opal dissolution and reprecipitation. Below the hydrate stability zone the pore space collapses and opal diagenesis can take place. The patchy occurrence of small amounts of hydrate in the porespace may account for the differences between acoustic models based on laboratory data and seismic profiles.

4.5.2 Reflector "X"

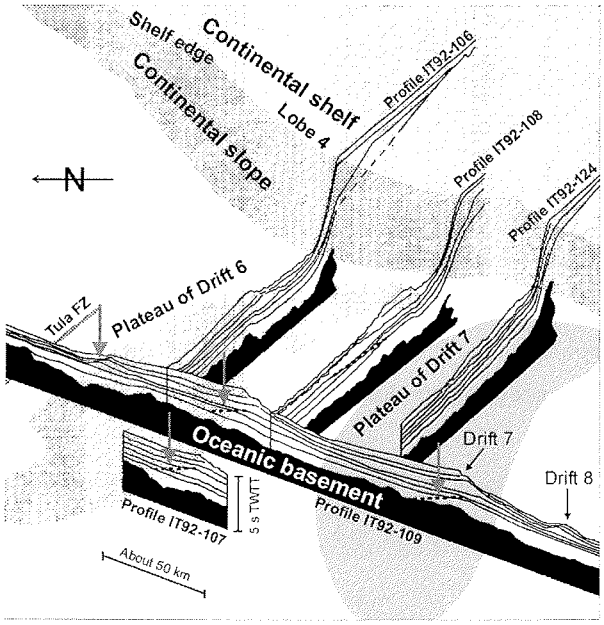

Fig. 4.1. Fence diagram of the Antarctic Peninsula shelf and slope using simplified line drawings of seismic multichannel profiles parallel and perpendicular to the margin. The locations of enigmatic Reflectors "X" and other paleo current indicators are marked (arrows). Figure modified from Rebesco et al. (1997).

An enigmatic Reflector "X" (Rebesco et al., 1997), that appears to cut across other horizons (Fig. 4.1) for almost 1s TWTT is observed beneath Drifts 5, 6, and 7 (Fig. 4.1). At Drift 7 Reflector "X" merges with the top of seismostratigraphic Unit V below the drift crest. The dip of this reflector is to the NE, at angles between 3 and 4 degrees (Rebesco et al., 1997). Reflector "X" is best seen beneath the gentle side of the drifts where it has a steeper dip than the underlying and overlying strata. However, it is continuous on the steeper side (SW side) of the drifts, where its dip is similar to the underlying and overlying strata. Two different

suggestions have been made regarding the nature and origin of Reflector "X" (also called EUT by McGinnis and Hayes, 1995):

- Reflector "X" may represent the traces of local diachronous hiati within areas of otherwise continuous deposition (Rebesco et al., 1997).
- Reflector "X" may be a low angle, gravitationally-induced detachment surface area (Rebesco et al., 1997).
- Reflector "X" may be a regional unconformity caused by a strong bottom current event or a bottom current reversal. Its orientation would then record an ancient bottom current direction opposite to that observed today.

The idea of Reflector "X" being the result of ancient current activity is appealing. The argument by Rebesco et al. (1997) regarding the different depth of this hiatus at different locations is not contradictory since currents can migrate over time. Episodes of erosion and redeposition may have occurred over a long period of time. By interpolating the ages at the base of the holes to the new ocean crust ages (Fig. 4.1) the age of the current reversal may be estimated to be ~ 22.6 Ma. During this time the Drake Pasage was not as deep and wide as it is today and may not have accomodated the ACC and the counter current of the ABW (Fig. 1.1). Additionally the passive margin has not reached further than the Mid shelf high (chapter 5) shifting the rise 50 km further NW relative to the shelf edge. At this time a distance of 50 km might have been sufficient to bring what is today the rise under the influence of a precursor of the ACC.

4.6 Discussion and Interpretation

4.6.1 Depositional Processes and Models for the Rise

On board the ship the lithostratigaphic working group and especially Nick Eyles (ODP Leg 178 Shipboard Scientific Party, 1999) developed a sequence stratigraphic framework for the rise. The model is based on three turbiditic facies L1-3 (Fig. 4.1) that are described in the classical TA to TE model of Bouma (1962) with additional refinement referring to the classification of muddy turbidites by Piper (1978). He further subdivided the TD and TE divisions of Bouma into laminated silt (D), laminated mud (E1), graded mud (E2), ungraded mud (E3), and pelagic or hemipelagic (H) intervals. Depending on the proximity of deposition the facies L1-2 lack one or two of the lowermost higher energetic subdivisions (Fig. 4.1). For

a detailed description of the subdivisions refer to cited literature or the ODP Leg 178 Initial Result volume. According to the shipboard interpretation, contourite facies *per se* does not occur alone as singular features but may be ancillary present in subdivisions TE1-3 to TE3-H (see facies C in Fig. 4.1).

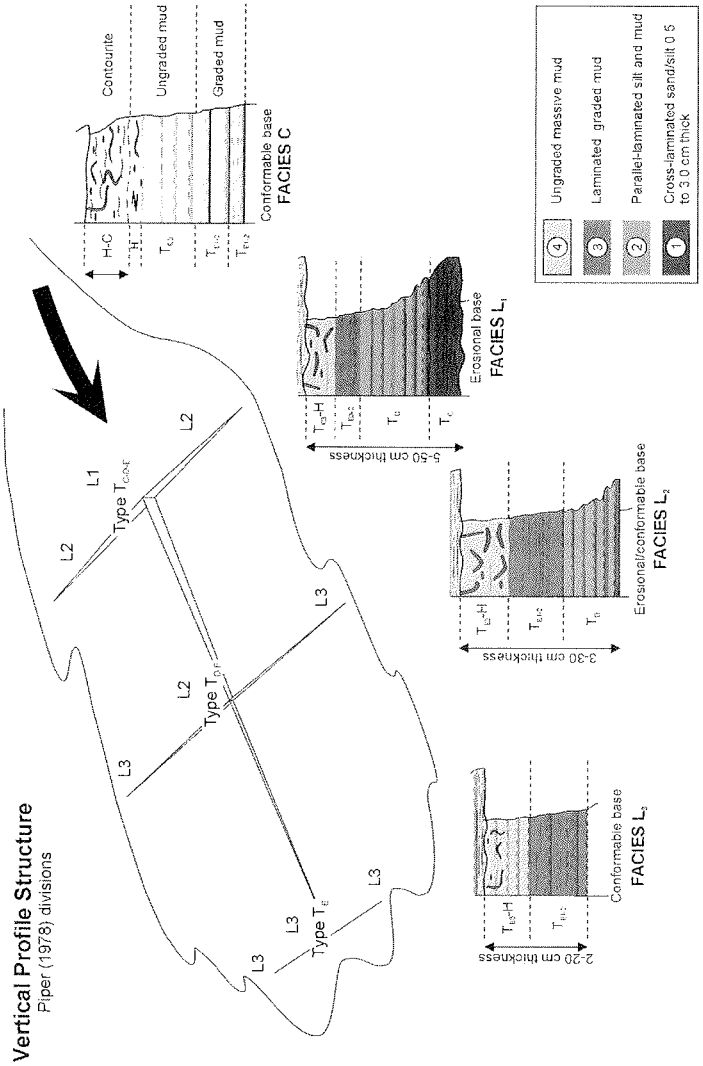

Fig. 4.1. Schematic diagram showing typical downslope and across-slope relationship between turbidite Facies L1, L2 , and L3 as proposed by Stow and Piper (1984). Schematic representation of internal structure of facies within turbidites recovered during Leg 178. The standard Bouma scheme is refined with a descriptive classification for muddy turbidites (Piper, 1978). Facies C (contourite) is similar in the lower part to Facies L3 but with a contourite influenced in the facies subdivisions H-C. Facies C can occur as an ancillary component in the hemipelagic H interval of fine-grained muddy turbidite Facies L1-3. Figure modified from ODP Leg 178 Shipboard Scientific Party 1999.

This theoretical scheme however has two main deficiencies:

- Fine-grained turbidites and contourites represent end members of a continuum of deep-sea sediments that accumulate in a very low energy setting and may be not distinguished by "hand lens powered" visual core description or sparse sampling (1 sample per meter).
- Facies L1-3 are entirely process-related and contains no strong links to margin-specific environmental parameters like ice or currents.

4.6.2 Integration of the Grain-Size Statistic Data Populations and the Facies Model

Fig. **4.1** presents a first attempt at integrating grain-size data into the facies model. None of the populations other than 1 is correlated with distinct facies types (L1-3). Nor does the first order cyclicity, which is linked to depositional energy, correlate with mean grain-sizes of the samples (Fig. 4.37). To overcome the limitations of the sequence stratigraphic facies model, the facies are broken down to their basic units, assuming that the sparse sampling was fine enough to resolve single process-related sediment volumes. Depositional processes thought to act during drift build-up and maintenance are:

1) Hemipelagic settling during times of slow and low depositional energy, often associated with intense bioturbation and an enrichment of IRD. The intensity of bioturbation, amount of ice-rafted debris, and extent of hemipelagic bed tops depend on the recurrence interval of turbidite events. Facies association TE3-H.
2) Deposition and partial erosion by means of bottom contour currents, causing winnowing of already deposited sediment. Resulting in coarse skewed grain-size frequency distribution curves. This process is highly variable in intensity at longer time periods and may affect a large spectrum of grain-sizes. At the same time this process influences all short-living depositional processes. The base units bof rapid depositional sequences (turbidite-, debris style sedimentation) may be not affected because they are quickly buried. Erosion and redeposition from bottom currents especially affects topic 1 processes and to a lesser extent processes described under topic 3. Facies association C, H to a lesser extent E-D.

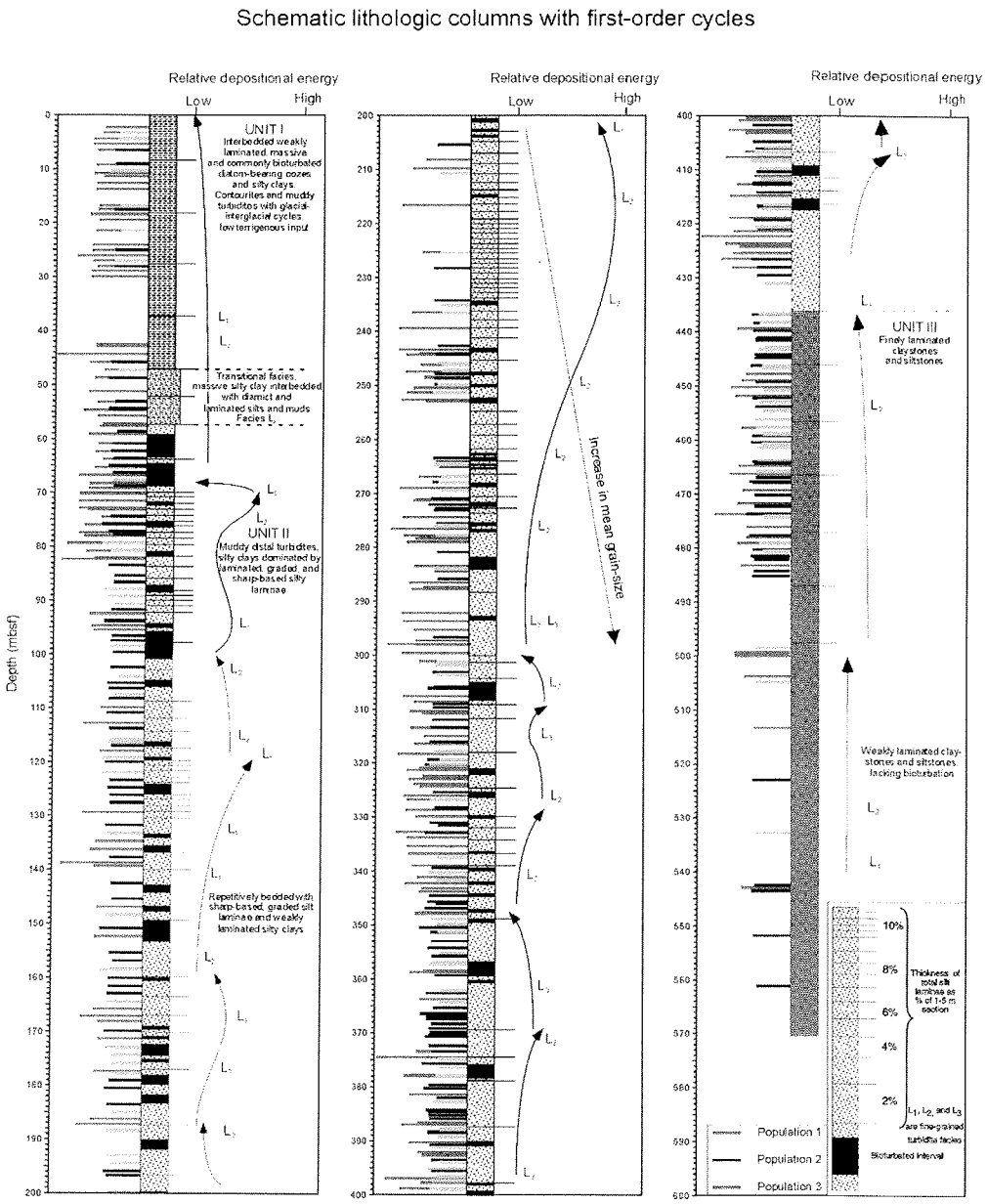

Fig. 4.1. Simplified schematic lithostratigraphy of Site 1095 showing dominant lithology, intensity of bioturbation, and distribution of turbidite Facies L1, L2, and L3. Arrows show broad trends in frequency of sand and silt laminations and facies types, attributed to long-term "first-order" cycles in lithostratigraphic Unit II according to the shipboard model. Grain-size populations 1-3 as defined within this chapter are scaled next to the descriptive units. The length of the bars refers to the relative mean grain-size of the populations.

3) Lower energy turbidites with no or minor basal erosion. These are attributed to slope failure under interglacial conditions (no grounded ice at the shelf edge). Under interglacial conditions the slope is fed with glacial meltwater debris, minor IRD and pelagic material. Entrainment to the rise occurs occasionally via distal overbank deposits and feeding of a nepheloid layer (Pudsey and Camerlenghi, 1998; Rebesco et al., 1996) that is then moved by bottom currents and acts as a distributor reaching remoter parts of the drift bodies. Facies association D-E.

4) Higher energy turbidites and debris flows. These are most likely to occur under conditions in which shelf ice is grounded and reaches to the shelf edge, periodically dumping eroded inland and shelf topset material. In addition, massive IRD input to the upper and lower slope reduces transport distances, allowing coarse and unsorted material to reach the drifts. The recurrence interval of successive turbidite events during shelf ice advances is probably short, which reduces the time for undisturbed hemipelagic accumulation. Facies association TC-TD.

4.6.2.1 Grain-Size Population 3

Population 3 has the lowest average mean (Fig. 4.1) but is the most variable population with respect to its skewness, mean and standard deviation (sorting) values (Fig. 4.1). The depositional process responsible for this characteristic must be continuously scalable in depositional energy, but at the same time retains distinctly better sorting, even for populations that show comparable mean values than does Population 2 (Fig. 4.1 C). Comparisons with core descriptions and the simplified lithological column (Fig. 4.1) link this population to bioturbated intervals. Bioturbated intervals are found in the sequence tops of all proposed facies. Sequence tops (depositional process 1) have the slowest accumulation rates and are subsequently longest exposed to the action of bottom currents and IRD input. However, the limitation of our study to the sortable silt fraction (10-63 μm) has effectively avoided the classical IRD spectrum (sand fraction). The fact that the sum frequency distribution curve of Population 3 is positively skewed (tail in the fines) is interpreted by Pudsey and Camerlenghi (1998) as an indicator of only minor current winnowing (removal of the fines) and, hence, as a negligible contribution of bottom currents to the depositional process. Instead the good correlation of opal content (Fig. 4.1) and skewness (Fig. 4.3 B) rather suggests that the constant influx of comparably coarse organic opal particles or fragments accumulated at sequence tops mask the true nature of the frequency distribution of this population (see also the good correlation of sand and diatom content in the paper of

Pudsey, in press). Another argument for the importance of bottom currents for the definition of Population 3 is the comparably better sorting of this population, since contourite currents are known to increase sorting of sediments (Folk, 1974).

Population 3 is therefore associated with facies subdivision TE3-H and C, and describes low energy hemipelagic, bioturbated sediments under the influence of fluctuating bottom currents. Together with the skewness, kurtosis and opal data the Population 3 density curve may as well be an anti-correlated sea-ice indicator. Accepting that the present link between atmospheric wind (polar easterlies) and bottom currents (westward flow of AABW) being true for the past, Population (especially the density curve, Fig. 4.1) is also positively correlated to bottom-current strength.

4.6.2.2 Grain-Size Population 2

Population 2 shows the smallest variability in standard deviation and mean grain size and has the same kind of tailing toward smaller skewness values as does Population 3 (Fig. 4.1). The depositional process responsible for this characteristic must be closely defined regarding energy and sorting, but at the same time must allow for continuous degrees of winnowing as expressed by the tailing toward smaller skewness values. Based on this observation, Population 2 is associated with facies subdivisions D-E and processes described under topic 3. Supporting this classification as „interglacial turbidite" is the continuous decline in mean grain size of Population 2 upsection, probably addressed to the build-up of the drift above the turbidite channels, making it more difficult to deposit coarser material on the drift crest. The large variability in skewness points to some bottom-current influence, especially on the finer grained members of this data population. The similarities in mean grain size to Population 1 may indicate that part of the deposited material of the „interglacial turbidites" is reworked organic material deposited on the slope. Other constituents probably contain distal meltwater debris from the Peninsula transported to the slope by shelf currents. From a mass flux point of view, sediment supply through mechanism 3 (Population 2) may represent the "cruising gear" supplying continuously small volumes throughout the drift evolution. The observed exponential decrease in mass flux with time (Fig. 4.3) may be related to the decrease of mean grain sizes deposited by this process in an upsection direction with time.

4.6.2.3 Grain-Size Population 1

Population 1 is the coarsest and most unsorted unit with negligible tailing along the skewness axis (Fig. 4.1). From Fig. 4.2 B it is evident that the average distribution curve of Population 3

is perfectly symmetrical. This would indicate the presence of no or only the subtle impact of bottom current. The depositional process responsible for this characteristic must be fast and high in depositional energy. Population 3 is therefore associated with facies subdivisions TD-TC and processes described under topic 4. Supporting this classification as „glacial turbidite" is the good correlation of Population 1 with intervals of > 63 µm (Fig. 4.4) and IRD time intervals (<250 µm) of the rise (Cowan, in press). Since it has been shown that the fine fraction data effectively avoid direct IRD influence (chapter 4.3) the question as to whether the ice-related Population 1 is strongest during a glacial period or occurs at the transition from a glacial to an interglacial (see Pudsey and Camerlenghi, 1998) is of minor importance (sample resolution is not fine enough to resolve single glacial-interglacial variations). Population 1 is seen here as a largely IRD-independent parameter that indicates advances of continental ice to the shelf edge with only short delay times of the sediment on the slope. Population 1 works as an ice indicator also in the lower part of the core where classical IRD definitions, e.g. by Cowan (in press) would fail.

Comparisons of the density curve calculated from Population 1 data (chapter 4.3) with a new global ice volume curve by Lear et al. (2000) shows, that the Messinian and the lower Pliocene have been times of reduced ice volume also reflected in the Population 1 data of the Antarctic Peninsula (Fig. 4.1). Estimates of how dramatic an early Pliocene deglaciation might have been are drawn based on assigning 100% global ice volume to the Pleistocene (Lear et al., 2000). Following the Lear study, global ice volume has been reduced by ~80% throughout the early Pliocene. When taking the Population 1 data is taken into consideration quantitatively, ice volume on the Antarctic Peninsula was reduced by more than 70% (assigning 100% to the maximum values occurring in the Pliocene). Starting from total different perspectives the findings of this study and that of Lear et al. (2000) are in excellent agreement. A deglaciation in the Messinian and early Pliocene is further supported by the eustatic data of Haq et al. (1987) which shows three successive sea-level highs starting in the Messinian and ending in the lowermost upper Pliocene.

These findings, of course, do not define the spatial extent of deglaciation in Antarctica. But a 70-80% reduction in ice volume should require at least ice-free low lands around Antarctica and possible time periods with no ice on the more exposed Antarctic Peninsula (see also remarks by Barrett, 2001).

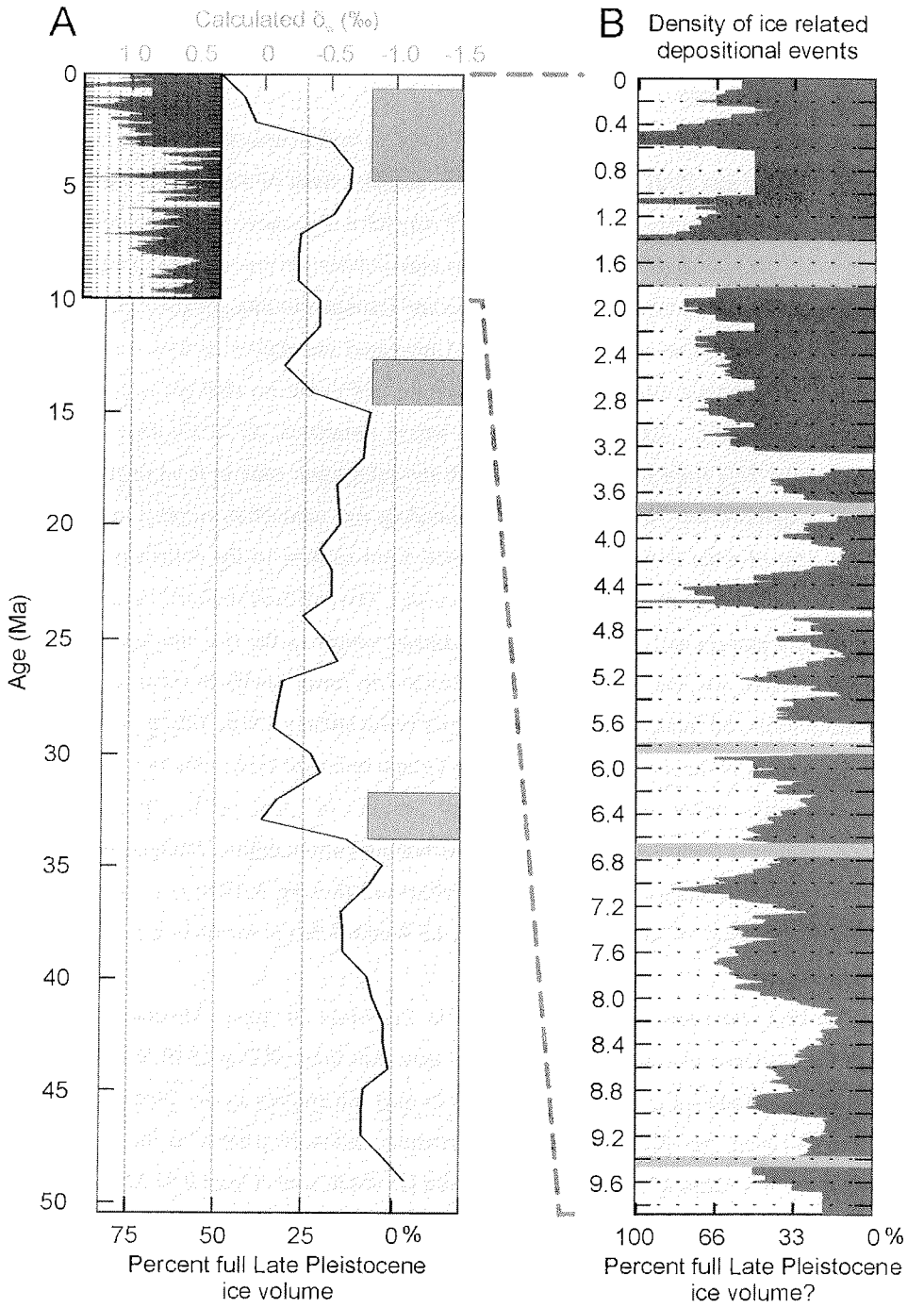

Fig. 4.1. Comparison of: **(A)** global ice volume curve from Lear et al., 2000 and **(B)** the Population 1 density data. The ice volume is calculated by removing the temperature effect from benthic foraminifera $\delta^{18}O$ data using a Ca-Mg thermometer. Dark gray boxes indicate times of major ice growth. (Part **(A)** of this figure is modified from Lear et al., 2000).

4.7 Summary: The Rise as a Recorder of Ice and Currents over Time

4.7.1 Eocene-Miocene

The story of what is today the rise and Drift 7 starts in mid-Eocene times at 42.7 Ma, when the ocean floor below Drift 7 was created on the northern flank of a now-subducted segment of the Phoenix ridge. At that time the study area may have been more than 600 km away from what is today the mid-shelf high (70 km/Ma assumed subduction rate and 21.3 km/Ma known average spreading rate). Deposition was pelagic and restricted to thin covers of the basement. At the Eocene-Oligocene transition (33.7 Ma) increased circulation around Antarctica and changes in atmospheric CO_2 (Pollard and DeConto, 2001) but no changes in bottom-water temperature (Lear et al., 2000) initiated ice growth in Antarctica. At 30 Ma the ridge crest to the west of the Tula fracture zone collided with the subduction zone in front of the Antarctic Peninsula magmatic arc. As a consequence, spreading and subduction stopped and the ocean crust segment of what is today Drift 7 remained fixed relative to the extinct magmatic arc (today's mid-shelf high may be the relict of this arc). The collision initiated the development of the passive margin and shelf evolution. Sediment supply to the rise site was still limited since the distinct arc and a back arc basin (today the inner shelf) blocked and collected sediment eroded and transported by ice or glacial outlet streams. After filling of the back arc basin the erosion of the arc probably provided enough sediment flux to the rise to build early drift structures under the bottom-current action of the ACC (Reflector "X", seismostratigraphic Unit V-IV). After 20 Ma the bottom-current regime changed and the drifts began to reorientate indicating the onset of a westward-flowing AABW contour current and possibly the existence of sufficient shelf ice in the Weddell Sea to maintain such a current via ABW formation.

Several indicators around the Antarctic Peninsula in upper Miocene times point toward the existence of a permanent ice cover since that time (IRD at ODP Site 325, Leg 35 (Hollister and Craddock et al., 1976; changes in clay mineralogy in the Weddell Sea, ODP Leg 113 (Kennett and Barker, 1990)). An irregular sawtooth pattern in the Population 1 density curve is witness of a dynamic, fluctuating ice sheet from at least 9.88 Ma on. The size of this ice sheet or the frequency with which it reaches the shelf edge increases with time and reaches high amplitudes between 8 and 6 Ma. Major declines occur around 9.7, 9.2-9, 8.4-8.1, and 7.3 Ma (Fig. 4.1). Major cooling and ice build-up since 15 Ma can also be inferred from a decline in bottom-water temperatures (Lear et al., 2000), a major eustatic sea-level drop (Haq et al., 1987) and steadily increasing $\delta^{18}O$ values (Zachos et al., 2001). The findings for the

Messinian Event (5.75-5.32; Bart and Warny, 2001 (if present at all, see chapter 4.4)) show an initial period of no ice advances to the shelf edge (5.9-5.6 Ma; Fig. 4.1) in good agreement with a high eustatic sea level followed by a short period of minor ice readvances starting at 5.6 Ma combined with a declining sea level (Haq et al., 1987). The biogenic opal content in this time interval is anti-correlated to the „ice indicator" and points toward increased sea-ice cover during the later phase of the Messinian Salinity Crisis. The cessation of Mediterranean Outflow Water, an important source-water constituent of the Northern Component Water (NCW; a predecessor to the modern North Atlantic Deep Water), may have reduced heat transfer to the CDW and hence fostered ice advance and sea-ice formation (Hillenbrand and Fütterer, in press).

4.7.2 Early Pliocene

Besides small episodic ice advances the early Pliocene and earliest late Pliocene is a time of reduced global and Antarctic ice volume (see chapter 1.2.2 for discussion). The reflooding of the Mediterranean (reestablishment of MOW) and the start of the Panamanian isthmus formation (Haug et al., 2001) stimulated a stronger thermohaline deep-water circulation in the Atlantic Ocean with maximum formation and convection of NCW acting as a heat transfer mechanism to the Antarctic Ocean (Berger and Wefer, 1996). High opal contents (Fig. 4.4) and higher carbonate productivity in the subpolar South Atlantic (Müller et al., 1991) indicate elevated surface-water temperatures and agree well with the scenario described and the idea of strongly reduced sea-ice cover. In this context it is interesting to notice that the early Pliocene is the only time when sedimentation rates at the distal Site 1095 exceeded rates at the more proximal Site 1096 (Fig. 4.1). This effect may be explained by a southward shift of the ABW contour current closer to the slope in the absence of sea ice. An intensified bottom-water circulation may have reduced apparent sedimentation rates at the proximal Site 1096 by lateral export. Accumulation at the rise dropped in the early Pliocene (4.8 Ma) marking the end of the actual drift growth stage spanning seismostratigraphic Units IV to IIc.

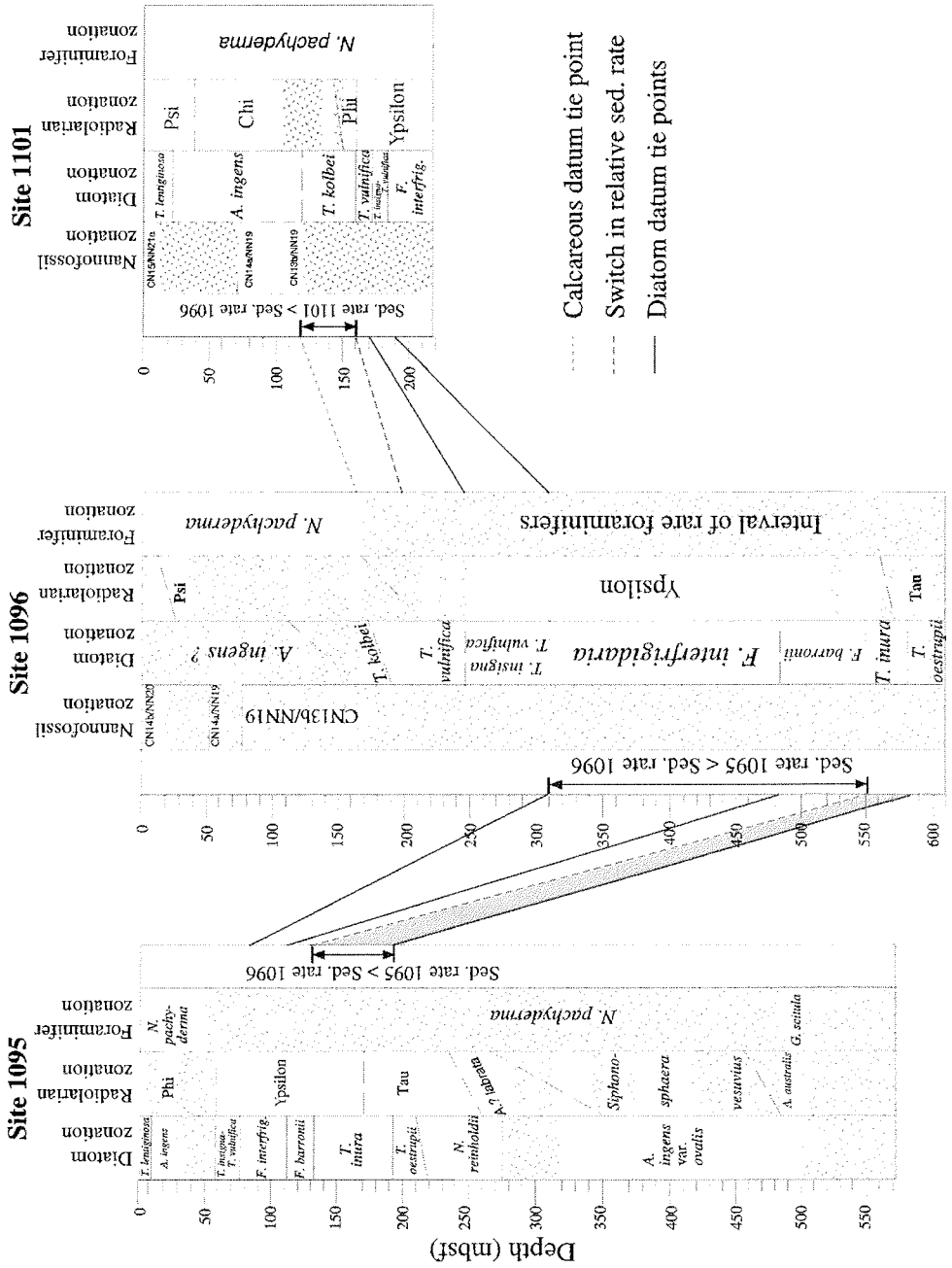

Fig. 4.1. Comparison of sedimentation at the rise Sites 1095, 1096, and 1101. Correlations are based on biostratigraphic tie points and indicate higher sedimentation rates at Site 1095 between 130 and 195 mbsf (lower Pliocene) compared to Site 1096. Courtesy: ODP Leg 178 Shipboard Scientific Party, 1999.

4.7.3 Late Pliocene - Present

The late Pliocene is characterized by an abrupt ice readvance at 3.2 Ma (Fig. 4.1) and a decline in surface productivity (Fig. 4.1) indicative of major cooling and sea-ice formation. This cooling is well documented in isotope and Mg/Ca thermometry (Zachos et al., 2001; Lear et al., 2000) and synchronized by the Northern Hemisphere Glaciation and decrease in NCW production.

During the Pleistocene the ice cover of the Antarctic Peninsula may have been more stable without the large amplitude long-term sawtooth-like fluctuations observed in the late Miocene (Fig. 4.1). It should be noted that Population 3 almost disappears between 3.0 and 1.3 Ma (Fig. 4.1) indicating a high energetic depositional environment dominated by turbiditic processes. The reduced importance of bottom-water currents at the rise during this period is again linked to low opal contents and assumed persistent sea-ice cover. A massive muddy turbidite between lithostratigraphic Unit I and II is interpreted as a debris flow unit (Fig. 4.1; ODP Leg 178, Shipboard Scientific Party 1999). A total of 11 sediment samples have been taken out of this interval and all except the uppermost show turbiditic or ice-related origin. These findings support the idea of very rapid deposition, leaving no time for hemipelagic material to accumulate or for bioturbation to take place. The process after this event is a prime suspect for having caused significant erosion of underlying strata (see discussion of various age models, chapter 4.4.1). This high-energy event represents a turning point in deposition energy linked to a major geometric change on the shelf (see chapter 5).

A slight increase in opal content around 0.9 Ma (Fig. 4.1) and declining ice-indicator values (Population 1 density curve, Fig. 4.1) from 0.5 Ma on might be related to a regional warming in the Antarctic Peninsula area that has yet not been observed in other parts of the Southern Ocean (Hillenbrand and Fütterer, in press). This trend in reduced ice volume on the Antarctic Peninsula is in contrast to the still increasing global ice volume by this time (Fig. 4.1). However, no evidence is seen for a collapse of the West Antarctic ice sheet as proposed by Scherer et al., 1998.

5 Linking the Shelf, Slope and Rise

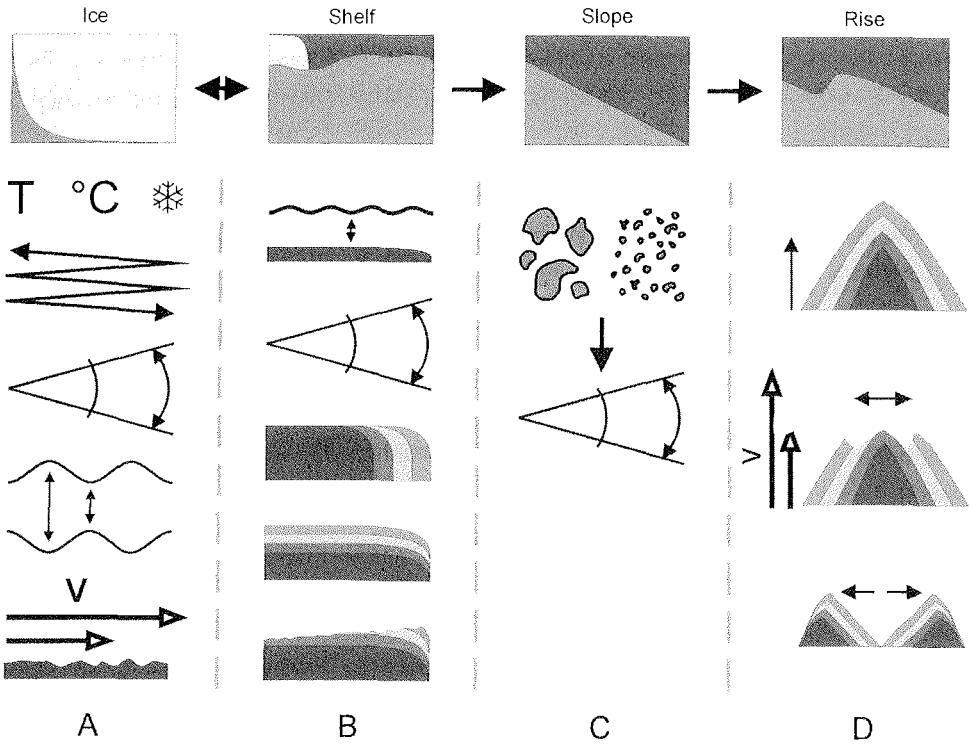

Fig. 5.1. Conceptual model illustrating dependencies and inter-relationships between the ice, shelf, slope and rise.

5.1 Mechanisms and Relationships

The attempts to reconstruct the glacial history of the West Antarctic Peninsula ice shield during ODP Leg 178 by drilling the shelf as a proximal and directly involved recorder has proven to be difficult and relatively crude. There was only low to no recovery due to inadequate drilling methods and discontinuity of strata. On the other hand, the drift record from the rise is continuous, easier to recover and of high resolution. But on the downside, the rise is a distal and indirect recorder influenced by many factors and therefore requires at least a principal understanding of the shelf record to aid its interpretation. Sediment eroded from the glacial valleys of the Antarctic Peninsula and later deposited on the rise passes two major intermediate and temporary depositional facilities - the inner and outer shelf and the slope - during its transport path.

Both intermediate depositional facilities primarily act as storage areas which retard and attenuate the ice signal that reaches or does not reach the rise. At times, however these storage facilities may also potentially act also as sources releasing stored sediment without a direct initiation through ice action. The different environments with their two modes, deposition or remobilisation, are linked by complex interrelationships and dependencies briefly summarized here.

In the absence of major fluvial systems ice is and has been the prime initial driving force behind erosion, transport and deposition at least during the last 10 Ma. Temperature, precipitation, valley slope, sub-ice bedrock roughness and the areal amount of occupation space determine ice thickness, ice-flow velocity, and the frequency of advances to the outer shelf or shelf edge.

The shelf in turn is influenced by the relative sea-level (either caused by ice flexure or „global" eustacy), leaving space for aggradation (storing sediment away) or progradation with or without shelf erosion piping sediment directly to the slope. Depending on the frequency and the extent of ice advances or the ice-loading history of the continent the shelf may become overdeepened and forms wide shelf basins parallel to the coastline which block sediments from reaching the rise.

There are many possible modes of ice-shelf interaction, three possible scenarios are briefly outlined:

- Ice advance at relative highstand (ice not grounded) leading to minor foresets at the slope and thin topset on the shelf
- Ice advance at relative highstand (ice grounded) leading to foresets and topset at the shelf
- Ice advance at relative lowstand (ice grounded) leading to new foresets and topset and existing foreset erosion

Most commonly, a decrease in ocean and atmospheric temperature will foster ice advance and growth which, in turn lowers the eustatic sea level and supports shelf erosion and the transport of coarse material to the shelf edge and slope. However the isostatic loading of the continent and shelf will eventually (10 –100 ka of years) increase the relative sea-level above the shelf and reduce the likeliness of grounding. This, in turn may act as negative feedback in cooler times by increasing ice-flow speed (loss of back stop) and reducing inland

ice thickness. In temperate climate conditions an isostatic rebound of the continent and shelves may partially compensate eustatic rises and retard ice decay and retreat from the shelf.

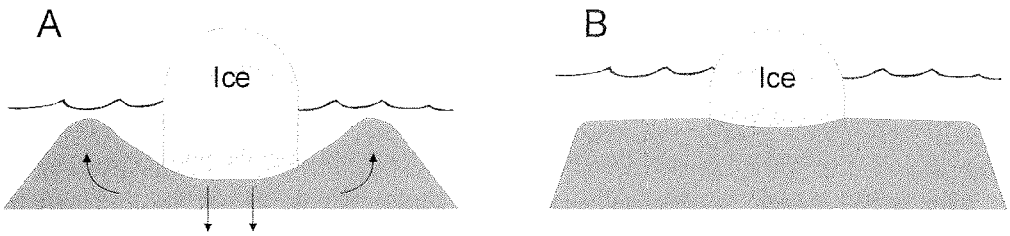

Fig. 5.1. Conceptual model of Glacial Isostatic Adjustment (GIA) affecting the continent, its shelves and the slope angles. **(A)** Full glacial conditions: landward-inclined shelf, low slope angles and low relative sea level. **(B)** Full interglacial or temperate conditions: seaward-inclined shelf, steep slopes and a sealevel highstand.

The slope is the second storage reservoir and its angle determines fast or retarded transport to the rise. The shelf angle is determined by the kind of material that is delivered (coarse material from an erosive glacial advance leads to steeper slopes than fine hemipelagic material and glacial outwash) and the isostatic stage of the shelf (inclined toward the land (low slope angles), inclined toward the ocean (steep slope angles; Fig. 5.1). The apparent observed steepening of the paleo slopes (foresets) with time may also be attributed to a continuing tilting of the shelf due to increased ice load on the continent with time.

A still landward-inclined shelf during a highstand under temperate conditions or intense topset formation under glacial conditions leads to reduced export of material to the slope and rise. Full glacial conditions with regular ice advances to the shelf edge and a low relative sea-level cause maximum erosion in the hinterland and on the shelf and lead to an increased export of material.

The rise as the actual terminal recorder adjusts its build-up rate to the amount of material delivered. Over time the storage capacity of the rise is reduced, meaning that the build-up of drift-bodies above the surrounding seafloor decreases the capacity to accumulate sediment and attenuates the continental ice signal (decrease in accumulation rate over time). In addition, all material from the slope (mass wasting) and the hemipelagic biogenic input are modified by bottom-water current (lateral sediment influx and export).

5.2 Shelf Evolution and Rise Build-Up Over the Last 10 Ma

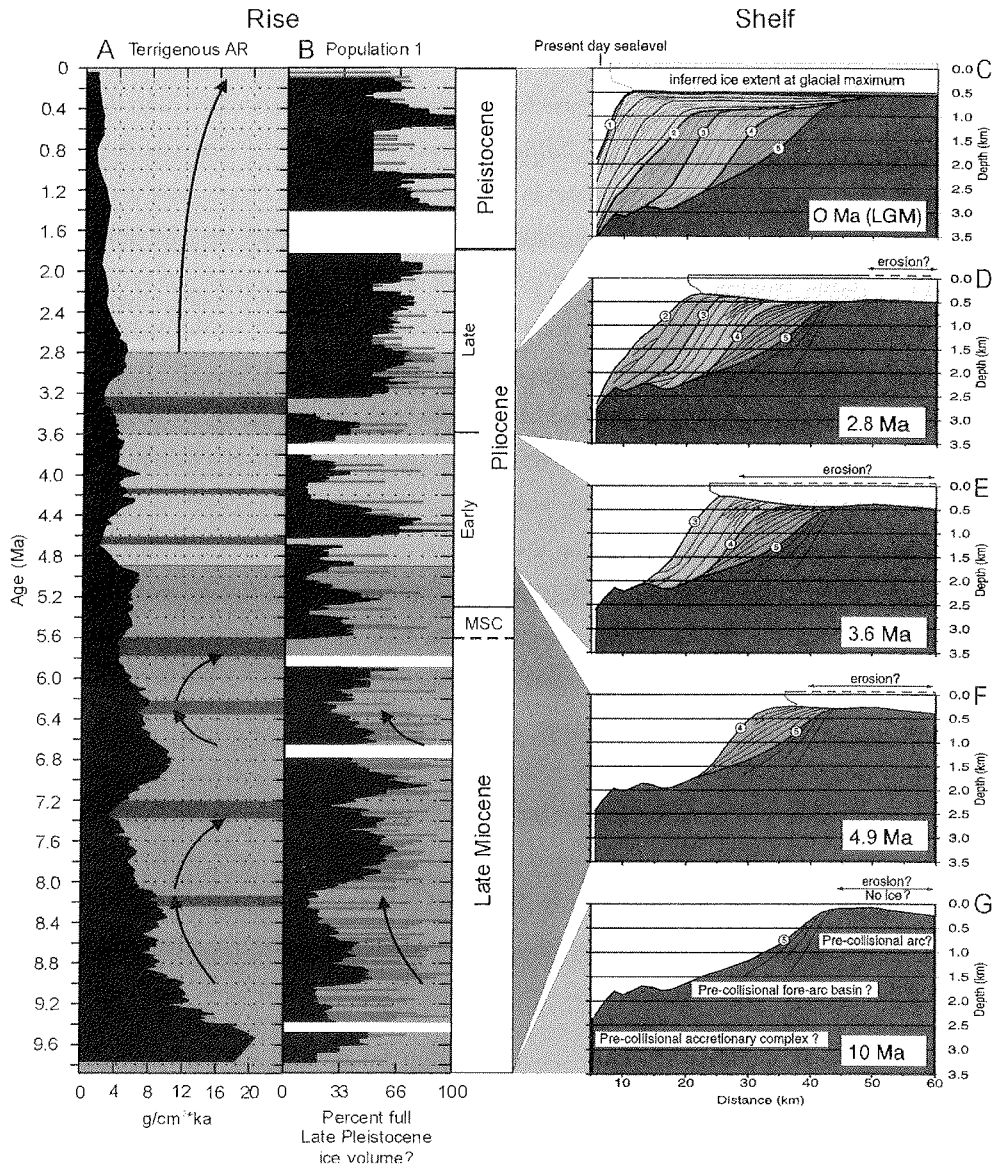

Fig. 5.1. Correlation of (**A**) terrigenous accumulation rates at the rise Site 1095 (dark bars = correlation bars) with (**B**) ice-indicator signal derived from grain-size data (light bars = gap in data). Note the lows in accumulation at times of reduced ice volume or decreased frequency of ice advauces to the shelf edge (MSC = Messinian Salinity Crisis). (**C-G**) Backstripping model of the shelf (Camerlenghi et al., 2001, with modified ages).

A comparison of the terrigenous accumulation rate (Fig. 5.1A) and the Population 1 density curve (Fig. 5.1B) reveals the dependency of the drift growth on ice input. Times of reduced ice volume commonly correlate with intervals of reduced accumulation. However, the decay of accumulation at the drift cannot be compensated by an increase in ice volume.

Following this rationale a decrease in ice activity (volume) should lead to decreasing accumulation rates. This behavior is well illustrated within intervals 9-8.2 Ma and 6.8-6.3 Ma. In some intervals however, the increase in glacial activity is associated with a decline in accumulation (8.1-7.3 Ma; 6.2-5.8 Ma; 2.8-0 Ma). This relationship may be attributed to periods of topset build-up caused either by Glacial Isostatic Adjustment (GIA) or eustatic effects. Times of topset build-up still allow ice-indicator material to reach the rise, but the bulk of continental derived sediment is stored on the shelf.

A recent backstripping model by Camerlenghi et al., (in press; Fig. 5.1C-G) based on depth-migrated seismic data (profile: I95-152; Fig. 2.1, chapter 2.2.2) illustrates the shelf evolution over the last 10 Ma. Together with the rise information it is possible to restore the stratigraphic intervals of topset build-up that are not preserved on the shelf due to erosion. The times given to the model steps (Fig. 5.1C-G) are tuned in reasonable biostratigraphic limits to match the rise record. As an example, the increase in rise accumulation rates starting at 3.2 Ma is certainly related to an increase in erosion in the hinterland and shelf during the start of the NHG (Northern Hemisphere Glaciation) and well constrained by an abrupt increase in the ice-indicator curve (Fig. 5.1B). The decline in accumulation starting at 2.8 Ma cannot however be explained by a decrease in ice volume or ice advancing frequency. The start of topset preservation and build-up at 2.8 Ma is therefore the only explanation for the decline in rise accumulation. The topset build-up and preservation may have been initiated by the time-delayed glacial isostatic response of the shelf and some accommodation space created during shelf erosion between 3.2 and 2.8 Ma prior to the GIA.

6 Thesis Summary

The rationale of this study has been to describe and characterize typical West Antarctic Peninsula continental margin depositional environments at three exemplary type locations: the outer continental shelf NW of Anvers Island, a late Pleistocene to Holocene depression of the overdeepened inner shelf (Palmer Deep) and the drifts of the continental rise. The main scientific objective at each setting was to obtain ice-sheet history information of the Antarctic Peninsula for the last 10 Ma. The study spans many time scales (thousands to millions of years) and employs tools of different resolution (from cm to tenths of meters). Seismic, downhole and laboratory tools and techniques were applied to record physical and chemical proxies for a multifaceted and differentiated understanding of the particular environments. Steps and conclusions toward an achievement of this aim in each individual depositional environment and the results of an attempt to link the shelf and the rise are summarized below.

The Shelf:

- A detailed seismostratigraphic characterization of the unique Antarctic inner and outer shelf along the passive margin of the West Antarctic Peninsula is complemented by logging information that is tied to the seismic profiles via a new continuous depth vs. velocity profile.
- The new velocity profile has been established by a compilation of more than 13 different data categories, non-standard processing techniques have been developed and applied especially for this task. Polynomial exclusion techniques with various orders and low-pass filtering reduced the noise of the initial data pool and produced a definite velocity depth profile that in turn is matched and brought in phase with the resistivity logging data. Subsequently, it was possible to correlate logging and core data to seismic units and single reflectors.
- Unit S1 at Site 1103 consists of a series of stacked lodgement tills deposited as basal moraines by advancing and retreating ice sheets, interrupted by finer, less clast-rich intervals possibly associated with interglacials.

  Seismostratigraphic Unit S3 at Site 1103 contains a diamictite / fine succession that represents upper slope deposits with a distal moraine-like source. The alternations of diamicts and fines may be related to advancing and retreating ice sheets with proximal

sources in glacial times and more distal sources in interglacials. Topsets and foresets are linked to the same depositional mechanism: ice-sheet advance and retreat. However the preservation potential on the slope is higher since all deposits below the paleo-shelf break are protected from direct ice erosion.

- The discovery of imbricated fabric with pebbles dipping to the south (information derived from downhole FMS images) demonstrates deposition below a N-S-oriented ice stream. The orientation is consistent with a major N-S-oriented outlet-trough on the shelf west of Anvers Island. The age of these deposits found in ~200 mbsf exceeds 2 Ma and witnesses the longevity of glacial outlet-troughs on the shelf.
- Logging data and FMS images in combination with lithological and biostratigraphic age constraints allow a close correlation of West Antarctic Peninsula shelf records with East Antarctic shelf records (Legs 178 and 188). Since 3.2 Ma or, at the latest, 2.3 Ma both shelves have evolved in a similar manner despite the many differences in margin type and overall setting (e.g. ice proximity and sediment supply). Similarities are confirmed in many other circum-Antarctic shelf records, best summarized in an upsection trend toward shelf aggradation combined with better topset preservation. To explain these similarities a strong external controlling factor is needed. Sea-level fall overcompensated by increased isostatic subsidence due to ice build-up (GIA) that affected the continent and the adjacent shelves is the most likely mechanism.

Palmer Deep:

- Based on morphological features of a new multibeam map of Palmer Deep and published low resolution seismic data, a new tectonic model in the context of the general margin evolution was established. Two major phases of deformation along one conjugate set of faults are addressed. Phase 1 is North-South compressional with a left lateral strike slip component and associated lateral E-W extensional escape. Phase 2 is North-South extensional with left lateral movement on the NW trending faults and right lateral movement on the NE trending faults. Phase 2 is linked to the back arc type Bransfield Strait extension.
- Cores from Palmer Deep (> 25 cm/ka sedimentation rates) provide a unique high resolution Holocene-to-latest Pleistocene record from the Antarctic Shelf. Palmer Deep strata is divided into 5 climato-stratigraphic zones on the base of core logs and sedimentology. Core-to-seismic correlation is possible on the basis of single reflectors

using synthetic seismograms and very high-resolution single channel Deep-Tow Boomer records. The strongest impedance contrasts are at the base of turbidites and at changes between massive, bioturbated and laminated units.

- With the aid of core-based acoustic models of the basin fill the climato-stratigraphic zones have been mapped in reflection seismic profiles of Sub-Basins I and III.
- The digitization of the data has been accomplished by newly designed processing software that significantly improved vertical (< 0.4 m) and horizontal resolution of the single channel seismic profiles. The digitized data also yield information on deeper strata so far inaccessible on the analog printouts. A first digital processed section from Sub-Basin I revealed a small scale mud diapir (> 4 m height, 30 m width, in ~1000 m water depth) with a feeder dike that is recognized cutting the slump and drape deposits at the base of the steep canyon slope. The load of slumps and gravity flow deposits on unconsolidated diatom ooze is believed to be responsible for the initiation of mud diapirism in the gas and fluid-rich sediment. This process of load introduced diapirism has never before been described in extensional basins of the Antarctic shelf.

The rise and its drifts:

- Large mounds on the continental rise along the Antarctic Peninsula margin between 63°S and 69°S and within 200 km of the shelf break have been interpreted as sediment drifts, separated by turbidity current channels. The internal seismostratigraphic drift architecture reveals an early pre-drift stage above the basement, a period of pronounced drift growth and a late period of drift maintenance.
- Attempts to improve core to seismic ties with the use of synthetic acoustic profiles have been only partially successfull. *In situ* velocity check shots with a downhole tool provided the most accurate depth vs. traveltime information.
- Fine-fraction (<63 μm) grain-size analyses of 530 samples from Holes 1095A, 1095B and 1095D allow assessment of the downhole grain-size distribution at Drift 7. A variety of methods of data processing, statistical treatment, and display techniques have been applied. Based on an approach by Friedmann, skewness and standard deviation (sorting) have been used to separate the grain-size data set into 3 populations.
- The assessment of these populations in the light of an existing sequence stratigraphic model resulted in a simple but process-related conceptual model of the facies building stones that make up the drift. Grain-size Populations 1 and 2 are correspondingly

identified as the result of glacial and interglacial mass wasting processes of the slope. Sediment samples of Population 3 are the result of hemipelagic settling modified by bottom-current activity.

- Using a special referenced moving window counting routine the Population 1 data has been transformed into a regional Antarctic Peninsula ice volume indicator curve and showed good agreement for the past 10 Ma with the Lear et al., 2000 data.
- Grain size, opal content and other core parameters prove that the early Pliocene is a time of reduced global and Antarctic ice volume and sea-ice extent. Never before and after the last 10 Ma was paleo productivity higher at the rise than during this time. This study concludes that during the early Pliocene Antarctic ice volume was reduced by 70%.
- During the late Miocene ice was highly dynamic with frequent advances and retreats. The upper Messinian to early late Pliocene was a time of repeated ice-sheet collapses. Starting at 3.2 Ma the ice sheet became a permanent feature, occupying the shelf during most of the glacial half cycles.

The new results from the Antarctic Peninsula illustrate the complex dependencies and inter-relationships between the continental ice, shelf, slope and rise. The quasi continuous drift record from the rise is the most suitable data set for an attempt to reconstruct the glacial history of the West Antarctic Peninsula ice shield. The distal and indirect record of the drifts is unique in its high resolution but influenced by many factors. Interpretations toward an ice-sheet history must be supplemented by a principal understanding of the shelf modes. The regional ice volume curve for the Antarctic Peninsula is the most significant finding of this thesis.

Further work should focus on a completion of data gaps in the grain-size record (refinement of the ice volume indicator curve) and the integration of multi-beam and single channel HDTB data in search of new diapiric features along the base of the basin slopes.

7 Excursus

7.1 Excursus 1: Seismic Modelling of Sediment Cores

7.1.1 Introduction

Any approach to modelling seismic waves travelling through sediments under *in situ* conditions requires a thorough look at the physical properties that influence wave propagation. This chapter will give a general summary of the nature of stress and strain and the propagation of stress and strain through elastic bodies as seismic waves. Relations between wave propagation and physical properties are discussed and several semi-empiric existing models and the unified model of Biot-Stoll (Stoll, 1989; Breitzke, 1997) are briefly introduced. Finally a practical approach to the correlation of reflection seismic record to sediment cores via synthetic seismograms is given. The Matlab routine „synseis" is briefly discussed at the end of the chapter.

7.1.2 Stress and Strain

Stress can be described as an internal force within a material. It is defined as force acting on a certain area:

$$S = \frac{F}{A} \qquad \text{(Eq. 7.1)}$$

S = Stress
F = Force
A = Area

The stress acting on an area of any surface within the material may be resolved into a component of normal stress perpendicular to the surface and a component of shear stress in the plane of the surface. Within a stressed body the components that result in pure normal stress define three orthogonal axes known as the principal axes of stress. Compressional and tensile stress are distinguished by the orientation of the stress directions toward or away from each other. Hydrostatic stress represents the case where all principal axes have the same magnitude. It is represented in fluids that do not transmit shear stress. In case of unequal

principal stresses the material is subject to shear stress along all internal surfaces except for the orthogonal planes that intersect the three principal stress axes.

The result of stress is strain either in the form of shape or volume changes. The elasticity of a material determines how much stress can be accomodated with a complete reversion to the original shape or how much the volume changes after removal of stress. If stress exceeds the elastic limits of the material the resulting strain will be irreversible; stress build-up may continue until the material fails. Within a linear stress / strain field four elastic moduli describe the relation between stress and strain.

Two elastic moduli are especially important for description of seismic waves: the compression or bulk modulus and the shear modulus. The bulk modulus describes the volume changes associated with stress while the shear modulus describes the dislocation of adjacent parallel planes as a consequence of applied shear forces (e.g. Kearey and Brooks, 1984).

$$K = \frac{\Delta P}{\Delta V / V} \qquad \text{(Eq. 7.2)}$$

K = compression modulus
ΔP = volume stress
$\Delta V / V$ = volume strain

$$\mu = \frac{\tau}{\tan(\theta)} \qquad \text{(Eq. 7.3)}$$

μ = shear modulus
τ = shear stress
$\tan(\theta)$ = shear strain angle

Another well known elastic modulus is the Young modulus, E. It describes the stress / strain relation for longitudinal stress and strain und is known best from Robert Hooke's Law:

$$E = \frac{S}{\Delta l / l} \qquad \text{(Eq. 7.4)}$$

S = Stress
$\Delta l / l$ = change in longitudinal direction

7.1.3 Seismic Waves

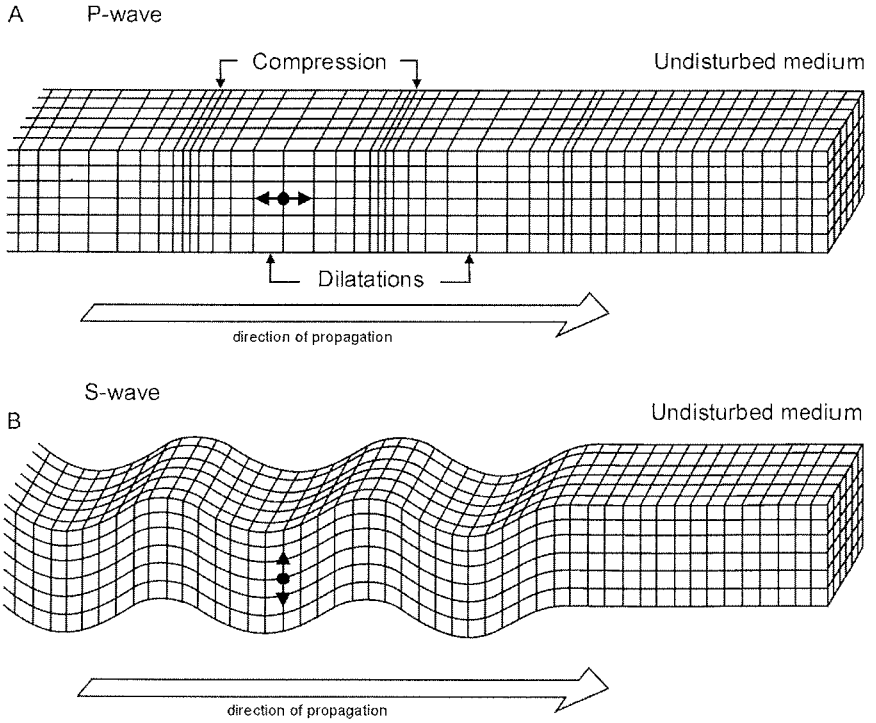

Fig. 7.1. Elastic deformations and ground particle motions associated with the propagation of body waves. (**A**) *P*-wave (compressional wave), (**B**) *S*-wave (shear wave) (after Bolt, 1982; Kearey and Brooks, 1984).

Seismic waves are a means by which stress and strain conditions travel from one point of a material to another (Fig. 7.1). Seismic waves may have their origin in earthquakes, explosions, or other shocks. Body and surface waves represent the two major types of seismic waves. For imaging the geological subsurface, body waves are most important. Considering a nearly one dimensional, perfectly elastic, isotropic and homogenous material of density ρ in which a stress / strain anomaly can propagate following the Young modulus E, a balance of forces exists between external forces on the small cross surface area A and accelerating internal forces. Using Hooke's Law this balance of forces can be expressed as:

$$E \frac{\delta^2 \Delta l}{\delta l^2} dx\, dA = \rho \frac{\delta^2 \Delta l}{\delta t^2} dx\, dA \qquad \text{(Eq. 7.1)}$$

Subsequent integration yields the one dimensional wave equation

$$\frac{\delta^2 \Delta l}{\delta l^2} = \frac{1}{v^2} \frac{\delta^2 \Delta l}{\delta t^2} \qquad \text{(Eq. 7.2)}$$

with the propagation velocity of waves (v) related to the E modulus as

$$v = \sqrt{\frac{E}{\rho}} \qquad \text{(Eq. 7.3)}$$

In general terms the elastic wave velocity is defined as

$$v = \sqrt{\frac{\text{elastic modulus of material}}{\text{density of material}}} \qquad \text{(Eq. 7.4)}$$

Similar to one-dimensional configurations, elastic moduli for the propagation of seismic waves in three-dimensional materials can be defined through statements like Eq. 7.5. Hence for compressional *P*-waves the velocity v_p is

$$v_p = \sqrt{\frac{\Psi}{\rho}} \qquad \text{(Eq. 7.5)}$$

where ψ is an elastic modulus combining bulk and shear moduli

$$\Psi = K + \frac{4}{3}\mu \qquad \text{(Eq. 7.6)}$$

In contrast the shear wave velocities v_s are defined by only one elastic modulus, namely the shear modulus

$$v_s = \sqrt{\frac{\mu}{\rho}} \qquad \text{(Eq. 7.7)}$$

All ideal elastic, isotropic and homogenous materials are defined by a maximum of two elastic moduli (Dresen et al., 1985). For natural materials such as water-saturated marine sediments the assumptions of homogeneity and isotropy are not valid. Several studies (e.g. Hamilton, 1970; Bachmann, 1985; Breitzke, 1997) have explored the influence of heterogeneities (e.g. porosity and grain-size) on the propagation of acoustic waves.

The „Time-Average-Equation" of Wyllie et al. (1956; 1958) and earlier studies by Wood (1941) introduce „inhomogeneity" as a two phase model taking the influence of pores and pore filling into account.

Time-Average-Equation

$$\frac{1}{v_p} = \frac{1-\Phi}{v_m} + \frac{\Phi}{v_w} \qquad \text{(Eq. 7.8)}$$

v_p = *P*-wave velocity
v_m = *P*-wave velocity of the matrix
v_w = *P*-wave velocity of the pore filling (e.g. water)
Φ = porosity

Similarly the bulk density of a material can be thought of as the mean of the densities of the two phases, matrix and pores (Dresen et al., 1985).

$$\rho = (1-\Phi)\rho_m + \Phi\rho_w \qquad \text{(Eq. 7.9)}$$

ρ = mean density of the material
ρ_m = density of the matrix
ρ_w = density of the pore filling (e.g. water)
Φ = porosity

In further empirical approaches researchers introduced additional variables to account for geotechnical parameters such as compaction (Nafe and Drake, 1957) or mineralogical parameters (Schön, 1984) such as the clay content of the matrix (Han et al., 1986; Klimentos, 1991).

The influence of grain-size (Fehr, 1991; Breitzke, 1997) or matrix intra- and extraporosity on the acoustic velocity for example with foraminifers has been thoroughly studied (Schreiber, 1968; Hamilton, 1982; Breitzke, 1997). Other semi - empirical approaches may account for special geological settings; the Wood Equation (Wood, 1941) is the best approximation of the porosity / *P*-wave velocity relation for unconsolidated sediment of the Arctic (Bergmann, 1996). A unified non-empiric model has been developed by Biot and Stoll (Stoll, 1989) for porosity values between 40 and 70%.

7.1.4 Biot-Stoll Model

Between 1941 and 1973 Maurice Biot developed a comprehensive theory for the mechanics of porous deformable media. This model is no longer dependant on ideal assumptions regarding the wave guiding natural material. All „imperfections" of a natural material, such as anisotropy, porosity gradients with lithification, and unelastic behavior (visco-elasticity, dissipative losses, attenuation, dispersion, divergency) are considered. Biot's theory predicts that, in the absence of boundaries (surfaces of abrupt discontinuity), three kinds of body waves, two dilational and one rotational shear wave, may exist in a porous medium. The dilational wave types can be further distinguished as „first type" and „second type" waves (Stoll, 1985). First type waves travel nearly in phase through the matrix and the pore space with small attenuation losses through viscosity. In contrast, second type waves are highly attenuated by the unelastic material properties and propagation through pore space and matrix is largely out of phase. For geophysical work in saturated sediments the second type waves are less important, and modelling approaches can be limited to first type waves (Stoll, 1989). A more thorough mathematical discussion can be found in Stoll and Bryan (1970), and Stoll (1974; 1989), who simplified, unified and transformed the Biot Theory into cases and a numerical routine, and Breitzke (1997) who focused more on geophysically relevant parts of the model following Stoll's nomenclature.

7.1.5 Correlation of Physical Property Data and Seismic Reflection Profiles

In contrast to modelling and measuring visco-elastic moduli and related parameters of sediments, it is far easier to measure the *P*-wave velocity directly and use this information for seismic correlation purposes. The *P*-wave velocity of marine sediments is dependent on lithology, porosity, bulk density, state of stress (e.g. directional tectonic stress or static isostatic load), fabric, internal fracturing, amount of free gas or gashydrate, pore space filling,

compaction and degree of diagenetic lithifaction affects the speed of *P*-waves and their attenuation and dispersion. Direct continuous *P*-wave measurements of sediment cores incorporate many of these dependencies.

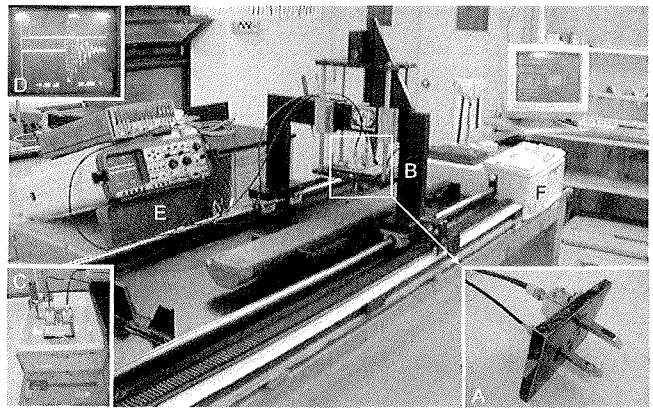

Fig. 7.1. The Halifax full wave acoustic recording unit DSV (Digital Sonic Velocimeter, Mayer et al., 1987): **(A)** transducer head with active and passive piezo elements, **(B)** tracksystem, **(C)** distilled water and transducer spacing calibration station, **(D)** full captured waveform on oscilloscope screen, **(E)** digital oscilloscope below function generator, **(F)** computer for software control and data storage via GPIB interface card.

In the early 1970's *P*-wave laboratory measurements left the experimental stage to become standard routine in many laboratories in the 1980's. The introduction of the semi-automated Halifax System, introduced in 1987 (Mayer et al., 1987; Courtney and Mayer, 1993a; 1993b; Fig. 7.1) and founding of GEOTEK in 1989, provided access to commercially available automated core loggers for the scientific community (Fig. 7.3). *P*-wave logging systems are now routinely used on board the *JOIDES RESOLUTION* drillship.

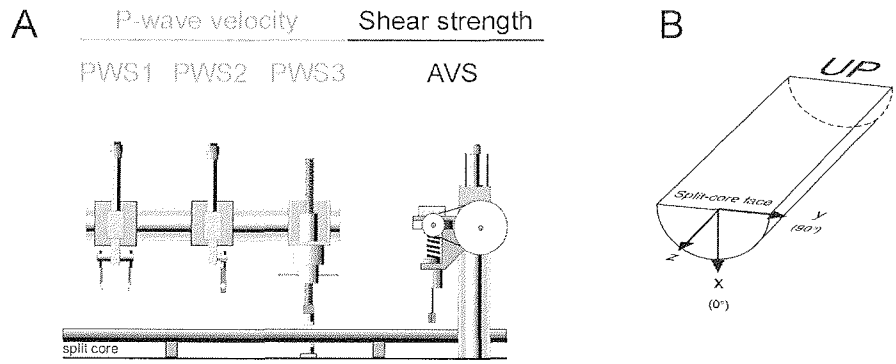

Fig. 7.2. Schematic representation of the semi-automatic *P*-wave and shear strength half core station on board the JOIDES RESOLUTION (Blum, 1997).

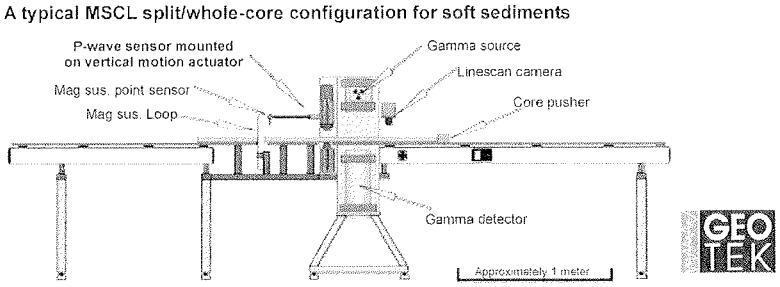

Fig. 7.3. A typical next generation multi sensor split / whole-core logger (MSCL) for soft sediment applications. Courtesy: GEOTEC (http://www.geotek.co.uk).

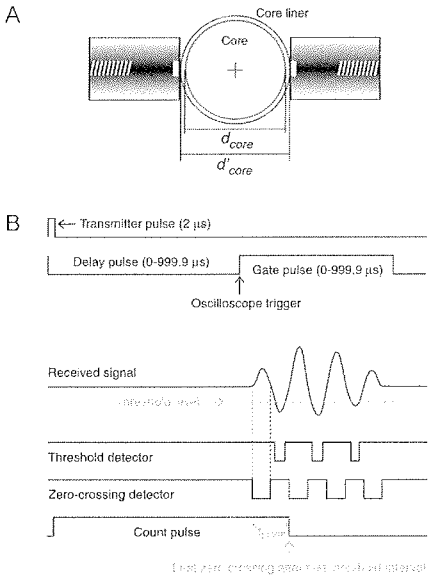

Fig. 7.4. The spring loaded transducers, equipped with linear variable-displacement transformers in contact with the core liner (**A**). (**B**) Chart to explain the timing of signal initiation and detection (modified from Blum, 1997).

Currently two acoustic systems are used on board the *JOIDES RESOLUTION* The PWS (*P*- Wave- Sensors) System (*P*-wave velocity, Fig. 7.2) is a direct successor of the Digital Sonic Velocimeter (DSV) developed at Dalhousie University and the Bedford Institute of Oceanography (Mayer et al, 1987; Fig. 7.1). The PWS system, introduced in 1991 as well as its predecessor DSV, is semi-automatic and works on split core sections or single specimens (Blum, 1997). The unit consists of three transducer receiver pairs (PWS1, PWS2, PWS3; Fig. 7.2A). PWS1 and PWS2 are used respectively for the longitudinal (along the z

axis of a core, Fig. 7.2B) and transverse (along the y axis of a core, Fig. 7.2B) *P*-wave velocity determination. Both systems are penetrative and therefore destructive to the core. Similar to the DSV system (Fig. 7.1), the PWS system is controlled by a digital oscilloscope (storage of received wavelet), a signal generator (trigger pulse for external oscilloscope timing and signal generation within the transmitter) and a differential amplifier. The third acoustic system of the PWS is a modified Hamilton frame for no-destructive measurements in the x direction of cores or for single specimen measurements.

In contrast to the semi - automated PWS system, the *P*-wave sensors of the MST (Multisensor Track Station) are fully automated and integrated into the measurement cycle of the MST (Fig. 7.3). The core is guided in discrete steps between two acoustic piezoelectric transducers. Acoustic coupling is accomplished through an epoxy resin surface and a water film from an automatic sprinkler system. The transducer pair is springloaded and equipped with linear variable-displacement transformers, that measure the diameter of the core and core liner. A 120V, 500 kHz pulse, sampled at 50 ns, is emitted with a repetition rate of 1 kHz. The pulse stimulates the piezoelement within the transducer to emit a compressional wavelet with approximately the same frequency but much longer wavelength than the initiating pulse. To avoid noise during the transit times a delay pulse (shorter than the traveltime) is emitted followed by a gate pulse or window. During the gate window two different detection routines are used to determine the transit time: the classical method of a treshold on the received auto gain amplified signal, and a zero crossing technique (see Fig. 7.4 for details). The actual traveltime is defined as the first zero crossing after the first low threshold detection event. A separation procedure subtracts either one wavelength (2us), for a positive, or 1.5 wavelengths, for a negative onset, from the transient time (time of transmitted pulse minus time of count pulse) to pick the actual onset of the received signal (Blum, 1997).

7.1.6 Synthetic Seismograms

The correlation of the continuous two-dimensional seismic survey profile information with one - dimensional physical property data from core or downhole logging is a key step within the seismostratigraphic interpretation process. It allows extrapolation of "spot" information (measured data and non-quantitative information such as descriptions) to a much larger area. Synthetic seismograms calculated from the physical property data can provide this link between the remotely derived image and the actually observed structures and measured properties of the cores. Additionally they allow assignment of true depth values to the reflectors.

Synthetic seismograms were computed for most of the drillsites of Leg 178 using MST, downhole logging data, Hamilton frame data and index property values. They provide the main parameters, density and *P*-wave velocity. The necessary acoustic wavelet was derived either from farfield signatures in water or from the sea-bottom reflection[18] next to the drill site (see "Rise" and "Palmer Deep" chapters for details). For simplified but effective "practical" correlation, acoustic waves are treated like electromagnetic waves in ray optics.

Density and *P*-wave velocity together define the acoustic impedance or acoustic hardness of a rock formation.

$$Z = \rho \cdot v_p \qquad \text{(Eq. 7.14)}$$

Z = impedance
ρ = bulk density
v_p = *P*-wave velocity

Downhole changes of impedance cause part of the propagating wave energy to reflect and travel back to the surface. Two principle situations have to be distinguished, the vertical and oblique incident case (Fig. 7.1).

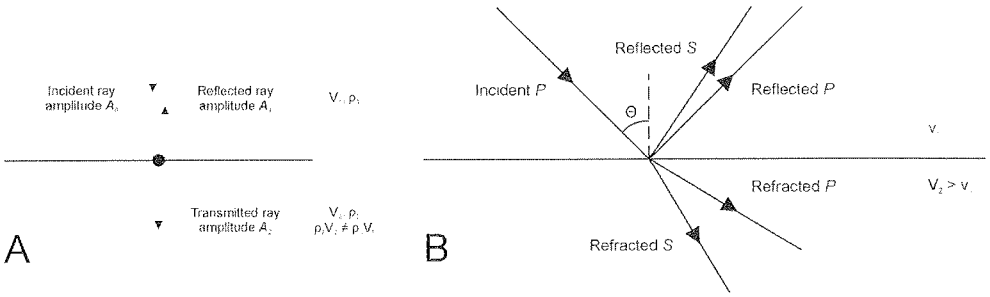

Fig. 7.1. **(A)** reflected and transmitted rays associated with a ray normally incident on an interface of acoustic contrast, **(B)** reflected and refracted *P*- and *S*-rays generated by a *P*-ray obliquely incident on an interface of acoustic impedance contrast.

[18] The sea – bottom reflection is a altered source signal representation (path through water column, uneven sea floor etc....)

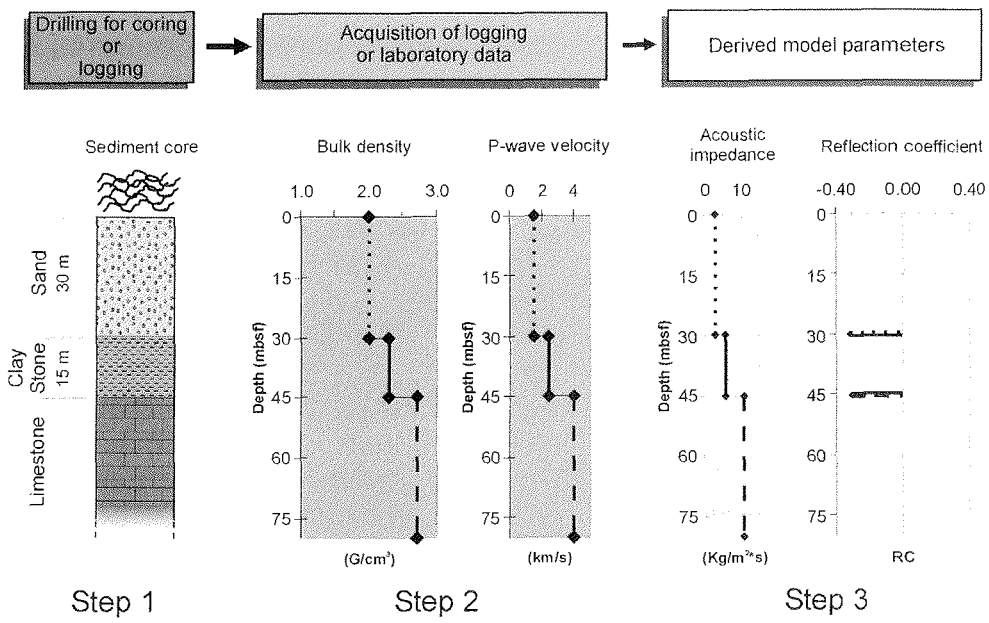

Fig. 7.2. Illustration of the main actions and parameters needed for the development of a simple earth model for core seismic correlations. **Step 1**, drilling provides access to subsurface information. **Step 2**, the geological profile is reduced to physical parameters. Determination of the *in situ* *P*-wave velocity is essential since it defines both the acoustic hardness of the profile and the position and spacing of reflections. The bulk density is commonly the other parameter used. If density data are nor available they can be replaced by other parameters that correlated with subsurface acoustic contrasts. **Step 3**, the parameters of step 2 are used to calculate the acoustic impedance and reflectivity coefficient.

To simulate the interaction between formation and propagating wave some simplifying assumptions are made. The travel path of the wave is assumed to be perfectly vertical, no multiple reflections between layers not taken into account, and attenuation and dispersion are not considered.

The degree of change in impedance at an acoustic discontinuity determines how much of the wave energy is reflected and how much continues to travel downward. The contrast in impedance is defined as the reflectivity coefficient R. The transmission coefficient T is defined by the ratio of the amplitudes of the initial waves and the amplitudes of the transmitted waves.

$$R_{1/2} = \frac{Z_2 - Z_1}{Z_2 + Z_1} \qquad \text{(Eq. 7.15)}$$

$R_{1/2}$ = reflectivity coefficient

Z_1 = impedance of layer 1

Z_2 = impedance of layer 2

$$T_{1/2} = \frac{A_2}{A_0} = \frac{2Z_1}{Z_1 + Z_2} \qquad \text{(Eq. 7.16)}$$

$Z_{1/2}$ = transmission coefficient

Z_1 = impedance of layer 1

Z_2 = impedance of layer 2

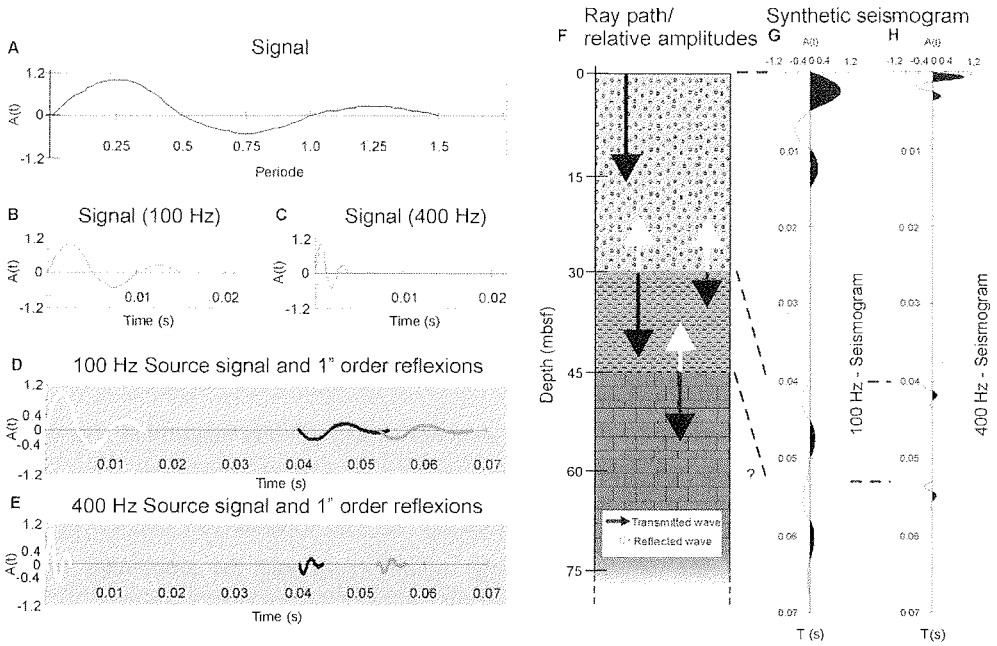

Fig. 7.3. Simplified illustration showing how source signal wavelets of the same amplitudes but different wavelengths travel through the earth model from Fig. 7.2. The ray path is indicated by direction of the arrows. The amounts of the reflected and transmitted amplitudes by the arrow length. Note the limitation due to interference of a wavelet with 100 Hz in detecting the 15 m thick clay stone layer. The 400 Hz wavelet reproduces all impedance contrasts unambiguously.

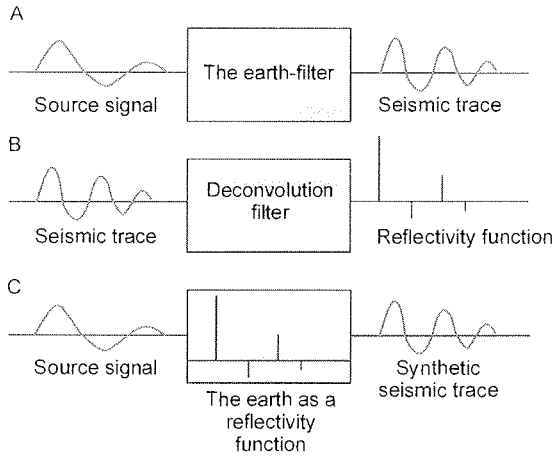

Fig. 7.4. The earth acts as a filter (**A**). The process of deconvolution (a filter operation) reduces the complex signal to a discontinuous reflectivity function or profile (**B**). If the reflectivity function of the earth model is known, a synthetic trace or reflective image of the subsurface can be produced (**C**).

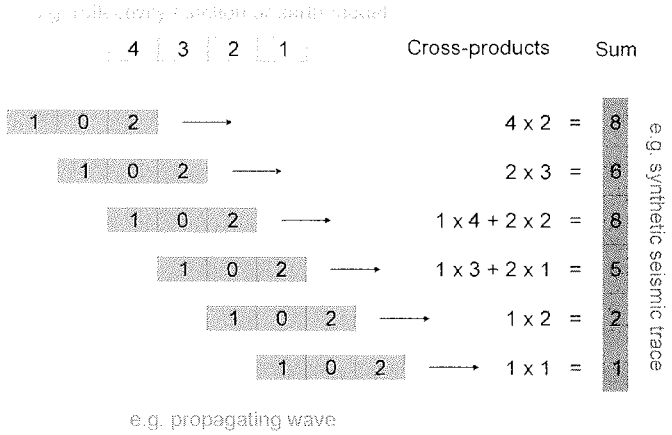

Fig. 7.5. Convolution of two digital functions illustrated with a numerical example. For the special case of a synthetic seismogram calculation, descriptive labels like "propagating wave" etc. are added (modified from Kearey and Brooks, 1984).

The combined reflectivity coefficients of adjacent layers of material with acoustic contrast form the reflectivity profile. The reflectivity profile is the impulse response of the earth-model. Thus the synthetic seismogram can be calculated by convoluting the source signal with the reflectivity model (Fig. 7.5). In other words the geological profile acts as a filter (Kearey and Brooks, 1984; Dresen, 1985) through which the source signal is altered (Fig. 7.4).

$$y(t) = ss(t) \cdot rfc(t) \qquad \text{(Eq. 7.17)}$$

y = synthetic trace (= filtered output)
ss = source signal (= filter input)
rcf = reflectivity coefficient (= impulse response of filter)

7.1.7 The Matlab Routine Synseis

The Matlab routine *synseis* automates and simplifies the generation of synthetic seismograms from core or logging data. The basic building blocks of this software are outlined in Fig. 7.1:

File Input: After typing in *synseis* at the Matlab environment prompt, the software requests three input files with path: these are handled internally as variables *zd* (depth versus density), *zv* (depth in meters versus *P*-wave velocity in meters / second), and *zs* (time in seconds versus amplitude). All input files are read in as either tab or space delimited ASCCI files. A standard error call - back routine informs the user in case of data access or read errors ("Cannot open file", "Existence?", "Permissions?", "Memory?, ...). The density and velocity information need not to have a common depth scale nor do the files need to have the same length.

Monotony Check: The user is prompted to decide whether a monotony check of the density or velocity depth scale is required. In the case of "yes" the monotony is checked and in case of a detected non-monotonous increase of the depth scale, the user is informed of the problematic input file lines via screen output. In case of monotony problems, the user should manually terminate the routine *"strg + Pause"* and resolve the input file problems prior to restarting *synseis*.

Subroutine Check: After a successful monotony check the user is prompted to check the density and velocity data quality. A similar routine, solocheck, was discussed in chapter 7.2. In addition to the features already discussed, the interactive graphic - supported subroutine check defines a common depth scale for density and velocity and reduces input column length to the length of the shorter input file. After performing the interactive data clean-up cycle (to eliminate outliers) the user is asked to perform smoothing and data reduction operations by reducing the sampling interval.

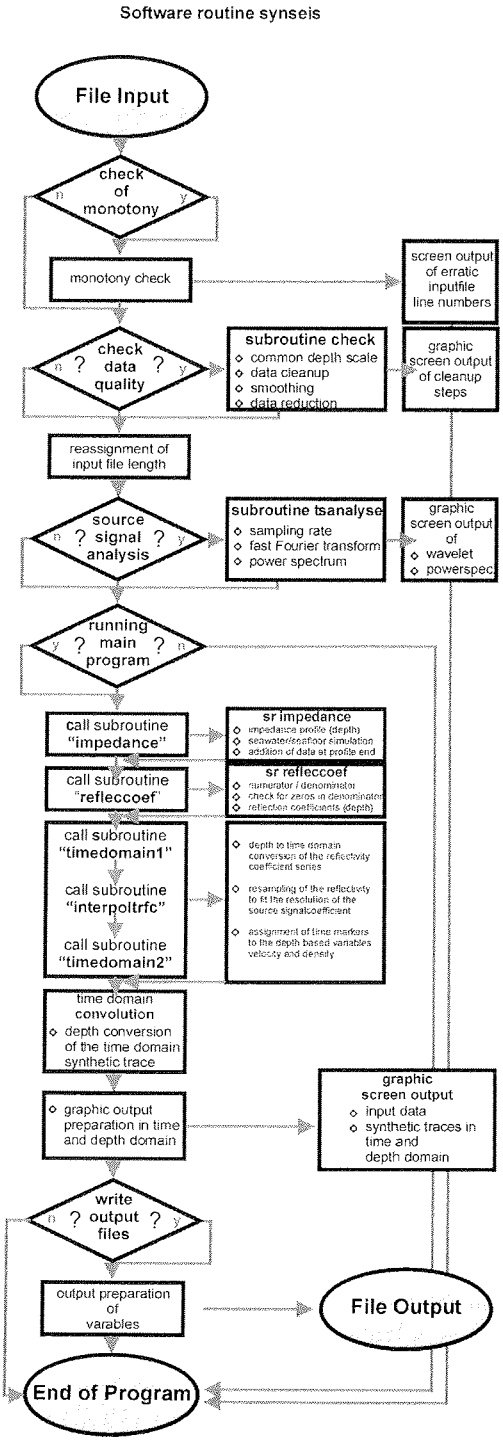

Fig. 7.1. Flow chart of Matlab routine synseis. A detailed explanation of the features and calculation steps is given in the text.

Source Signal Check: After reassigning the new input data file length to the main program, the user is prompted to perform a short source signal analysis or to skip it. In the case of "yes" subroutine "tsanalyze" is called. The subroutine "tsanalyze" analyzes the input source signal file (e.g. sampling rate) and performs a fast Fourier transform to determine the frequency content. The original wavelet, together with a power spectrum, is subsequently shown as a graphic output. Following the input parameter modification and clean-up routines, the user is prompted to start the actual process of synthetic trace calculation. In the case of "no" the routine *synseis* is terminated. In the case of "yes", a series of calculations is performed in form of subroutines that report preliminary results back to the main program. No user interaction is required for the following 5 subroutines.

Impedance in Depth Domain: The subroutine "impedance" calculates the impedance function for the previously - generated equally - spaced common depth profile. To avoid hard artificial reflections at the end of the profile (Mosher, 1993; Bergmann, 1996; Billard, 1990; Fehr, 1991) artificial low contrast noise is added to the end of the impedance profile. The artificial noise is based on the last real density and velocity value. The additon is necessary because the length of the final synthetic trace will be longer than the reflectivity input file (see Fig. 7.1, and Kearey and Brooks, 1994 for explanation). Additionally the water / sea floor interface must be simulated by adding one seawater density and one seawater velocity value at the beginning of the velocity and density profile. In a real seismic section the reflection caused by the water / sea floor boundary is commonly the strongest. This is only partly due to the impedance contrast of the sea floor; it is also due to the fact that this boundary is the first major reflection of the seismic source signal.

Reflectivity Coefficients in Depth Domain: The previously calculated impedance profile of subroutine "impedance" is the new input variable for subroutine "refleccoef". Within "refleccoef" the numerator and denominator of the reflectivity coefficient are calculated separately from the impedance values. Prior to the coeffient calculation all denominators are checked for zero values. In case of existing zeros, the values are replaced by small values close to zero.

Transformation to the Time Domain: Subroutines "timedomain1", "interpoltrfc", and "timedomain2" transform the depth - based reflectivity profile calculated within subroutine "refleccoef" into a time - based reflectivity series. An interpolation step is necessary to assure the same sampling interval for the reflectivity coefficient series and the source wavelet. The "timedomain2" assigns matching time markers to the previously depth - based velocity and density variables.

Convolution and Additional Reconversion to Depth Scale: This is the time domain convolution of the source signal with the reflectivity series; for details see Fig. 7.5. After convolution a second depth scaled synthetic trace is generated.

Graphic Output: After the convolution processing the data are prepared for display within a data display preparation programming-code block. Two main output windows are prepared and subsequently displayed on the screen. The time domain window shows the altered input density and velocity values, the impedance function, the reflectivity coefficient series and the synthetic trace in the time domain. This first output window can be exported in postscript format via the MATLAB environment. It is followed by the second graphic output window after hitting any key on the keyboard. The second graphic output window contains the same variable as the first one, but shown plotted against the depth scale.

File Output: Following the graphic output the user is prompted to exit the program or hcontinue with the last feature of the routine, the column - oriented tab - delimited ASSCI file output of almost all calculated values. Ten ASSCI files are generated to a user specified folder:

zdout.txt	interpolated and possibly cleaned depth / density file
zvout.txt	interpolated and possibly cleaned depth / velocity file
tsout.txt	interpolated source signal time / amplitude file
tdout.txt	interpolated and possibly cleaned time / density file
tvout.txt	interpolated and possibly cleaned time / velocity file
zimout.txt	depth / impedance file
timout.txt	time / impedance file
zrfcsout.txt	depth / reflectivity coefficient file
trfcsout.txt	time / reflectivity coefficient file
tzout.txt	time / depth file
trfclout.txt	time / reflectivity coefficient with artificially added extensions file
tsynout.txt	time / synthetic amplitudes file
zsynout.txt	depth / synthetic amplitudes file
tsynoutf.txt	time / synthetic amplitudes with artificially added extensions file

7.1.8 Example

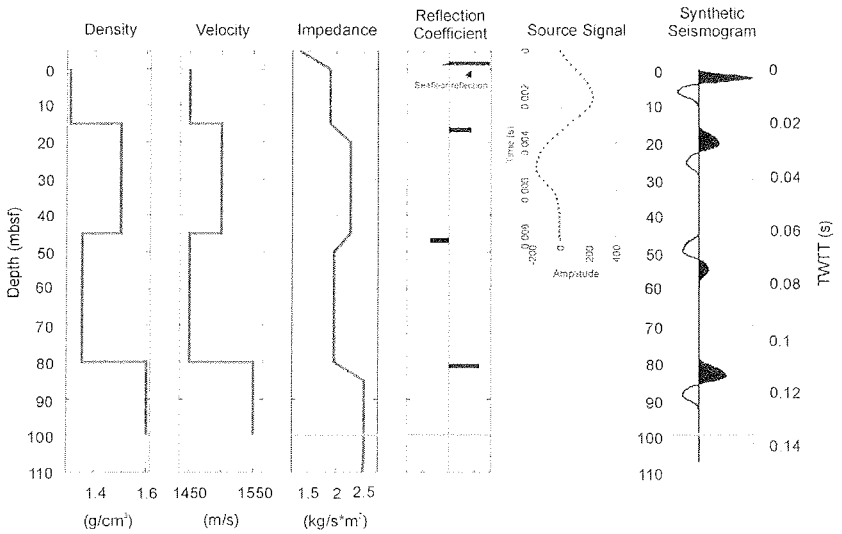

Fig. 7.1. The parameters of the simplified earth model similar to the examples introduced in previous figures (e.g. Fig. 7.2) have been used as input variables for the Matlab routine synseis. The original two graphic output files are reduced to one file with a depth and time scale along the synthetic trace figure.

The example (Fig. 7.1) shows a simplified earth model with four impedance contrasts. Values are added at the end of the actual data set to avoid a hard reflection at the end of the profile. To perform the convolution of a source signal (with a wavelength of several meters, sampled at discrete time intervals) and a reflectivity profile given in length units (e.g. in case of the MST data: 2 cm spacing) it is necessary to transform the reflectivity profile in time dependent variables with the same time resolution than the used source signal. All calculations are made using the Matlab® v.5 routine "synseis" introduced in this chapter.

7.1.9 Conclusions

- Predictive acoustic modelling of the sea floor is a complex approach dependent on numerous physical properties that can`t be acquired in real time and have to be recalculated to meet in-situ conditions.
- The applied seismic profile to core correlation approach using laboratory or logging derived density and acoustic *P*-wave velocity data and derived synthetic seismograms is in most cases sufficient to combine continuous seismic line information and detailed bore hole spot information.

- The newly developed software "synseis" is a user interactive shareware program written by the author, that allows to use raw downhole and MST data to calculate synthetic seismograms in time and depth domain. The data can be checked for monotony and outliers prior to the convolution step.

7.2 Excursus 2: A new automated data clean-up procedure for physical property data of cores

7.2.1 Introduction

A common problem to fast data analysis and trend recognition in physical property data of cores is

a) large data sets
b) the abundance of outliers and erroneous data.

This short chapter is introducing a fast and automated and interactive technique to overcome the problem of outliers in large data sets that often mask true trends when plotted. Standard techniques including smoothing and filtering, always incorporate erroneous values into the final data presentation. In case of using core physical properties (e.g. density and velocity data) for the calculation of synthetic seismograms for example, outliers, erroneous smoothened data can have a dominant effect on position and amplitude of reflectors of the synthetic trace.

A routine written in Matlab is used to handle large amounts of data in a standardized way. The routine removes values that are larger or smaller than values of a defined percentage above or below a multiple polynomial regression curve. The removed values are getting replaced by linear interpolations of neighbor values. The order of the polynomial fit and the cutoff borders are user defined. The correction is done in two successive steps. During a first step usually smaller order polynomials and wider thresholds are used. The second step takes the output data of the first step and more restrictive correction terms can be applied. Special care is taken of values at the beginning and end by automatically reducing the order of the polynomes to avoid unrealistic trends based on view data points.

The process is user-interactive and graphically supported to allow an easy evaluation of each processing step.

7.2.2 Example

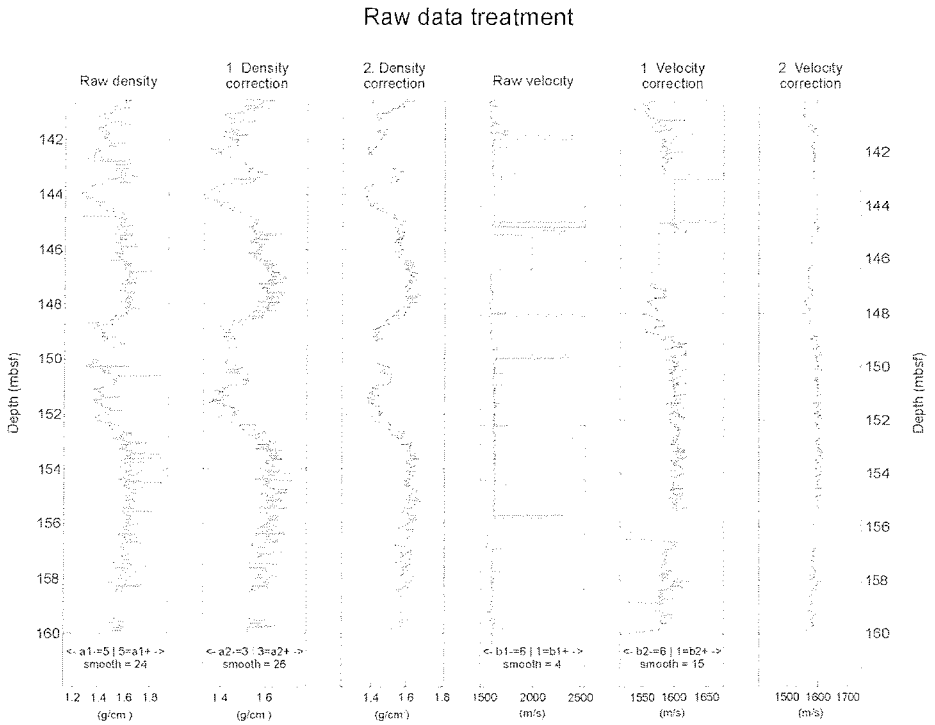

Fig. 7.1. Example of the data "cleaning" process used to remove extreme values and artifacts from raw data sets before constructing a synthetic seismogram.

Example of MST data of a 20 m core section (ODP Leg 178, Site 1095). The Multisensor Track density and velocity data are cleaned in two successive steps. The parameter a (lower part of each figure column) indicates the % of the cut-off tolerance below and above a polynomial fit of order *n* through the original unaltered data. The value *smooth* stands for the used polynomial order.

7.2.3 Interactive Matlab Code

The matlab code "check" is compatible with Matlab® 5.3. The routine „solo - check" in the current version is part of the synthetic seismic package „synseis" subroutine „check" developed during this thesis.

Literature

Abelmann, A., Gersonde, R., and Spiess, V., 1990. Pliocene - Pleistocene paleoceanography in the Weddell Sea - siliceous microfossils evidence. *In* Bleil, U., and Thiede J. (Eds.), *Geological History of the Polar Regions: Arctic versus Antarctic:* NATO ASI Series C: 308, Dordrecht (Kluwer Acad. Publ.), 729 - 759.

Ackermann, J., 2000. New Eyes on the Ocean. *National Geographic* (October): 86 - 115.

Acton, G.D., Barton, C., and Leg 178 Shipboard Scientific Party, subm. Palmer Deep composite depth scales for ODP Leg 178 Sites 1098 and 1099, *Proc. ODP, Scientific Results, 178*: College Station, TX (Ocean Drilling Program).

Alley, R.B., Blankenship, D.D., Rooney, S.T., and Bentley, C.R., 1989. Sedimentation beneath ice shelves: The view from Ice Stream B. *Mar. Geol.*, 85: 101-120.

Alonso, B., Anderson, J.B., Diaz, J.T., and Bartek, L.R., 1992. Plio-Pleistocene seismic stratigraphy of the Ross Sea: Evidence for multiple ice sheet grounding episodes. *In* Elliot, D.H. (Ed.), *Contributions to Antarctic Research III:* Antarctic Research Series, 57: Washington, D.C. (AGU), 93-103.

Andersen, J.U., 1963. An improved pretreatment for mineralogy analysis of samples containing organic matter. *Clays and Clay Minerals*, 10: 380-388.

Anderson, J.B., and Bartek, L.R., 1992. Cenozoic glacial history of the Ross Sea revealed by intermediate resolution seismic reflection data combined with drill site information. *In* Kennett, J.P., and Warnke, D.A. (Eds.), *The Antarctic Palaeoenvironment: A perspective on global change:* Antarctic Research Series, 56: Washington, D.C. (AGU), 231-263.

Anderson, L.D., and Ravelo, A.C., in press. Data Report: Biogenic opal in Palmer Deep sediments, Site 1098, Leg 178. *In* Barker, P.F., Camerlenghi, A., Acton, G.D., and Ramsay, A.T.S. (Eds.), *Proc. ODP, Scientific Results,* 178: College Station, TX (Ocean Drilling Program).

Armand, L.K., 1997. *The use of diatom transfer functions in estimating sea-surface temperature and sea-ice cores from the southeast Indian Ocean.* Ph.D. Thesis, Australian National University, Canberra, 391 pp.

Bachmann, R.T., 1985. Acoustic and physical property relationships in marine sediment. *J. Acoust. Soc. Am.*, 78: 616-621.

Bard, E., 1988. Correction of accelerator mass spectrometry ^{14}C ages measured in planktonic foraminifera: paleoceanographic implications. *Paleoceanography*, 3 (6): 635-645.

Bard, E., Labeyrie, L., Arnold, M., Labracherie, M., Pichon, J., Duprat, J., and Duplessy, J., 1989. AMS-^{14}C ages measured in deep sea cores from the southern ocean: implications for sedimentation rates during Isotope Stage 2. *Quaternary Research*, 31: 309-317.

Barker, H.N., and Austin, A., 1994. Crustal diapirism in Bransfield Strait, West Antarctica: Evidence for distributed extension in marginal-basin formation. *Geology*, 22: 657-660.

Barker, P.F., 1982. The Cenozoic subduction history of the Pacific margin of the Antarctic Peninsula: Ridge crest-trench interactions. *Journal of the Geological Society of London*, 139: 787-801.

Barker, P.F., 1995. The proximal marine sediment record of Antarctic climate since the late Miocene. *In* Cooper, A.K., Barker, P.F., and Brancolini, G. (Eds.), *Geology and Seismic Stratigraphy of the Antarctic Margin*, 1. Am. Geophys. Union Antarct. Res. Ser., 68: 25-57.

Barker, P.F., and Burrell, J., 1977. The opening of Drake Passage. *Marine Geology*, 25: 15-34.

Barker, P.F., and Camerlenghi, A., 1999. An approach to Antarctic glacial history: the aims of Leg 178. *In* Barker, P.F., Camerlenghi, A., Acton, G.D., et al., *Proc. ODP, Init. Repts.*, 178, 1-44 [CD-ROM]. Available from: Ocean Drilling Program, Texas A&M University, College Station, TX 77845-9547, U.S.A.

Barker, P.F., and Dalziel, I.W.D., 1983. Progress in geodynamics in the Scotia Arc region. *American Geophysical Union Geodynamic Series*, 9: 137-170.

Barker, P.F., Barrett, P.J., Camerlenghi, A., Cooper, A.K., Davey, F.J., Domack, E.W., Escutia, C., Kristoffersen, Y., and O'Brien, P.E., 1998. Ice sheet history from Antarctic continental margin sediments: the ANTOSTRAT approach. *Terra Antarct.*, 5(4): 737-760.

Barker, P.F., Barrett, P.J., Cooper, A.K., et al., 1999. Antarctic glacial history from numerical models and continental margin sediments. *Palaeogeography, Palaeoclimatology, Palaeoecology*, 150: 247-267.

Barker, P.F., Camerlenghi, A., and Acton, G.D. (Eds.), 1999. *Proc. ODP, Init. Reports*, 178: College Station, TX (Ocean Drilling Program).

Barker, P.F., in press. Data report: Composite depths and spliced sections for Leg 178 Sites 1095 and 1096, Antarctic Peninsula continental rise. *In* Barker, P.F., Camerlenghi, A., Acton, G.D., and Ramsay, A.T.S. (Eds.), *Proc. ODP, Sci. Results*, 178: College Station, TX (Ocean Drilling Program).

Barrett, P.J., 1999. Antarctic climate history over the last 100 million years. *Terra Antarctica Reports*, 3: 53-72.

Barrett, P.J., 1996. Antarctic paleoenvironment through Cenozoic times - A review. *Terra Antarctica*, 3(2): 103-119.

Barrett, P.J., 2001. Cenozoic Antarctic glacial history - checks from the margin. *In* Florindo, F., and Cooper, A.K. (Eds.), *The geologic record of the Antarctic ice sheet from drilling, coring and seismic studies: Quaderni di Geofisca*, 16, 13-15.

Barrett, P.J., Bleakley, N.L., Dickinson, W.W., Hannah, M.J., and Harper, M.A., 1997. Distribution of siliceous microfossils on Mount Feather, Antarctica, and the age of the Sirius Group. *In* Ricci, C.A. (Ed.), *The Antarctic Region: Geological Evolution and Processes:* Siena (Terra Antarctica Publication), 763-770.

Bart, P.F., and Anderson, J.B., 1995. Seismic record of glacial events affecting the Pacific margin of the Northwestern Antarctic Peninsula. *In*: Cooper, A.K., Barker, P.F., and Brancolini, G. (Eds.), *Geology and seismic stratigraphy of the Antarctic margin:* Antarctic Research Series, 68: Washington, D.C. (AGU), 75-96.

Bart, P.J., and Warny, S.A., 2001. An evaluation of the Messinian salinity crisis: Implications of new palynological results on the interpretation of late Miocene Antarctic ice sheet

evolution. *In* F. Florindo, and A.K. Cooper (Eds.), *The geologic record of the Antarctic ice sheet from drilling, coring and seismic studies: Quaderni di Geofisca*, 16, 17.

Bateman, R.M., 1985. *Log Quality Control*: Boston (Int. Human Resour. Dev. Corp. Press).

Belkin, I.M., and Gordon, A.L., 1996. Southern Ocean fronts from the Greenwich meridian to Tasmania. *Journal of Geophysical Research*, 101(C2): 3675-3696.

Berger, W.H., and Wefer, G., 1996. Expeditions into the past: Paleoceanographic studies in the South Atlantic. *In* Wefer, G., Berger, W.H., Siedler, G., and Webb, D.J. (Eds.), *The South Atlantic: Present and Past Circulation:* Berlin-Heidelberg (Springer), 363-410.

Berggren, W.A., Kent, D.V., Swisher, C.C., and Aubry, M.-P., 1995. A revised Cenozoic geochronology and chronostratigraphy. *In* Berggren, W.A., Kent, D.V., Aubry, M.-P., and Hardenbol, J. (Eds.), *Geochronology, Time Scales and Global Stratigraphic Correlation*: SEPM, Spec. Publ. 9: 129-212.

Bergmann, U., 1996. Interpretation digitaler Parasound Echolotaufzeichnungen im östlichen Arktischen Ozean auf der Grundlage physikalischer Sedimenteigenschaften. *Berichte zur Polarforschung*, 183: Bremerhaven (Alfred Wegener Institut für Polar- und Meeresforschung), 164 pp.

Berner, R.A., 1999. A new look at the long-term carbon cycle. *GSA Today*, 9(11): 1-6.

Billard, K., 1990. Geophysical modelling of the Lahave clay and Emerald silt formations, Lahave Basin: Halifax, NS (Dalhousie University), 77 pp.

Blum, P., 1997. Physical properties handbook: A guide to the ship board measurement of physical properties of deep-sea cores. ODP Tech. Note, 26. *available from* http://www-odp.tamu.edu/publications/tnotes/tn26/INDEX.HTM.

Boggs, S., 1987. *Principles of Sedimentology and Stratigraphy*: New York (Macmillan), 784 pp.

Bolt, B.A., 1982. *Inside the Earth*: San Francisco (Freeman), 191 pp.

Bouma, A.H., 1962. *Sedimentology of some flysch deposits: A graphic approach to facies interpretation:*Amsterdam (Elsevier).

Boyce, R.E., 1976. Definitions and laboratory techniques of compressional sound velocity parameters and wet-water content, wet-bulk density, and porosity parameters by gravimetric and gamma ray attenuation techniques. *In* Schlanger, S.O., et al. (Eds.), *Initial Reports of the Deep Sea Drilling Project:* Washington, D.C. (U.S. Gouvernment Printing Office), 33, 931-958.

Breitzke, M., 1997. Elastische Wellenausbreitung in marinen Sedimenten - Neue Entwicklungen der Ultraschall Sedimentphysik und Sedimenttechnographie. *Berichte der Universität Bremen, Fachbereich Geowissenschaften*, 104: Bremen (Universität Bremen), 298 pp.

Brewer, T.S., Rex, D., Guise, P.G., and Hawkesworth, C.J., 1996. Geochronology of Mesozoic tholeiitic magmatism in Antarctica: Implication for the development of the failed Weddell Sea rift system. *In* Storey, B., King, E.C., and Livermore, R. (Eds.), *Weddell Sea Tectonics:* London (Special Publication of the Geological Society, London), 185 - 208.

Brown, K., and Westbrook, G.K., 1988. Mud diapirism and subcretion in the Barbados Ridge accretionary complex: The role of fluids in accretionary processes. *Tectonics*, 7(3): 613-640.

Brückmann, W., 1989. Typische Kompaktionsabläufe mariner Sedimente und ihre Modifikation in einem rezenten Akkretionskeil (Barbados Ridge). *Geologie, Paläontologie, Stratigraphie,* 5(Reihe A): 135 pp.

Burling, R.W., 1961. Hydrology of circumpolar waters south of New Zealand. *New Zealand Department of Science and Industrial Research Bulletin*, 143: 66.

Camerlenghi, A., Crise, A., Pudsey, C.J., et al., 1997. Ten-month observation of the bottom current regime across a sediment drift of the Pacific margin of the Antarctic Peninsula. *Antarct. Science*, 9(4): 426-433.

Camerlenghi, A., Rebesco, M., De Santis, L., Volpi, V., and DeRossi, A., in press. The Antarctic Peninsula Pacific Margin: Modelling flexure and decompaction with constraints from ODP Leg 178 Initial Results. *In* Gamble, J., Skinner, D., and Henrys, S. (Eds.), *Proceedings of the VIII° International Symposium on Antarctic Earth Sciences* (New Zealand J. Geol. Geophys, Royal Soc. New Zealand).

Cande, S.C., and Kent, D.V., 1995. Revised calibration of the geomagnetic polarity time scale for the Late Cretaceous and Cenozoic. *J. Geophys. Res.*, 100: 6093-6095.

Carlson, R.L., Gangi, A.F., and Snow, K.R., 1986. Empirical reflection travel time versus depth and velocity versus depth functions for the deep-sea sediment column. *J. Geophys. Res.*, 91: 8249-8266.

Cavalieri, D.J., and Parkinson, C.L., 1981. Large - scale variations in observed Antarctic sea ice extent and associated atmospheric circulation. *Monthly Weather Reviews*, 109: 2323 -2336.

Compton, R.R., 1985. *Geology in the field:* Chichester (John Wiley & Sons), 389 pp.

Cooper, A.K., Barrett, P.J., Hinz, K., Traube, V., Leitchenkov, G., and Stagg, H.M.J., 1991. Cenozoic prograding sequences of the Antarctic continental margin: A record of glacio-eustatic and tectonic events. *Marine Geology*, 102: 175-213.

Courtney, R.C., and Mayer, L., 1993a. Acoustic properties of fine-grained sediments from Emmerland Basin: Toward an inversion for physical properties using the Biot-Stoll model. *J. Acoust. Soc. Am.*, 93: 3193-3200.

Courtney, R.C., and Mayer, L., 1993b. Calculation of acoustic parameters by a filter correlation. *J. Acoust. Soc. Am.*, 93: 1145-1154.

Cowan, E.A., in press. Identification of the glacial signal from the Antarctic Peninsula since 3.0 Ma at Site 1101 in a continental rise sediment drift. *In* Barker, P.F., Camerlenghi, A., Acton, G.D., and Ramsay, A.T.S. (Eds.), *Proc. ODP, Sci. Results 178:* College Station, TX (Ocean Drilling Program).

Cunningham, W.L., Leventer, A., Andrews, J.T., Jennings, A.E., and Licht, K.J., 1999. Late Pleistocene-Holocene marine conditions in the Ross Sea, Antarctica: Evidence from the diatom record. *Holocene*, 9(2): 129-139.

Curtis, M.L., and Storey, B.C., 1996. A review of geological constraints on the pre-break-up position of the Ellsworth Mountains within Gondwana: Implications for Weddell Sea evolution. *In* Storey, B., King, E.C., and Livermore, R. (Eds.), *Weddell Sea Tectonics*

and Gondwanaland Break-up: London (Special Publication of the Geological Society, London), 11-30.

Dalziel, I.W.D., and Elliot, D.H., 1982. West Antarctica: Problem child of Gondwanaland. *Tectonics*, 1: 3-19.

Dalziel, I.W.D., Garrett, S. W., Grunow, A. M., Pankhurst, R. J., Storey, P. C., and Vennum, W. R., 1987. The Ellsworth-Whitmore mountains crustal block: Its role in the tectonic evolution of West Antarctica. *In* McKenzie, G.D. (Ed.), *Gondwana Six: Structure, Tectonics and Geophysics:* Geophysics Monogr., 40: 173 - 182.

DeConto, R.M., and Pollard, D., 2001. The early glacial history of Antarctica: A new modelling perspective. *In* Florindo, F., and Cooper, A.K. (Eds.), *The geologic record of the Antarctic ice sheet from drilling, coring and seismic studies*: Quaderni di Geofisica, 16, 45-47.

Defelice, D.R., and Wise, S.W., 1981. Surface lithofacies, biofacies, and diatom diversity patterns as models for delineation of climatic change in the southeast Atlantic Ocean. *Mar. Micropal.*, 6: 29-70.

Denton, G.H., Prentice, M.L., and Burckle, L.H., 1991. Cainozoic history of the Antarctic Ice Sheet. *In* Tingey, R.J. (Ed.), *The Geology of Antarctica:* Oxford (Oxford University Press), 365 - 433.

Domack, E., Leventer, A., Dunbar, R., Taylor, F., Brachfeld, S., Sjunneskog, C., and Shipboard Scientific Party, 2001. Chronology of the Palmer Deep Site, AntarcticPeninsula: A Holocene paleoenvironmental reference for the circum-Antarctic. *Holocene*, 1: 1-9.

Domack, E.W., and Leg 178 Shipboard Scientific Party, 1998. Mysteries of the Palmer Deep revealed: ODP Leg 178 to the Antarctic Peninsula. *JOI/USSAC Newsletter*, 11(3): 1-24.

Domack, E.W., Jull, A.J.T., Anderson, J.B., Linick, T.W., and Williams, C.R., 1989. Application of tandem accelerator mass-spectrometer dating to late Pleistocene-Holocene sediments of the East Antarctic continental shelf. *Quaternary Research*, 31: 277-287.

Domack, E.W., Jull, A.J.T., and Nakao, S., 1991. Advance of East Antarctic outlet glaciers during the Hypsithermal: Implications for the volume state of the Antarctic ice sheet under global warming. *Geology*, 19: 1059-1062.

Domack, E.W., Leventer, A., Brachfeld, S., Chong, A., Dunbar, R., Manley, P., Reynolds, P.D., and Taylor, F., 1999. Paleoenvironmental investigations using sediment cores, Antarctic Peninsula. *Cruise Report NBP99-03*, 19 pp.

Domack, G., Leventer, A., Reynolds, P., Mucciarone, D., Howat, I., Dunbar, R., Taylor, F., Brachfeld, S., Clark, K., Maxwell, A., Woolford, T., Chong, A., Tewksbury, D., and Manley, P., 1999. Nathaniel B. Palmer Cruise 99-03. *Antarctic News: Newsletter forParticipants of the U. S. Undergraduate Antarctic Program*(2): 10 pp.

Dowsett, H.J., and Cronin, T.M., 1990. High eustatic sea-level during the middle Pliocene: Evidence from the southeastern U.S. Atlantic Coastal Plain. *Geology*, 18: 435-438.

Dreimanis, A., 1976. Tills: their origin and properties. *In*: Legget, R.F. (Ed.), *Glacial till*: Royal Society of Canada, Spec. Publ. 12, 11-49.

Dresen, L., Gebrande, H., Harjes, H.-P., Hubral, P., and Miller, H., 1985. Seismische Verfahren. *In* Bender, F. (Ed.), *Angewandte Geowissenschaften, 2: Methoden der Angewandten Geophysik und mathematische Verfahren in den Geowissenschaften*: Stuttgart (F. Enke Verl.), 156-298.

Dresen, L., 1985. Flözwellenseismik für die untertägige Steinkohlenerkundung. *In* Bender, F. (Ed.), *Angewandte Geowissenschaften, 2: Methoden der Angewandten Geophysik und mathematische Verfahren in den Geowissenschaften*: Stuttgart (F. Enke Verl.), 261-293.

Ehrmann, W.U., and Mackensen, A., 1992. Sedimentological evidence for the formation of an East Antarctic ice sheet in Eocene/Oligocene time. *Palaeogeography, Palaeoclimatology, Palaeoecology*, 93: 85-112.

Eldholm, O., and Thiede, J., 1980. Cenozoic continental separation between Europe and Greenland. *Palaeogeography, Palaeoclimatology, Palaeoecology*, 30: 243-259.

Ercilla, G., Baraza, J., Alonso, B., and Canals, M., 1998. Recent geological processes in the Central Bransfield Basin (Western Antarctic Peninsula). *In* Stoker, M.S., Evans, D., and Cramps, A. (Eds.), *Geological Processes on Continental Margins: Sedimentation, Mass-Wasting and Stability:* London (Special Publication of the Geological Society, London), 205-216.

Escutia, C., Moerz, T., Williams, T., Lauer-Leredde, C., Jaramillo, J.M., in press. Correlation between core, logging, physical properties and seismic data at Site 1103 in the Antarctic Peninsula. *Palaeogeography, Palaeoclimatology, Palaeoecology*.

Exon, N., Kennett, J., Malone, M., and Shipboard Scientific Party, 2000. The opening of the Tasmanian Gateway drove global Cenozoic paleoclimatic and paleoceanographic changes: results of Leg 189. *JOIDES Journal*, 26(2): 11-18.

Eyles, N., 1993. Earth's glacial record and its tectonic setting. *Earth-Sci. Rev.*, 35: 1-248.

Eyles, N., Daniels, J., Osterman, L.E., and Januszczak, N., 2001. Ocean Drilling Program Leg 178 (Antarctic Peninsula): Sedimentology of glacially influenced continental margin topsets and foresets. *Mar. Geol.*, 178: 135-156.

Fehr, S.D., 1991. A geoacoustic model for the upper sediments of Emerald Basin: Halifax, NS (Dalhousie University), 293 pp.

Fitzgerald, P., 1999. Cretaceous - Cenozoic tectonic evolution of the Antarctic Plate. *Terra Antarctica Reports*, 3: 109-130.

Flint, R.F., Sanders, J.E., and Rogers, J., 1960. Diamictite, a substitute term for symictite. *Geol. Soc. Am. Bull.*, 71: 1809.

Folk, R.L., 1974. *Petrology of Sedimentary Rocks*. Houston, TX (Hemphill), 182 pp.

Forsyth, D.W., 1975. Fault Plane Solutions and Tectonics of the South Atlantic and Scotia Sea. *J. Geophys. Res.*, 80(11): 1429-1443.

Francis, J.E., 1999. Evidence from fossil plants for Antartic paleoclimates over the past 100 million years. *Terra Antarctica Reports*, 3: 43-52.

Friedman, G.M., 1961. Distinction between dune, beach, and river sands from their textural characteristics. *J. Sed. Petrology*, 31: 514-529.

Friedman, G.M., 1962. On sorting, sorting coefficients, and the log normality of the grain-size distribution of sandstones. *J. Geol., 70*: 737-753.

Friedman, G.M., 1967. Dynamic processes and statistical parameters compared for size frequency distribution of beach and river sands. *J. Sed. Petrology*, 37: 327-354.

Friedman, G.M., 1979. Address of the retiring President of the International Association of Sedimentologists: Differences in size distributions of populations of particles among sands of various origins. *Sedimentology*, 26: 3-32.

Fritsch GmbH Laborgerätebau, 1994. *Benutzer-Handbuch Laser Partikel Sizer "analysette 22"*: Idar-Oberstein (Fritsch GmbH Laborgerätebau), 225 pp.

Gambôa, L.A.P., and Maldonaldo, P.R., 1990. Geophysical investigations in the Bransfield Strait and in the Bellingshausen Sea-Antarctica. *In* John, B.S. (Ed.), *Antarctica as an exploration frontier-hydrocarbon potential, geology and hazards*: Am. Assoc. Pet. Geol. Stud. Geol., 31: 127-141.

Gersonde, R.E.A., 1997. Impact of the Eltanin asteroid in the southeast Pacific 2,2 million years ago. *Nature*, 390 (6658): 357-363.

Gonzáles-Casado, J.M., Giner-Robles, J.L., and López-Martínez, J., 2000. Bransfield Basin, Antarctic Peninsula: Not a normal backarc basin. *Geology*, 28(11): 1043-1046.

Gordon, A.L., 1972a. On the interaction of the Antarctic circumpolar current and the Macquarie Ridge. *In* Hays, D.E. (Ed.), *Antarctic Oceanology II, The Australian-New Zealand Sector:* Washinghton, D.C. (AGU), 71-78.

Gordon, A.L., 1972b. Oceanography of Antarctic waters. *In* Reid, J.L. (Ed.) *Antarctic Oceanology*. 15. Antarct. Res. Ser. 1: 167-203.

Gordon, A.L., 1988. Spatial and temporal variability within the Southern Ocean. *In* Sahrhage, D. (Ed.), *Antarctic Ocean and Resources Variability:* Berlin (Springer), 41-56.

Gordon, J.E., and Harkness, D.D., 1992. Magnitude and geographic variation of the radiocarbon content in Antarctic marine life: Implications for reservoir corrections in radiocarbon dating. *Quaternary Science Reviews*, 11: 697-708.

Griffith, J.C., 1967. Scientific Methods in Analysis of Sediments: New York (McGraw-Hill), 508 pp.

Grunow, A.M., Hanson, R., and Wilson, T., 1996. Were aspects of Pan-African deformation linked to Iapetus opening? *Geology*, 24: 1063-1066.

Grunow, A.M., Kent, D.V., and Dalziel, I.W.D., 1991. New paleomagnatic data from Thurston Island: Implications for the tectonics of West Antarctica and Weddell Sea opening. *J. Geophys. Res.*, 98 (B11): 17,935-17,954.

Hambrey, J.M., Werner, U.E., and Larsen, B., 1991. Cenozoic glacial record of the Prydz Bay Continental Shelf, East Antarctica. *In* Barron, J., Larsen, B., Baldauf, J.G., et al. (Eds.), *Proc. ODP, Sci. Results*, 119: College Station, TX (Ocean Drilling Program), 77-132.

Hamilton, E.L., 1970. Sound velocity and related properties of marine sediments. *J. Geophys. Res.*, 76: 4423-4446.

Hamilton, E.L., Bachmann, R.T., Berger, W.H., Johnson, T.C., and Mayer, L.A., 1982. Acoustic and related properties of calcareous deep-sea sediments. *J. Sed. Petrology*, 52: 733-753.

Han, D.-H., Nur, A., and Morgan, D., 1986. Effects of porosity and clay content on wave velocities in sandstones. *Geophysics*, 51: 2093-2107.

Haq, B.U., Hardenbol, H., and Vail, P.R., 1987. The chronology of fluctuating sea-level since the Triassic. *Science*, 235: 1156-1167.

Haq, B.U., Hardenbol, J., and Vail, P.R., 1988. Mesozoic and Cenozoic chronostratigraphy and cycles of sea-level change. *In* Wilgus, D. (Ed.), *Sea-level changes - An integrated approach:* Society of Economic Paleontologists and Mineralogists Special Publication, 42: 71-108.

Hardage, B.A., 1985. Vertical seismic profiling: a measurement that transfers geology to geophysics. *In* Berg, O.R., and Woolverton, D.G. (Eds.), *Seismic Stratigraphy II: An Integrated Approach.* AAPG Mem., 26:13-36.

Hassler, L.E., and Cowan, E.A., in press. Characteristics of ice-rafted pebbles from the continental rise sediment drifts west of the Antarctic Peninsula (Sites 1095, 1096, and 1101) *In* Barker, P.F., Camerlenghi, A., Acton, G.D., and Ramsay, A.T.S. (Eds.) *Proc. ODP, Sci. Results,* 178: College Station, TX (Ocean Drilling Program).

Haug, G.H., Tiedemann, R., Zahn, R., and Ravelo, A.C., 2001. Role of Panama uplift on oceanic freshwater balance. *Geology*, 29(3): 207-210.

Hawkes, D.D., 1981. Tectonic segmentation of the Northern Antarctic Peninsula. *Geology*, 9: 220-224.

Hellmer, H.H., 1989. Ein zweidimensionales Modell zur thermohalinen Zirkulation unter dem Schelfeis. *In* Riemann, F. (Ed.), *Berichte zur Polarforschung,* 60: 87 pp.

Hillenbrand, C.-D., and Ehrmann, W., in press. Distribution of clay minerals in drift sediments on the continental rise west of the Antarctic Peninsula, ODP Leg 178, Sites 1095 and 1096. *In* Barker, P.F., Camerlenghi, A., Acton, G.D., and Ramsey, A.T.S. (Eds.), *Proc. ODP, Sci. Results*, 178: College Station, TX (Ocean Drilling Program).

Hillenbrand, C.-D., and Fütterer, D.K., in press. Neogene deposition of opal on the continental rise west of the Antarctic Peninsula, ODP Leg 178, Sites 1095, 1096, and 1101. *In* Barker, P.F., Camerlenghi, A., Acton, G.D., and Ramsey, A.T.S. (Eds.), *Proc. ODP, Sci. Results*, 178: College Station, TX (Ocean Drilling Program).

Hinz, K., Block, M., 1983. Results of geophysical investigations in the Weddell Sea and Ross Sea. *Proc. 11th World Pet. Congress*, 79-91.

Hoffmann, E.E., 1985. The large-scale horizontal structure of the Antarctic circumpolar current from FGGE drifters. *J. Geophys. Res.,* 90: 7087-7097.

Hollister, C.D., Craddock, C., and Bogdanov, Y. A., 1976. *Init. Repts., DSDP.* 35, Washington, D.C. (U.S. Govt. Printing Office) 929 pp.

Hovland, M., Backman, J., Coakley, B., Collett, T., Darby, D., Foucher, J.P., Francis, T., Gelfgat, M., Gorshkovsky, A., Jokat, W., Kaminski, M., Kristoffersen, Y., Takahashi, K., Thiede, J., Wiley, C., and Zachos, J., 2001. The high-Antarctic drilling challenge: Excerpts from the final report of the Arctic's role in global change Program Planning Group (APPG). *JOIDES Journal*, 27(1): 7-20.

Howard, W.R., and Prell, W.L., 1992. Late Quaternary surface circulation of the Southern Indian Ocean and its relationship to orbital variations. *Paleoceanography*, 7(1): 79-117.

Hutchins, R.W., McKeown, D., and King, L.H., 1976. A deep tow high resolution seismic system for continental shelf mapping. *Geoscience Can.*, 3: 95-100.

Huybrechts, P., 1993. Glaciological modelling of the late Cenozoic east Antarctic ice sheet: Stability or dynamism. *Geograf. Ann.*, 70A: 221-238.

Ingólfsson, Ó., Hjort, C., Bergman, P.A., Björk, S., Colhoun, E., Goodwin, I.D., Hall, B., Hirakawa, K., Melles, M., Möller, P., and Prentice, M.L., 1998. Antarctic glacial history since the last glacial maximum; an overview of the record on land. *Antarctic Science*, 10(3): 325-344.

Ishman, S.E., and Rieck, H.J., 1992. A late Neogene Antarctic glacio-eustatic record, Victoria Land Basin Margin, Antarctica. *In* Kennett, J.P., and Warnke, D.A. (Eds.), *The Antarctic Paleoenvironment: A perspective on global change:* Antarctic Research Series, 56: 327-347.

Jankowsky, E.J., and Drewry, D.J., 1981. The structure of West Antarctica from geophysical studies. *Nature*, 291: 17-21.

Kasten, S., and Joergensen, B.B., 2000. Sulfate reduction in marine sediments. *In* Schulz, H.D., and Zabel, M. (Eds.), *Marine Geochemistry:*Berlin, (Springer), 263-281.

Kearey, P., and Brooks, M., 1984. An introduction to geophysical exploration. *Geoscience Texts,* 4: Oxford (Blackwell Scientific Publications), 299 pp.

Kellogg, D.E., and Kellogg, T.B., 1996. Diatoms in South Pole ice: Implications for eolian contamination of Sirius Group deposits. *Geology*, 24: 115 -118.

Kennett, J.P., and Barker, P.F., 1990. Latest Cretaceous to Cenozoic climate and oceanographic developments in the Weddell Sea, Antarctica: An ocean-drilling perspective. *In* Barker, P.F., Kennett, J.P. (Eds.), *Proc. ODP, Sci. Results:* College Station, TX (Ocean Drilling Program) 113: 937-960.

Kennett, J.P., and Hodell, D., 1995. Stability or instability of Antarctic Ice Sheets during warm climates of the Pliocene? *GSA Today*, 5(1): 9-13.

Kennett, J.P., and Hodell, D.A., 1993. Evidence for relative climatic stability of Antarctica during the early Pliocene: A marine perspective. *Geogr. Ann.*, 75A: 205-220.

Kim, Y., Kim, H.-S., Larter, R.D., Camerlenghi, A., Gambôa, L.A.P., and Rudowski, S., 1995. Tectonic deformation in the upper crust and sediments at the South Shetland Trench. *In* Cooper, A.K., Barker, P.F., and Brancolini, G. (Eds.), *Geology and Seismic Stratigraphy of the Antarctic Margin:* Antarctic Research Series, 68: 157-166.

Kimura, K., 1982. Geological and geophysical survey in the Bellingshausen Basin, off Antarctica. *Antarctic Record*, 75: 12-24.

Kirby, M.E., 1993. *High resolution seismic stratigraphy and sedimentology of Holocene glacial marine deposits in the Palmer Deep, Bellingshausen Sea, Antarctica.* B.A. Thesis, Clinton, NY (Hamilton College), 60 pp.

Kirby, M.E., Domack, E.W., and McClennen, C.E., 1998. Magnetic stratigraphy and sedimentology of Holocene glacial marine deposits in the Palmer Deep, Bellingshausen Sea, Antarctica: Implications for climate change? *Marine Geology*, 152: 247-259.

Kleinschmidt, G., 1997. Antarktis, bei der Erforschung der Paläogeodynamik unverzichtbares Fragment früherer Großkontinente. *Cour. Forsch.-Inst. Senckenberg*, 201: 243-257.

Klepeis, K.A., and Lawver, L.A., 1996. Tectonics of the Antarctic-Scotia plate boundary near Elephant and Clarence Islands, West Antarctica. *J. Geophys. Res.*, 101(B9): 20211-20231.

Klimentos, T., 1991. The effects of porosity - permeability - clay content on the velocity of compressional waves. *Geophysics*, 56: 1930-1939.

Kreutz, K.J., Mayewski, P.A., Twickler, L.D., Whitlow, S.I., and Pittalwala, I.I., 1997. Bipolar changes in atmospheric circulation during the Little Ice Ages. *Science*, 277: 1294-1296.

Kuvaas, B., and Kristoffersen, Y., 1991. The Crary Fan: A trough-mouth fan on the Weddell Sea continental margin, Antarctica. *Marine Geology*, 97: 354-362.

LaBrecque, J.L., and Cande, S.C., 1985. Total intensity magnetic anomaly profiles. I:n South Atlantic Ocean and adjacent Antarctic continental margin, 13, Ocean Margin Drilling Program. *In* LaBrecque, J.L. (Ed.), *Regional Atlas Series,* 13*:* Mar. Sci. Int., Woods Hole, MA, sheet 9.

Larter, R.D., and Barker, P.F., 1989. Seismic stratigraphy of the Antarctic Peninsula Pacific margin: A record of Pliocene-Pleistocene ice volume and paleoclimate. *Geology*, 17(8): 731-734.

Larter, R.D., and Barker, P.F., 1991. Effects of ridge crest-trench interaction on Antarctic-Phoenix spreading: Forces on a young subducting plate. *J. Geophys. Res.,* 96: 19583-19607.

Larter, R.D., and Cunningham, A.P., 1993. The depositional pattern and distribution of glacial-interglacial sequences on the Antarctic Peninsula Pacific margin. *Mar. Geol*, 109: 203-219.

Larter, R.D., Rebesco, M., Vanneste, L.E., Gamboa, L.A.P., and Barker, P.F., 1994. Seismic reflection investigations on the Pacific margin of the Antarctic Peninsula. *In* Cooper, A.K., Barker, P.F., and Brancolini, G. (Eds.), *Geology and Seismic Stratigraphy of the Antarctic Margin*, 1. Am. Geophys. Union Antarct. Res. Ser., 68: 271-274.

Larter, R.D., Rebesco, M., Vanneste, L.E., Gamboa, L.A.P., and Barker, P.F., 1997. Cenozoic tectonic, sedimentary and glacial history of the continental shelf west of Graham Land, Antarctic Peninsula. *In* Barker, P.F., and Cooper, A.K. (Eds.), *Geology and Seismic Stratigraphy of the Antarctic Margin*, 2. Am. Geophys. Union Antarct. Res. Ser., 71: 1-27.

Lawver, L.A., Gahagan, L. M., and Coffin, M. F., 1992. The development of paleoseaways around Antarctica. *In* Kennet, J.P., Warnke, D.A. (Ed.), *The Antarctic paleoenvironment: A perspective on global change I:* Antarctic Research Series, 56: Washington D.C. (AGU), 7-30.

Lawver, L.A., Gahagan, L.M., and Dalziel, I.W.D., 1999. A tight fit-early Mesozoic Gondwana. A plate reconstruction perspektive. *In* Motoyoshi, Y., and Shiraishi, K. (Eds.), *Origin and Evolution of Continents: Proceedings of the International Symposium "Origin and Evolution of Continents": Memoirs of National Institute of Polar Research:* Tokyo, 214-229.

Lawver, L.A., Keller, R.A., Fisk, M.R., and Strelin, J.A., 1995. Bransfield Basin, Antarctic Peninsula: Active extension behind a dead arc. *In* Taylor, B. (Ed.), *Back Arc Basins: Tectonic and Magmatism:* Amsterdam (Plenum Press), 315-342.

Lawver, L.A., Royer, J.-Y., Sandwell, D.T., and Scotese, C.R., 1991. Evolution of the Antarctic continental margins. *In* Thomson, M.R.A., Crame, J.A., and Thomson, J.W.

(Eds.), *Geological Evolution of Antarctica:* Cambridge (Cambridge University Press), 533-540.

Lawver, L.A., Sloan, B.J., Barker, D.H.N., Ghidella, M., Von Herzen, R.P., Keller, R.A., Klinkhammer, G.P., and Chin, C.S., 1996. Distributed, active extension in Bransfield Basin, Antarctic Peninsula: Evidence from multibeam bathymetry. *GSA Today*, 6 (11): 1-6.

Lear, C.H., Elderfield, H., and Wilson, P.A., 2000. Cenozoic deep-sea temperatures and global ice volumes from Mg/Ca in benthic foraminiferal calcite. *Science*, 287: 269-272.

Lemke, P., Trinkle, E.W., and Hasselmann, K., 1981. Stochastic dynamic analysis of Polar sea ice variability. *Journal of Physical Oceanography*, 10: 2100-2120.

Leventer, A., Domack, E.W., Ishman, S.E., Brachfeld, S., McClennen, C.E., and Manley, P., 1996. Productivity cycles of 200-300 years in the Antarctic Peninsula region: understanding linkages among the sun, atmosphere, oceans, sea ice, and biota. *Geol. Soc. Am. Bull.*, 108: 1626-1644.

Lodolo, E., and Camerlenghi, A., 2000. The occurrence of BSRs on the Antarctic Margin. *In* Max, M.D. (Ed.), *Natural gas hydrate in oceanic and permafrost environments:* Dordrecht (Kluwer), *Coastal Systems and Continental Margins*, 5, 199-212.

Lozano, J.A., and Hays, J.D., 1976. Relationship of radiolarian assemblages to sediment types and physical oceanography in the Atlantic and western Indian Ocean sectors of the Antarctic Ocean. *Geological Society of America, Memoir*, 145: 303-336.

Lutjeharms, J.R.E., Walters, N.M., and Allanson, B.R., 1985. Oceanic frontal systems and biological enhancement. *In* Siegfried, W.R., Condy, P.R., and Laws, R.M. (Eds.) *Antarctic nutrient cycles and food webs:* Berlin (Springer), 11-21.

Luyten, J.R., Pedlosky, J., and Stommel, H., 1983. The ventilated thermocline. *J. Phys. Oceanogr.*, 13: 292-309.

Maldonaldo, A., Larter, R.D., and Aldaya, F., 1994. Forearc tectonic evolution of the South Shetland margin, Antarctic Peninsula. *Tectonics*, 13: 1345-1370.

Matthews, M.D., 1991. The effect of pretreatment on size analysis. *In* Syvitski, J.P.M. (Ed.), *Principles, methods, and application of particle size analysis*: Cambridge (Cambridge University Press), pp. 34-42.

Mayer, L., Courtney, R.C., and Moran, K., 1987. *Novel acoustics application / sea floor engineering*: IEEE Conference, 1-5, 139 pp.

McCave, I.N., Bryant, R.J., Cook, H.F., and Coughanowr, C.A., 1986. Evaluation of a laser-diffraction-size analyser for use with natural sediments. *J. Sed. Petrology*, 56 (4): 561-564.

McCave, I.N., Manighetti, B., and Beveridge, N.A.S., 1995a. Circulation in the glacial North Atlantic inferred from grain-size measurements. *Nature*, 374: 149-152.

McCave, I.N., Manighetti, B., and Robinson, S.G., 1995b. Sortable silt and fine sediment size / composition slicing: Parameters for paleocurrent speed and paleoceanography. *Paleoceanography*, 10(3): 593-610.

McGinnis, J.P., and Hayes, D.E., 1995. The roles of down-slope and along-slope depositional processes: Southern Antarctic Peninsula continental rise. *In:* Cooper, A.K., Barker, P.F.,

and Brancolini, G. (Eds.), *Geology and Seismic Stratigraphy of the Antarctic Margin.* Am. Geophys. Union, Antarct. Res. Ser., 68: 141-156.

Miller, K.G., Fairbanks, R.G., and Mountain, G.S., 1987. Tertiary oxygen isotope synthesis, sea-level history, and continental margin erosion. *Paleoceanography*, 2: 1 - 19.

Miller, K.G., Wright, J.D., and Fairbanks, R.G., 1991. Unlocking the Ice House: Oligocene-Miocene oxygen isotopes, eustasy, and margin erosion. *J. Geophys. Res.*, 96 (4): 6829-6848.

Moerz, T., and Moran, K., 1999. Alteration von sedimentphysikalischen Parametern während der Probenlagerung. *Zbl. Geol. Paläont.,* Teil I (Heft 5-6): 461-473.

Moerz, T., and Wolf-Welling, T.C.W., in press. Fine-fraction grain-size distribution data from Site 1095 offers links to an unbiased discrimination of depositional processes (ODP Leg 178, Western Antarctic Peninsula). *In* Barker, P.F., Camerlenghi, A., Acton, G.D., and Ramsay, A.T.S. (Eds.), *Proc. ODP, Sci. Results*, 178: College Station, TX (Ocean Drilling Program).

Moerz, T., Laronga, R., Lauer-Leredde, C., Escutia, C., and Wolf-Welling, T.C.W., in press. Composite velocity profile of shelf Site 1103 (ODP Leg 178, Western Antarctic Peninsula). *In* Barker, P.F., Camerlenghi, A., Acton, G.D., and Ramsay, A.T.S. (Eds.), *Proc. ODP, Sci. Results*, 178: College Station, TX (Ocean Drilling Program).

Mosher, D.C. et al., 1993. Seismic stratigraphy of the Ontong Java Plateau. *In* Berger, W.H., et al. (Eds.), *Proc. ODP, Sci. Results*, 130: College Station, TX (Ocean Drilling Program), 33-49.

Müller, D.W., Hodell, D.A., and Cisielski, P.F., 1991. Late Miocene to earliest Pliocene (9.8-4.5 Ma) paleoceanography of the subantarctic Southeast Atlantic: stable isotopic, sedimentologic, and microfossil evidence. *In* Ciesielski, P.F., Kristofferson, Y., et al. (Eds.), *Proc. ODP, Sci. Results,* 114*:* College Station, TX (Ocean Drilling Program), 459-474.

Müller, P.J., and Schneider, R., 1993. Production and pelagic dissolution of biogenic silica in the Southern Ocean. *Geochim. Cosmochim. Acta,* 46: 491-501.

Nafe, J.E., and Drake, C.L., 1957. Variation with depth in shallow and deep water marine sediments of porosity density and the velocities of compressional and shear waves. *Geophysics*, 22: 523-552.

Nowlin, W.D., and Zenk, W., 1988. Westward bottom currents along the margin of the South Shetland Island Arc. *Deep-Sea Research,* 35: 269-301.

Nürnberg, D., and Müller, R.D., 1991. The tectonic evolution of the South Atlantic from late Jurassic to present. *Tectonophysics*, 19: 27-53.

O'Brien, P.E., Cooper, A.K., Richter, C., Macphail, M., Truswell, E.M., and Shipboard Scientific Party, 2000. Milestones in Antarctic Ice Sheet history – preliminary results from Leg 188 drilling in Prydz Bay, Antarctica. *JOIDES Journal,* 26(2): 4-10.

Orsi, A.H., Whitworth, T., and Nowlin, W.D., 1995. On the meridional extent and fronts of the Antarctic Circumpolar Current. *Deep-Sea Research*, 42(5): 641-673.

Osterman, L.E., Poore, R.Z., and Barron, J., 2001. Climate Variability of the Holocene, Site 1098, Palmer Deep, Antarctica. In: Barker, P.F., Camerlenghi, A., Acton, G.D. and.

Ramsay, A.T.S (Eds.), *Proc. ODP., Sci. Results*, 178: College Station, TX (Ocean Drilling Program).

Paillard, D., Labeyrie, L. and Yiou, P., 1996. Macintosh program performs time-series analysis, *Eos Transact. AGU,* 77: 379 pp.

Park, Y.-H., Gambéroni, L., and Charriaud, E., 1993. Frontal structure, water masses, and circulation in the Crozet Basin. *J. Geophys. Res., B,* 98(7): 12,361- 12,385.

Parkinson, C.L., 1992. Interannual variability of monthly Southern Ocean sea ice distributions. *J. Geophys. Res., B,* 97: 5349-5363.

Parkinson, C.L., 1994. Spatial patterns in the length of the sea ice season in the Southern Ocean, 1979-1986. *J. Geophys. Res., B,* 99: 16327-16339.

Pickard, G.L., and Emery, W.J. (Eds.), 1982. *Descriptive physical oceanography:* Oxford, New York, Toronto, Sydney, Paris, Frankfurt (Pergamon Press), 249 pp.

Pickering, K.T., Hiscott, R., and Hein, F.J., 1989. *Deep-marine environments: Clastic sedimentation and tectonics*: London (Unwin Hyman).

Piper, D.J.W., 1978. Turbidite muds and silts on deepsea fans and abyssal plains. *In* Stanley, D.J., and Kelling, G. (Eds.), *Sedimentation in submarine canyons, fans and trenches:* Stroudsburg, PA (Dowden, Hutchinson and Ross),163-175.

Pollard, D., and DeConto, R.M., 2001. Modelling of Antarctic ice-sheet initiation in the early Oligocene using a coupled GCM and dynamic ice-sheet model. *In*: Florindo, F., and Cooper, A.K. (Eds.), *The geologic record of the Antarctic ice sheet from drilling, coring and seismic studies:* Quaderni di geofisica, 16: Roma, 151-152.

Posewang, J., and Mienert, J., 1999. The enigma of double BSRs: Indicators for changes in the hydrate stability field. *Geo-Mar. Lett.*, 19: 157-163.

Powell, C.M.A., 1993. Assembly of Gondwanaland - Open Forum. *In* Findlay, R.H., Unrug, R., Banks, M.R., and Veevers, J.J. (Eds.), *Gondwana eight*: Balkema, Rotterdam, 219-237.

Prentice, M.L., and Matthews, R.K., 1991. Tertiary ice sheet dynamics: The snow gun hypothesis. *J. Geophys. Res.,B,* 96 (4): 6811-6827.

Pribnow, D.F.C., Kinoshita, M., and Stein, C.A., 2000. *Thermal data collection and heat flow recalculations for Ocean Drilling Program Legs 101-180. DFG Pr471/2*: Hannover (Institut für Geowissenschaftliche Gemeinschaftsaufgaben (GGA)), 25 pp.

Prinz, H., 1991. *Abriß der Ingenieurgeologie:* Stuttgart (F. Enke Verl.), 2. Ed., 466 pp.

Pudsey, C.J., and Camerlenghi, A., 1998. Glacial-interglacial deposition on a sediment drift on the Pacific Margin of the Antarctic Peninsula. *Antarct. Sci.,* 10: 286-308.

Pudsey, C.J., Barker, P.F., and Larter, R.D., 1994. Ice sheet retreat from the Antarctic Peninsula shelf. *Continental Shelf Research*, 14: 1647-1675.

Pudsey, C.J., in press. 12. Data Report: Grain-size data, Sites 1095, 1096, and 1101, Antarctic Peninsula continental rise. *In* Barker, P.F., Camerlenghi, A., Acton, G.D., and Ramsay, A.T.S. (Eds.), *Proc. ODP, Sci. Results*, 178: College Station, TX (Ocean Drilling Program).

Quilty, P.G., 1993. Coastal east Antarctic Neogene sections and their contribution to the ice sheet evolution debate. *In* Kennett, J.P., and Warnke, D.A. (Eds.), *The Antarctic*

paleoenvironment: A perspective on global change: Antarctic Research Series, 60: 251-264.

Quilty, P.G., 1996. The Pliocene environment of Antarctica. *Papers and Proceedings of the Royal Society of Tasmania*, 130: 1-8.

Rabiner, L.R., and B. Gold, 1975. *Theory and Application of Digital Signal Processing.* Englewood Cliffs, NJ (Prentice-Hall), 241 pp.

Rebesco, M., Camerlenghi, A., and Zanolla, C., 1998a. Bathymetry and morphogenesis of the continental margin west of the Antarctic Peninsula. *Terra Antarct.*, 5(4): 715-728.

Rebesco, M., Camerlenghi, A., De Santis, L., Domack, E.W., and Kirby, M.E., 1998b. Seismic stratigraphy of Palmer Deep: a fault-bounded late Quaternary sediment trap on the inner continental shelf, Antarctic Peninsula Pacific margin. *Marine Geology*, 151: 89-110.

Rebesco, M., Larter, R.D., Barker, P.F., Camerlenghi, A., and Vanneste, L.E., 1997. The History of Sedimentation on the Continental Rise West of the Antarctic Peninsula, Geology and Seismic Stratigraphy of the Antarctic Margin, Part 2. *Antarctic Research Series*, 71: 29-49.

Rebesco, M., Larter, R.D., Camerlenghi, A., and Barker, P.F., 1996. Giant sediment drifts on the continental rise of the Antarctic Peninsula. *Geo-Mar. Lett.,* 16: 65-75.

Rintoul, S.R., Donguy, J.-R. , and Roemmich, D.H., 1997. Seasonal evolution of upper ocean thermal structure between Tasmania and Antarctica. *Deep-Sea Research*, 44: 1185-1202.

Robin, G.d.Q., 1983. The climate record in polar ice sheets: Cambridge (Cambridge University Press), 212 pp.

Sarnthein, M., Winn, K., Jung, S.J.A., Duplessy, J.-C., Labeyrie, L., Erlenkeuser, H., and Ganssen, G., 1994. Changes in east Atlantic deepwater circulation over the last 30,000 years: Eight time slice reconstructions. *Paleoceanography*, 9 (2): 209-267.

Scherer, R.P., 1993. There is direct evidence for collapse of the West Antarctic ice sheet. *Journal of Glaciology*, 39: 716 - 722.

Scherer, R.P., Aldahan,A., Tulaczyk, S., Possnert, G., Engelhardt, H., and Kamb, B., 1998. Pleistocene Collapse of the West Antarctic ice sheet. *Science*, 281:82-85.

Schlumberger, 1991. *Log Quality Control Reference Manual.* Houston, TX (Schlumberger Educational Services), 30-39 and 112-115.

Schlumberger, 1996. *Log Interpretation Principles/Applications.* Houston, TX (Schlumberger Educational Services).

Schön, J., 1984. *Petrophysik: Physikalische Eigenschaften von Gesteinen und Mineralen*: Stuttgart (F. Enke Verl.), 405 pp.

Schreiber, B.C., 1968. Sound velocity in deep sea sediments. *J. Geophys. Res.*, 73: 1259-1268.

Schweitzer, P.N., 1995. *Monthly averaged polar sea-ice concentration.* Virginia (U.S. Geological Survey Data Series) CD, Ed.1. DDS-27.

Shackleton, N.J., Hall, M.A., and Pate, D., 1995. Pliocene stable isotope stratigraphy of Site 846. *In* Pisias, N.G., Mayer, L.A., Janecek, T.R., Palmer-Julson, A., and van Andel,

T.H. (Eds.), *Proc. Ocean Drill. Program Sci. Results*, 138: College Station, TX (Ocean Drilling Program), 337-353.

Shevenell, A.E., Domack, E.W., and Kernan, G.M., 1996. Record of Holocene paleoclimate change along the Antarctic Peninsula: Evidence from glacial marine sediments, Lallemand Fjord. *Pap. Proc. R. Soc. Tas.*, 130(2): 55-64.

Shipboard Scientific Party, 1989. Leg 119: Site 739. *In* Barron, J., Larsen, B., et al. (Eds.), *Proc. ODP, Init. Repts.*, 119: College Station, TX (Ocean Drilling Program), 289-344.

Shipboard Scientific Party, 1999. Palmer Deep (Sites 1098 and 1099). *In*: P.F. Barker, A. Camerlenghi, G.D. Acton, et al. (Editors), *Proc. ODP, Init. Repts., 178: available from* http://www.odp.tamu.edu/publications/178_IR/chap_07/chap_07.htm. (1999-08- 31).

Shipboard Scientific Party, 1999a. Leg 178: Explanatory notes. *In* Barker, P.F., Camerlenghi, A., Acton, G.D., et al. (Eds.), *Proc. ODP, Init. Repts.*, 178, 1-174 [CD-ROM]. Available from: Ocean Drilling Program, Texas A&M University, College Station, TX 77845-9547, U.S.A.

Shipboard Scientific Party, 1999b. Leg 178: Shelf transect (Sites 1100, 1102 and 1103). *In* Barker, P.F., Camerlenghi, A., Acton, G.D., et al. (Eds.), *Proc. ODP, Init. Repts.*, 178, 1-174 [CD-ROM]. Available from: Ocean Drilling Program, Texas A&M University, College Station, TX 77845-9547, U.S.A.

Shipboard Scientific Party, 1999c. Leg 178: Site 1095. *In* Barker, P.F., Camerlenghi, A., Acton, G.D., et al. (Eds.), *Proc. ODP, Init. Repts.*, 178, 1-174 [CD-ROM]. Available from: Ocean Drilling Program, Texas A&M University, College Station, TX 77845-9547, U.S.A.

Shipboard Scientific Party, 1999d. Leg 178. Summary. *In* Barker, P.F., Camerlenghi, A., Acton, G.D., et al. (Eds.), *Proc. ODP, Init. Repts.*, 178: College Station, TX (Ocean Drilling Program), 1–60.

Shipboard Scientific Party, 2000. Leg 189. The Tasmanian gateway between Australia and Antarctica – paleoclimate and paleoceanography. *In* Barker, P.F., Camerlenghi, A., Acton, G.D., et al. (Eds.), *Proc. ODP, Preliminary Report,* 189: College Station, TX (Ocean Drilling Program), 123 pp.

Sievers, H.A., and Nowlin, W.D., 1984. The Stratification and Water Masses at Drake Passage. *J. Geophys. Res.*, 89(C6): 10,489-10,514.

Sjunneskog, C., and Taylor, F., 2001. Postglacial marine diatom record of the Palmer Deep, Antarctic Peninsula (ODP Leg 178, Site 1098) I: Total diatom abundance. *Paleoceanography*: 16.

Smellie, J.L., Pankhurst, R.J., Thomson, M.R.A., and Davies, R.E.S., 1984. The geology of the South Shetland Islands: VI. Stratigraphy, geochemistry and evolution. *British Antarctic Survey Scientific Report*, 85: 1-85.

Sowers, T., and Bender, M., 1995. Climate records covering the last deglaciation. *Science*, 269: 210-213.

Sprintall, J., Peterson, R., Roemmich, D., and Gallo, J., 1997. High Resolution XBT/XCTD Measurements across Drake Passage. *International WOCE Newsletter*, 29: 18-19.

Steig, E.J., Brook, E.J., White, J.W.C., Sucher, C.M., Bender, M.L., Lehmann, S.J., Morse, D.L., Waddington, E.D., and Clow, G.D., 1998. Synchronous climate changes in Antarctica and the North Atlantic. *Science*, 282: 92-95.

Stoll, R.D., 1974. Acoustic waves in saturated sediments. *In* Hampton, L. (Ed.), *Physics of sound in marine sediments*: New York (Plenum Press), 19-39.

Stoll, R.D., 1985. Marine sediment acoustics. *J. Acoust. Soc. Am.*, 77: 1789-1799.

Stoll, R.D., 1989. *Sediment Acoustics*: Berlin (Springer Verl.), 153 pp.

Stoll, R.D., and Bryan, G.M., 1970. Wave attenuation in saturated sediments. *J. Acoust. Soc. Am.*, 47: 1440-1447.

Storey, B.C., 1997. An active mantel mechanism for Gondwana break-up. *Terra Nova*, 9 (Abstract Supplement No. 1): 217-218.

Storey, B.C., Vaughan, A.P.M., and Millar, I.L., 1996. Geodynamic evolution of the Antarctic Peninsula during Mesozoic times and its bearing on Weddell Sea history. *In* Storey, B.C., King, E.C., and Livermore, R.A. (Eds.), *Weddell Sea Tectonics and Gondwana Break-up:* London (Geol. Soc. Spec. Publ. London) 108, 87-103.

Stow, D.A.V., and Piper, D.J.W., 1984. Deep-water fine-grained sediments: facies models. *In* Stow, D.A.V., and Piper, D.J.W. (Eds.), *Fine-Grained Sediments: Deep-Water Processes and Facies:* London (Geol. Soc. Spec. Publ. London), 15, 611-645.

Studinger, M., 1998. Interpretation und Analyse von Potentialfelddaten im Weddellmeer, Antarktis: der Zerfall des Superkontinents Gondwana. *In* F. Riemann (Ed.), *Berichte zur Polar - und Meeresforschung,* 276: Bremerhaven, 134 pp.

Stuiver, M., Reimer, P.J., Bard, E., Beck, J.W., Burr, G.S., Hugen, K.A., Kromer, B., McCormac, G., van der Plicht, J., and Spurk, M., 1998. INTCAL 98 radiocarbon age calibration, 24,000-0 cal BP. *Radiocarbon*, 40 (3): 1041-1083.

Talley, L.D., 1996. Antarctic Intermediate Water in the South Atlantic. *In*: Wefer, G., Berger, W.H., Siedler, G., and Webb, D.J. (Eds.), *The South Atlantic: Present and past Circulation*: Berlin, Heidelberg (Springer), 219-238.

Tanahashi, M., 2001. Geology of northern offshore of Antarctic Peninsula. *In* Florindo, F., and Cooper, A.K. (Eds.), *The geologic record of the Antarctic ice sheet from drilling, coring and seismic studies:* Quaderni di geofisca, 16: Roma, 177-178.

Tarney, J., Weaver, S.D., Saunders, A.D., Pankhurst, R.J., and Barker, P.F., 1982. Volcanic evolution of the northern Antarctic Peninsula and the Scotia arc. *In* Thorpe, R.S. (Ed.), *Evolution of Andesite Volcanic Provinces*: John Wiley & Sons (Chichester), 371-399.

Taylor, F., 1999. *Sedimentary diatom assemblages of Prydz Bay and Mac.Robertson Shelf, East Antarctica, and their use as paleoecological indicators.* Ph.D. Thesis, University of Tasmania, 284 pp.

Taylor, F., and Sjunneskog, C., 2001. Postglacial marine diatom record of the Palmer Deep, Antarctic Peninsula (ODP Leg 178, Site 1098) II: Diatom assemblages. Paleoceanography: 39 pp.

Tchernia, P., 1980. *Descriptive Regional Oceanography*: Oxford (Pergamon Marine Series Press, 3): 43-84; pl. 1-3, 10-19.

Ten Brink, U.S., and Cooper, A.K., 1992. Modeling the bathymetry of Antarctic continental margins. *In* Yoshida, Y., Kaminuma, K., and Shiraishi, K. (Eds.), *Recent Progress in Antarctic Earth Science*: Tokyo (Terra Scientific Publishing), 763-772.

Ten Brink, U.S., Schneider, C., and Johnson, A.H., 1995. Morphology and stratal geometry of the Antarctic continental shelf: Insights from models. *In* Cooper, A.K., Barker, P.F., and Brancolini, G. (Eds.), *Geology and seismic stratigraphy of the Antarctic margin*: Antarctic Research Series, 68: Washington, D.C. (AGU), 1-24.

Thiede, J. (Ed.), 1986. *Zur geologischen Geschichte der Polarmeere und ihrer Wassermassen: Paläophysiographie, Paläoklimatologie, Paläontologie, Sedimentation und Ozeanographie*: Geologisch-Paläontologisches Institut und Museum der Christian-Albrechts-Universität (Kiel), 312 pp.

Tiedemann, R., and Franz, S.O., 1997. Deep-water circulation, chemistry, and terrigenous sediment supply in the equatorial Atlantic during the Pliocene, 3.3 - 2.6 Ma and 5 - 4.5 Ma. *In* Shackleton, N.J., Curry, W.B., Richter, C., and Bralower, T.J. (Eds.), *Proc. ODP, Sci. Results:* College Station, TX (Ocean Drilling Program), 154, 299 - 318.

Tiedemann, R., Sarnthein, M., and Shackleton, N.J., 1994. Astronomic timescale for the Pliocene Atlantic $\delta^{18}O$ and dust flux records of Ocean Drilling Program Site 659. *Paleoceanography*, 9: 619-638.

Tinivella, U., Camerlenghi, A., and Rebesco, M., in press. Seismic velocity analysis on the continental shelf transect, ODP Leg 178, Antarctic Peninsula. *In* Barker, P.F., Camerlenghi, A., Acton, G.D., et al. (Eds.), *Proc. ODP, Sci. Results,* 178: College Station, TX (Ocean Drilling Program).

Vanneste, L.E., and Larter, R.D., 1995. Deep-tow boomer survey on the Antarctic Peninsula Pacific margin: An investigation of the morphology and acoustic characteristics of late Quaternary sedimentary deposits on the outer continental shelf and upper slope. *In* Cooper, A.K., Barker, P.F., and Brancolini, G. (Eds.), *Geology and seismic stratigraphy of the Antarctic margin:* Antarctic Research Series, 68: 97-121.

Volpi, V., Camerlenghi, A., Moerz, T., Corubolo, P., Rebesco, M., and Tinivella, U., in press. Data report: Physical properties relevant to seismic stratigraphic studies, continental rise Sites 1095, 1096, and 1101, ODP Leg 178, Antarctic Peninsula. *In* Barker, P.F., Camerlenghi, A., Acton, G.D., and Ramsay, A.T.S. (Eds.), *Proc. ODP, Sci. Results*, 178, College Station, TX (Ocean Drilling Program).

Von Bernuth, G., 1988. Laser-Partikel-Sizer "analysette 22": Ein Labor- und Betriebsmeßgerät zur Messung von Partikelgrößenverteilungen an mineralischen und synthetischen Rohstoffen. *TiZ*, 5: 6 pp.

Weaver, P.P.E., Carter, L., and Neil, H.L., 1998. Response of surface water masses and circulation to late Quaternary climate changes east of New Zealand. *Paleoceanography*, 13(1): 70-83.

Webb, P.N., and Harwood, D.M., 1991. Late Cenozoic glacial history of the Ross Embayment, Antarctica. *Quaternary Science*, 10: 215-223.

Webb, P.-N., and Harwood, D.M., 1993. Pliocene fossil Nathofagus (Southern Beech) from Antarctica: phytogeography, dispersal strategies, and survival in high-latitude glacial-

deglacial environments. *In* Alden, J.E.A. (Ed.), *Forest Development in Cold Climates:* New York (Plenum Press), 135-163.

Webb, P.N., Harwood, D.M., McKelvey, B.C., Mercer, J.H., and Stott, L.D., 1984. Cenozoic marine sedimentation and ice volume variation on the East Antarctic craton. *Geology*, 12 (5): 287-291.

White, R.S., and McKenzie, D.P., 1989. Magmatism at rift zones: The generation of volcanic continental margins and flood basalts. *J. Geophys. Res., B*, 94: 7685- 7729.

White, W.B., and Peterson, R.G., 1996. An Antarctic circumpolar wave in surface pressure, wind, temperature and sea-ice extent. *Nature,* 380: 699-702.

Wolf, T.C.W., 1991. Paläo-ozeanographisch-klimatische Entwicklung des nördlichen Nordatlantiks seit dem späten Neogen (ODP Legs 105 und 104, DSDP Leg 81). *GEOMAR Report*, 5: 92pp.

Wolf-Welling, T.C.W., Moerz, T., Hillenbrand, C.-D., Pudsey, C.J., and Cowan, E., in press. 15. Data Report: Bulk sediment parameters ($CaCO_3$, TOC, and >63 μm) of Sites 1095, 1096, and 1101, and coarse-fraction analysis of Site 1095 (ODP Leg 178, Western Antarctic Peninsula). *In* Barker, P.F., Camerlenghi, A., Acton, G.D., et al., *Proc. ODP, Sci. Results*, 178: College Station, TX (Ocean Drilling Program).

Wood, A.B., 1941. *A Textbook of Sound*: London (Bell & Sons), 578 pp.

Wright, J.D., Miller, K.G., and Fairbanks, R.G., 1992. Early and middle Miocene stable isotopes: implications for deepwater circulation and climate. *Paleoceanography*, 7: 357-389.

Wyllie M.R.J., Gregory, A.R., and Gardner, G.H.F., 1958. An experimental investigation of factors affecting elastic wave velocities in porous media. *Geophysics,* 23: 459-493.

Wyllie, M.R.J., Gregory, A.R., and Gardner, L.W., 1956. Elastic wave velocities in heterogeneous and porous media. *Geophysics*, 22: 41-70.

Zachos, J.C., Lohmann, K.C., Walker, J.C.G., and Wise, S.W., 1993. Abrupt climate change and transient climates during the Paleogene: A marine perspective. *J. Geol.*, 101: 191-213.

Zachos, J.C., Pagani, M., Sloan, L., Thomas, E., and Billups, K., 2001. Trend, rhythms, and aberrations in global climate 65 Ma to present. *Science*, 292: 686-693.

„Berichte zur Polarforschung"
Eine Titelübersicht der Hefte 1 bis 376 (1981 - 2000) erschien zuletzt im Heft 413 der nachfolgenden Reihe „Berichte zur Polar- und Meeresforschung". Ein Verzeichnis aller Hefte beider Reihen sowie eine Zusammenstellung der Abstracts in englischer Sprache finden Sie im Internet unter der Adresse:
http://www.awi-bremerhaven.de/Resources/publications.html

Ab dem Heft-Nr. 377 erscheint die Reihe unter dem Namen:
„Berichte zur Polar- und Meeresforschung"

Heft-Nr. 377/2000 – „Rekrutierungsmuster ausgewählter Wattfauna nach unterschiedlich strengen Wintern" von Matthias Strasser

Heft-Nr. 378/2001 – „Der Transport von Wärme, Wasser und Salz in den Arktischen Ozean", von Boris Cisewski

Heft-Nr. 379/2001 – „Analyse hydrographischer Schnitte mit Satellitenaltimetrie", von Martin Losch

Heft-Nr. 380/2001 – „Die Expeditionen ANTARKTIS XI/1-2 des Forschungsschiffes POLARSTERN 1998/1999", herausgegeben von Eberhard Fahrbach und Saad El Naggar.

Heft-Nr. 381/2001 – „UV-Schutz- und Reparaturmechanismen bei antarktischen Diatomeen und *Phaeocystis antarctica*", von Lieselotte Riegger.

Heft-Nr. 382/2001 – „Age determination in polar Crustacea using the autofluorescent pigment lipofuscin", by Bodil Bluhm.

Heft-Nr. 383/2001 – „Zeitliche und räumliche Verteilung, Habitatspräferenzen und Populationsdynamik benthischer Copepoda Harpacticoida in der Potter Cove (King George Island, Antarktis)", von Gritta Veit-Köhler.

Heft-Nr. 384/2001 – „Beiträge aus geophysikalischen Messungen in Dronning Maud Land, Antarktis, zur Auffindung eines optimalen Bohrpunktes für eine Eiskerntiefbohrung", von Daniel Steinhage.

Heft-Nr. 385/2001 – „Actinium-227 als Tracer für Advektion und Mischung in der Tiefsee", von Walter Geibert.

Heft-Nr. 386/2001 – „Messung von optischen Eigenschaften troposphärischer Aerosole in der Arktis" von Rolf Schumacher.

Heft-Nr. 387/2001 – „Bestimmung des Ozonabbaus in der arktischen und subarktischen Stratosphäre", von Astrid Schulz.

Heft-Nr. 388/2001 – „Russian-German Cooperation SYSTEM LAPTEV SEA 2000: The Expedition LENA 2000", edited by Volker Rachold and Mikhail N. Grigoriev.

Heft-Nr. 389/2001 – „The Expeditions ARKTIS XVI/1 and ARKTIS XVI/2 of the Research Vessel 'Polarstern' in 2000", edited by Gunther Krause and Ursula Schauer.

Heft-Nr. 390/2001 – „Late Quaternary climate variations recorded in North Atlantic deep-sea ostracodes", by Claudia Didié.

Heft-Nr. 391/2001 – „The polar and subpolar North Atlantic during the last five glacial-interglacial cycles", by Jan. P. Helmke.

Heft-Nr. 392/2000 – „Geochemische Untersuchungen an hydrothermal beeinflußten Sedimenten der Bransfield Straße (Antarktis)", von Anke Dählmann.

Heft-Nr. 393/2001 – „The German-Russian Project on Siberian River Run-off (SIRRO): Scientific Cruise Report of the Kara-Sea Expedition 'SIRRO 2000' of RV 'Boris Petrov' and first results", edited by Ruediger Stein and Oleg Stepanets.

Heft-Nr. 394/2001 – „Untersuchung der Photooxidantien Wasserstoffperoxid, Methylhydroperoxid und Formaldehyd in der Troposphäre der Antarktis", von Katja Riedel.

Heft-Nr. 395/2001 – „Role of benthic cnidarians in the energy transfer processes in the Southern Ocean marine ecosystem (Antarctica)", by Covadonga Orejas Saco del Valle.

Heft-Nr. 396/2001 – „Biogeochemistry of Dissolved Carbohydrates in the Arctic", by Ralph Engbrodt.

Heft-Nr. 397/2001 – „Seasonality of marine algae and grazers of an Antarctic rocky intertidal, with emphasis on the role of the limpet *Nacilla concinna* Strebel (Gastropoda: Patellidae)", by Dohong Kim.

Heft-Nr. 398/2001 – „Polare Stratosphärenwolken und mesoskalige Dynamik am Polarwirbelrand", von Marion Müller.

Heft-Nr. 399/2001 – „North Atlantic Deep Water and Antarctic Bottom Water: Their Interaction and Influence on Modes of the Global Ocean Circulation", by Holger Brix.

Heft-Nr. 400/2001 – „The Expeditions ANTARKTIS XVIII/1-2 of the Research Vessel 'Polarstern' in 2000" edited by Victor Smetacek, Ulrich Bathmann, Saad El Naggar.

Heft-Nr. 401/2001 – „Variabilität von CH_2O (Formaldehyd) - untersucht mit Hilfe der solaren Absorptionsspektroskopie und Modellen" von Torsten Albrecht.

Heft-Nr. 402/2001 – „The Expedition ANTARKTIS XVII/3 (EASIZ III) of RV 'Polarstern' in 2000", edited by Wolf E. Arntz and Thomas Brey.

Heft-Nr. 403/2001 – „Mikrohabitatansprüche benthischer Foraminiferen in Sedimenten des Südatlantiks", von Stefanie Schumacher.

Heft-Nr. 404/2002 – „Die Expedition ANTARKTIS XVII/2 des Forschungsschiffes 'Polarstern' 2000", herausgegeben von Jörn Thiede und Hans Oerter.

Heft-Nr. 405/2002 – „Feeding Ecology of the Arctic Ice-Amphipod *Gammarus wilkitzkii*. Physiological, Morphological and Ecological Studies", by Carolin E. Arndt.

Heft-Nr. 406/2002 – „Radiolarienfauna im Ochotskischen Meer - eine aktuopaläontologische Charakterisierung der Biozönose und Taphozönose", von Anja Nimmergut.

Heft-Nr. 407/2002 – „The Expedition ANTARKTIS XVIII/5b of the Research Vessel 'Polarstern' in 2001, edited by Ulrich Bathmann.

Heft-Nr. 408/2002 – „Siedlungsmuster und Wechselbeziehungen von Seepocken (Cirripedia) auf Muschelbänken

(*Mytilus edulis* L.) im Wattenmeer", von Christian Buschbaum.

Heft-Nr. 409/2002 – „Zur Ökologie von Schmelzwassertümpeln auf arktischem Meereis - Charakteristika, saisonale Dynamik und Vergleich mit anderen aquatischen Lebensräumen polarer Regionen", von Marina Carstens.

Heft-Nr. 410/2002 – „Impuls- und Wärmeaustausch zwischen der Atmosphäre und dem eisbedeckten Ozean", von Thomas Garbrecht.

Heft-Nr. 411/2002 – „Messung und Charakterisierung laminarer Ozonstrukturen in der polaren Stratosphäre", von Petra Wahl.

Heft-Nr. 412/2002 – „Open Ocean Aquaculture und Offshore Windparks. Eine Machbarkeitsstudie über die multifunktionale Nutzung von Offshore-Windparks und Offshore-Marikultur im Raum Nordsee", von Bela Hieronymus Buck.

Heft-Nr. 413/2002 – „Arctic Coastal Dynamics. Report of an International Workshop. Potsdam (Germany) 26-30 November 2001", edited by Volker Rachold, Jerry Brown and Steve Solomon.

Heft-Nr. 414/2002 – „Entwicklung und Anwendung eines Laserablations-ICP-MS-Verfahrens zur Multielementanalyse von atmosphärischen Einträgen in Eisbohrkernen", von Heiko Reinhardt.

Heft-Nr. 415/2002 – „Gefrier- und Tauprozesse im sibirischen Permafrost – Untersuchungsmethoden und ökologische Bedeutung", von Wiebke Müller-Lupp.

Heft-Nr. 416/2002 – „Natürliche Klimavariationen der Arktis in einem regionalen hochauflösenden Atmosphärenmodell", von Wolfgang Dorn.

Heft-Nr. 417/2002 – „Ecological comparison of two sandy shores with different wave energy and morphodynamics in the North Sea", by Iris Menn.

Heft-Nr. 418/2002 – „Numerische Modellierung turbulenter Umströmungen von gebäuden", von Simón Domingo López.

Heft-Nr. 419/2002 – „Scientific Cruise Report of the Kara-Sea Expedition 2001 of RV „Academic Petrov": The German-Russian Project on Siberian River Run-off (SIRRO) and the Project „ESTABLISH", edited by Ruediger Stein and Oleg Stepanets.

Heft-Nr. 420/2002 – „Vulkanologie und Geochemie pliozäner bis rezenter Vulkanite beiderseits der Bransfield-Straße / West-Antarktis", von Andreas Veit.

Heft-Nr. 421/2002 – „POLARSTERN ARKTIS XVII/2 Cruise Report: AMORE 2001 (Arctic Mid-Ocean Ridge Expedition)", by J. Thiede et al.

Heft-Nr. 422/2002 – „The Expedition „AWI of RV „L'Atalante" in 2001", edited by Michael Klages, Benoit Mesnil, Thomas Soltwedel and Alain Christophe with contributions of the participants.

Heft-Nr. 423/2002 – „Über die Tiefenwasserausbreitung im Weddellmeer und in der Scotia-Sea: Numerische Untersuchungen der Transport- und Austauschprozesse in der Weddell-Scotia-Konfluenz-Zone", von Michael Schodlok.

Heft-Nr. 424/2002 – „Short- and Long-Term Environmental Changes in the Laptev Sea (Siberian Arctic) During the Holocene", von Thomas Müller-Lupp.

Heft-Nr. 425/2002 – „Characterisation of glacio-chemical and glacio-meteorological parameters of Amundsenisen, Dronning Maud Land, Antarctica", by Fidan Göktas.

Heft-Nr. 426/2002 – „Russian-German Cooperation SYSTEM LAPTEV SEA 2000: The Expedition LENA 2001", edited by Eva-Maria Pfeiffer and Mikhail N. Grigoriev.

Heft-Nr. 427/2002 – „From the Inner Shelf to the Deep Sea: Depositional Environments on the West Antarctic Peninsula Margin – A Sedimentological and Seismostratigraphic Study (ODP Leg 178)", by Tobias Mörz.

* vergriffen/out of print.
** nur noch beim Autor/only from the author.